A thesis submitted in partial fulfilment of the requirements for the Degree of

DOCTOR OF PHILOSOPHY

by

ASTA HEINESEN

INHOMOGENEOUS COSMOLOGY AND OBSERVATIONAL IMPLICATIONS

UNIVERSITY OF CANTERBURY
School of Physical & Chemical Sciences
2019

all homogeneous universes are alike;
every inhomogeneous universe is inhomogeneous in its own way.

ABSTRACT

We introduce a generalization of the 4−dimensional averaging window function of Gasperini, Marozzi and Veneziano (2010) that may prove useful for a number of applications. The covariant nature of spatial scalar averaging schemes to address the averaging problem in relativistic cosmology is an important property that is implied by construction, but usually remains implicit. We employ here the approach of Gasperini *et al.* for two reasons. First, the formalism and its generalization presented here are manifestly covariant. Second, the formalism is convenient for disentangling the dependencies on foliation, volume measure, and boundaries in the averaged expressions entering in scalar averaging schemes. These properties will prove handy for simplifying expressions, but also for investigating extremal foliations and for comparing averaged properties of different foliations directly. The proposed generalization of the window function allows for choosing the most appropriate averaging scheme for the physical problem at hand, and for distinguishing between the role of the foliation itself and the role of the volume measure in averaged dynamic equations. We also show that one particular window function obtained from this generalized class results in an averaging scheme corresponding to that of a recent investigation by Buchert, Mourier and Roy (2018) and, as a byproduct, we explicitly show that the general equations for backreaction derived therein are covariant.

Parameters that quantify the acceleration of cosmic expansion are conventionally determined within the standard Friedmann-Lemaître-Robertson-Walker (FLRW) model, which fixes spatial curvature to be homogeneous. Generic averages of Einstein's equations in inhomogeneous cosmology lead to models with non-rigidly evolving average spatial curvature, and different parametrizations of apparent cosmic acceleration. The timescape cosmology is a viable example of such a model without dark energy. Using the largest available supernova data set, the Joint Light-curve Analysis (JLA) catalogue, we find that the timescape model fits the luminosity distance-redshift data with a likelihood that is statistically indistinguishable from the standard spatially flat Lambda Cold Dark Matter (ΛCDM) cosmology by Bayesian comparison. In the timescape case cosmic acceleration is non-zero but has a marginal amplitude, with best-fitting apparent deceleration parameter, $q_0 = -0.043^{+0.004}_{-0.000}$. Systematic issues regarding standardization of supernova light curves are analysed. Cuts of data at the statistical homogeneity scale affect light curve parameter fits independent of cosmology.

A cosmological model dependence of empirical changes to the mean colour parameter is also found. Irrespective of which model ultimately fits better, we argue that as a competitive model with a non-FLRW expansion history, the timescape model may prove a useful diagnostic tool for disentangling selection effects and astrophysical systematics from the underlying expansion history.

We also perform a further analysis using the JLA catalogue. We examine the fit of a class of exact scaling solutions with dynamical spatial curvature formulated in the framework of a scalar averaging scheme for relativistic inhomogeneous spacetimes. In these models, global volume acceleration may emerge as a result of the non-local variance between expansion rates of clusters and voids, the latter gaining volume dominance in the late-epoch Universe. We find best-fit parameters for a scaling model of backreaction that are reasonably consistent with previously found constraints from SNIa, CMB, and baryon acoustic oscillations data. The quality of fit of the scaling solutions is indistinguishable from that of the ΛCDM model and the timescape cosmology from an Akaike Information Criterion (AIC) perspective. This indicates that a broad class of models can account for the $z \lesssim 1$ expansion history.

We develop methods for investigating baryon acoustic oscillation (BAO) features in cosmological models with non-trivial (but slowly varying) averaged spatial curvature: models that are not necessarily flat, close to flat, nor with constant spatial curvature. The class of models to which our methods apply include Lemaître-Tolman-Bondi models, modified gravity cosmologies, and inhomogeneous cosmologies with backreaction – in which we do not have a prediction of the shape of the spatial 2-point correlation function, but where we nevertheless expect to see a BAO feature in the present-day galaxy distribution, in the form of an excess in the galaxy 2-point correlation function. We apply our methods to the Baryon Oscillation Spectroscopic Survey (BOSS) dataset, investigating both the ΛCDM and timescape cosmological models as case studies. The correlation functions measured in the two fiducial models contain a similarly-pronounced BAO feature. We use the relative tangential and radial BAO scales to measure the anisotropic Alcock-Paczyński distortion parameter, ϵ, which is independent of the underlying BAO preferred scale. We find that ϵ is consistent with zero in both fiducial cosmologies, indicating that models with a different spatial curvature evolution can account for the relative positions of the tangential and radial BAO scale. We validate our methods using ΛCDM mock catalogoues.

We investigate – in a generic setting – the regime of applicability of the Alcock-

Paczyński (AP) scaling conventionally applied to test different cosmological models, given a fiducial measurement of the BAO characteristic scale in the galaxy 2-point correlation function. We quantify the error in conventional AP scaling methods, for which our ignorance about the true cosmology is parameterised in terms of two constant AP scaling parameters evaluated at the effective redshift of the survey. We propose a new, and as it turns out, improved version of the constant AP scaling, also consisting of two scaling parameters. The two constant AP scaling methods are almost indistinguishable when the fiducial model used in data reduction, and the 'true' underlying cosmology do not differ substantially in terms of metric gradients or when the redshift range of the measurements is small. When the fiducial model and the 'true' model differ substantially in terms of metric gradients, the two AP scaling methods differ in general. Our new methods can be applied to existing analysis through a reinterpretation of the results of the conventional AP scaling. This reinterpretation might be important in model universes where curvature gradients above the scale of galaxies are significant (and cannot be ignored by a suitable smoothing process).

We test our theoretical findings on ΛCDM mock catalogues where the underlying space-time model is known. The conventional constant AP scaling methods are surprisingly successful for pairs of large-scale metrics, but eventually break down when pathological models which allow for large metric gradients are tested. The new constant AP scaling methods proposed in this paper are efficient for all test models examined. We find systematic errors of $\sim$1% in the recovery of the BAO scale when the true model is distant from the fiducial, which are not attributed to any constant AP approximation. The level of systematics is robust to the exact fitting method employed. This indicates that the error budget of the BAO acoustic scale measurements in the standard literature is underestimated.

ACKNOWLEDGMENTS

I would like to thank my supervisor David Wiltshire for his careful reading of this thesis, and for the always interesting discussions and collaboration we have had in general. I wish to thank Thomas Buchert and his group for hospitality at the ENS, Lyon, France. I want to thank Chris Blake, Thomas Buchert, Lawrence Dam, Célia Desgrange, Yong-Zhuang Li, Pierre Mourier, and David Wiltshire for nice collaboration and scientific discussions. This work was supported by the UC doctoral scholarship and by Catalyst grant CSG-UOC1603 administered by the Royal Society of New Zealand. I am grateful for the support given by the funds: 'Knud Højgaards Fond', 'Torben og Alice Frimodts Fond', and 'Max Nørgaard og Hustru Magda Nørgaards Fond'.

CONTENTS

CHAPTER 1

Introduction

Cosmology is the discipline of describing overall dynamic properties of the Universe in an averaged or statistical sense. We have limited observational access to the Universe which we inhabit. Our information about the Universe is obtained indirectly, primarily through photons but also through neutrinos and gravitational waves. Thus the primary cosmological data comes in the form of a two-dimensional snap shot of energy and polarisation of photons arriving from different points of our past light cone. This picture has a depth in 'time' of approximately 14 billion years. The task is to work our way backwards from this picture to gain an understanding of our Universe.

For a cosmology founded on general relativistic principles, this aim is hard to obtain for at least three reasons:

(i) In General Relativity a global and canonical notion of time is not in general expected to exist. There is no unique and general way of extending the eigen-time of a world line to a global time parameter at each point in space-time. Thus, global dynamics is not easily defined since a natural 'laboratory frame' is missing. A cosmological model would usually describe congruences of fundamental observers following source fluid flows, and would naturally attempt to build global frames based on such a family of observers. However, the identification of observer congruences in our space-time, that 'at present day' involves a complicated hierarchy of structure, is a difficult task. Moreover, a congruence of fluid-comoving observers does not build global rest frames in the presence of vorticity (expected to appear on small scales), so that alternative definitions of observers-based spatial sections may be required.

(ii) Averages and statistical descriptions are not naturally formulated within General Relativity. Tensor quantities are intrinsic to the tangent-space in which they live; while there are ways of mapping tensor quantities between tangent-spaces, such

mappings are not unique. Furthermore, point particles as matter sources are not compatible with the formulation of General Relativity. For these reasons statistical matter descriptions are highly involved in General Relativity.

(iii) Cosmological data are limited in quantity and precision due to our single world-line section – which has close to zero extension when compared to the age of the Universe – from which we can perform observations, and due to the conditions for viewing the Universe from this world-line section. Einstein's equations as formulated as an initial value problem demand data as prescribed on spatial hypersurfaces, which include the interior of the light cone. The overwhelming complexity of General Relativity (GR) on the one hand and the poor constraining power of data on the other, make simplifying assumptions crucial for building a general relativistic model which can be constrained by data.

Many of the conceptual difficulties of macroscopic general relativity have historically been avoided in cosmology by assuming approximate decoupling of scales and imposing exact spatial homogeneity and isotropy for the assumed general relativistic solution for space-time valid on the largest scales. Such assumptions date back to the very founding of general relativistic cosmology.

When Albert Einstein first applied the theory of general relativity to cosmology in 1917 [1], he noted that *'on account of the lack of uniformity in the distribution of matter, the metrical structure of this continuum must necessarily be extremely complicated'*, but further made the remark that for the purpose of modelling the largest scales we might think of the matter distribution as being uniformly distributed. In the same paper he noted that *'the most important fact that we draw from experience as to the distribution of matter is that the relative velocities of the stars are very small as compared with the velocity of light. So I think that for the present we may base our reasoning upon the following approximative assumption'*. Einstein's first approximation was to model the matter distribution of the Universe as a perfect dust source – with all matter being at rest in some appropriate frame of reference – and to further model the matter distribution and the corresponding metric as spatially homogenous and isotropic.

The initial investigations of Einstein made within a static universe assumption laid the groundwork of many later important theoretical contributions in the 1920s and

1930s by Friedman, Lemaître, Robertson, Walker, Milne, Einstein, de Sitter, and others, e.g., [2, 3, 4, 5, 6, 7, 8] on *dynamical* space-time generalisations[1] – which attracted much attention after the important discovery[2] [9, 10] that the recorded redshift of distant objects was consistent with being proportional to their distance from us, indicating expansion of space itself. These theoretical contributions formed the Friedman-Lemaître-Robertson-Walker (FLRW) class of cosmological models which constitute the foundation of most modern cosmology. The FLRW class of space-times obey the same translational and rotational symmetries as the original class of static space-times investigated by Einstein.

At the time of the pioneering paper by Einstein galactic structures were not known, massive gravitational objects such as black holes and neutron stars had not been observed (directly or indirectly), and the matter distribution of the Universe was believed to be similar to the distribution of stars in our galaxy. The discovery in the 1920s by Edwin Hubble [11] that many distant objects previously classified as 'nebulae' were in fact galaxies beyond the Milky Way changed how astronomers perceived the Universe. Based on his own investigations on the statistical distribution of galaxies (or 'extra-galactic nebulae') Hubble concluded that *'The counts with large reflectors conform rather closely with the theory of sampling for a homogeneous population'* and that *'There are as yet no indications of a super-system of nebulae analogous to the system of stars'* [12]. Hubble's conclusions were artefacts of sparse sampling though, and it turned out that super-systems of galaxies do exist in the form of galaxy clusters and filaments. The mapping of structure in our Universe has become still more refined over the past century, and modern maps reveal a rich hierarchy of structure known as the 'cosmic web' [13, 14].

The continued unraveling of the complicated matter distribution of our Universe since the foundation of FLRW cosmology might cast into doubt the accuracy of the modelling assumptions about homogeneity and isotropy of the 'large-scale metric structure' initially made by Einstein in 1917. In modern cosmology the high level of isotropy of the cosmic microwave background (CMB) [15] together with the Copernican princi-

[1] Milne's universe, which is the hyperbolic slicing of Minkowski space-time, is perhaps better described as a 'kinematical' model.

[2] Georges Lemaître [9] was the first to fit the distance–redshift relation to available data, but his contribution was not noticed by most of the scientific community. After the widespread attention given to the paper of Edwin Hubble [10], Lemaître's paper was translated and republished.

ple [16] is – rather than Einstein's original arguments relying on the distribution of stars in our galaxy – taken as justification of modelling the largest scales by a space-time with exact spatial translational and rotational symmetries.

The first measurement of the CMB was done by Penzias and Wilson[3] in 1965 [15]. The discovery of the CMB as a snapshot of the early Universe epoch ∼14 billion years ago known as recombination is one of the most remarkable discoveries done in physics. In addition to carrying information about the epoch of recombination, the photons of the CMB carry projected information about all epochs of our Universe from recombination until today. The high degree of isotropy of the CMB as revealed in later detailed measurements – which when adjusting for the dipole structure is only broken with fluctuations of order 10^{-5} – is remarkable in its own right. It does not only suggest that the Universe started out in a very simple state, it also reveals that the isotropic temperature distribution of photons as initialised during the epoch of recombination has to a large degree been preserved despite the complicated structure of the cosmic web that the photons have travelled through. The CMB remains the most compelling observational argument for (statistical) homogeneity and isotropy to date.

It is naturally of interest what conclusions can be *rigorously* drawn about the geometric properties of the Universe – and in particular whether the historical assumption of modelling the Universe by an FLRW geometry can be rigorously justified – based on the CMB. In 1968 Ehlers, Geren, and Sachs proved that for a solution of Einstein's equations with the only matter source being a radiative fluid with an isotropic distribution function, the space-time is either stationary, given by an FLRW solution, or a special solution with non-zero rotation and acceleration of the radiation fluid [18]. Thus, in the investigated idealised case with a perfectly isotropic CMB as seen by fundamental observers in a non-static universe, the FLRW ansatz about homogeneity and isotropy is rigorously justified.

While the Ehlers–Geren–Sachs theorem is an interesting result in the literature it is not applicable to our Universe where the CMB radiation is not perfectly isotropic in any frame, and where the present epoch is dominated by an irregular matter distribution of non-zero rest mass. Attempts have been made to generalise the Ehlers–Geren–Sachs theorem to situations with more generic matter content and where the distribution

[3] The CMB had already been detected by McKellar in 1941 [17] but not recognised as being of cosmic origin.

function of the radiation is *almost* isotropic with respect to a class of observers – where in some cases it might be proved that the space-time is 'almost' FLRW (or 'almost' stationary). Such a theorem was given by Stoeger, Maartens, and Ellis [19] who assumed a matter source composed of a dust fluid source in addition to the radiation fluid, and again generalised by Räsänen [20] to generic matter content. However, while the settings in such generalisations are more realistic, they still suffer from very restrictive assumptions on the derivatives of the radiation energy as measured by a class of observers. As discussed in [20], the derivatives of the energy distributions of the photons – which are not directly observed – are related to the local geometry which can realistically exhibit large local variations. The extent to which the mathematical idealisation of exact symmetries usually made in cosmology are compatible with the Universe we inhabit is still an open question.

The modern paradigm of cosmology, the Lambda Cold Dark Matter (ΛCDM) model, is an FLRW model beginning in a hot big bang which contains four energy components: a cosmological constant denoted by Λ and associated with dark energy; cold dark matter (abbreviated CDM); and ordinary matter and radiation known in the standard model of particle physics. In ΛCDM cosmology the approach for describing structure on cosmological scales involves linear perturbations around an FLRW model [21, 22, 23, 24] and is often referred to as 'standard model perturbation theory'. The fields of physical interest in standard model perturbation theory are gauge-invariant perturbation degrees of freedom of the physical space-time defined relative to a background space-time, where the gauge freedom represents a family of first-order changes of the diffeomorphism between the background space-time and the physical space-time. Newtonian N-body simulations are most often invoked in describing structure formation beyond the linear regime [25, 26, 27].

Standard model perturbation theory can be used for calculating the anticipated structure at different epochs and scales within the ΛCDM model. Other examples of predictions of the standard model perturbation theory are the Sachs-Wolfe effect and the *integrated* Sachs-Wolfe effect [28]. The Sachs-Wolfe effect describes anisotropy in the temperature distribution of photons arising from the inhomogeneities in the matter distribution at the epoch of recombination due to the additional redshift or blueshift of photons exiting over- and underdensities. The *integrated* Sachs-Wolfe effect is due to the integrated effect of inhomogeneities along the null rays from the epoch of recombination to the present epoch – the relative wavelength of photons traversing

respectively potential wells and hills change due to the 'stretch' of potentials caused by the expansion of space – and is a probe of dark energy in the standard model of cosmology.

Some of the main observational probes which have lead to the paradigm of the ΛCDM model and the current constraints on its parameters are the CMB, supernovae of type Ia (SNIa), and baryon acoustic oscillation (BAO) measurements. We briefly review these cosmological probes. We shall discuss SNIa and BAO measurements in more detail in chapters 3, 4, and 5.

In the decades leading up to the discovery of the CMB as being of cosmic origin studies of physical processes in expanding plasma and the abundance of light elements were carried out. In the 1920s and 1930s theoretical studies for understanding the relative abundance of hydrogen and helium observed were carried out [29, 30, 31] and the notion of a thermal expansion history within the FLRW class of models was formulated in [32] as well as the prediction that expansion of space would cool but preserve an initial blackbody radiation spectrum. However, these early works were focusing mainly on a single thermodynamic equilibrium for understanding abundances of light elements. In 1942 it was proposed that non-equilibrium processes had to be studied in order to account for abundances [33]. A few years later the theory of big bang nucleosynthesis was founded [34, 35, 36, 37, 38]. It was proposed from these studies that the Universe must have been radiation dominated by the time of nucleosynthesis [36] – changing the perception up to that point that the Universe around the epoch of the formation of the first light isotopes was dominated by ordinary matter with non-zero rest mass. A background radiation which would be observable today at around a temperature of 5°K was furthermore predicted as a consequence of the decoupling of photons and electrons[4] [37, 38] – this prediction is impressively close to the today known mean temperature of the CMB of 2.725°K.

The measurement of the CMB and the identification of it as being of cosmic origin [15] thus established the theory of nucleosynthesis and the hot big bang model. Since the initial measurement the precision and angular resolution of the CMB temperature map has been improved tremendously [39, 40, 41, 42, 43, 44], including mapping of the polarisation of the photons as well. These improvements have allowed for an abundance

[4] Gamow and others were unaware of McKellar's 1941 observations of the absorption spectra of interstellar molecules [17], with a feature which in the benefit of hindsight was realised to arise from the CMB.

of cosmological investigations. An important realisation which came out of studying the temperature variations of the CMB was that these were not large enough to account for the structure of the present day epoch [39]. This conclusion was in line with the already noted seemingly lack of matter to account for rotation curves of stars in the outskirts of galaxies as modelled by Newtonian gravity. This established the need for introducing the cold dark matter component in the ΛCDM model.

In 185 CE Chinese astronomers recorded the observation of a new bright star on the sky, and noted that it remained in the sky for approximately eight months. This 'guest star' is believed to be the first recorded supernova event by humans. The Danish astronomer Tycho Brahe was the first to carefully document a supernova event (not knowing at the time that it was a supernova). In 1572 he noted the appearance of a new star in the constellation Cassiopeia. Since it was at that time believed that everything beyond the moon and planets was fixed, other observers at the time assigned the event to be within the Earth's atmosphere. However, Tycho Brahe noted that the object remained in the same spot night after night, and that 'it must lie far away'.

Modern supernovae observation was initiated in the 1960s where astronomers discovered that the maximum magnitude of supernovae could be used as approximate standard candles [45] and thus as a probe of astronomical distances. SNIa events are believed to be due to matter accreted from a binary companion onto a white dwarf star. Since the resulting explosion involves exceeding the Chandrasekhar mass limit, the energy emitted in the explosion is largely insensitive to the initial conditions. The intrinsic scatter of the peak apparent magnitude as measured in individual frequency-bands is too large for supernovae to be directly used as precise standard candles and standardisation techniques are in practice required. In 1993 a breakthrough was made when an empirical relation – the Philips relation – was discovered [46] between the peak of the supernova light curve in the rest frame B-band and its decay over 15 days for a subclass of SNIa, allowing to standardise supernovae.

The dark energy component Λ – introduced already in the first general relativistic cosmology paper by Einstein [1] but later rejected by himself as his 'biggest blunder' – of the ΛCDM paradigm first became an established part of the concordance cosmology in 1998, when one of the most important discoveries in cosmology was made [47, 48]: the luminosity distances and redshifts of SNIa are well matched to the expansion history of a spatial homogeneous and isotropic Friedmann-Lemaître-Robertson-Walker (FLRW) model only if the Universe began an epoch of accelerated expansion late in cosmic

history. Since gravity with matter obeying the strong energy condition[5] is universally attractive, this demands a cosmological constant, Λ, or some other unknown source of spatially homogeneous dark energy violating the strong energy condition.

It should be noted that there are large systematics (systematic errors) involved in supernovae analysis and that the use of supernovae as standard candles relies on empirical methods of standardisation, as will be discussed in more detail in chapters 3 and 4. Complementary observations are therefore desirable. Independently of SNIa, since the late 1990s maps of the CMB and galaxy catalogues have been found to independently require late epoch cosmic acceleration in the FLRW model. Despite this success in terms of consistency, the nature of dark energy remains a mystery for fundamental physics.

The study of BAO features in the recent-epoch matter distribution is, together with the CMB and supernovae, a cornerstone of observational cosmology. In the ΛCDM cosmology, sound waves in the primordial plasma, and the subsequent decoupling of photons from the baryons, produce a characteristic scale in the distribution of the baryons at the drag epoch [49, 50], which is predicted to be visible in the matter distribution of today. The characteristic scale in the matter distribution can be used as a 'standard ruler', and can provide a complementary mapping of the expansion history to that of standard candles.

The basic object typically used to study BAOs in the matter distribution is the 2-point correlation – which is an autocorrelation in spatial separation of the matter distribution. Formulations of 2-point correlation function statistics for galaxies were studied before the theory of BAOs was formulated. Hubble considered statistical counts of galaxies or 'extra-galactic nebulae' in circles defined from central nebulae [12]. Such unnormalised number counts results in irregular number counts for modern galaxy catalogoues, which is generally ascribed to galaxy evolution and observational biases[6]. The version of the 2-point correlation function used in most modern cosmology was formulated Peebles in the 1970s [52] – with corresponding estimators formulated in the following years, see, e.g., [53]. For estimators based on the work of Peebles, the

[5] The strong energy condition stipulates that the projection of the Ricci tensor $R_{\mu\nu}$ onto a any time-like vector field U^μ must satisfy $R_{\mu\nu}U^\mu U^\nu \geq 0$, which through Raychaudhuri's equation ensures that gravity focuses bundles of matter.

[6] However, see the discussions in [51] where it is argued that the irregularities in number counts are signatures of the violation of FLRW assumptions.

number counts are normalised by analogous number counts in artificial random Poisson catalogues to correct for observational biases and systematics in unnormalised number counts.

The BAO feature, in the form of an excess in the spatial 2-point correlation function of the matter distribution [54, 55] was first detected in the distribution of galaxies by [56, 57] and, since then, more precisely measured by large-volume galaxy surveys such as the WiggleZ Dark Energy Survey [58] and the Baryon Oscillation Spectroscopic Survey [59]. The BAO feature has also been detected using the Lyman-α absorption line of hydrogen as a tracer of the matter distribution [60, 61]. The visibility of a characteristic scale in the 2-point matter distribution, at around the expected acoustic scale from CMB constraints [62], is a success of the ΛCDM cosmology as a self-consistent framework for the interpretation of cosmological observations.

The ΛCDM cosmological model is overall successful in describing available data. However, it has foundational mysteries as described in the above – physically unexplained dark components must account for 95% of the energy content of the universe – and observational tensions between different probes [63, 64, 65, 66, 67, 68], that motivate a continued exploration of alternative models. The statistical and systematic errors in current data, and the observational degeneracy of different physical phenomena, makes it difficult to discriminate between ΛCDM and alternative cosmologies. With next-generation surveys by facilities such as the Large Synoptic Survey Telescope (LSST), Gaia, Euclid, the Dark Energy Spectroscopic Instrument (DESI) and the Square Kilometre Array (SKA), we will enter a new level of precision in data, that must be matched by theoretical precision in order to improve our understanding of the Universe.

Inhomogeneous cosmology is a field within cosmology in which solutions to the foundational mysteries of the ΛCDM paradigm are sought within the gravitational physics of general relativity, with focus on the complexities in space-time dynamics that arises when matter is not perfectly homogeneously distributed over spatial sections of our Universe. In the field of inhomogeneous cosmology we are interested in studying the failure of the FLRW idealisation as an accurate description of geometry on the largest scales and as a global background metric for the structure in our Universe – meaning the failure of it to describe averaged matter dynamics and the motions of test particles, and its failure to serve as a background space-time for all 'cosmological matter fields'.

Investigations of inhomogeneous and/or anisotropic general relativistic universe models go back to the early days of general relativistic cosmology. Space-times which are spatially homogeneous but not necessarily isotropic are known as the Bianchi class of models. The relevant 3-dimensional Riemanian spaces were classified by Bianchi [69] before general relativity was founded – for early applications in general relativity, see for instance [70, 71, 72]. In the 1930s Lemaître [4] and Tolman [73] developed particular classes of spherically symmetric models. In 1947 Bondi discussed spherically symmetric and pressure-free space-times [74] and extended work done by Lemaître and others – these space-times are in the literature referred to as Lemaître-Tolman-Bondi (LTB) models. One of the first frameworks introduced for addressing inhomogeneous *and* anisotropic models in cosmology was the Swiss cheese class of space-times developed in 1945 by Einstein and Straus [75]. The Swiss cheese models allow one to consider non-perturbative structure in a general relativistic framework, albeit in a highly idealised setting with the Schwarzschild solution representing compact objects embedded in an FLRW space-time. Exact space-time solutions which preserve the axial symmetry of the LTB models, but which are not in general spherically symmetric were formulated by Szekeres in 1975 [76], and are denoted the Szekeres models. The Swiss cheese models can be generalised by replacing the Schwarzschild solution with any Szekeres solution – for instance an LTB model – provided that the Israel junction conditions are satisfied [77, 78].

Some early approaches to applying averaging operations to study statistical space-time properties in general relativistic cosmology are found in the work by Isaacson in 1968 [79, 80]. Such work relies on limiting procedures around a pre-defined background cosmological model, and are thus only useful if a background which is everywhere close to the physical metric tensor in the way prescribed by the procedure indeed exists as a good approximation. The work on limiting procedures around a pre-defined background space-time was developed further in 1989 by Burnett in a vacuum-setting [81]. A recently proposed generalisation of the work of Burnett to non-vacuum space-times by Green and Wald [82] has received attention in the cosmological community.

There are many possible specifications and approaches which could be taken for addressing various aspects of the broad problems posed in the field of inhomogeneous cosmology. A central concept in the field of inhomogeneous cosmology is the that of *backreaction* – i.e., the way that physics on small and intermediate scales affects or is 'reacting back' on the large scale dynamical description of the Universe. Different ap-

proaches to the field of inhomogeneous cosmology in general have different operational definitions of backreaction, which can be hard to directly compare.

The problem of finding the best smoothed cosmological model description of an inhomogeneous universe is sometimes referred to as the 'fitting problem' [83]. In one of the earliest papers discussing the fitting problem in detail [84], the fitting problem is defined as follows.

Definition 1. The issue facing us then is as follows: we contemplate on the one hand, a ('lumpy') cosmological model $U = \{M, g_{ab}, u_a, \mu, n\}$ comprising a manifold M, metric tensor $g_{ab}(x^i)$, normalised 4-velocity $u_a(x^i) : u^a g_{ab} u^b = -1$ (see, e.g., Ellis 1971), dynamical matter variables symbolised here by the energy density μ (but in general including other quantities such as the pressure p), and other matter variables symbolised here by the galaxy number density n (but in general including more detailed specification of the distribution of luminous matter in the Universe), which together give a realistic representation of the Universe including all inhomogeneities down to some specified length scale L; and on the other an idealised, completely smoothed-out (...) model $U' = \{M', g'_{ab}, u'_a, \mu', n'\}$. Our problem is how to determine a 'best fit' between these two cosmological models.

As opposed to the limiting procedures outlined by Isaacson, Burnett, Green, and Wald [79, 80, 81, 82], the aim as outlined in the above formulation of the fitting problem is not to characterise small scale behaviour relative to a pre-defined background space-time. The formulation of the fitting problem as proposed by Ellis defines the very task as *obtaining* the best fit background or average effective cosmological model given a physical inhomogeneous space-time. While the fitting problem could be formulated more broadly than in definition 1, most modern work done in inhomogeneous cosmology on formulating large scale dynamical equations for our Universe largely follows this definition.

The stating of the fitting problem in definition 1 presupposes a 'local' general relativistic cosmological solution with a well defined fluid description with 'local' matter density degrees of freedom μ and a well defined 'local' time-direction and time-measure of the matter given by u^a and g_{ab}. Consequently most of the work done in the fitting problem of cosmology does not deal with the coarse-graining that allows us to actually write the Universe in a hydrodynamic description on the largest scales. (However, see [85, 86] for relevant discussions on this issue.) Most work assumes an underlying

general relativistic manifold with a hydrodynamic cosmic matter source, and focuses on the last part of smoothing in order to obtain homogeneous evolution equations on the form of Friedmann's equations of standard cosmology with additional source terms due to backreaction of small scale inhomogeneities in the accurate description, U, on the large scale effective description U' [84, 87, 88, 89, 90, 91, 92, 93, 94]. In this thesis, we shall mainly approach the fitting problem in the spirit of its classical formulation in definition 1. However, we shall also discuss observational tests of the timescape scenario [95, 96, 97, 98], which approaches the fitting problem in a different spirit.

The choice of mathematical framework in which to address fundamental questions in inhomogeneous cosmology is closely related to the interpretation of the fitting problem. All frameworks for addressing the fitting problem are designed for replacing 'microscopic' degrees of freedom of a given universe with statistical 'macroscopic' or 'cosmological' degrees of freedom through some prescription. The notion of 'microscopic' and 'macroscopic' must be specified and depends on which levels of the cosmological hierarchy of structure are addressed.

Modern non-perturbative theoretical approaches to cosmological averaging and the fitting problem rely on either considering averages of simplified exact model space-times – for instance Swiss cheese, LTB, or Szekeres models – or to consider averaging operations for almost generic space-times and to apply simplifying assumptions on the resulting averaged equations directly. There are advantages to both procedures. Considering exact model cosmologies is useful for studying phenomena and observables in a well defined setting where symmetries potentially allow for analytic and intuitive results. Averaging of exact solutions can provide insight into how well defined average quantities relate to the microscopic properties of the given space-time. Studies of exact general relativistic solutions have the disadvantage that the simplifying assumptions imposed might greatly limit the applications of the results to the actual Universe.

Making simplifying assumptions on the macroscopic variables of an already averaged micro-state instead, has the advantage that one need not impose exact symmetries on the micro-state in order to obtain simple results for the macroscopic dynamical system of equations. A given macroscopic constraint might be compatible with several micro-states with very different properties. A disadvantage of macroscopic simplifying assumptions is that it might turn out not to be consistent with a realistic micro-state description. In this sense, assumptions made on the macro-state are associated with the danger of being arbitrary and physically uncontrolled with respect to local physics.

Here, we shall briefly introduce a few of the most discussed averaging operations in the literature. Each of these averaging schemes can be applied in different spirits and with different simplifying assumptions.

An example of a concrete approach to relativistic averaging in cosmology is the tensor averaging scheme of Zalaletdinov [99, 100, 101], where the full tensorial Einstein field equation $G_{\mu\nu} = \frac{8\pi G}{c^4} T_{\mu\nu}$, where $G_{\mu\nu} = R_{\mu\nu} - \frac{1}{2} g_{\mu\nu} R$ is the Einstein tensor, is averaged in order to yield a new set of covariant equations on a given scale $\langle G \rangle_{\mu\nu} = \frac{8\pi G}{c^4} \langle T \rangle_{\mu\nu}$, where $\langle\rangle$ denotes a particular averaging operation designed to preserve the covariance of any averaged tensorial field. The averaged metric $\langle g \rangle_{\mu\nu}$ resulting from the same averaging procedure is in general not a solution to the averaged Einstein equations. One might denote the difference between the Einstein tensor of $\langle g \rangle_{\mu\nu}$ and the average of the local Einstein tensor $\langle G \rangle_{\mu\nu}$ the backreaction term. While the averaging scheme of Zalaletdinov preserves the tensorial form of the Einstein equations, the price for doing so is to introduce additional structure in the averaging operation, which might have little physical justification. The rather complicated averaging procedure also makes it hard to apply the theoretical results to concrete examples.

Another tensorial averaging scheme proposed is that of Korzyński [94]. The tensorial averaging procedure assigns coarse–grained expansion, shear and vorticity to a finite–sized comoving domain of a predefined fluid in a coordinate–independent manner. Because of the divergence theorem, the coarse grained fluid variables are only sensitive to the properties of the boundary surrounding the given domain. The averaging procedure by Korzyński avoids the additional structure which is introduced by Zalaletdinov, and thus appears simpler and perhaps more physically grounded and intuitive.

The most well studied averaging scheme in the field of inhomogeneous cosmology is the scalar averaging scheme proposed by Buchert [87, 88]. Here, the Einstein field equation is projected according to a 'physically preferred' time-like vector field, which is usually dictated by a four-velocity field of a fundamental congruence of observers. A spatial scalar averaging scheme is then employed for averaging the projected equations. The spatial hypersurfaces on which the averaging operation is applied are again determined by a physically preferred time-like vector field (which must be irrotational in order to properly define the spatial surfaces).

The disadvantage of Buchert's scheme is that averaged tensorial objects are not defined, and thus objects which would have been natural to define, such as aver-

aged tensorial fluid variables or an averaged metric tensor, can never be formulated in Buchert's scheme. However, see chapter 4 where we discuss the possibility of formulating an effective metric or 'template metric' within which to interpret cosmological observations in Buchert's scheme. The timescape scenario [95, 96] proposes another form of an effective metric within which to interpret statistical averages of Buchert's scheme when a single space-time solution is not appropriate for describing all cosmic space-time dynamics, and bimetric or multiple-metric models must be invoked.

The advantage of Buchert's scheme is that it provides a simple and intuitive set of equations of averaged space-time variables. The dynamical equations can easily be recasted into a form similar to the FLRW equations of standard cosmology, and therefore provide the opportunity to directly study differences with FLRW dynamical behaviour. Terms affecting the dynamics of the volume of a domain – which can be thought of as an effective scale-factor in the language of FLRW cosmology – which have no FLRW counterpart are denoted backreaction terms. This quantification of backreaction has received attention as it formalises the possibility of emergent effective energy sources with dark energy-like signature from structure on smaller scales [102].

Buchert's averaging scheme has been generalised in various ways, for instance in [90, 91] where spatial averaging is defined in a more general way than initially done in Buchert's scheme and where the formulation is done in a manifestly covariant way (meaning non-coordinate based). We shall consider the generalised framework proposed in [90, 91] as a starting point of our analysis on covariant scalar averaging in chapter 2. We test a particular class of models, the 'scaling solutions', built from Buchert's averaging scheme in chapter 4, where Buchert's equations for a dust universe are presented in (4.1)–(4.4).

The work by Korzyński and Buchert primarily focuses on fluid variables and the assignment of averaged variables to physically motivated spatial domains of space-time. A different starting point that is more observational in spirit is to consider light cone averaging, where the light cone of a single observer or a class of observers is studied and where observational quantities such as redshift, flux of photons, the size of physical objects as they appear on the sky, etc., are of primary interest. An attempt to define observer based averaging is for instance made in [92, 103], where averaging over null surfaces – physically representing light cones of observers – is defined. An advantage of this scheme is that it can be formulated within the same overall framework as the spatial scalar averaging [90, 91], which might result in interesting combinations or

comparisons of the light cone and the spatial averaging scheme. However, it is not clear how the various null cone averages defined in [92, 103] are related to observables, and the scheme is perhaps mainly a mathematically interesting idea, and not necessarily the most useful scheme for providing physical insight relevant for cosmological observation.

Work has been done on relating global variables of Buchert's scheme to the measurements of 'typical observers' in statistically homogeneous and isotropic universes [104, 105]. Here the averaged redshift and averaged angular diameter distance for multiple typical observers are considered. The procedure provides physical insight for how average quantities defined on spatial surfaces can be expected to relate to typical measurements of observers – even though the results are not derived fully rigorously and rely on arguments about statistical homogeneity and isotropy and the rate of evolution of structure.

The timescape scenario [95, 96] employs the Buchert averaging scheme in a bimetric scenario partitioning space-time into tubes of overdense wall regions and underdense void regions. Average observables are hypothesized to be given by an effective metric arising from matching radial null lines of an effective volume average metric and the 'local' metric of the overdense wall regions where observers are situated.

Another interesting procedure for light cone averaging has been suggested by Uzun [106] where a particular representation of the propagation of a bundle of null rays is given. It is argued that phase space averaging of null bundles might be formulated in this setting. The exact procedure has yet to be developed.

The few of many possible tools for defining a macroscopic cosmological theory of our universe discussed here, should hopefully give an idea about the complexity and the richness of the issues faced in inhomogeneous cosmology in formulating a macroscopic dynamical theory of our Universe.

The outline of this thesis is as follows. In chapter 2 we will introduce a generalisation of the $4-$dimensional averaging window function of Gasperini, Marozzi and Veneziano (2010) [91] that may prove useful for a number of applications. The proposed generalisation of the window function allows one to choose the most appropriate averaging scheme for the physical problem at hand, and to distinguish between the role of the foliation itself and the role of the volume measure in averaged dynamic equations. The manifestly covariant form of the averaging scheme introduced, allows one to write already existing results in the literature on explicitly covariant form.

In chapter 3 we use the the Joint Light-curve Analysis (JLA) SNIa catalogue to test luminosity distance-redshift relation of the timescape model. We test the quality of fit of the timescape model against that of the standard spatially flat ΛCDM model by both frequentist and Bayesian comparison. Systematic issues regarding standardisation of supernova light curves are discussed in the analysis. Systematics at and around an approximate statistical homogeneity scale are of special interest in our analysis.

In chapter 4 we perform yet another model test on the JLA SNIa catalogue. We examine the fit of a class of exact scaling solutions with dynamical spatial curvature formulated in the framework of Buchert's averaging scheme [87, 88] for smoothing over inhomogenieties. We examine best-fit parameters of the scaling solutions and investigate consistency with previously found constraints from SNIa, CMB, and BAO data. We examine the quality of fit of the scaling solutions relative to the ΛCDM model, the timescape model, and the Milne model.

In chapter 5 we develop methods for investigating BAO features in cosmological models with non-trivial curvature. We apply our methods to the Baryon Oscillation Spectroscopic Survey (BOSS) dataset, investigating both the ΛCDM and timescape cosmological models as case studies.

In chapter 6 we use the methods developed in chapter 5 to investigate the regime of applicability of the Alcock-Paczyński (AP) scaling conventionally applied in BAO analysis to measure distance scales using a fiducial cosmological model. We propose a new and more efficient version of the conventional AP scaling. We test our theoretical findings for specific test cases using ΛCDM mock catalogues.

CHAPTER 2

On the covariance of scalar averaging and backreaction in relativistic inhomogeneous cosmology

In this chapter we focus on quantifications of the non-linear backreaction of smaller scales on the large scale evolution that involves averaging of 'local' quantities. We shall focus only on averaging schemes for space-time scalars as done in [87, 88], and later generalized by many authors (see, e.g. the reviews [89, 107] and references therein). The use of such averaging schemes presupposes the existence of a 'local' fluid description in a 'local' metric theory. However, we do not assume an averaged homogeneous and isotropic fluid as a source for a large-scale statistical geometry: geometry and matter couple at the fluid resolution scale. The average behaviour is formulated directly from the physics at this 'local' scale, and inhomogeneities at local scales appear explicitly in the resulting generalizations of the Friedmann equations, reflecting the non-commutativity of averaging and evolution in time.

In this chapter we introduce a 4−dimensional averaging window function that generalizes the window function presented in [90, 91] for integration over hypersurfaces. There are multiple purposes in doing so. First, we shall often be interested in a fluid-intrinsic averaging operation (when a fundamental fluid exists in our space-time); such intrinsic formulation will in general not be compatible with the class of window functions considered in [90, 91]. Second, the generalized scheme allows for maximal freedom in the choices of averaging domain and volume measure, while still being compact and easy to interpret. Covariance is built explicitly into the averaging scheme, guaranteeing that any generalization of the Buchert scheme formulated from this will be coordinate-independent by construction. Third, the introduction of the new window function has applications for further investigations on extremal foliations and on the dependence of averaged quantities on the foliation. Such studies are beyond the scope of this chapter,

but will be considered in future work [108].

We are solely concerned with *covariance* here; we do not consider gauge-invariance as defined in standard model perturbation theory.[1] In standard model perturbation theory the fields of interest are perturbation degrees of freedom of the space-time metric defined relative to a background metric. These fields are defined in terms of components of the metric and the background metric and *do not* transform as tensors in the differential geometry definition of a tensor, i.e. they are not covariant. This includes the Bardeen variables, which are 'gauge-invariant' in this context, i.e. they are invariant under first-order changes of the diffeomorphism between the background manifold and the physical space-time manifold, but they are not 4−scalars.

We emphasize that there is no reference to a background space-time in this chapter, and that we use the conventional general relativistic wording throughout. When referring to scalar degrees of freedom we mean quantities that do not transform under arbitrary coordinate transformations. When we refer to 'gauge' degrees of freedom in this chapter, this will be in the broad sense of the word, i.e. as redundant degrees of freedom in the parameterization of a physical system.

This chapter is organized as follows. In section 2.1 we introduce the averaging scheme as formulated in terms of a covariant window function. We discuss the interpretation of the generalized adapted volume measure entering this scheme and we give examples of relevant subcases. In section 2.2 we discuss the commutation rule for such an averaging operation and apply it to the conservation of regional rest mass. The averaged Einstein equations for a general fundamental fluid source are derived in section 2.3 for a general window function, expressed in such a way that boundary terms vanish by construction, except for the average energy conservation law. We consider domains propagated along the fluid world lines as a special case that allow for a more transparent interpretation of the averaged equations. We conclude in section 2.4.

2.1 The averaging scheme

We now introduce the averaging scheme used to quantify averaged dynamics in this chapter. This averaging formalism is a direct generalization of that presented in [91],

[1] We emphasize the focus of this chapter on covariant variables only, in distinction to [90] where both covariance and standard model perturbation theory gauge invariance are discussed.

the difference being that we allow for an arbitrary volume measure on the selected hypersurfaces. We discuss the interpretation of the generalized volume measure, and highlight several relevant subcases of the averaging scheme in relation to the existing literature.

2.1.1 The window function

Following [90, 91] we consider scalar functions integrated over space-time domains that are selected out of the space-time 4−manifold $\mathcal{M}$ by appropriate choices of window functions. In the context of this chapter we shall consider window functions that single out compact regions of 3−dimensional spatial hypersurfaces. Averaging over 3−dimensional hypersurfaces is natural when we want to describe the evolution of averaged properties of spatial sections of the Universe.

Here we shall consider a slightly broader class of $3+1$ window functions than in [90, 91], to allow for arbitrary positive volume measures on the hypersurface of integration. Hence, we do not restrict ourselves to having the volume measure coincide with the adapted volume measure in the frame of the foliation. Such a more general volume measure is natural in several settings, some of which we shall investigate below. This furthermore allows us to make explicit which properties of the averaged expressions are related to the foliation and which are related to the volume measure. When investigating foliation dependence [108] the separation of these contributions will be useful.

We shall consider the broad class of window functions

$$W_{A,A_0,B,B_0,\boldsymbol{V}} = -V^\mu\nabla_\mu(\mathcal{H}(A_0-A))\mathcal{H}(B_0-B) = (V^\mu\nabla_\mu A)\,\delta(A_0-A)\mathcal{H}(B_0-B)\,, \quad (2.1)$$

where A is a scalar with time-like gradient that determines the spatial foliation of integration (with hypersurfaces $A = const.$) and B is a scalar with space-like (or possibly null) gradient that is used to bound the averaging domain. A_0 and B_0 are constants that respectively select a specific hypersurface of the foliation ($A = A_0$) and the domain's spatial boundary ($B = B_0$). $\boldsymbol{V}$ is an arbitrary time-like vector field, that need not be normalized, and that will in general not be normal to the hypersurfaces defined by A. $\mathcal{H}$ is the unit step function; we use the convention $\mathcal{H}(0) = 1$ throughout. We shall call A the hypersurface scalar, B the boundary scalar, and $\boldsymbol{V}$ the volume measure vector. We shall drop the subscripts denoting the dependencies of W in the

following.

This form of the window function generalizes that of [91] through the freedom of choice of the volume measure vector, which in [91] is restricted to being the unit normal vector $\boldsymbol{n}$ to the hypersurfaces defined by A. $\boldsymbol{V}$ determines the volume measure on the hypersurfaces defined by A. This corresponds to considering the usual oriented volume element

$$\mathrm{d}V^\lambda = -n^\lambda \frac{\sqrt{g}}{6}\, n^\mu \epsilon_{\mu\nu\varrho\sigma}\, \mathrm{d}x^\nu \wedge \mathrm{d}x^\varrho \wedge \mathrm{d}x^\sigma \qquad ; \qquad n_\mu = \frac{-\nabla_\mu A}{(-g^{\nu\sigma}\nabla_\nu A \nabla_\sigma A)^{1/2}}, \tag{2.2}$$

(where $g \equiv -\det(g_{\mu\nu})$, and ϵ is the Levi-Civita symbol) projected along the vector $\boldsymbol{V}$. Thus, the integration measure that we use on the surfaces defined by constant A is

$$\mathrm{d}\mathcal{V} \equiv V_\mu\, \mathrm{d}V^\mu\ . \tag{2.3}$$

We can think of $V_\mu\, \mathrm{d}V^\mu$ as the flux of $\boldsymbol{V}$ through the infinitesimal volume $\mathrm{d}V^\mu$.

If $\boldsymbol{V}$ is taken to be the normal vector $\boldsymbol{n}$ to the $A = const.$ hypersurfaces, we simply recover the Riemannian volume measure of the hypersurfaces, $\mathrm{d}\mathcal{V} = n_\mu\, \mathrm{d}V^\mu$. Alternatively, we may take the volume measure vector $\boldsymbol{V}$ to be a 4−velocity field $\boldsymbol{u}$ of physical interest, in general tilted with respect to the normal $\boldsymbol{n}$. In this case, the integration measure defined in (2.3) becomes

$$\begin{aligned}
\mathrm{d}\mathcal{V} \equiv u_\mu\, \mathrm{d}V^\mu &= -u_\mu n^\mu \frac{\sqrt{g}}{6}\, n^\lambda \epsilon_{\lambda\nu\varrho\sigma}\, \mathrm{d}x^\nu \wedge \mathrm{d}x^\varrho \wedge \mathrm{d}x^\sigma \\
&= \gamma \frac{\sqrt{g}}{6}\, n^\lambda \epsilon_{\lambda\nu\varrho\sigma}\, \mathrm{d}x^\nu \wedge \mathrm{d}x^\varrho \wedge \mathrm{d}x^\sigma \\
&= \gamma \frac{\sqrt{g}}{6}\, (-\nabla_\nu A \nabla^\nu A)^{-1/2}\, \epsilon_{\ ijk}\, \mathrm{d}\bar{x}^i \wedge \mathrm{d}\bar{x}^j \wedge \mathrm{d}\bar{x}^k = \gamma\, n_\mu\, \mathrm{d}V^\mu\ ,
\end{aligned} \tag{2.4}$$

where $\bar{x}^\mu = (A, \bar{x}^i)$ is an adapted coordinate system to the foliation of A, and where $\gamma \equiv -\boldsymbol{u}\cdot\boldsymbol{n}$ is the tilt, or Lorentz factor, between the normal of the hypersurfaces and the 4−velocity $\boldsymbol{u}$. The infinitesimal volume element $\mathrm{d}\mathcal{V}$ measures the local proper volume (around $A = A_0$) of the fluid element defined by the infinitesimal fluid flow tube that intersects the hypersurface $\{A = A_0\}$ at the points of the time coordinate (in the $\bar{x}^\mu$ basis) $A = A_0$ and of the spatial coordinates spanning the range $[\bar{x}^i, \bar{x}^i + \mathrm{d}\bar{x}^i]$. The Riemannian volume measure $n_\mu\, \mathrm{d}V^\mu$ of this fluid element as it intersects the hypersurface $\{A = A_0\}$, is its volume measure in the frame defined by $\boldsymbol{n}$, and it is thus

Lorentz-contracted with respect to $\mathrm{d}\mathcal{V}$. Hence, the choice $\boldsymbol{V} = \boldsymbol{u}$ introduces a local proper volume measure of the fluid as the Riemannian volume measure multiplied by the local Lorentz factor γ.

2.1.2 Averages of scalars

We define the integral over a scalar S over the space-time domain $\{A = A_0,\, B \leq B_0\}$ singled out by the window function W as follows:

$$I_W(S) \equiv \int_{\mathcal{M}} \mathrm{d}^4x \, \sqrt{g}\, S\, W \,, \tag{2.5}$$

and we define the average of a scalar S as

$$\langle S \rangle_W \equiv \frac{\int_{\mathcal{M}} \mathrm{d}^4x \, \sqrt{g}\, S\, W}{\int_{\mathcal{M}} \mathrm{d}^4x \, \sqrt{g}\, W} = \frac{I_W(S)}{\mathcal{V}} \,, \tag{2.6}$$

where $\mathcal{V} \equiv I_W(1)$ is the volume of the domain as measured by $\mathrm{d}\mathcal{V}$. The functional dependencies of $I_W(S)$ and $\langle S \rangle_W$ on the variables of W are kept implicit for ease of notation, and we shall also drop the window function index W in what follows.

2.1.3 Examples of window functions

We now present several possible choices for the window function, adapted to specific descriptions.

2.1.3.1 Riemannian averages:

As discussed above, the choice $\boldsymbol{V} = \boldsymbol{n}$ implies integration with respect to the Riemannian volume element of the hypersurfaces determined by A in the definitions (2.5)–(2.6) for integration and averages. This choice corresponds to the averaging formalisms that are often used in the literature for general foliations, in addition to specific (not always covariantly defined) conditions on the propagation of the domain boundary (see a comprehensive list of such general foliation extensions of [87, 88] in the literature comparison investigated in [109]). This is the choice made in [91], where the propagation of the domain is in principle kept general, but is specified as following the normal vector, $\boldsymbol{n} \cdot \boldsymbol{\nabla} B = 0$, when derivation of averaged Einstein equations is considered.

2.1.3.2 Lagrangian window functions:

One can also use the integration measure arising from $\boldsymbol{V} = \boldsymbol{u}$, where $\boldsymbol{u}$ is the generator of flow lines of a physical fluid, together with the requirement of a domain propagating along the fluid flow, $\boldsymbol{u} \cdot \boldsymbol{\nabla} B = 0$. We do not at this point specify the time function A. We call such a choice a *Lagrangian* window function, since the spatial domain is comoving with the fluid, and the volume measure is defined as the proper volume measure of the fluid elements.

The proper volume element of the fluid (2.4) and the associated volume and averages as defined by (2.6) are equivalent to those of [110], here derived from a manifestly covariant window function. This explicitly shows that all results derived from the integration of scalars with this choice of volume element in [110] are covariant, as well as the former results of [87, 88] obtained with the same volume element in the case of a fluid-orthogonal foliation ($\boldsymbol{V} = \boldsymbol{u} = \boldsymbol{n}$).

2.1.3.3 Mass-weighted averages:

Consider a fluid with 4−velocity $\boldsymbol{u}$ and with an associated conserved local rest mass current $\boldsymbol{M}$,

$$M^\mu = \varrho u^\mu \qquad ; \qquad \nabla_\mu M^\mu = 0 \,, \tag{2.7}$$

where ϱ is the rest mass density. We can define a mass-weighted Lagrangian average by choosing $V^\mu = M^\mu$ in (2.1) and $\boldsymbol{u} \cdot \boldsymbol{\nabla} B = 0$. This mass-weighted average corresponds to that formulated for irrotational dust in fluid-orthogonal foliations in [111], but here expressed in the explicitly covariant formalism and extended to arbitrary fluids and foliations.

2.1.3.4 Other weighted averages:

As illustrated by the previous example, the freedom of choice of $\boldsymbol{V}$ allows for any weighting of the averages. One may thus use the window function (2.1) to define, e.g., averages weighted by curvature, or by other functions related to curvature degrees of freedom in the spirit of the 'q-average' of Sussman [112, 113][2], writing the corresponding

[2] Note that the 'q-average' is constructed for the specific metrics of the Lemaître-Tolman-Bondi and Szekeres models by introducing a weighting in the average that is defined from metric degrees of

window function under a manifestly covariant form.

2.1.3.5 Extensions to light cone averages:

One may choose a boundary scalar with null gradient such that $\{B = B_0\}$ defines the past light cone of a given event, as studied in [92] in the case $\boldsymbol{V} = \boldsymbol{n}$. Integrals and averages are then taken over the spatial region defined by the interior of the light cone at time $A = A_0$.

Because $\boldsymbol{V}$ is not constrained to be the unit normal vector to the $A = const.$ hypersurfaces, the formalism can also be straightforwardly extended to averaging over past light cones by choosing A as the appropriate scalar with light-like gradient and $\boldsymbol{V}$ as a fixed time-like vector, e.g. the 4-velocity $\boldsymbol{u}$ of a fluid source. One might then also replace B by a scalar of time-like gradient; another averaging operator discussed in [92] is recovered in this case if $\boldsymbol{V}$ is taken as the normalized gradient of B. For either a space-like or a time-like $\boldsymbol{\nabla} B$, such a window function would then select a bounded part of the past light cone of a given event. The variations of integrals or averages with respect to A_0 then provide information on *drift* effects as this event changes, while the description of time evolution along a fixed past light cone would instead require an analysis of variations with respect to B_0.

2.2 The Buchert-Ehlers commutation rule

We now give a generalization of the commutation rule [114], [87, 88, 115, 116], and the corresponding manifestly covariant version [91]. We focus on different possible rewritings of the commutation rule, which can prove useful for interpretation and for compactness of averaged equations. We then apply it to a Lagrangian window function and to the evolution of the fluid rest mass within the integration domain.

---

freedom in a particular coordinate system. It is therefore not formulated in a manifestly covariant way. However, we may simply extend the definition of the weighting to any other coordinate system, by requiring the weighing to be invariant under the change of coordinates. With such an extension the weighting function is per construction a 4−scalar, and the 'q-average' is covariant.

2.2.1 General formulation

The essential insight of scalar averaging schemes is that time-derivatives and averaging operations do not commute in general. The commutation rule for the integral can be derived by differentiating the expression for $I(S)$ in the form (2.5) with respect to A_0:

$$\begin{aligned} I(S)' &= \int_{\mathcal{M}} \mathrm{d}^4x\sqrt{g}\, S\, V^\nu \nabla_\nu A \left(\frac{\partial}{\partial A_0}\delta(A_0 - A)\right) \mathcal{H}(B_0 - B) \\ &= \int_{\mathcal{M}} \mathrm{d}^4x\sqrt{g}\, S\, V^\nu \nabla_\nu A \left(-\frac{\partial}{\partial A}\delta(A_0 - A)\right) \mathcal{H}(B_0 - B) \\ &= \int_{\mathcal{M}} \mathrm{d}^4x\sqrt{g}\, S\, V^\nu \nabla_\nu A \left(-\frac{Z^\mu}{Z^\nu \nabla_\nu A}\nabla_\mu \delta(A_0 - A)\right) \mathcal{H}(B_0 - B) \\ &= \int_{\mathcal{M}} \mathrm{d}^4x\sqrt{g}\, W \frac{\nabla_\mu \left(S Z^\mu \frac{V^\kappa \nabla_\kappa A}{Z^\sigma \nabla_\sigma A}\, \mathcal{H}(B_0 - B)\right)}{V^\nu \nabla_\nu A} \\ &= I\left(\frac{Z^\mu \nabla_\mu S}{Z^\sigma \nabla_\sigma A}\right) + I\left(\frac{S\, \nabla_\mu \left(Z^\mu \frac{V^\kappa \nabla_\kappa A}{Z^\sigma \nabla_\sigma A}\right)}{V^\nu \nabla_\nu A}\right) - I\left(\frac{S\, Z^\mu \nabla_\mu B\, \delta(B_0 - B)}{Z^\sigma \nabla_\sigma A}\right), \end{aligned} \tag{2.8}$$

with the notation $' \equiv \partial/\partial A_0$, and where $\boldsymbol{Z}$ is an arbitrary vector field obeying $\boldsymbol{Z}\cdot\boldsymbol{\nabla}A \neq 0$ everywhere. The third line of (2.8) follows from $\boldsymbol{Z}\cdot\boldsymbol{\nabla}(\delta(A_0 - A)) = (\boldsymbol{Z}\cdot\boldsymbol{\nabla}A)\,\partial_A(\delta(A_0 - A))$, and the fourth line follows from partial integration, with the convention $\mathcal{H}(0) = 1$ implying $\mathcal{H}(x)\delta(x) = \delta(x)$.

$\boldsymbol{Z}$ represents the freedom of the direction in which we define local time derivatives with respect to A. Non-commutativity is given by the failure of the boundary to be parallel-transported along $\boldsymbol{Z}/(\boldsymbol{Z}\cdot\boldsymbol{\nabla}A)$ and by the change of volume measure along the flow lines of $\boldsymbol{Z}/(\boldsymbol{Z}\cdot\boldsymbol{\nabla}A)$. We denote the first term of (2.8) the evolution term, the second term the expansion term, and the third term the boundary term.

The full result (2.8) is not dependent on $\boldsymbol{Z}$, but different choices of $\boldsymbol{Z}$ allow us to trade between the three terms in (2.8). For instance, we can make the boundary terms disappear by choosing $\boldsymbol{Z}$ such that $\boldsymbol{Z}\cdot\boldsymbol{\nabla}B = 0$,[3] i.e., the boundary term contribution does not appear if the direction chosen for time derivation follows the propagation of the boundary. Similarly, we might make the evolution term vanish by choosing a $\boldsymbol{Z}$ such that $\boldsymbol{Z}\cdot\boldsymbol{\nabla}S = 0$. [4] The rate of evolution of the volume $I(1)$ and the commutation

[3] Taking $\boldsymbol{Z}$ to be time-like or null automatically ensures $\boldsymbol{Z}\cdot\boldsymbol{\nabla}A \neq 0$ if $\boldsymbol{\nabla}A$ is time-like.

[4] Note, however, that if $\boldsymbol{\nabla}S \propto \boldsymbol{\nabla}A$, then this choice is not possible, and the evolution term cannot

rule for the average follow from (2.8) and are given respectively by

$$\frac{I(1)'}{I(1)} = \left\langle \frac{\nabla_\mu \left(Z^\mu \frac{V^\kappa \nabla_\kappa A}{Z^\sigma \nabla_\sigma A} \right)}{V^\nu \nabla_\nu A} \right\rangle - \left\langle \frac{Z^\mu \nabla_\mu B \; \delta(B_0 - B)}{Z^\sigma \nabla_\sigma A} \right\rangle \; ; \tag{2.9}$$

$$\langle S \rangle' = \frac{I(S)'}{I(1)} - \langle S \rangle \frac{I(1)'}{I(1)} =$$

$$\left\langle \frac{Z^\mu \nabla_\mu S}{Z^\sigma \nabla_\sigma A} \right\rangle + \left\langle \frac{\left(S - \langle S \rangle \right) \nabla_\mu \left(Z^\mu \frac{V^\kappa \nabla_\kappa A}{Z^\sigma \nabla_\sigma A} \right)}{V^\nu \nabla_\nu A} \right\rangle - \left\langle \frac{\left(S - \langle S \rangle \right) Z^\mu \nabla_\mu B \; \delta(B_0 - B)}{Z^\sigma \nabla_\sigma A} \right\rangle . \tag{2.10}$$

Again, we might trade between the three terms in (2.10) by changing $\boldsymbol{Z}$, e.g., we can still make the third term vanish by choosing $\boldsymbol{Z}$ to be a time-like vector field comoving with the spatial boundaries of the domain.

When it is possible to choose a time-like $\boldsymbol{Z}$ such that $\nabla_\mu \left(Z^\mu \frac{V^\kappa \nabla_\kappa A}{Z^\sigma \nabla_\sigma A} \right) = 0$, and $Z^\mu \nabla_\mu B = 0$ simultaneously, there is a sense in which time-derivative and the averaging operation commute in (2.8) and (2.10): in this case it is possible to construct flow lines along which the only contribution to the change of $\langle S \rangle$ is the change of S itself. This is the case for a mass-weighted window function (see section 2.1.3.3). In this case, $\boldsymbol{Z} = \boldsymbol{u}$ satisfies the above requirements, so that the commutation rule (2.10) reduces to

$$\langle S \rangle' = \left\langle \frac{u^\mu \nabla_\mu S}{u^\sigma \nabla_\sigma A} \right\rangle . \tag{2.11}$$

Hence, there is commutation of this particular averaging operation and time-derivative along the flow lines of $\boldsymbol{u}$, generalizing this result obtained for irrotational dust in the fluid-orthogonal foliation [111]. This commutation is, however, obtained at the expense of a more complicated definition required for a physical volume (and associated scale factor). In this setting, the 'volume' $I(1)$ actually corresponds to a total rest mass within the integration domain, as described in subsection 2.2.3. Thus, as noticed in [111], defining a physical volume would require to compensate for the weighting by ϱ, e.g. by considering $I(1/\varrho)$.

We may choose $\boldsymbol{Z}$ to be the most convenient vector field for simplifying the commutation rules, or may choose it from a geometric motivation as, e.g. in [91], where

be put to zero.

$\boldsymbol{Z}$ is chosen to coincide with the normal to the hypersurfaces. Alternatively, one may choose a physical vector field for $\boldsymbol{Z}$, e.g. $\boldsymbol{Z} = \boldsymbol{u}$, where $\boldsymbol{u}$ is the $4-$velocity of a physical fluid of interest. In this formulation the terms in (2.8) and (2.10) can be interpreted in terms of evolution along physical flow lines of a fluid and its expansion.

2.2.2 Application to the case of a Lagrangian window function

Let us consider a Lagrangian window function as defined in subsection 2.1.3.2. Writing the commutation rule (2.8) with $\boldsymbol{Z} = \boldsymbol{u}$ we have in this case

$$I(S)' = I\left(\frac{u^\mu \nabla_\mu S}{u^\sigma \nabla_\sigma A}\right) + I\left(\frac{S\,\nabla_\mu u^\mu}{u^\sigma \nabla_\sigma A}\right) \quad ; \quad I(1)' = I\left(\frac{\nabla_\mu u^\mu}{u^\sigma \nabla_\sigma A}\right) , \tag{2.12}$$

where the first contribution comes from the change of S along the flow lines of $\boldsymbol{u}$, and the second contribution from the expansion $\nabla_\mu u^\mu$ of the fluid. Note the normalization $u^\sigma \nabla_\sigma A$, which is a change of measure between the proper time parameter τ of the fluid and the foliation parameter A along each fluid flow line. Hence, this normalization reduces to unity if and only if A is a proper time of $\boldsymbol{u}$.

The analogous commutation rule for the average (2.10) yields

$$\langle S \rangle' = \left\langle \frac{u^\mu \nabla_\mu S}{u^\sigma \nabla_\sigma A} \right\rangle + \left\langle \frac{(S - \langle S \rangle)\nabla_\mu u^\mu}{u^\sigma \nabla_\sigma A} \right\rangle . \tag{2.13}$$

There are at least two natural ways of choosing A in the Lagrangian spirit of formulating the window function. In cases where $\boldsymbol{u}$ is irrotational, it is then proportional to the gradient of a scalar α, and we can choose A to define a foliation in the rest frame of the fluid (i.e. fluid-orthogonal hypersurfaces) by $A = \alpha$. An alternative natural choice of A is a proper time parameter τ of $\boldsymbol{u}$ [110, 109]. This has the advantage of being always possible, even if $\boldsymbol{u}$ has vorticity, and of providing a clear physical interpretation of A as the time parameter in evolution equations for average quantities. However, the time-like nature of $\boldsymbol{\nabla}\tau$ can in general not be guaranteed. Note that the above conditions define classes of foliation scalars, i.e. further specifications are required to determine them uniquely.[5] A choice of proper time foliation can be simultaneously

[5] The *proper time foliation* $A = \tau$ is only specified up to an additive function β obeying $\boldsymbol{u} \cdot \boldsymbol{\nabla}\beta = 0$. The *fluid frame foliation* $A = \alpha$ is only specified up to a reparametrization, $A = f(\alpha)$, for any non-decreasing function f of α. This freedom can be denoted a gauge freedom, since it can be viewed as a time reparametrization within the original foliation itself. See 2.A for further details

fluid-orthogonal only when the fluid is irrotational and geodesic.[6]

2.2.3 Total rest mass of the averaging domain

Consider a conserved local rest mass current $M^\mu = \rho u^\mu$ as in (2.7). We can define a total rest mass within the domain at $A = A_0$ as

$$M(A_0) \equiv \int_{\mathcal{M}} \mathrm{d}^4x \, \sqrt{g} \, M^\mu \nabla_\mu (\mathcal{H}(A - A_0)) \mathcal{H}(B_0 - B) \, , \tag{2.14}$$

i.e., as $I(1)$ for a window function with $V^\mu = M^\mu$ (e.g. the mass-weighted window function, see subsection 2.1.3.3). Applying (2.8) gives the evolution of $M(A_0)$ which, due to the local conservation of M^μ, reduces to a single boundary term

$$M(A_0)' = - \int_{\mathcal{M}} \mathrm{d}^4x \, \sqrt{g} \, M^\mu \nabla_\mu B \; \mathcal{H}(A - A_0) \, \delta(B_0 - B) \, , \tag{2.15}$$

i.e. the evolution of mass is given by the flux of the mass current M^μ out of the averaging domain. Thus, $M(A_0)$ is constant in A_0 when the domain is comoving with the fluid elements, $\boldsymbol{u} \cdot \boldsymbol{\nabla} B = 0$. For such a comoving integration domain, $M = M(A_0)$ (for any A_0), as defined by (2.14), corresponds to the total conserved rest mass of the fluid within the domain. In this case, the additional requirement $\boldsymbol{V} = \boldsymbol{u}$ sets a Lagrangian window function (as defined in subsection 2.1.3.2). The conserved total rest mass within the domain then takes the natural form $M = I(\varrho)$. For other volume measures, in general, $I(\varrho)$ would not correspond to the rest mass within the domain and would not be conserved, due to a weighting or due to the volume not being measured in the fluid's local rest frames. (For instance, for the hypersurfaces Riemannian volume measure, $\boldsymbol{V} = \boldsymbol{n}$, and still for a comoving domain, the integrated rest mass would have to be written $M = I(\gamma\varrho)$ with $\gamma = -\boldsymbol{n} \cdot \boldsymbol{u}$.) A Lagrangian window function $\{\boldsymbol{V} = \boldsymbol{u}$, $\boldsymbol{u} \cdot \boldsymbol{\nabla} B = 0\}$ thus appears as a particularly natural choice to follow and characterize a given collection of fluid elements, if a preferred fluid frame with an associated rest mass

on gauge freedom in the labelling of hypersurfaces.

[6] A fluid-orthogonal foliation implies that $\boldsymbol{u} = \boldsymbol{n} = -N\boldsymbol{\nabla} A$ with the lapse $N = (-\boldsymbol{\nabla} A \cdot \boldsymbol{\nabla} A)^{-1/2}$. The vorticity of $\boldsymbol{u}$ thus has to vanish, which is part of Frobenius' theorem. It also implies that the 4−acceleration $\boldsymbol{a}$ of the fluid relates to the lapse variations as $a^\mu = N^{-1} \, b^{\mu\nu} \nabla_\nu N$ [117, 110], with $\boldsymbol{b}$ the fluid-orthogonal projector. If A is additionally required to be a proper time function for the fluid, $\boldsymbol{u} \cdot \boldsymbol{\nabla} A = 1$, then $N = 1$ everywhere and $\boldsymbol{a} = 0$. This shows that the fluid flow must also be geodesic.

current is present in the model universe. We shall focus again in subsection 2.3.3.1 on domains that follow the propagation of the fluid—hence preserving the associated rest mass—as a subcase of particular interest of more general averaged evolution equations, to which we turn now.

2.3 The averaged Einstein equations

The general averaging formalism and the commutation rule are applied below to scalar projections of the Einstein equations. The resulting system of averaged evolution equations allows for a covariant definition of *cosmological backreaction terms*. We shall then explicitly provide the simpler form taken by these equations for a domain that follows the fluid world lines, and we discuss the natural choices $\boldsymbol{V} = \boldsymbol{n}$ and $\boldsymbol{V} = \boldsymbol{u}$.

2.3.1 Local variables and relations

In this subsection we consider an averaging domain defined by a time-like propagation of its boundary. We thus assume that a unit time-like propagation vector field $\boldsymbol{P}$ can be defined such that it satisfies $\boldsymbol{P} \cdot \boldsymbol{\nabla} B = 0$, at least on the domain's boundary $\{B = B_0\}$. Applying the commutation rules (2.8)–(2.10) with the choice $\boldsymbol{Z} = \boldsymbol{P}$ will then ensure the vanishing of the boundary terms in these equations.

Kinematic variables may then be defined for this vector field by decomposing its gradient with respect to $\boldsymbol{P}$ and its null-space as follows, using the orthogonal projector $\mathbf{k}$ with components $k_{\mu\nu} = g_{\mu\nu} + P_\mu P_\nu$:

$$\begin{aligned}
&\nabla_\mu P_\nu = -P_\mu a^P_\nu + \frac{1}{3}\Theta_P\, k_{\mu\nu} + \sigma^P_{\mu\nu} + \omega^P_{\mu\nu}\,;\\
&\quad a^P_\mu = P^\nu \nabla_\nu P_\mu\,;\ \Theta_P = k^{\mu\nu}\nabla_\mu P_\nu\,;\ \sigma^P_{\mu\nu} = k^\alpha_{(\mu} k^\beta_{\nu)} \nabla_\alpha P_\beta - \frac{1}{3}\Theta_P\, k_{\mu\nu}\,;\ \omega^P_{\mu\nu} = k^\alpha_{[\mu} k^\beta_{\nu]} \nabla_\alpha P_\beta\,;\\
&\quad \sigma^2_P = \frac{1}{2}\,\sigma^P_{\mu\nu}\,\sigma^{P,\mu\nu}\ ;\ \ \omega^2_P = \frac{1}{2}\,\omega^P_{\mu\nu}\,\omega^{P,\mu\nu}\,. \qquad (2.16)
\end{aligned}$$

Assuming the presence of a preferred non-singular fluid flow as a source, with 4−velocity $\boldsymbol{u}$, the (fully general) energy-momentum tensor is naturally decomposed with respect

to $\boldsymbol{u}$ and its null-space:

$$T_{\mu\nu} = \epsilon\, u_\mu u_\nu + 2\, q_{(\mu} u_{\nu)} + p\, b_{\mu\nu} + \pi_{\mu\nu} \ ;$$
$$\epsilon \equiv u^\mu u^\nu T_{\mu\nu} \ ; \quad q_\mu \equiv -b^\alpha_{\ \mu} u^\beta T_{\alpha\beta} \ ; \quad p \equiv \frac{1}{3}\, b^{\mu\nu} T_{\mu\nu} \ ; \quad \pi_{\mu\nu} \equiv b^\alpha_{\ \mu} b^\beta_{\ \nu} T_{\alpha\beta} - p\, b_{\mu\nu} \ , \tag{2.17}$$

where $\mathbf{b}$ is the projector onto the fluid's rest frames, with components $b_{\mu\nu} = g_{\mu\nu} + u_\mu u_\nu$. It may alternatively be decomposed using $\boldsymbol{P}$. In particular, one can define the energy density E_P and pressure $S_P/3$, in the frames defined by $\boldsymbol{P}$, from, respectively:

$$E_P \equiv P^\mu P^\nu T_{\mu\nu} \ ; \quad S_P = k^{\mu\nu} T_{\mu\nu} \ . \tag{2.18}$$

These variables are related to the fluid rest frame energy density ϵ, pressure p, and to the non-perfect fluid contributions *via*

$$E_P - \epsilon = \frac{1}{2}\big[E_P + S_P - (\epsilon + 3p)\big] = (\epsilon + p)\big[(u^\mu P_\mu)^2 - 1\big] + 2\,(u^\mu P_\mu)(P^\nu q_\nu) + \pi_{\mu\nu} P^\mu P^\nu \ . \tag{2.19}$$

The following Raychaudhuri equation for $\boldsymbol{P}$ is then obtained by combining the Einstein equation projected twice along $\boldsymbol{P}$, and its trace:

$$P^\mu \nabla_\mu \Theta_P = -\frac{1}{3}\Theta_P^2 - 2\sigma_P^2 + 2\omega_P^2 + \nabla^\mu a_\mu^P - 4\pi G(E_P + S_P) + \Lambda \ . \tag{2.20}$$

We define an effective scalar 3−curvature for the null-space of $\boldsymbol{P}$ (which is not hypersurface forming if $\omega_P^2 \neq 0$) as follows:

$$\mathcal{R}_P \equiv \nabla_\mu P^\nu \nabla_\nu P^\mu - \nabla_\mu P^\mu \nabla_\nu P^\nu + R + 2R_{\mu\nu} P^\mu P^\nu \ . \tag{2.21}$$

This definition of effective 3−curvature reduces to the scalar 3−curvature of the $\boldsymbol{P}$-orthogonal hypersurfaces when they exist (i.e., for $\omega_P^2 = 0$, by Frobenius' theorem). Such a generalization of the hypersurface-based notion is not unique; here we follow a similar definition as that of, e.g. [118]. This convention implies the following relation in the form of an energy constraint:

$$\frac{2}{3}\Theta_P^2 = -\mathcal{R}_P + 2\sigma_P^2 - 2\omega_P^2 + 16\pi G\, E_P + 2\Lambda \ . \tag{2.22}$$

2.3.2 Averaged evolution equations

We use the general window function (2.1) and define an effective 'scale factor' a as $a = (I(1)/I(1)_{\mathbf{i}})^{1/3}$, where the subscript $\mathbf{i}$ denotes a value on some initial hypersurface $A = A_{\mathbf{i}}$.

As noted for the example of the mass-weighted average [111], it should be kept in mind that this definition is only relevant as a scale factor if it can be interpreted as a typical length derived from a volume, i.e. only when the choice of integration measure defined by $\boldsymbol{V}$ allows for the interpretation of $I(1)$ as a volume. Another definition of 'scale factor' that does relate it to a physical volume (e.g. to $I(1/\varrho)$ in the case of the mass-weighted average) may otherwise be more appropriate. It should also be noted, that the effective 'scale factor' a in general does not have an interpretation in terms of mean redshift of null bundles (the averaging scheme presented in this chapter is too general to make a direct link to statistical light propagation). However, when $I(1)$ does measure a volume, and under the assumptions that (i) the frame of averaging is associated with statistical homogeneity and isotropy, that (ii) structures are slowly evolving (allowing null-rays to probe the statistical homogeneity scale), and that (iii) typical emitters and observers of light are reasonably close to being in the averaging frame, a might be interpreted as the inverse of a 'statistical redshift' averaged over many observers and emitters [119]. More generally, only assuming a choice of window function such that $I(1)$ measures a physical volume, a should merely be interpreted as an effective length scale of an averaging region defined in a given foliation.

Averaging the above equations (2.22) and (2.21) with the averaging definition (2.6), and making use of the volume evolution rate (2.9) and the commutation rule (2.10) with the choice $\boldsymbol{Z} = \boldsymbol{P}$, implying $\boldsymbol{Z} \cdot \boldsymbol{\nabla} B = 0$, yields the following evolution equations for a:

$$3\left(\frac{a'}{a}\right)^2 = 8\pi G \left\langle \frac{\epsilon}{(P^\mu \nabla_\mu A)^2} \right\rangle + \Lambda \left\langle \frac{1}{(P^\mu \nabla_\mu A)^2} \right\rangle - \frac{1}{2}\left\langle \frac{\mathcal{R}_P}{(P^\mu \nabla_\mu A)^2} \right\rangle - \frac{1}{2}\mathcal{Q} - \frac{1}{2}\mathcal{T}\,; \tag{2.23}$$

$$3\frac{a''}{a} = -4\pi G \left\langle \frac{\epsilon + 3p}{(P^\mu \nabla_\mu A)^2} \right\rangle + \Lambda \left\langle \frac{1}{(P^\mu \nabla_\mu A)^2} \right\rangle + \mathcal{Q} + \mathcal{P} + \frac{1}{2}\mathcal{T}\,. \tag{2.24}$$

These equations feature three backreaction terms, a *kinematical backreaction* $\mathcal{Q}$, a *dynamical backreaction* $\mathcal{P}$, and an *energy-momentum backreaction* $\mathcal{T}$ that captures the

difference of the energy densities as measured in two different frames (see [109]). These backreaction terms are defined as follows:

$$
\begin{aligned}
\mathcal{Q} &\equiv \frac{2}{3}\left[\left\langle \frac{\Theta_P^2}{(P^\rho\nabla_\rho A)^2}\right\rangle - \left\langle \frac{\Theta_P + \Gamma_P^{-1}\, P^\mu\nabla_\mu\Gamma_P}{P^\rho\nabla_\rho A}\right\rangle^2\right] - \left\langle \frac{2\sigma_P^2}{(P^\mu\nabla_\mu A)^2}\right\rangle + \left\langle \frac{2\omega_P^2}{(P^\mu\nabla_\mu A)^2}\right\rangle ;\\
\mathcal{P} &\equiv \left\langle \frac{\nabla^\mu a_\mu^P}{(P^\mu\nabla_\mu A)^2}\right\rangle + \left\langle \frac{\Theta_P}{(P^\rho\nabla_\rho A)^2}\left(2\,\frac{P^\mu\nabla_\mu\Gamma_P}{\Gamma_P} - \frac{P^\mu\nabla_\mu(P^\nu\nabla_\nu A)}{P^\sigma\nabla_\sigma A}\right)\right\rangle\\
&\quad + \left\langle \frac{\Gamma_P^{-1}\, P^\mu\nabla_\mu(P^\nu\nabla_\nu\Gamma_P)}{(P^\mu\nabla_\mu A)^2}\right\rangle - \left\langle \frac{\Gamma_P^{-1}\, P^\mu\nabla_\mu\Gamma_P}{(P^\rho\nabla_\rho A)^2}\;\frac{P^\nu\nabla_\nu(P^\kappa\nabla_\kappa A)}{P^\sigma\nabla_\sigma A}\right\rangle ;\\
\mathcal{T} &\equiv -16\pi G\left\langle \frac{E_P-\epsilon}{(P^\mu\nabla_\mu A)^2}\right\rangle ,
\end{aligned}
\tag{2.25}
$$

with the energy difference $E_P-\epsilon$ given by (2.19), and with the ratio of 'Lorentz factors' $\Gamma_P \equiv (V^\mu\nabla_\mu A)/(P^\nu\nabla_\nu A) = (-V^\mu n_\mu)/(-P^\nu n_\nu)$, $-V^\mu n_\mu$ being a Lorentz factor when $\boldsymbol{V}$ is normalized.

From the requirement of (2.23) being the integral of (2.24) we get the integrability condition:

$$
\begin{aligned}
&\mathcal{Q}' + 6\frac{a'}{a}\mathcal{Q} + 2\left\langle \frac{\mathcal{R}_P}{(P^\sigma\nabla_\sigma A)^2}\right\rangle' + 2\frac{a'}{a}\left\langle \frac{\mathcal{R}_P}{(P^\sigma\nabla_\sigma A)^2}\right\rangle + \mathcal{T}' + 4\frac{a'}{a}\mathcal{T} + 4\frac{a'}{a}\mathcal{P}\\
&\quad = 16\pi G\left(\left\langle \frac{\epsilon}{(P^\sigma\nabla_\sigma A)^2}\right\rangle' + 3\frac{a'}{a}\left\langle \frac{\epsilon+p}{(P^\sigma\nabla_\sigma A)^2}\right\rangle\right) + 2\Lambda\left\langle (P^\sigma\nabla_\sigma A)^{-2}\right\rangle' .
\end{aligned}
\tag{2.26}
$$

Defining the kinematic variables of the fluid from the decomposition of the $4-$velocity gradient,

$$
\begin{aligned}
&\nabla_\mu u_\nu = -u_\mu a_\nu + \frac{1}{3}\Theta\, b_{\mu\nu} + \sigma_{\mu\nu} + \omega_{\mu\nu} ;\\
&\quad a_\mu = u^\nu\nabla_\nu u_\mu ;\ \Theta = b^{\mu\nu}\nabla_\mu u_\nu ;\ \sigma_{\mu\nu} = b^\alpha_{(\mu}b^\beta_{\nu)}\nabla_\alpha u_\beta - \frac{1}{3}\Theta\, b_{\mu\nu} ;\ \omega_{\mu\nu} = b^\alpha_{[\mu}b^\beta_{\nu]}\nabla_\alpha u_\beta ;\\
&\quad \sigma^2 = \frac{1}{2}\sigma_{\mu\nu}\sigma^{\mu\nu} ;\ \ \omega^2 = \frac{1}{2}\omega_{\mu\nu}\omega^{\mu\nu} ,
\end{aligned}
\tag{2.27}
$$

we can express the energy-momentum conservation equation projected onto the fluid frame as follows:

$$
-u^\mu\nabla_\nu T^\nu_{\ \mu} = u^\mu\nabla_\mu\epsilon + \Theta(\epsilon+p) + a^\mu q_\mu + \nabla_\mu q^\mu + \pi_{\mu\nu}\,\sigma^{\mu\nu} = 0 .
\tag{2.28}
$$

One can then divide this relation by $(P^\mu\nabla_\mu A)^2$, take the average and apply the commutation rule (2.8) with $\boldsymbol{Z} = \boldsymbol{u}$. This yields the average energy conservation law satisfied by the right-hand side of (2.26):

$$\left\langle \frac{\epsilon}{(P^\sigma\nabla_\sigma A)^2} \right\rangle' + 3\frac{a'}{a}\left\langle \frac{\epsilon+p}{(P^\sigma\nabla_\sigma A)^2} \right\rangle = -\left\langle \frac{\Theta}{\dot{A}}\,\frac{p}{(P^\sigma\nabla_\sigma A)^2} \right\rangle + \left\langle \frac{\Theta}{\dot{A}} \right\rangle \left\langle \frac{p}{(P^\sigma\nabla_\sigma A)^2} \right\rangle$$
$$+ \left\langle \frac{\dot{\Gamma}/\Gamma}{\dot{A}} - \frac{(u^\mu\nabla_\mu B)\,\delta(B_0-B)}{\dot{A}} \right\rangle \left\langle \frac{p}{(P^\sigma\nabla_\sigma A)^2} \right\rangle - \left\langle \frac{\epsilon}{(P^\sigma\nabla_\sigma A)^2}\,\frac{(u^\mu\nabla_\mu B)\,\delta(B_0-B)}{\dot{A}} \right\rangle$$
$$+ \left\langle \frac{\epsilon}{(P^\sigma\nabla_\sigma A)^2}\,\frac{2(\dot{\Gamma_P}/\Gamma_P) - (\dot{\Gamma}/\Gamma) - 2(\ddot{A}/\dot{A})}{\dot{A}} \right\rangle - \left\langle \frac{a_\mu q^\mu + \nabla_\mu q^\mu + \pi_{\mu\nu}\sigma^{\mu\nu}}{\dot{A}\,(P^\sigma\nabla_\sigma A)^2} \right\rangle , \quad (2.29)$$

with $\Gamma \equiv (V^\mu\nabla_\mu A)/(u^\nu\nabla_\nu A) = (-V^\mu n_\mu)/\gamma$, and using the shorthand notation $\dot{S}$ for the proper-time covariant derivative along $\boldsymbol{u}$ of a scalar S, $\dot{S} \equiv u^\mu\nabla_\mu S$. This average conservation equation features two boundary terms that provide the variations in volume and average energy density due to the flux of fluid elements across the domain's boundary if $u^\mu\nabla_\mu B \neq 0$.

The above system of averaged equations (2.23,2.24,2.26,2.29) is covariant since it only features explicitly covariant terms. The form of these equations is moreover globally preserved under a change of the parametrization of the foliation (using a non-decreasing function of A instead of A, preserving the set of hypersurfaces), but the individual terms they contain are not. This is no different from the time-parameter dependence of the expansion and acceleration terms of the Friedmann equations in homogeneous and isotropic cosmologies. This freedom of relabelling the hypersurfaces is important to keep in mind when interpreting averaged evolution equations: as for any parametric equations, e.g. acceleration terms (as second derivatives with respect to a parameter) can be tuned in any desirable way, including the change of sign, by an appropriate change of the parameter. This is discussed in more detail in the specific context of the above averaged equations in 2.A. This interpretation issue is simply solved by the choice of a time label with a clear physical meaning for the hypersurfaces. Such a choice can be made specifically for the physical model considered, or from more general conditions, such as taking τ itself as the parameter A when working within a foliation at constant fluid proper time τ (see the related remarks that conclude subsection 2.2.2).

This general set of averaged equations is naturally expressed in terms of geometric

variables such as the extrinsic curvature or the intrinsic scalar 3−curvature of the $A = const.$ hypersurfaces for a domain propagation along the normal vector field, i.e., for $\boldsymbol{P} = \boldsymbol{n}$. In this case, and for $\boldsymbol{V} = \boldsymbol{n}$ (i.e. for Riemannian averages), this system corresponds to the averaged system derived in [91], with the addition of the integrability condition and the general form of the averaged energy conservation law.

For a general propagation vector $\boldsymbol{P}$, the explicit contribution of the geometric variables in the above equations can also be recovered by an alternative writing. It can be done by splitting $\boldsymbol{P}$ into a component along $\boldsymbol{n}$ and a component orthogonal to $\boldsymbol{n}$, $\boldsymbol{P} = \gamma_P(\boldsymbol{n} + \boldsymbol{v}_P)$ with $\gamma_P = -\boldsymbol{P}\cdot\boldsymbol{n}$ and $\boldsymbol{n}\cdot\boldsymbol{v}_P = 0$. The contributions from the decomposition of the gradient of $\boldsymbol{P}$ to the averaged equations can then be expressed in terms of the extrinsic curvature of the hypersurface, e.g. by applying the following split in the commutation rule:

$$\frac{\nabla_\mu\left(P^\mu \frac{V^\rho\nabla_\rho A}{P^\sigma\nabla_\sigma A}\right)}{V^\nu\nabla_\nu A} = \frac{\Theta_P + \Gamma_P^{-1}\,P^\mu\nabla_\mu\Gamma_P}{P^\rho\nabla_\rho A} = -N\mathcal{K} + N\frac{\nabla_\mu(V^\nu n_\nu\, v_P^\mu)}{V^\rho n_\rho} + \frac{N n^\mu\nabla_\mu(V^\nu n_\nu)}{V^\rho n_\rho}\,,$$

with the lapse function $N \equiv (\nabla^\mu A\nabla_\mu A)^{-1/2}$ and the trace of the extrinsic curvature $\mathcal{K} \equiv -\nabla_\mu n^\mu$. The set of equations using this decomposition will then simplify when using the Riemannian volume measure of the hypersurfaces, $\boldsymbol{V} = \boldsymbol{n}$. In the comoving domain case, $\boldsymbol{P} = \boldsymbol{u}$, this returns one of the sets of equations obtained in [109] when geometric variables–based expressions for the spatial Riemannian volume measure and a domain comoving with the fluid flow are considered.

2.3.3 Examples of applications

2.3.3.1 Comoving domains:

We now specify the above results to the case of a domain comoving with the fluid, i.e. for which $\boldsymbol{u}\cdot\boldsymbol{\nabla}B = 0$. One can thus take $\boldsymbol{P} = \boldsymbol{u}$. The adapted local Raychaudhuri equation (2.20) and energy constraint (2.22) are then expressed in terms of rest frame variables of the fluid:

$$\dot\Theta = -\frac{1}{3}\Theta^2 - 2\sigma^2 + 2\omega^2 + \nabla_\mu a^\mu - 4\pi G(\epsilon + 3p) + \Lambda\,; \tag{2.30}$$

$$\frac{2}{3}\Theta^2 = -\mathcal{R} + 2\sigma^2 - 2\omega^2 + 16\pi G\epsilon + 2\Lambda\,, \tag{2.31}$$

with the effective scalar 3−curvature of the rest frames of $\boldsymbol{u}$ [118],

$$\mathcal{R} \equiv \nabla_\mu u^\nu \nabla_\nu u^\mu - \nabla_\mu u^\mu \nabla_\nu u^\nu + R + 2R_{\mu\nu}u^\mu u^\nu \,. \tag{2.32}$$

The corresponding evolution equations for the effective 'scale factor' a (which may still not be the most appropriate definition in cases where $I(1)$ is not interpreted as a volume) are then written as follows:

$$3\left(\frac{a'}{a}\right)^2 = 8\pi G\left\langle\frac{\epsilon}{\dot{A}^2}\right\rangle + \Lambda\left\langle\frac{1}{\dot{A}^2}\right\rangle - \frac{1}{2}\left\langle\frac{\mathcal{R}}{\dot{A}^2}\right\rangle - \frac{1}{2}\mathcal{Q}\,; \tag{2.33}$$

$$3\,\frac{a''}{a} = -4\pi G\left\langle\frac{\epsilon+3p}{\dot{A}^2}\right\rangle + \Lambda\left\langle\frac{1}{\dot{A}^2}\right\rangle + \mathcal{Q} + \mathcal{P}\,. \tag{2.34}$$

The energy-momentum backreaction vanishes since $\boldsymbol{P} = \boldsymbol{u}$, and the kinematical and dynamical backreaction terms reduce to the following:

$$\mathcal{Q} \equiv \frac{2}{3}\left(\left\langle\frac{\Theta^2}{\dot{A}^2}\right\rangle - \left\langle\frac{\Theta+\dot{\Gamma}/\Gamma}{\dot{A}^2}\right\rangle^2\right) - 2\left\langle\frac{\sigma^2}{\dot{A}^2}\right\rangle + 2\left\langle\frac{\omega^2}{\dot{A}^2}\right\rangle\,; \tag{2.35}$$

$$\mathcal{P} \equiv \left\langle\frac{\nabla_\mu a^\mu}{\dot{A}^2}\right\rangle + \left\langle\frac{\Theta}{\dot{A}^2}\left(2\,\frac{\dot{\Gamma}}{\Gamma} - \frac{\ddot{A}}{\dot{A}}\right)\right\rangle + \left\langle\frac{\ddot{\Gamma}/\Gamma}{\dot{A}^2}\right\rangle - \left\langle\frac{\left(\ddot{A}/\dot{A}\right)\left(\dot{\Gamma}/\Gamma\right)}{\dot{A}^2}\right\rangle\,. \tag{2.36}$$

The integrability condition (2.26) now becomes

$$\begin{aligned}&\mathcal{Q}' + 6\frac{a'}{a}\mathcal{Q} + 2\left\langle\frac{\mathcal{R}}{\dot{A}^2}\right\rangle' + 2\frac{a'}{a}\left\langle\frac{\mathcal{R}}{\dot{A}^2}\right\rangle + 4\frac{a'}{a}\mathcal{P}\\ &= 16\pi G\left(\left\langle\frac{\epsilon}{\dot{A}^2}\right\rangle' + 3\frac{a'}{a}\left\langle\frac{\epsilon+p}{\dot{A}^2}\right\rangle\right) + 2\Lambda\left\langle\frac{1}{\dot{A}^2}\right\rangle'\,,\end{aligned} \tag{2.37}$$

where the right-hand side obeys the averaged energy conservation law (2.29) that reduces to

$$\left\langle \frac{\epsilon}{\dot{A}^2} \right\rangle' + 3\frac{a'}{a}\left\langle \frac{\epsilon+p}{\dot{A}^2} \right\rangle = -\left\langle \frac{\Theta}{\dot{A}}\frac{p}{\dot{A}^2} \right\rangle + \left\langle \frac{\Theta+\dot{\Gamma}/\Gamma}{\dot{A}} \right\rangle \left\langle \frac{p}{\dot{A}^2} \right\rangle + \left\langle \frac{\epsilon}{\dot{A}^2}\left(\frac{\dot{\Gamma}/\Gamma - 2\ddot{A}/\dot{A}}{\dot{A}}\right) \right\rangle - \left\langle \frac{q^\mu a_\mu + \nabla_\mu q^\mu + \pi_{\mu\nu}\sigma^{\mu\nu}}{\dot{A}^3} \right\rangle . \tag{2.38}$$

Remarks: The requirement $\boldsymbol{u}\cdot\boldsymbol{\nabla}B = 0$ in the choice of the window function corresponds to the definition of an averaging domain that follows the fluid flow. It thus ensures by construction the preservation over time of the collection of fluid elements to be averaged, in particular preserving their total rest mass (as shown in subsection 2.2.3) when it can be defined. For a non-weighted average that allows for the interpretation of $I(1)$ as a volume (e.g. for a Lagrangian window function, $\boldsymbol{V} = \boldsymbol{u}$, or for a Riemannian volume measure, $\boldsymbol{V} = \boldsymbol{n}$), the scale factor a corresponds to a typical spatial scale related to the domain volume.

2.3.3.2 Lagrangian window function:

The above equations for a comoving domain, $\boldsymbol{u}\cdot\boldsymbol{\nabla}B = 0$, simplify further when in addition the fluid proper volume measure is used, $\boldsymbol{V} = \boldsymbol{u}$, yielding a Lagrangian window function. This corresponds to setting $\Gamma = 1$ in equations (2.33)–(2.38) above, dropping all terms that depend on its evolution. The system of averaged equations in the framework corresponding to the Lagrangian window function in [110, 109] is thus recovered, under an equivalent, here manifestly covariant form. As discussed in the above references, it becomes particularly transparent in a foliation by hypersurfaces of constant fluid proper time, $A = \tau$.

Remarks: The Lagrangian window function choice, based on a preferred fluid 4−velocity field, is especially adapted to analyzing average properties within single-fluid cosmological models. This could apply, e.g. to the description of a dark matter-dominated late Universe within a dust model, or to the radiation-dominated era within a model of a pressure-supported fluid. It can as well be used in a model involving several non-comoving fluids, e.g. to describe a mixture of dark matter and radiation with different 4−velocities. In this case, it would require choosing one of the fluids to be

followed through its evolution together with its proper volume measure. The total energy-momentum tensor would then have to be decomposed with respect to the corresponding frame, in which contributions from the other fluids will generally appear in the form of non-perfect fluid terms [120].

2.3.3.3 Riemannian volume averages:

As discussed at the end of subsection 2.3.2, the choice of a Riemannian volume measure ($\boldsymbol{V} = \boldsymbol{n}$) is the most adapted for analyzing averaged geometric properties of the hypersurfaces themselves, e.g. by providing expressions of the averaged equations in terms of the extrinsic curvature of the hypersurfaces. This is expected since the scale factor and averages are then based on the intrinsic spatial volume form of the hypersurfaces. The evolution equations for the scale factor with such a choice and for a comoving domain ($\boldsymbol{u} \cdot \boldsymbol{\nabla} B = 0$) may be obtained from equations (2.33)–(2.38) by setting $\Gamma = 1/\gamma$. This gives a manifestly covariant system of equations equivalent to that given in Appendix B of [109], also expressed in terms of the rest frame fluid variables. Recovering the dependence in the geometric variables such as the trace of extrinsic curvature then requires rewriting these local quantities along the lines suggested at the end of subsection 2.3.2.

Remarks: The choice of a Riemannian volume measure ($\boldsymbol{V} = \boldsymbol{n}$) is especially suited for studying the behaviour of hypersurfaces defined from geometric conditions, such as the (in General Relativity frequently used) Constant Mean Curvature requirement.

The averaged equations for this volume measure take their simplest form for a propagation of the domain along the normal vector $\boldsymbol{n}$ ($\boldsymbol{n} \cdot \boldsymbol{\nabla} B = 0$). The evolution equations for such a choice of propagation of the domain can be directly obtained in terms of the geometric variables from the general equations of subsection 2.3.2, recovering the framework and results of [91].

The geometric propagation of the domain ($\boldsymbol{n} \cdot \boldsymbol{\nabla} B = 0$) does in general not preserve volume elements associated with a fluid four-velocity field $\boldsymbol{u}$. Preservation of fluid elements holds, for instance, for an irrotational fluid model with averaging defined in the corresponding global fluid rest frames, with $\boldsymbol{n} = \boldsymbol{u}$. In a more general cosmological setting, one may assume on large scales that vorticity effects may be neglected, at least near the domain boundary, allowing for a foliation where a propagation of the domain boundary along the normal vector would approximate a comoving propagation ($\boldsymbol{u} \cdot$

$\boldsymbol{\nabla} B = 0$). One may also assume a choice of hypersurfaces where statistical homogeneity holds for all observables, effectively leaving the evolution equations defined over such a choice of hypersurfaces invariant under the increase of scale of the domain B_0 above a suitable homogeneity scale cut-off. This would then allow for a computation of averages over a global range ($B_0 \longrightarrow +\infty$), effectively eliminating the need for distinguishing the possible propagations of the domain boundary for this choice; see [119] for an investigation of this framework.

2.3.3.4 Light propagation:

As discussed in subsection 2.1.3.5, an alternative choice for the domain boundary would be that of binding it to the past light cone of a given event by choosing the appropriate scalar B with light-like gradient, covering the evolution of the average properties of spatial sections in the interior of this light cone.

Alternatively one might consider the case where A has light-like gradient such that $A = A_0$ singles out a null surface that might be associated with the light cone of an observer, and where B has time-like or space-like gradient (e.g. $\boldsymbol{\nabla} B$ being proportional to an irrotational fluid 4-velocity $\boldsymbol{u}$). Variation of average properties with respect to emitting times of the sources along a given cone then requires a variation of the parameter B_0, while the above results for the dependence in A_0 would provide insight on drift effects as the observer changes. These situations have been investigated in detail with similar covariant averaging schemes and their application in an adapted coordinate system in [92], see also [103].

Remarks: Averaging domains defined from the light cone are natural candidates for connecting the averaging formalism discussed in this chapter with observations. It is important to keep in mind that the formalism presented in this chapter is general, allowing for averaging over hypersurfaces of arbitrary globally hyperbolic space-times. In particular, the average equations only implicitly depend on the metric of space-time. While we consider this being an advantage, as it allows to express average properties independently of a specific form of the space-time metric, it implies the need for further specifications and assumptions in order to connect the general result to observations. For example, assumptions must be made in order to interpret averaged quantities defined over spatial hypersurfaces in terms of (averaged) energy, flux, etc., of photon bundles emitted by matter sources and absorbed by specified classes of observers.

Such an interpretation may become more natural if the formalism is specified to light cone averaging [92], but further assumptions would still be needed in order to close the system of averaged equations (e.g. by specifying a model for the inhomogeneous metric [103]), and to relate the obtained averages to observational results obtained within an inhomogeneous geometry. It is beyond the scope of this chapter to go into details about the difficult task of establishing connections between averaged cosmological evolution equations and (statistical) observations of selected observers. For papers addressing the link between the averaging formalism and its observational interpretation, see e.g. [121, 119] (with a covariant formalism for global spatial averages in the second case), and [106, 122] for local and bi-local investigations.

2.4 Discussion

Covariance is a requirement for any physical theory, and a cornerstone in the formulation of General Relativity. In this chapter we have investigated scalar covariant formulations of global dynamics relevant for the description of backreaction effects in cosmology. We have considered a generalized window function, allowing for arbitrary foliation, spatial boundary, and volume measure.

We provided an explicitly covariant form for the commutation rule and for the spatially averaged scalar parts of Einstein's equations, with the associated integrability condition, using this general window function. The absence of restrictions imposed on the energy-momentum tensor of the fluid sources allows us to apply these schemes to the early Universe as well as to the matter-dominated later stages, and they cover all spatial scales down to which the fluid approximation can be considered as valid. Backreaction terms are introduced from these equations, and are thus also expressed under a manifestly covariant form. We then applied these results to the physically relevant subcase of a comoving domain.

We have given a procedure for providing several possible decompositions of the commutation rule and the resulting averaged equations. This allows us, for example, to get rid of boundary terms, or to keep them as transparent boundary flux terms, for any choice of domain propagation. We have discussed the effect on averaged equations of a relabelling of the hypersurfaces in a given foliation, and we have stressed the importance of being able to physically interpret the chosen label.

The formalism used in this chapter provides a unifying framework encompassing

various scalar averaging schemes that have been suggested or could be used for the description of averaged properties of cosmological models. It can be straightforwardly adapted to a given specific scheme by suitably choosing the window function. Several examples of such possible applications were given. In particular, we have shown that the manifestly covariant averaging scheme used in this chapter reduces to the averaging scheme considered in [109] for a so-called Lagrangian window function, providing covariant formulas for the latter scheme. The explicit selection of the foliation by a scalar function in the scheme used in this chapter also makes it suitable for the forthcoming investigation of foliation dependence of averaged expressions [108], and it may be helpful for other related considerations.

Appendix 2.A Freedom of labelling hypersurfaces

Here we investigate in more detail the consequences of a change of the hypersurfaces' label A (without change of the hypersurfaces) for the terms appearing in the evolution equations for the effective scale factor a.

Any transformation of the form

$$A \mapsto f(A), \tag{2.39}$$

where f is a strictly monotonically increasing function, is a transformation of the foliation of A onto itself (i.e. the same set of hypersurfaces is considered, with a different parametrization), since

$$n_\mu = -\frac{\nabla_\mu f(A)}{\sqrt{-\nabla_\nu f(A)\nabla^\nu f(A)}} = -\frac{\nabla_\mu A}{\sqrt{-\nabla_\nu A \nabla^\nu A}} \,. \tag{2.40}$$

The class of transformations (2.39) is thus a gauge of the foliation.

This seemingly innocent parametrization freedom can cause issues if we are naively evaluating averaged quantities without paying attention to the interpretation on what the time label A represents in the equations. As an example, the interpretation of the Friedmann equations under their usual form relies on the fact that their time parameter has a transparent meaning as the eigentime of ideal fundamental observers.

Let us consider an integrand

$$S\,W = -SV^\mu \nabla_\mu(\mathcal{H}(A_0 - A))\,\mathcal{H}(B_0 - B)\,, \tag{2.41}$$

where the vector $SV^\mu\mathcal{H}(B_0 - B)$ is invariant under reparametrizations (2.39) of A. (This is for instance the case if S, $\boldsymbol{V}$ and B, B_0 are independent of A or only depend on it *via* the normal vector $\boldsymbol{n}$.) Under such a reparametrization, the integral $I(S) = I(S)_{A,A_0}$ (recovering provisionally an explicit indication of the dependence in A and

A_0 of the window function) becomes

$$I(S)_{A,A_0} \mapsto I(S)_{f(A),f(A_0)} = I(S)_{A,A_0} \ , \tag{2.42}$$

where we have used that

$$\mathcal{H}(f(A_0) - f(A)) = \mathcal{H}(A_0 - A) \ , \tag{2.43}$$

for strictly increasing functions f. Such an integral thus only depends on the chosen foliation and the selected slice, but not on the parametrization, and we can remove the subscript notation A, A_0 in the following.

Derivatives with respect to the parameter transform as

$$\frac{\partial I(S)}{\partial A_0} \mapsto \frac{\partial I(S)}{\partial (f(A_0))} = \frac{1}{f'(A_0)} \frac{\partial I(S)}{\partial A_0}, \tag{2.44}$$

while second derivatives become

$$\frac{\partial^2 I(S)}{\partial A_0^2} \mapsto \frac{\partial^2 I(S)}{\partial (f(A_0))^2} = \frac{1}{f'(A_0)^2} \frac{\partial^2 I(S)}{\partial A_0^2} - \frac{f''(A_0)}{f'(A_0)^3} \frac{\partial I(S)}{\partial A_0}. \tag{2.45}$$

We can therefore tune first derivatives by any positive rescaling $f'(A_0)$ through the transformations (2.39), while second derivatives may even be canceled or change sign, since $f''(A_0)$ is not constrained in its sign. The above results similarly apply to the average $\langle S \rangle$ and its derivatives with respect to A_0.

We conclude that, without a physical interpretation of the hypersurface label A, statements about the magnitude of first-order derivatives (2.44), as well as *any* statements (about magnitude or sign) about second-order derivatives (2.45), are degenerate with the choice of A. This applies for instance to the left-hand sides of the averaged dynamical equations (2.23)–(2.24), or (2.33)–(2.34), that are proportional to $(\partial I(1)/\partial A_0)^2$ and $\partial^2 I(1)/\partial A_0^2$, assuming that $\boldsymbol{V}$, B and B_0 are defined independently of A or only depend on it *via* the normal vector $\boldsymbol{n}$.

Under the same assumption, the conclusions about parametrization-dependence also hold for the terms on the right-hand sides of (2.23)–(2.24). Most of them can be written as $\langle\, S/(P^\sigma \nabla_\sigma A)^2 \,\rangle$ with a scalar S that is unchanged under the reparametrization (2.39), even when it depends on A, such as Γ_P, and would thus rescale by a factor $f'(A_0)^2$, as does $(\partial I(1)/\partial A_0)^2$. The only exception is the combination of terms

$\left\langle -(\Theta_P + \Gamma_P^{-1} P^\mu \nabla_\mu \Gamma_P)\, P^\nu \nabla_\nu (P^\sigma \nabla_\sigma A)\, (P^\rho \nabla_\rho A)^{-3} \right\rangle$ appearing in $\mathcal{P}$ in (2.24), which would transform as

$$\left\langle -\frac{(\Theta_P + \Gamma_P^{-1} P^\mu \nabla_\mu \Gamma_P)\, P^\nu \nabla_\nu (P^\sigma \nabla_\sigma A)}{(P^\rho \nabla_\rho A)^3} \right\rangle \mapsto$$
$$\frac{1}{f'(A_0)^2} \left\langle -\frac{(\Theta_P + \Gamma_P^{-1} P^\mu \nabla_\mu \Gamma_P)\, P^\nu \nabla_\nu (P^\sigma \nabla_\sigma A)}{(P^\rho \nabla_\rho A)^3} \right\rangle - \frac{f''(A_0)}{f'(A_0)^3} \frac{\partial I(1)}{\partial A_0}\,, \tag{2.46}$$

i.e. in the same way as $\partial^2 I(1)/\partial A_0^2$. These identical transformations of both sides of the averaged evolution equations ensure the preservation of the form of these equations under a reparametrization. The same remarks hold for the equations (2.33)–(2.34) with $\boldsymbol{P} = \boldsymbol{u}$ in this case.

CHAPTER 3

Apparent cosmic acceleration from supernovae Ia

In this chapter we test the timescape model [95, 96, 97] on the Joint Light-curve Analysis (JLA)[123] catalogue of type Ia supernovae. We compute constraints on cosmological parameters, and compare the quality of the fit to that of the ΛCDMmodel and the empty universe. We investigate robustness of our results to cut-offs in data conditioned on redshift. Of special interest is the stability of the results at and around an approximate statistical homogeneity scale of around $\gtrsim$ 70–120 h^{-1}Mpc as estimated within the ΛCDMframework.

The timescape model has passed a number of independent observational tests [124, 125, 126, 98, 127]. Its distance–redshift relation is very close to that of particular Λ cold dark matter (ΛCDM) models over small redshift ranges, but effectively interpolates [97, 128] between spatially flat ΛCDM cosmologies with different values of Ω_{M0} and $\Omega_{\Lambda 0}$ over larger redshift ranges. In particular, when the timescape model is fit to the angular diameter distance of the sound horizon in the CMB then the spatially flat ΛCDM model with the closest comoving distance at redshifts $z \gtrsim 100$ has a value of Ω_{M0} 15–27% lower than that of the spatially flat ΛCDM model with the closest comoving distance at redshifts $z < 1.2$ [97, 128].

Geometric tests of the timescape expansion history are most developed [97], and give rise to measures [129, 130] which will definitely distinguish both the timescape model and other alternatives [131, 132] from the standard FLRW model using *Euclid* satellite data [133]. On the other hand, tests of the CMB anisotropy spectrum in the timescape model are at present limited by systematic uncertainties of 8–13% in parameters which relate to the matter content [127]. This is a consequence of backreaction schemes having not yet been applied to the primordial plasma.

3.1 Supernova redshift-distance analysis

In the case of the redshift range probed by SNIa the difference between the timescape and ΛCDM cosmologies is comparable to the systematic uncertainties that arise between different methods for fitting the light curves of SNIa to obtain "standard candles". In particular, in the last full analysis of the timescape model (using data available in 2010) [125] found significant differences between data reduced by the MLCS2k2 (Multicolor Light-Curve Shape) fitter [134] and the SALT/SALT2 (Spectral Adaptive Light-curve Template) fitters [135, 136]. While the relative Bayesian evidence was sometimes 'positive' (but not very strong), the conclusion as to which cosmological model fitted better depended on the light-curve fitting method. Consequently the empirical nature of light-curve fitting may mask effects due to the underlying expansion history if this deviates from the FLRW geometry.

The significantly larger Joint Light-curve Analysis (JLA) SNIa catalogue [123] now makes possible a renewed comparison of the timescape and ΛCDM models, as well as further investigation of the systematics of light-curve fitting. Recently, [137] (NGS16) have used the JLA catalogue to reinvestigate systematic issues associated with SNIa light-curve fitting within FLRW cosmologies using the SALT2 method. They adopted maximum likelihood estimators (MLE) that take into account the underlying Gaussianity of particular light-curve parameters [138]. NGS16 concluded that the significance for cosmic acceleration, as compared to an empty Milne model (or any cosmology with constant expansion), is "marginal" (at $\lesssim 3\sigma$ significance). This conclusion was challenged by [139] (RH16), who introduced 12 additional light-curve parameters to allow for possible unaccounted systematics, concluding that the 2.8σ significance found by NGS16 increased to 3.7σ for a general FLRW model, or to 4.2σ for the spatially flat case. However, RH16 did not consider whether the increased model complexity was justified from a Bayesian standpoint.

In the SALT2 method each observed supernova redshift is used to determine a theoretical distance modulus,

$$\mu \equiv 25 + 5 \log_{10} \left(\frac{d_L}{\text{Mpc}} \right) , \tag{3.1}$$

where d_L is the luminosity distance for each cosmological model. This is then compared

to the observed distance modulus, which is related to the supernova light-curve by

$$\mu_{\rm SN} = m_{\rm B}^* - M_{\rm B} + \alpha x_1 - \beta c, \tag{3.2}$$

where $m_{\rm B}^*$ is the apparent magnitude at maximum in the rest-frame B band, $M_{\rm B}$ is the corresponding absolute magnitude of the source, x_1 and c are empirical parameters that describe the light-curve stretch and colour corrections for each supernova, while α and β are parameters that are assumed to be constant for *all* SNIa.

The theoretical distance modulus (3.1) is determined for a bolometric flux, which is not directly measured. The SALT2 [135, 136] relation (3.2) can thus be viewed as a model for a band correction, $\Delta\mu_{\rm B}$, that is linear in the variables x_1 and c,

$$\Delta\mu_{\rm B} \equiv (m - M) - (m_{\rm B}^* - M_{\rm B}) = \alpha x_1 - \beta c, \tag{3.3}$$

where m and M are the bolometric apparent and absolute magnitudes in the observer and emitter rest frames respectively.

In the SALT2 method, the light-curve parameters are simultaneously fit together with the free cosmological parameters on the entire data set.

NGS16 assumed that all SNIa in the JLA catalogue [123] are characterized by parameters, $M_{\rm B}$, x_1 and c, drawn from the same independent global Gaussian distributions, with means $M_{\rm B,0}$, $x_{1,0}$ and c_0, and standard deviations $\sigma_{M_{\rm B,0}}$, $\sigma_{x_{1,0}}$ and σ_{c_0} respectively. These 6 free parameters were then fitted along with the light-curve parameters α, β and the cosmological parameters.

RH16 claimed that the mean light-curve stretch and colour parameters, $x_{1,0}$ and c_0, of the Gaussian distributions analysed by NGS16 show some redshift dependence. This may be partially due to astrophysical effects in the host population, or – particularly for the colour parameter – may arise from the colour–luminosity relation combined with redshift–dependent detection limits. In other words, Malmquist type biases may not be completely corrected for in the JLA catalogue [123]. In the absence of a known astrophysical model for such corrections, RH16 introduced 12 additional empirical parameters by replacing the global Gaussian means according to

$$x_{1,0} \to x_{1,0,J} + x_{z,J} z, \qquad \text{and} \qquad c_0 \to c_{0,J} + c_{z,J} z, \tag{3.4}$$

where the index J runs over the four independent subsamples in the JLA catalogue: (1)

SNLS (SuperNova Legacy Survey); (2) SDSS (Sloan Digital Sky Survey); (3) nearby supernovae; (4) HST (Hubble Space Telescope), with $x_{z,4} = 0$, $c_{z,4} = 0$ on account of limited HST data. The widths $\sigma_{x_{1,0}}$, σ_{c_0} were still treated as global parameters.

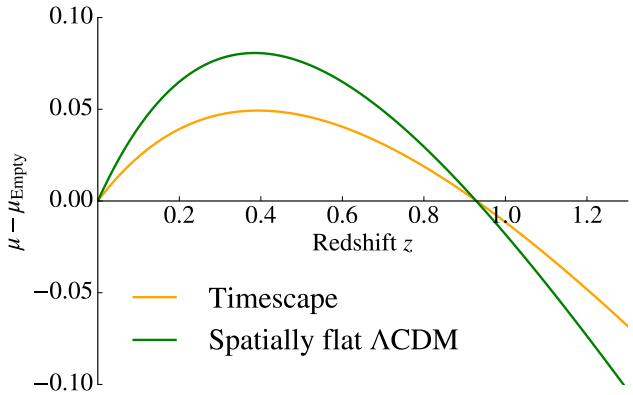

Figure 3.1: The residual distance moduli $\mu_{\Lambda\rm CDM}(z) - \mu_{\rm empty}(z)$ and $\mu_{\rm TS}(z) - \mu_{\rm empty}(z)$ with the same H_0. The best-fitting parameters of Table 3.2 are assumed: $\Omega_{M0} = 0.365$ for spatially flat ΛCDM and $f_{\rm v0} = 0.778$ for timescape. For redshifts $z < 0.927$ over which $\mu_{\rm TS}(z) < \mu_{\Lambda\rm CDM}(z)$, the maximum difference between the ΛCDM and timescape distance moduli is $\mu_{\Lambda\rm CDM}(z) - \mu_{\rm TS}(z) = 0.031$ at $z = 0.372$.

We perform a Bayesian comparison of fits of the JLA catalogue [123] to the luminosity distance-redshift relation for the spatially flat ΛCDM model, and for the timescape model [95, 96, 97, 98]. We first use the MLE methodology of NGS16 directly, and then investigate the effect of changes to light-curve fitting suggested by RH16. An empty universe with constant expansion rate is also analysed, as a convenient demarcation of accelerating from non-accelerating expansion in the FLRW case.

Details of the theoretical luminosity distances used in (3.1) are given in Appendix 3.A. The model differences that we are testing are best appreciated by comparing the distance moduli of the timescape and spatially flat ΛCDM models relative to an empty universe, as shown in Fig. 3.1. The timescape distance modulus, $\mu_{\rm TS}(z)$, is closer to ΛCDM than the empty case. Nonetheless, $\mu_{\rm TS}(z)$ is always closer to $\mu_{\rm empty}(z)$ than $\mu_{\Lambda\rm CDM}(z)$ is, a consequence of cosmic acceleration being an apparent effect in the timescape model.

Further technicalities about systematic issues in implementing the SALT2 method are discussed in Appendix 3.B.

Cosmological parameter	Prior distribution	Range
Timescape: $f_{\rm v0}$	Uniform	$[0.500, 0.799]$
Flat ΛCDM: $\Omega_{M0} = 1 - \Omega_{\Lambda 0}$	Uniform	$[0.143, 0.487]$
Nuisance parameters	**Prior distribution**	**Range**
α	Uniform	$[0, 1]$
$x_{1,0}$	Uniform	$[-20, 20]$
$\sigma_{x_{1,0}}$	Uniform on $\log_{10}\sigma_{x_{1,0}}$	$[-5, 2]$
β	Uniform	$[0, 4]$
c_0	Uniform	$[-20, 20]$
σ_{c_0}	Uniform on $\log_{10}\sigma_{c_0}$	$[-5, 2]$
$M_{\rm B,0}$	Uniform	$[-20.3, -18.3]$
$\sigma_{M_{\rm B,0}}$	Uniform on $\log_{10}\sigma_{M_{\rm B,0}}$	$[-5, 2]$
Additional stretch and colour parameters for models II-VIII	Uniform	$[-20, 20]$

Table 3.1: All nuisance parameters in each model have identical priors. In the timescape model Ω_{M0} is defined in terms of $f_{\rm v0}$ hence we take the latter to be the more 'fundamental' parameter and assign the prior to it.

3.2 Statistical methods

3.2.1 The likelihood construction

We adopt the likelihood construction [138] used by NGS16. The likelihood, $\mathcal{L}$, is the probability density of the observed data – here $(\hat{z}, \hat{m}^*_{\rm B}, \hat{x}_1, \hat{c})_i$, $i = 1, 2, \ldots, N$ on N supernovae – given a model, M. The likelihood can be written as [138]

$$\begin{aligned}\mathcal{L} &\equiv \mathcal{P}\left[(\hat{z}, \hat{m}^*_{\rm B}, \hat{x}_1, \hat{c})_i \,|\, {\rm M}\right] \\ &= \int {\rm d}M^N_{\rm B}\, {\rm d}x^N_1\, {\rm d}c^N\, \mathcal{P}\left[(\hat{z}, \hat{m}^*_{\rm B}, \hat{x}_1, \hat{c})_i \,|\, (M_{\rm B}, x_1, c)_i, {\rm M}\right]\, \mathcal{P}\left[(M_{\rm B}, x_1, c)_i \,|\, {\rm M}\right], \end{aligned} \tag{3.5}$$

where hatted quantities denote measured data values including all experimental noise, and unhatted quantities are intrinsic parameters that characterize the statistical distributions from which the supernovae are drawn. Only the intrinsic parameters satisfy the SALT2 relation (3.2). The empirical light-curve model (3.2) and the theoretical distance modulus (3.1) together constitute the model, M.

The expansion in (3.5) allows one to explicitly model the intrinsic scatter of the supernovae. For the NGS16 model (I) we assume that the intrinsic parameters of each supernova are drawn from identical independent Gaussian distributions

$$\begin{aligned}\mathcal{P}[(M_{\rm B}, x_1, c)_i \,|\, {\rm M}] &= \prod_i^N \mathcal{P}[(M_{{\rm B},i}, x_{1,i}, c_i) \,|\, {\rm M}] \\ &= \prod_i^N \mathcal{N}(M_{{\rm B},i}\,;\, M_{{\rm B},0}, \sigma_{M_{{\rm B},0}})\, \mathcal{N}(x_{1,i}\,;\, x_{1,0}, \sigma_{x_{1,0}})\, \mathcal{N}(c_i\,;\, c_0, \sigma_{c_0}),\end{aligned} \tag{3.6}$$

where $\mathcal{N}(y\,;\, y_0, \sigma) \equiv (2\pi\sigma^2)^{-1/2} \exp\left[-(y-y_0)^2/(2\sigma^2)\right]$ for each triple $\{y, y_0, \sigma\}$, with $3N \times 3N$ diagonal covariance matrix $\Sigma_l = \text{diag}\left(\sigma^2_{M_{{\rm B},0}}, \sigma^2_{x_{1,0}}, \sigma^2_{c_0}, \sigma^2_{M_{{\rm B},0}}, \dots\right)$. The experimental part of the likelihood (3.5), $\mathcal{P}\left[(\hat{z}, \hat{m}^*_{\rm B}, \hat{x}_1, \hat{c})_i \,|\, (M_{\rm B}, x_1, c)_i, {\rm M}\right]$ is assumed to be a Gaussian in the intrinsic supernova parameters, and the covariance matrix of experimental statistical and systematic uncertainties is denoted Σ_d. Performing the integral in (3.5) one obtains the final expression of the likelihood [137]

$$\begin{aligned}\mathcal{L} &= \mathcal{P}\left[(\hat{z}, \hat{m}^*_{\rm B}, \hat{x}_1, \hat{c})_i \,|\, {\rm M}\right] = \mathcal{P}\left[(\hat{m}^*_{\rm B} - \mu(\hat{z}), \hat{x}_1, \hat{c})_i \,|\, {\rm M}\right] \\ &= \left[(2\pi)^{3N} \det\left(\Sigma_d + A^\intercal \Sigma_l A\right)\right]^{-1/2} \\ &\quad \times \exp\left[-\tfrac{1}{2}\left(\hat{Z} - Y_0 A\right)\left(\Sigma_d + A^\intercal \Sigma_l A\right)^{-1}\left(\hat{Z} - Y_0 A\right)^\intercal\right]\end{aligned} \tag{3.7}$$

where $\hat{Z} = (\hat{m}^*_{{\rm B},1} - \mu(\hat{z}_1), \hat{x}_{1,1}, \hat{c}_1, \hat{m}^*_{{\rm B},2} - \mu(\hat{z}_2), \dots)$ is a $3N$-dimensional row vector containing the distance modulus residual and light-curve data, $Y_0 = (M_{{\rm B},0},\, x_{1,0},\, c_0,\, M_{{\rm B},0},\, \dots)$ is a $3N$-dimensional row vector of the intrinsic Gaussian means, and A is the block diagonal matrix that propagates Y_0 to

$$Y_0 A = (M_{{\rm B},0} - \alpha x_{1,0} + \beta c_0,\, x_{1,0},\, c_0,\, \dots).$$

Note that the cosmological model enters only explicitly through the conversion $\mu(\hat{z})$ of the observed redshift to a distance modulus. There can, however, be implicit model dependence in the experimental covariance matrix[1] Σ_d or in corrections made to data prior to the analysis.

[1] The propagation of the error σ_z to σ_μ depends on the model. However, by (3.24)–(3.26), to leading order for small z, $\sigma_\mu \simeq 5\sigma_z/(z \ln 10)$ for all cases.

To implement the RH16 parametrization (3.4) we replace (3.6) by

$$\begin{aligned}
&\mathcal{P}[(M_{\rm B}, x_1, c)_i \,|\, {\rm M}] \\
&\quad = \prod_{J=1}^{4} \prod_{i=1}^{N_J} \mathcal{N}(M_{{\rm B},i},\, M_{{\rm B},0},\, \sigma_{M_{{\rm B},0}}) \\
&\qquad \times \mathcal{N}(x_{1,i},\, x_{1,0,J} + x_{z,J}\hat{z},\, \sigma_{x_{1,0}})\, \mathcal{N}(c_i,\, c_{0,J} + c_{z,J}\hat{z},\, \sigma_{c_0}).
\end{aligned} \tag{3.8}$$

We recover (3.7) with the one difference: in place of three repeated entries, the vector Y_0 is now partitioned into different pieces for each subsample, $Y_0 = (M_{{\rm B},0},\, x_{1,0,1} + x_{z,1}\hat{z}_1,\, c_{0,1} + c_{z,1}\hat{z}_1,\, \ldots,\, M_{{\rm B},0},\, x_{1,0,2} + x_{z,2}\hat{z}_i,\, c_{0,2} + c_{z,2}\hat{z}_i, \ldots, \ldots,$ $M_{{\rm B},0}, x_{1,0,4}, c_{0,4})$.

From the likelihood (3.7) we can define frequentist confidence regions and goodness of fit measures or alternative Bayesian versions of these, following conventional statistical procedures summarized in Appendix 3.C.

In practice, estimating the Bayesian evidence is a computationally intensive task, much more so than what is required to obtain parameter estimates. We use standard Markov Chain Monte Carlo (MCMC) methods to sample parameter space. We estimate the evidence using the publicly available MultiNest [140] code,[2] with Python interface PyMultinest [142], for the efficient evaluation of the evidence integral (3.34) with likelihood (3.7). The accuracy of the Bayesian evidence estimate is controlled by the number of 'live' points, $n_{\rm live}$, with an error $\sigma \sim O(n_{\rm live}^{-1/2})$. In our analysis we choose 1000 points for the 8 or 9 parameter base model and add 100 more points for each additional parameter.

3.2.2 Choice of priors

Given the sensitivity of the Bayes factor to priors it is important these are chosen as objectively as possible. The choice of priors are summarized in Table 3.1.

[2] This package is based on the Nested sampling algorithm [141].

Model	Ω_{M0}	α	$x_{1,0}$	$\sigma_{x_{1,0}}$	β	c_0	σ_{c_0}	$M_{\mathrm{B},0}$	$\sigma_{M_{\mathrm{B},0}}$
Timescape	$0.309^{+0.070\ (1\sigma)\ 0.127\ (2\sigma)}_{-0.088\ (1\sigma)\ 0.210\ (2\sigma)}$	0.134	0.1050	0.899	3.13	-0.0211	0.0689	-19.1	0.104
Spatially flat ΛCDM	$0.365^{+0.033\ (1\sigma)\ 0.066\ (2\sigma)}_{-0.031\ (1\sigma)\ 0.060\ (2\sigma)}$	0.134	0.1061	0.899	3.14	-0.0215	0.0688	-19.0	0.104
Empty universe	–	0.133	0.1013	0.900	3.13	-0.0204	0.0690	-19.0	0.106

Table 3.2: Best-fitting MLE parameters corresponding to the likelihood $\mathcal{L}(\mathrm{Data}|\mathrm{M})$ with the model M representing the cosmological model, the SALT2 procedure and the intrinsic distributions of SNIa parameters. SNIa at redshifts $z < 0.033$ (statistical homogeneity scale) are excluded. Confidence limits are given for the one free cosmological parameter. In the timescape case this corresponds to $f_{\mathrm{v}0} = 0.778^{+0.063\ (1\sigma)\ 0.155\ (2\sigma)}_{-0.056\ (1\sigma)\ 0.104\ (2\sigma)}$. The value of $M_{\mathrm{B},0}$ is obtained for $h = 0.668$ for the timescape, and $h = 0.7$ for the two FLRW models. The difference of parameters from NGS16 is principally due to the SHS cut at $z_{\mathrm{min}} = 0.033$, the effect of which is seen in Fig. 3.2.

3.2.2.1 Nuisance parameters

All nuisance parameters are common to both timescape and ΛCDM models and we therefore assign the same priors to both models. Where possible,[3] we adopt priors that have been used in previous Bayesian studies of the SALT2 method [138, 143]. The standard deviations $\{\sigma_{x_{1,0}}, \sigma_{c_0}, \sigma_{M_{\mathrm{B},0}}\}$ are 'scale' parameters (of the residuals) and so it is more appropriate to assign a log-uniform prior to these parameters. The priors for the nuisance parameters are wide to ensure the most likely regions of parameter space are supported, and provided they are wide enough, this will have no overall effect on the Bayes factor (as the evidence of each model will be similarly scaled).

3.2.2.2 Cosmological parameters

Only one free cosmological parameter can be constrained by supernovae: Ω_{M0} for spatially flat ΛCDM or $f_{\mathrm{v}0}$ for the timescape model. Conventionally, the combination of Ω_{M0} and H_0 for the standard cosmology is strongly constrained by the CMB acoustic peaks [144]. Measurements of the Baryon Acoustic Oscillation (BAO) scale in galaxy clustering statistics [145, 59] at low redshifts and the Lyman α forest [61, 145] provide independent constraints. In the case of the timescape model, however, our ability to model the CMB is still limited by systematic uncertainties of 8–13% [127].

We therefore determine priors for $f_{\mathrm{v}0}$ in the timescape model using best present

[3] Given the complications introduced by empirical changes (3.4) to $x_{1,0}$, c_0, we adopt uniform priors for for these parameters.

knowledge. For the CMB we use results of a model-independent analysis of the acoustic peaks [146] with Planck satellite data, and choose a prior from a 95% confidence fit of the angular scale of the sound horizon. To date BAO studies all implicitly assume the FLRW model, and do not yet provide an equivalent model independent constraint. We therefore adopt a prior using FLRW-model estimates of the angular diameter of the BAO scale, including the full range of values which are currently in tension [61, 145, 59]. We take generous 95% confidence limits determined by assuming that *either* the low redshift galaxy clustering results [145, 59] *or* the $z = 2.34$ Lyman-α results [61] are correct. Priors for the spatially flat ΛCDM model are determined by an identical methodology. Further details are given in Appendix 3.D.

3.3 Results

3.3.1 Analysis with supernova parameters drawn from global Gaussian distributions

Since there is a degeneracy between the Hubble constant, H_0, and the magnitude, $M_{\rm B,0}$, we fix H_0 for each model. The value of $M_{\rm B,0}$ then depends on this choice. We are then left with one free cosmological parameter, the matter density parameter Ω_{M0} in the spatially flat ΛCDM model, and the present epoch void fraction $f_{\rm v0}$ in the timescape model. We can alternatively define an effective "dressed matter density parameter" $\Omega_{M0} = \frac{1}{2}(1 - f_{\rm v0})(2 + f_{\rm v0})$ [95, 97], which takes similar numerical values to the concordance ΛCDM model, allowing likelihood functions to be plotted on the same scale. (This parameter does not obey the Friedmann equation sum rule, however.) The 9 parameters $\{\Omega_{M0}, \alpha, x_{1,0}, \sigma_{x_{1,0}}, \beta, c_0, \sigma_{c_0}, M_{\rm B,0}, \sigma_{M_{\rm B,0}}\}$ are then fit for each model by determining the likelihood function with all parameters other than Ω_{M0} (or $f_{\rm v0}$) treated as nuisance parameters. The empty universe has 8 parameters since $\Omega_{M0} = 0$.

3.3.1.1 Statistical homogeneity scale cuts

An important systematic issue in the timescape cosmology is the fact that an average expansion law only holds on scales greater than the statistical homogeneity scale (SHS) $\gtrsim 70$–$120\, h^{-1}$Mpc [147, 148]. This corresponds to a CMB rest frame redshift of order $z \sim 0.023$–0.04. In fact, SNIa analyses using the MLCS method have typically excluded

SNIa below a cutoff at $z = 0.024$ [149]. However, the JLA catalogue [123] includes 53 SNIa, with $z < 0.024$.

Following [125] we determine cosmological model distances in the CMB frame, but make a redshift cut at the SHS, taken at $\sim 100\,h^{-1}$Mpc. Furthermore, to examine the effect of the SHS cut on the fit of light-curve parameters, we perform the entire analysis while progressively varying the minimum redshift in the range $0.01 \leq z_{\rm min} < 0.1$; i.e., up to a redshift 3 times larger than the SHS. Systematic effects associated with the SHS can then be revealed. Our key results will be quoted for a cut at $z_{\rm SHS} = 0.033$ in the CMB rest frame. The best-fitting MLE parameters with $z_{\rm min} = 0.033$ are presented in Table 3.2.

For the priors given in Table 3.1 the Bayesian evidence in favour of the timescape model relative to the spatially flat ΛCDM model is $\ln B = 0.085 \pm 0.01$ with $z_{\rm min} = 0.033$, or $\ln B = 0.600 \pm 0.007$ with $z_{\rm min} = 0.024$. Since $|\ln B| < 1$ the two models[4] are statistically indistinguishable. This conclusion is insensitive to $\mathrm{O}(1\sigma)$ changes to the width of the uniform priors on $f_{\rm v0}$ and Ω_{M0}, or to variations of the minimum redshift as shown in Fig. 3.2(e).

While the Bayes factors do not show significant variation with $z_{\rm min}$, the values of particular best-fitting light-curve parameters show a marked change at the SHS. As shown in Fig. 3.2, there is a marked 30% jump in c_0 as $z_{\rm min}$ is varied from 0.01 up to $z \simeq 0.033$, when compared to the subsequent fluctuations if $z_{\rm min}$ is increased up to 0.1. For $x_{1,0}$ there is a similar jump, although a linear trend remains in the range $0.033 < z_{\rm min} < 0.1$. The parameter β parameter shows a small (3%) jump up to the SHS followed by ±1% fluctuations, while α remains relatively constant, fluctuating by ±2% over the whole range.

Since the light-curve parameters are remarkably close for all three cosmologies while showing a jump as the SHS emerges (distinct from the residual c_0 trend for the empty model with $z_{\rm min} \gtrsim 0.05$) there is clear evidence for some systematic effect at precisely the scale where we expect it.

[4] Both models have positive relative Bayesian evidence compared to the empty model. Although the evidence is not particularly strong, $|\ln B_2| \sim 2.2$ incorporates priors which demand standard recombination for both ΛCDM and timescape. By that criterion the empty model is simply ruled out.

Timescape	k	Ω_{M0}	$\langle x_{1,0}\rangle$	$\langle c_0\rangle$	$\langle x_z\rangle$	$\langle c_z\rangle$	BIC	$\Delta_{\rm BIC}$	$\ln E$	C_b	$\ln B_1$	$f_{\rm v0}$
I (NGS16)	9	0.309	0.105	-0.021			-185.0		80.38	8.53		0.778
II	10	0.278	-0.073	-0.021	0.511		-199.6	-14.6	81.67	9.28	-1.28	0.802
III	15	0.278	-0.183	-0.021	0.806		-169.9	15.1	66.46	14.11	13.93	0.801
IV	10	0.000	0.104	0.002		-0.065	-249.9	-64.9	78.52	9.19	1.86	1.000
V	15	0.010	0.092	0.054		-0.351	-157.7	27.3	81.29	14.15	-0.91	0.993
VI	11	0.000	-0.071	0.001	0.499	-0.062	-189.7	-4.7	79.35	10.21	1.94	1.000
VII (RH16)	21	0.000	-0.123	0.054	0.490	-0.348	-200.0	-15.0	65.85	19.47	14.53	1.000
VIII	16	0.000	-0.085	0.061	0.501	-0.348	-229.3	-44.3	82.03	15.30	-1.65	1.000
Flat ΛCDM	k	Ω_{M0}	$\langle x_{1,0}\rangle$	$\langle c_0\rangle$	$\langle x_z\rangle$	$\langle c_z\rangle$	BIC	$\Delta_{\rm BIC}$	$\ln E$	C_b	$\ln B_1$	$\ln B_2$
I (NGS16)	9	0.365	0.106	-0.021			-192.5		80.30	8.93		0.08
II	10	0.353	-0.069	-0.021	0.503		-241.2	-48.7	81.64	10.01	-1.34	0.03
III	15	0.353	-0.186	-0.021	0.847		-159.8	32.7	66.62	14.60	13.68	-0.16
IV	10	0.303	0.106	-0.002		-0.057	-192.9	-0.4	79.60	9.98	0.70	-1.08
V	15	0.296	0.093	0.052		-0.354	-228.5	-36.0	83.77	14.87	-3.47	-2.47
VI	11	0.292	-0.069	-0.002	0.501	-0.057	-179.1	13.4	80.87	10.97	2.89	-1.52
VII (RH16)	21	0.286	-0.127	0.051	0.534	-0.352	-155.3	37.2	68.97	20.58	11.33	-3.12
VIII	16	0.286	-0.080	0.059	0.499	-0.354	-232.8	-40.3	84.95	15.89	-4.65	-2.92
Empty	k	Ω_{M0}	$\langle x_{1,0}\rangle$	$\langle c_0\rangle$	$\langle x_z\rangle$	$\langle c_z\rangle$	BIC	$\Delta_{\rm BIC}$	$\ln E$	C_b	$\ln B_1$	$\ln B_2$
I (NGS16)	8	-	0.101	-0.020			-181.5		78.18	8.11		2.20
II	9	-	-0.078	-0.019	0.517		-190.1	-8.6	79.92	9.02	-1.74	1.75
III	14	-	-0.095	-0.020	0.749		-218.9	-37.4	64.43	13.75	13.76	2.03
IV	9	-	0.098	0.002		-0.054	-185.7	-4.2	78.56	9.05	-0.37	-0.03
V	14	-	0.087	0.054		-0.336	-180.4	1.1	79.85	14.19	-1.66	1.45
VI	10	-	-0.072	0.002	0.489	-0.051	-186.3	-4.8	79.62	10.17	0.23	-0.27
VII (RH16)	20	-	-0.122	0.054	0.460	-0.332	-198.7	-17.2	64.31	18.68	13.88	1.55
VIII	15	-	-0.081	0.061	0.482	-0.334	-221.4	-39.9	80.74	14.89	-2.55	1.30

Table 3.3: Selected parameters fit for $z_{\rm min} = 0.033$, with the following empirical models for light-curve parameters: (I) constant $x_{1,0}$, constant c_0; (II) global linear $x_{1,0}$, constant c_0; (III) split linear $x_{I,1,0}$, constant c_0; (IV) constant $x_{1,0}$, global linear c_0; (V) constant $x_{1,0}$, split linear $c_{0,I}$; (VI) global linear $x_{1,0}$, global linear c_0; (VII) split linear $x_{1,0}$, split linear c_0; (VIII) global linear $x_{1,0}$, split linear c_0. Notes: $k \equiv$ number of free parameters; quantities $\langle\Phi\rangle \equiv (\sum N_I\,\Phi_I)/(\sum_{I=1}^4 N_I)$ denote an average over subsamples with $I = 1\ldots4$ for $x_{1,0,I}$, $c_{0,I}$ and $I = 1\ldots3$ for $x_{z,I}$, $c_{z,I}$ for split models or $\langle\Phi\rangle \equiv \Phi$ otherwise; BIC = Bayesian Information Criterion; E = Bayesian evidence; C_b = Bayesian complexity; $\Delta_{\rm BIC} = {\rm BIC}_{\rm model} - {\rm BIC}_{\rm I}$ and $\ln B_1 = \ln(E_{\rm I}/E_{\rm model})$ are evaluated with cosmological model fixed; $\ln B_2 = \ln(E_{\rm TS}/E_{\rm model})$ is evaluated with light-curve model fixed.

3.3.2 Analysis with linear redshift variation for mean stretch and colour parameters

Although RH16 considered four distinct subsamples, the mean stretch parameter actually shows a global increasing trend in the ΛCDM case evident in [139, Fig. 1, left panels]. Our procedure of varying the minimum redshift cut on the whole sample also isolates any global trend. Such a trend is indeed evident in Fig. 3.2(c) beyond the SHS, with $x_{1,0}$ increasing 40% as the minimum sample redshift increases from $z_{\rm min} = 0.033$ to $z_{\rm min} = 0.1$. Beyond $z_{\rm min} = 0.034$ an equivalent global trend in the mean colour parameter, c_0, is not evident in Fig. 3.2(d), however, except in the case of the empty universe, which shows a 13% decrease in c_0 between $z_{\rm min} = 0.034$ and $z_{\rm min} = 0.1$. A global shift in $x_{1,0}$ would seem more consistent with an astrophysical systematic in the source population, rather than sampling biases with different thresholds for different samples.

To fully understand the differences that arise on making the RH16 changes (3.4), we have also investigated the effect of adding a smaller number of free parameters, by considering linear z relations in just one of the parameters $x_{1,0}$ or c_0, and the difference between global linear relations and a split by subsamples. The advantage of our fully Bayesian approach is that not only can we compare the relative Bayesian evidence for different cosmological models with the same light-curve parameters, but we can also compare the merits of different empirical light-curve models. The values of the Bayesian evidence are shown in Table 3.3, along with a selection of parameters. The changes to the parameters α and β are negligible between models, and are not tabulated. We do not tabulate all additional (up to 12) parameters for the case of the split subsamples, but an average.

3.3.2.1 Stretch parameter $x_{1,0}$

Consistent with remarks above, relative to the baseline NGS16 model I, light curve model II provides positive (but not strong) Bayesian evidence for a global linear trend in $x_{1,0}$ independent of cosmological model, with $\ln B_1 = 1.28, 1.34, 1.74$ for the timescape, ΛCDM and empty models respectively. The BIC evidence for the same conclusion is very strong (timescape, ΛCDM models) or strong (empty model). By contrast model III gives strong evidence $|\ln B_1| > 13$ against a split linear law in $x_{1,0}$ independent of cosmological model. The Bayesian penalty for introducing new empirical parameters

depends on the choice of the priors, but our conclusion is robust to reasonable changes. Furthermore, the frequentist BIC statistic $\Delta_{\rm BIC}$ also strongly disfavours model III relative to models I, II in the ΛCDM and timescape cases.

3.3.2.2 Colour parameter c_0

In contrast to the stretch parameter, results involving the colour parameter vary greatly with cosmological model. Despite model IV having the global minimum BIC statistic for timescape, $\ln B_1$ shows no significant evidence[5] for any global linear redshift law. Relative Bayesian evidence for a split linear law in c_0 is marginal for timescape, positive for the empty universe, and strong for ΛCDM, with $\ln B_1$ = -0.91, -1.66 and -3.47 respectively.

The original RH16 model VII suffers similar problems to model III in terms of Bayesian evidence, evidently on account of the split linear law in $x_{1,0}$. However, model VIII has the strongest Bayesian evidence of all models. It adds a global linear redshift law in $x_{1,0}$ to model V. The improvement in Bayesian evidence for model VIII relative to model V is marginal for timescape and the empty universe, and positive for ΛCDM, with $\Delta \ln B_1 = -0.74$, -0.89 and -1.18 respectively.

Although $\ln B_2$ for model VIII gives positive (but not strong) relative evidence for ΛCDM over timescape, any conclusion drawn from this depends on additional empirical light-curve parameters which now depend on the cosmological model[6]. Furthermore, since the maximum likelihoods are comparable, the difference in Bayesian evidence is primarily due to the timescape maximum likelihood being driven to the unphysical limit $f_{\rm v0} \to 1$ for any light-curve model with linear variations in c_0, as is shown in Fig. 3.3, which compares likelihoods in Ω_{M0} (or $f_{\rm v0}$) for the NGS16 and RH16 models for two choices of $z_{\rm min}$.

Very similar results were found by [125] in applying SALT2 without the methodology of NGS16, leading to a large discrepancy in the predictions of the SALT2 and MLCS2k2 fitters for timescape. Since direct application of the NGS16 methodology to the JLA catalogue agrees with some previous MLCS2k2 fits to smaller data sets [124, 125], we conclude that systematics similar to linear redshift variations in c_0 may

[5] The empty universe has marginal evidence, consistent with Fig. 3.2(d) for $z_{\rm min} > 0.05$.

[6] Some of the largest differences occur in the SNLS subsample: $c_{0,\Lambda{\rm CDM}} = 0.0483$ and $c_{0,{\rm TS}} = 0.0565$, a 17% difference. For the NGS16 model, by contrast, differences are 2%.

be the key to earlier discrepancies.

3.3.2.3 Cosmological model dependency of linear redshift changes to SALT2 methodology

To understand the origin of such differences consider the Taylor series expansions (3.24)–(3.26) for the timescape, spatially flat ΛCDM and empty universe models, as given in Appendix 3.A. Leading coefficients for (3.24) and (3.25) are shown graphically in Fig. 3.4 as a function of the free cosmological parameter.

All cosmologies show improvement to a global increase in $x_{1,0}$ with redshift and piecewise decreases in c_0, including the empty model which has no free parameter to adjust. However, if we incorporate linear corrections $x_z z$ to $x_{1,0}$, or $c_z z$ to c_0, in the SALT2 relation, then the difference of (3.2) and (3.24)–(3.26) gives a potential degeneracy between empirical parameters x_z or c_z and changes in the free cosmological parameter if the linear term in (3.24)–(3.26) can be changed without greatly altering the next most important $\mathrm{O}(z^2)$ term. Such a possibility is admitted by ΛCDM but not timescape.

For ΛCDM, the $\mathrm{O}(z)$ term in (3.25) is linear in Ω_{M0}, and the $\mathrm{O}(z^2)$ term is quadratic in Ω_{M0} with a minimum at $\Omega_{M0} = \frac{8}{27} = 0.296$. For model V with split linear redshift laws in c_0 only, the best-fitting Ω_{M0} coincides precisely with this minimum. The decrease in Ω_{M0} by adding a global linear z dependence to $x_{1,0}$ is approximately the same, $\Delta\Omega_{M0} = -0.01$, in going from model V to VIII, or from model I to II. The difference in (3.25) between models I and VII/VIII,

$$\begin{aligned}\mu_{\Lambda\mathrm{CDM}}(0.286) - \mu_{\Lambda\mathrm{CDM}}(0.365) &= 0.1287\, z - 0.0085\, z^2 \\ &\quad - 0.0481\, z^3 + 0.0249\, z^4 + 0.0161\, z^5 - 0.0232\, z^6 + \ldots \end{aligned} \tag{3.9}$$

is dominated by the linear redshift changes, with negligible changes in the $\mathrm{O}(z^2)$ term.

By contrast the terms in the Taylor series (3.24) for timescape are very slowly varying monotonic functions of $f_{\mathrm{v}0}$ on the range $0.6 < f_{\mathrm{v}0} \leq 1.0$ (as shown in Fig. 3.4), so changes in μ_{TS} are much more constrained. The difference in (3.24) between models

I and VII/VIII, is

$$\mu_{\rm TS}(1.0) - \mu_{\rm TS}(0.778) = 0.0674\,z + 0.0444\,z^2 \\ - 0.0242\,z^3 + 0.0190\,z^4 - 0.0193\,z^5 + 0.0173\,z^6 + \ldots \qquad (3.10)$$

A large change in $f_{\rm v0}$ is required make changes in $\mu_{\rm TS}$ comparable to the ΛCDM case, and the effect of increasing $f_{\rm v0}$ increases both the $\mathrm{O}(z)$ and $\mathrm{O}(z^2)$ terms. As seen in Fig. 3.5, the likelihood is consequently peaked along narrow ridges in the $(x_z,f_{\rm v0})$ and $(c_{z,J},f_{\rm v0})$ planes, with almost constant values of x_z and $c_{z,J}$ and no upper bound on $f_{\rm v0}$.

3.4 Discussion

Our study has a number of important consequences. Firstly, the timescape and spatially flat ΛCDM model luminosity distance–redshift fits to the JLA catalogue are statistically indistinguishable using either the approach of NGS16, or with modifications to only the mean stretch parameter. As shown in Table 3.3 the Bayesian complexity, C_b, is lower (better) for timescape than for ΛCDM, for every choice of light-curve model.

This completely reframes a debate [137, 139, 143, 150, 151] about whether cosmic acceleration is marginal or not, within the confines of a FLRW expansion history. Current supernova data does not distinguish between the standard ΛCDM model and the non-FLRW expansion history of the timescape model, which has non-zero apparent cosmic acceleration but with a *marginal amplitude*. The apparent deceleration parameter (3.23) for the best-fitting value of Table 3.2 is $q_0 \equiv q(f_{\rm v0}) = -0.043^{+0.004}_{-0.000}$.

Within the class of FLRW models the significance of cosmic acceleration is often assessed by comparison to the empty universe model. That model is unphysical, since standard nucleosynthesis and recombination can never occur in a universe with $a(t) \propto t$ regardless of its matter content.[7] The timescape model has positive $\ln B_2$ compared to the empty universe.[8] Nonetheless, $|\mu_{\rm TS}(z) - \mu_{\rm empty}(z)| < |\mu_{\Lambda{\rm CDM}}(z) - \mu_{\rm empty}(z)|$ (c.f. Fig. 3.1) at late epochs, for a simple physical reason. The timescape model is

[7] In particular, the $R_h = ct$ model is unphysical for this reason [152].

[8] This is true for the NGS16 model I and all light-curve models for which $\ln B_1$ shows an improvement independent of cosmology, viz. models II, V, VIII.

void dominated at $z < 1$, and the expansion of individual voids is close to an empty universe. While the timescape model has apparent acceleration at late epochs, its expansion law is closer to that of an empty universe than that of the ΛCDM model.

The second important consequence of our study is that allowing linear changes with redshift to the mean colour parameter, c_0, produces cosmological model dependency. Since the redshift–distance relation of the timescape model effectively interpolates [97, 128] between those of spatially flat ΛCDM models with different values[9] of Ω_{M0}, particular care must be taken with piecewise linear relations in redshift.

The improved 16 parameter model VIII (this being a better fit than the original 21 parameter RH16 model) has positive Bayesian evidence for ΛCDM relative to the timescape model. However, this is contingent on degeneracies in the likelihood function between the free cosmological parameter and additional empirical parameters. The RH16 parametrization allows the ΛCDM deceleration parameter $q_0 = -1 + \frac{3}{2}\Omega_{M0}$ contained in the $\mathrm{O}(z)$ term of the Taylor series (3.25) to be adjusted[10] near the global minimum $\Omega_{M0} = 0.296$ of the $\mathrm{O}(z^2)$ term in (3.25). However, the same procedure drives the timescape free parameter to an unphysical limit, $f_{\mathrm{v}0} \to 1$. No fundamental model underlies the empirical parametrization (3.4). Variations in c_0 are most plausibly related to selection effects, given we cannot fit them by a global law. However, selection effects would be more correctly modelled by removing the tail of a Gaussian distribution rather than shifting its mean linearly in redshift.

Our results show that NGS16 did not account for every possible selection bias that remains in the JLA catalogue, consistent with some comments of RH16. Nonetheless, NGS16 are correct to point out the possible pitfalls in fitting SNIa data when empirical light-curve parameters are mixed with the cosmological parameters of a single class of cosmological models. If SNIa are to be used to distinguish cosmological models, then systematic uncertainties and selection biases should be corrected in as model independent manner as possible *before* the data is reduced.

A related issue which remains to be explored is the extent to which the corrections for selection biases that have already been made in the JLA catalogue depend on the

[9] Note that the Planck best-fitting value $\Omega_{M0} = 0.3175$ [144] is lower than the best-fitting value for the spatially flat ΛCDM model value $\Omega_{M0} = 0.365$ from Table 3.2, consistent with the timescape expectation.

[10] For the NGS16 model I and models VII/VIII one has best fits $q_0 = -0.453$ and $q_0 = -0.571$ respectively. The respective spatially flat ΛCDM values quoted by [139], namely $q_0 = -0.412$, -0.552, (or $\Omega_{M0} = 0.392$, 0.299), differ mostly on account of our SHS cut at $z_{\min} = 0.033$.

FLRW model. [123] follow a procedure of [153, Sec. 6.2], who used the SNANA package to estimate selection biases. Simulated data (using the FLRW model) is used in such estimates. While efforts have been made to consider different dark energy equations of state [153], models which do not satisfy the Friedmann equation fall outside the scope of such analyses.

Whether or not the timescape model is ultimately a better fit than the standard FLRW model, it may provide a useful diagnostic tool in comparing methods for SNIa light-curve reduction purely at the empirical level. In particular, it has an analytic non-FLRW redshift–distance relation which is very close to that of the ΛCDM model, but which is considerably more constrained in the free parameter $f_{\rm v0}$ than the ΛCDM model is in Ω_{M0}.

Finally, Figs. 3.2(b),(c),(d) show evidence for a $\simeq 100\,h^{-1}$Mpc statistical homogeneity scale which has an effect on global fits of light-curve parameters – most notably a 30% shift of c_0 – *independent of the cosmological model*. These systematics, which occur at a scale relevant from independent observations [147, 148], must be explained irrespective of the cosmological model.

The analysis of this chapter has been repeated in [154] after the publication of the Pantheon catalogue of SNIa [155]. The Pantheon catalogue, consisting of 1048 SNIa, include the majority of the SNIa from the JLA catalogue with the addition of a subset of the Pan-STARRS1 survey of SNIa. Distance moduli in the Pantheon catalogue are determined by a modification of the SALT2 relation [135, 136], in which additional corrections are made for for the mass of the host galaxy and where a 'bias correction' is made using ΛCDM N-body simulations.

There are no publicly available data from Pantheon similar to the (almost) model-independent publicly available JLA catalogue, which makes repeating the analysis of this chapter with the Pantheon catalogue impossible. What is provided in the Pantheon catalogue are distance moduli obtained using assumptions intrinsic to ΛCDM models. In [154] the following steps were adopted: (i) use the publicly available ΛCDM reduced data in the form ΛCDM deduced distance moduli from Pantheon to produce Bayes factors similar to those reported in this chapter, but keeping in mind that the statistical analysis is not fully consistent because of the strong model assumptions used to reduce data; (ii) repeat the analysis of this chapter with the SNIa contained in both the JLA and the Pantheon catalogue – i.e. using the JLA catalogue with the 94 SNIa unique to the JLA sample removed.

The common subsample of 646 SNIa present in both the JLA and the Pantheon catalogue was analysed in order to directly compare the difference in data reported for the same supernovae and the impact on cosmological data analysis. For a redshift cut of $z_{\min} = 0.24$ the logarithm of the Bayes factor, $\ln B = \ln(E_{\rm TS}/E_{\Lambda{\rm CDM}})$, for the common subsample of JLA was found to be $\ln B = 1.4$ in favour of the timescape model (whereas $\ln B = 0.6$ for the full JLA sample with the same redshift cut). For the common subsample of Pantheon it was found that $\ln B = -1.6$ in favour of the ΛCDM model. The large difference in Bayes factor for the same set of SNIa when employing the Pantheon and the JLA data reduction methods respectively highlight the importance of model independent data reduction.

The results using the subset of the JLA catalogue induced changes of order $\sim 10\%$ for all best fits parameters of the analysis, and for some parameters also significantly changed the systematics in redshift with respect to the results in figure 3.2 found for the full JLA sample. The best fit parameters and their trends as a function of redshift cut $z_{\min}$ as found in [154] are shown in figure 3.6. Some trends in redshift cut seem to be reduced when removing the 94 SNIa unique to the JLA sample – see, e.g., the trend in $x_{1,0}$ below and around the ΛCDM estimated homogenate scale of $z \sim 0.03$. Other trends seem to be introduced or enhanced, as for instance an additional trend in c_0 for redshifts of $z \gtrsim 0.05$. Best fit values of Ω_M decrease by roughly 10% for ΛCDM when the full sample with no cut in redshift is considered, and thereby gets closer to the latest inferred value $\Omega_M = 0.315 \pm 0.007$ reported by Planck [62].

No arguments have been presented in [155] as to why 94 SNIa of the JLA sample were removed. The order 10% changes induced by removing a subset of supernovae are in line with the indications of this chapter, that unknown and poorly quantified systematics are strongly dominating the error budget of supernovae analysis.

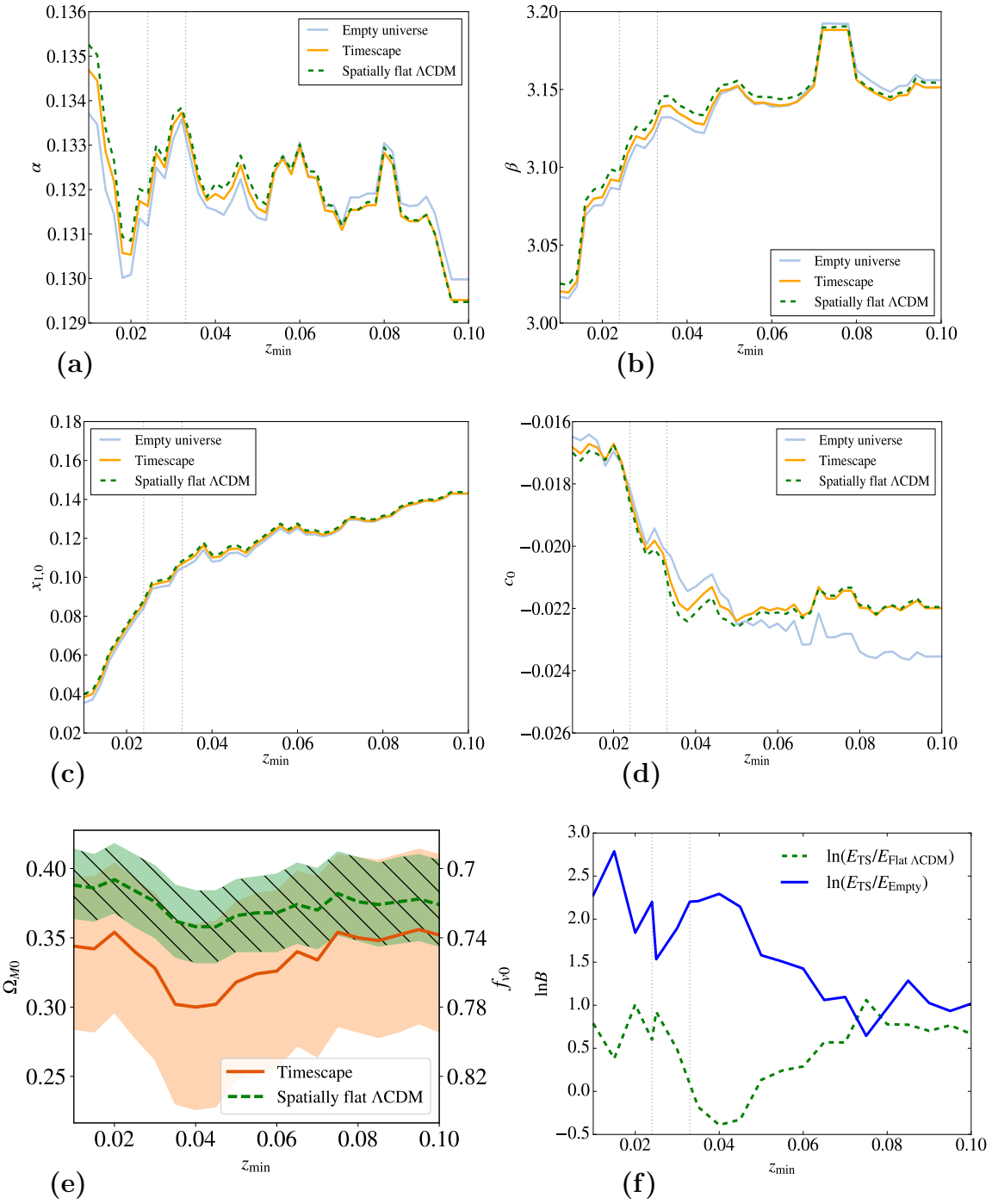

Figure 3.2: MLE best-fitting parameters, and Bayes factor, for the NGS16 model as $z_{\min}$ is varied: **(a)** α; **(b)** β; **(c)** $x_{1,0}$; **(d)** c_0; **(e)** Ω_{M0} (or f_{v0}) with 1σ bounds; **(f)** $\ln B = \ln(E_{TS}/E_{model})$. Vertical dotted lines at $z_{\min} = 0.024$ and $z_{\min} = 0.033$ indicate the expected rough redshift range of an emerging statistical homogeneity scale.

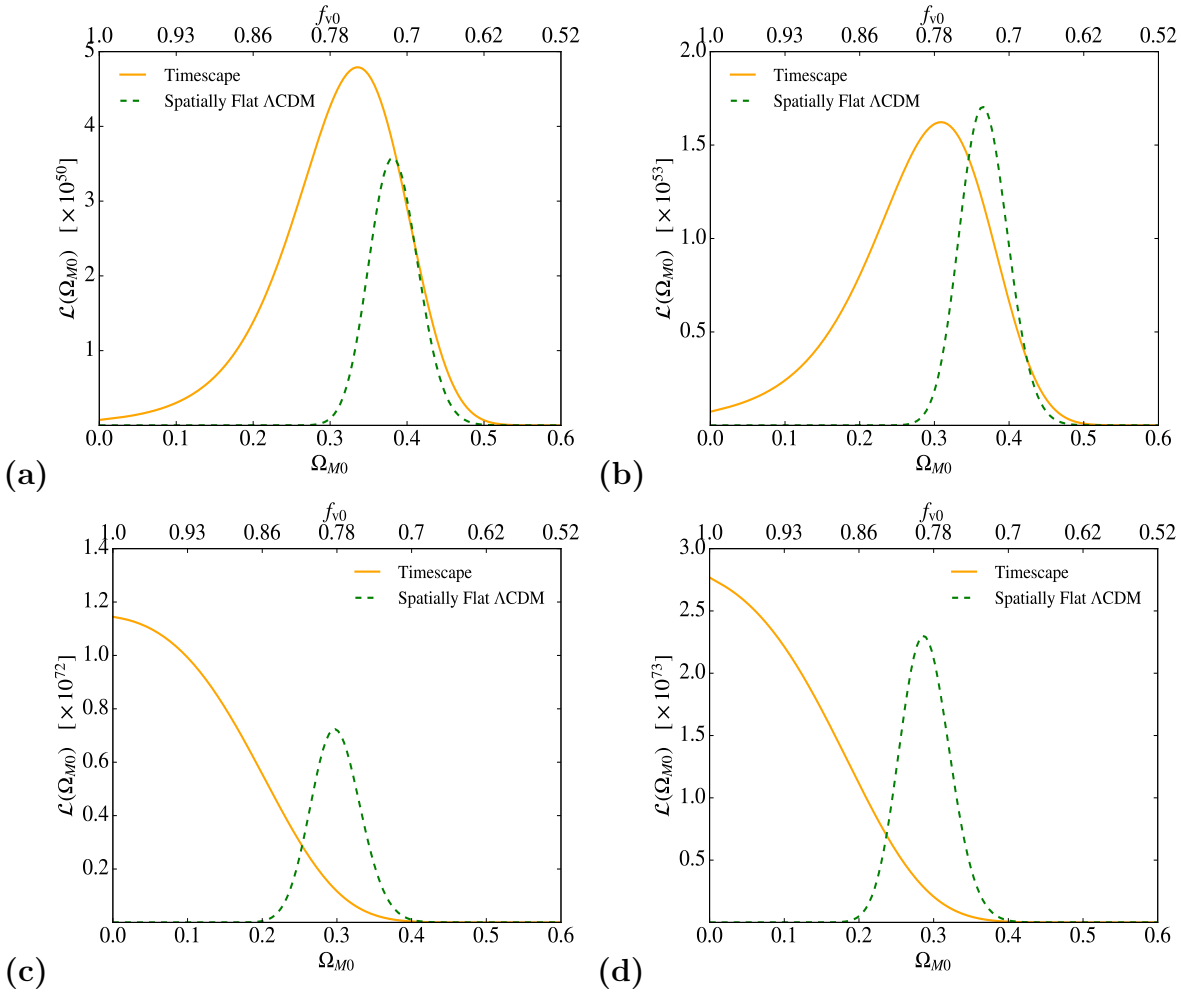

Figure 3.3: Profile likelihoods in Ω_{M0} and $f_{\rm v0}$ for model I (NGS16) and model VII (RH16): **(a)** NGS16, $z_{\rm min} = 0.024$; **(b)** NGS16, $z_{\rm min} = 0.033$; **(c)** RH16, $z_{\rm min} = 0.024$; **(d)** RH16, $z_{\rm min} = 0.033$. Model IV, V, VI and VIII results are very similar to model VII.

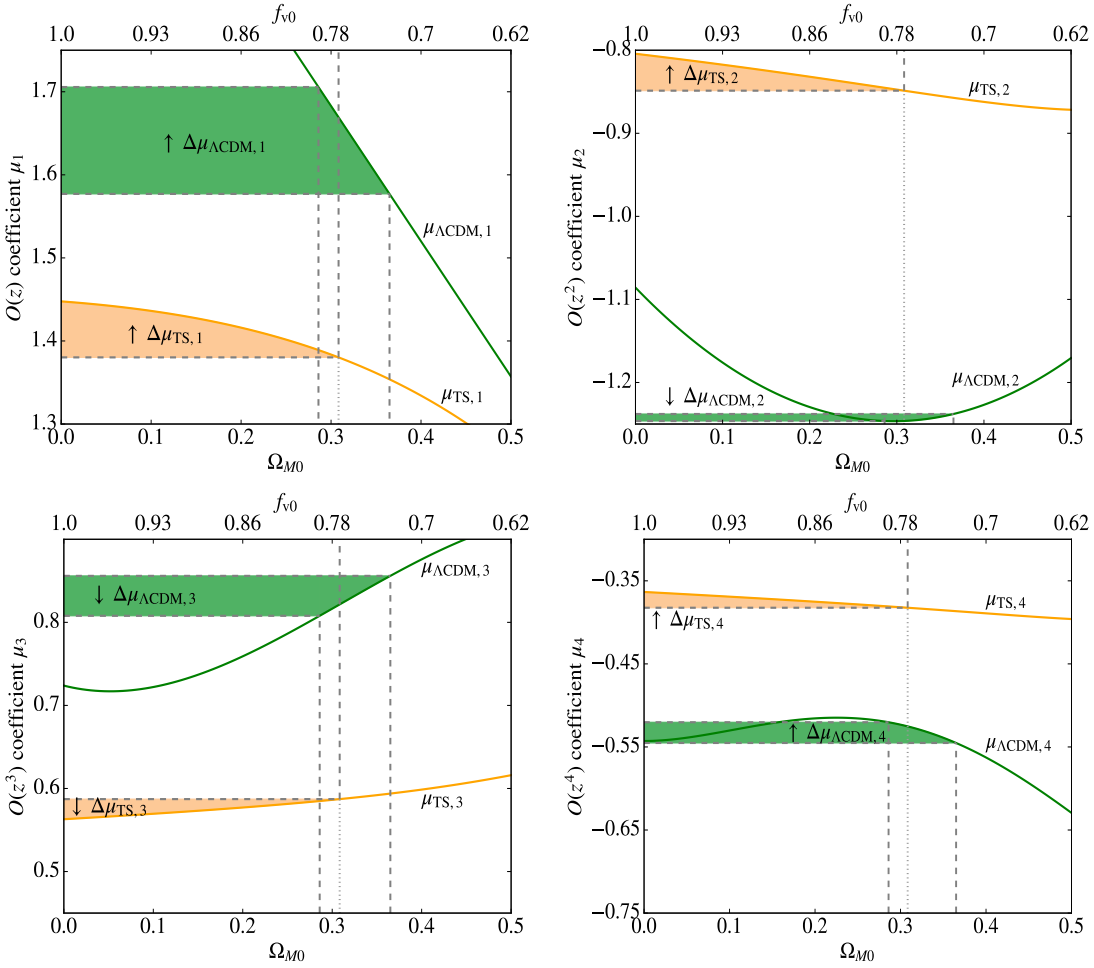

Figure 3.4: Coefficients in the Taylor series (3.24), (3.25), $\mu = \mu_0(z) + \sum_{n=1} \mu_n z^n$, of the spatially flat ΛCDM and timescape models, as a function of the free cosmological parameter, Ω_{M0} or f_{v0}. For timescape the coefficients $\mu_{TS,n}$ are very slowly varying monotonic functions of f_{v0} on the range $0.6 < f_{v0} \leq 1$, whereas the coefficients $\mu_{\Lambda CDM,n}$ are polynomials of order n. For each n, $|\mu_{TS,n}| < |\mu_{\Lambda CDM,n}|$, reflecting the "flatter" distance modulus (cf. Fig. 3.1). Linear changes of Ω_{M0} can become degenerate with empirical light-curve parameters linear in z for parameters close to the minimum of $\mu_{\Lambda CDM,2}$ at $\Omega_{M0} = 0.296$. The change in the coefficients between NGS16 model I and models VII/VIII is indicated.

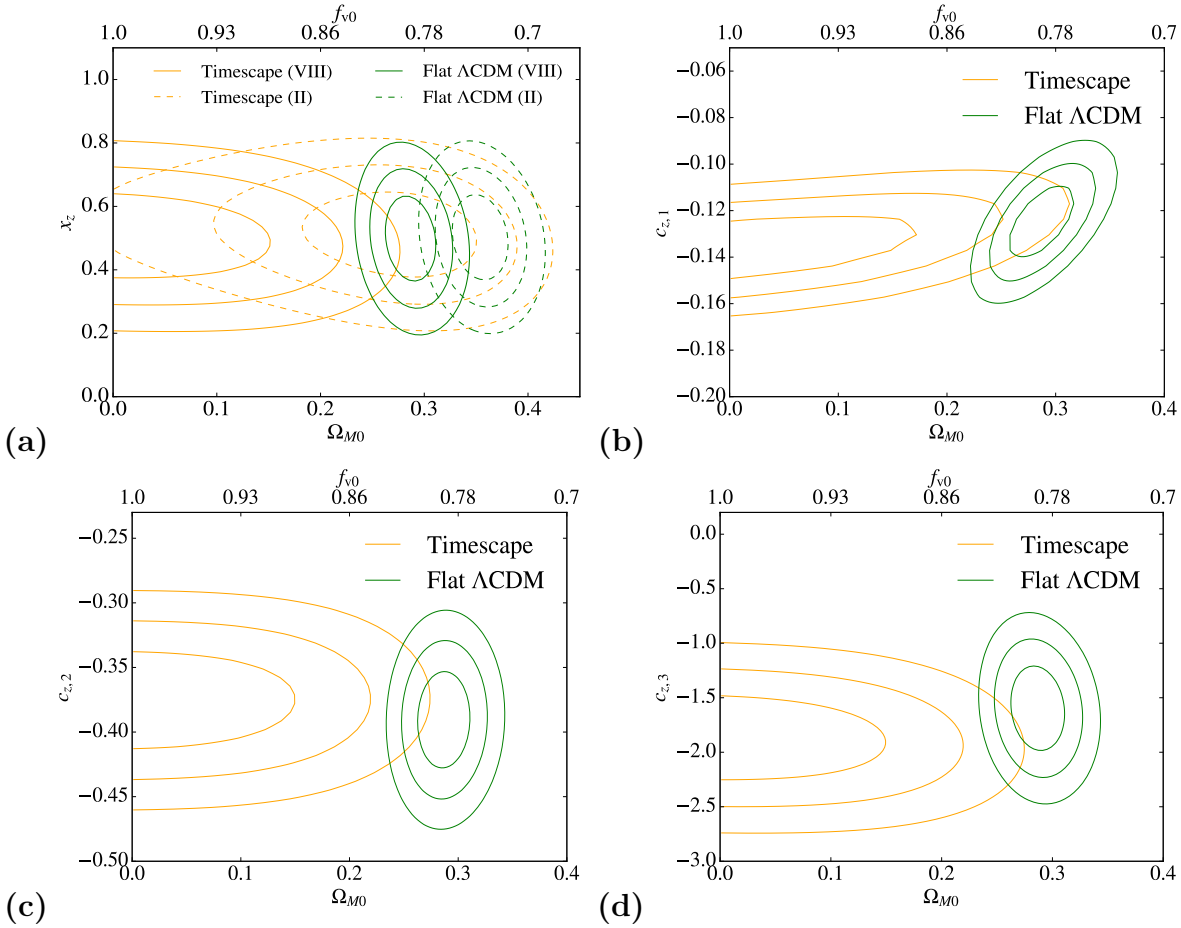

Figure 3.5: Likelihood function contours for model VIII with $z_{\min} = 0.033$ projected in the planes: **(a)** (x_z, Ω_{M0}); **(b)** $(c_{z,1}, \Omega_{M0})$ (SNLS sample, mean redshift $\langle z \rangle = 0.636$); **(c)** $(c_{z,2}, \Omega_{M0})$ (SDSS sample, mean redshift $\langle z \rangle = 0.199$); **(d)** $(c_{z,3}, \Omega_{M0}$ (low z sample with $z > 0.033$, mean redshift $\langle z \rangle = 0.0495$). 67.3%, 95.5%, and 99.7% confidence contours are shown. In panel **(a)** x_z contours for model II are also shown to demonstrate the effect of adding the $c_{z,J}$ parameters. For spatially flat ΛCDM the maximum likelihood is driven to the vicinity of the minimum $\Omega_{M0} = \frac{8}{27}$ of the $\mathrm{O}(z^2)$ Taylor series term (3.25). The timescape Taylor series (3.24) consists of slowly varying monotonic functions of f_{v0}, and the maximum likelihood is driven to the edge of parameter space, $f_{v0} \to 1$.

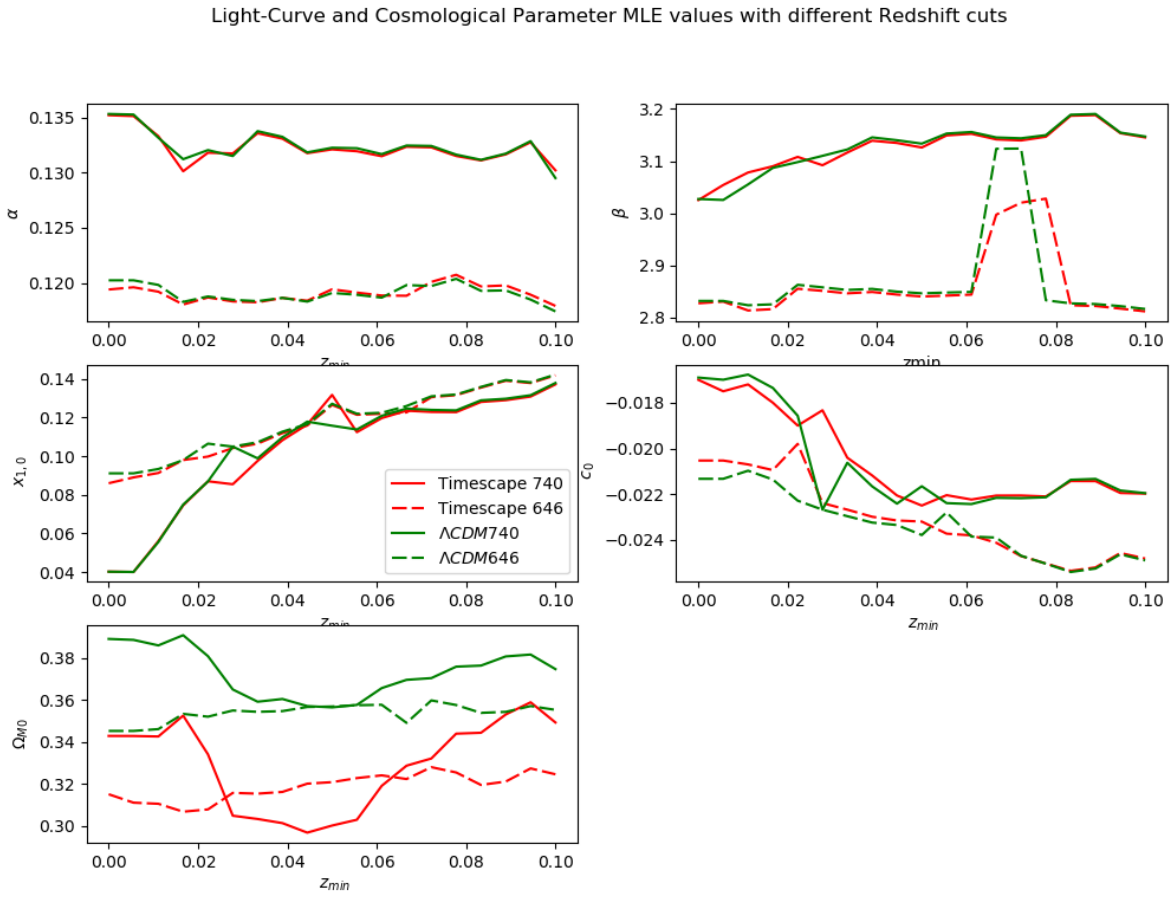

Figure 3.6: MLE best-fitting parameters for the NGS16 model as $z_{\min}$ is varied for ΛCDM (green) and timescape (red). Full drawn lines represent the analysis with the full JLA catalogue of this paper (740 SNIa), and dashed lines represent the JLA subset (646 SNIa).

Appendix 3.A Luminosity distances in the FLRW and timescape cosmologies

We compare SNIa observations to distance moduli (3.1) for theoretical luminosity distances determined from the FLRW and timescape models. Regardless of the matter content of the universe, the distance modulus for any general FLRW model can be expanded as a Taylor series of derivatives of the scale factor $a(t)$ for small redshifts, z. This leads to a distance modulus [156]

$$\begin{aligned}\mu_{\rm FLRW} &= 25 + 5\log_{10}\left(\frac{\mathsf{c}\,z}{H_0\,\mathrm{Mpc}}\right)\\ &+ \frac{5}{\ln 10}\Big\{\tfrac{1}{2}(1-q_0)z + \tfrac{1}{24}\Big[9{q_0}^2 - 10q_0 - 7 - 4j_0 - \Omega_{k0}\Big]z^2\\ &\quad + \tfrac{1}{24}\Big[s_0 + 5 - 10{q_0}^3 - 16{q_0}^2 - 9q_0 + j_0\,(8q_0+7)\\ &\quad\quad - 4\Omega_{k0}\,(q_0+1)\Big]z^3 + \ldots\Big\},\end{aligned} \tag{3.11}$$

where c is the speed of light, and H_0, q_0, j_0, s_0 and Ω_{k0} are the present values of the Hubble, deceleration, jerk, snap and spatial curvature parameters: $H(t) \equiv a^{-1}\partial_t a$; $q(t) \equiv -a^{-1}H^{-2}\partial_t^2 a$; $j(t) \equiv a^{-1}H^{-3}\partial_t^3 a$; $s(t) \equiv a^{-1}H^{-4}\partial_t^4 a$; $\Omega_k(t) \equiv -k\mathsf{c}^2(Ha)^{-2}$.

The luminosity distance-redshift relation in the ΛCDM model is given exactly by

$$\begin{aligned} d_L &= \frac{(1+z)\mathsf{c}}{H_0\sqrt{|\Omega_{k0}|}}\,\mathrm{sinn}\left(\sqrt{|\Omega_{k0}|}\int\limits_{1/(1+z)}^{1}\frac{\mathrm{d}y}{\mathcal{H}(y)}\right),\\ \mathcal{H}(y) &\equiv \sqrt{\Omega_{R0} + \Omega_{M0}y + \Omega_{k0}y^2 + \Omega_{\Lambda 0}y^4}\,,\\ \mathrm{sinn}(x) &\equiv \begin{cases}\sinh(x), & \Omega_{k0} > 0\\ x, & \Omega_{k0} = 0\\ \sin(x), & \Omega_{k0} < 0\end{cases}, \end{aligned} \tag{3.12}$$

where Ω_{R0}, Ω_{M0} and $\Omega_{\Lambda 0}$ are respectively the present epoch values of the radiation,

non-relativistic matter and cosmological constant density parameters, which at all epochs obey the Friedmann equation sum rule $\Omega_R + \Omega_M + \Omega_k + \Omega_\Lambda = 1$. Since $\Omega_{R0} = 4.15\times10^{-5}h^{-2}$, the radiation term can be neglected on the distance scales of supernovae. Furthermore, for FLRW models Ω_{k0} is constrained to be close to zero by the angular diameter distance of the sound horizon in the CMB. Thus we will restrict attention to the spatially flat ΛCDM model, with two effective free parameters, H_0 and $\Omega_{M0} \simeq 1 - \Omega_{\Lambda0}$. We use eq. (3.12) with $\Omega_{k0} = 0$, $\Omega_{R0} = 0$, for computations but note that in the Taylor series (3.11), $q_0 = -1 + \frac{3}{2}\Omega_{M0}$, $j_0 = 1$, $s_0 = 1 - \frac{9}{2}\Omega_{M0}$.

We also consider the FLRW model with linear expansion $a(t) \propto t$. This solution is obtained by setting $\Omega_{k0} = 1$, $\Omega_{R0} = \Omega_{M0} = \Omega_{\Lambda0} = 0$ in (3.12) or $\Omega_{k0} = 1$, $q_0 = j_0 = s_0 = \cdots = 0$ in (3.11). Following NGS16 we denote this the *empty universe*, but note any matter content is admissible as long as the luminosity distance is exactly $d_L = \mathsf{c}\, z(1 + \frac{1}{2}z)/H_0$.

The timescape model [95, 96, 97, 98], does not evolve by the Friedmann equation, and its distance modulus does not yield a Taylor series that coincides with (3.11) beyond the leading Hubble term. Instead observables are determined by conformally matching radial null geodesics of the regional "finite infinity" geometry of observers in gravitationally bound systems to a statistical geometry determined by fitting a spherically symmetric metric to a solution [96, 97, 98] of the Buchert equations [87, 88].

For the purpose of supernova distance analysis, the radiation density parameter (though somewhat differently calibrated to the CMB [98]) is negligible at the present epoch. To an accuracy of 0.3% the expansion history at late epochs is then given analytically [96, 97]. The "dressed" luminosity distance, d_L, and angular diameter distance, d_A, are given by

$$d_L = (1+z)^2 d_A, \tag{3.13}$$

$$d_A = \mathsf{c}\, t^{2/3} \int_t^{t_0} \frac{2\,\mathrm{d}t'}{(2 + f_{\rm v}(t'))(t')^{2/3}} = \mathsf{c}\, t^{2/3}(\mathcal{F}(t_0) - \mathcal{F}(t)), \tag{3.14}$$

$$\mathcal{F}(t) \equiv 2t^{1/3} + \frac{b^{1/3}}{6} \ln\left(\frac{(t^{1/3} + b^{1/3})^2}{t^{2/3} - b^{1/3}t^{1/3} + b^{2/3}}\right) + \frac{b^{1/3}}{\sqrt{3}} \tan^{-1}\left(\frac{2t^{1/3} - b^{1/3}}{\sqrt{3}\, b^{1/3}}\right), \tag{3.15}$$

where the volume-average time parameter, t, is defined implicitly in terms of the redshift by

$$z + 1 = \frac{(2 + f_{\rm v}){f_{\rm v}}^{1/3}}{3 f_{\rm v0}^{1/3} \bar{H}_0 t} = \frac{2^{4/3} t^{1/3}(t + b)}{f_{\rm v0}^{1/3} \bar{H}_0 t (2t + 3b)^{4/3}}\,, \tag{3.16}$$

$b \equiv 2(1-f_{\rm v0})(2+f_{\rm v0})/(9f_{\rm v0}\bar{H}_0)$, $f_{\rm v0}$ is the present epoch value of the void volume fraction,

$$f_{\rm v}(t) = \frac{3f_{\rm v0}\bar{H}_0 t}{3f_{\rm v0}\bar{H}_0 t + (1-f_{\rm v0})(2+f_{\rm v0})}\,, \tag{3.17}$$

and $\bar{H}_0$ is the "bare Hubble constant" related to the observed Hubble constant by $\bar{H}_0 = 2(2+f_{\rm v0})H_0/(4{f_{\rm v0}}^2 + f_{\rm v0} + 4)$. The parameter t is related to the time parameter, τ, measured by typical observers in bound structures by

$$\tau = \tfrac{2}{3}t + \frac{2(1-f_{\rm v0})(2+f_{\rm v0})}{27f_{\rm v0}\bar{H}_0}\ln\left(1 + \frac{9f_{\rm v0}\bar{H}_0 t}{2(1-f_{\rm v0})(2+f_{\rm v0})}\right). \tag{3.18}$$

While the void volume fraction, f_v, 3.17 is a natural parameter in the timescape cosmology, it is often useful to consider the reparametrisation

$$\Omega_M = \Omega_M = \tfrac{1}{2}(1-f_{\rm v})(2+f_{\rm v})\,, \tag{3.19}$$

where Ω_M is the dressed matter parameter of the timescape model.

The effective dressed scale factor $a(\tau)$ is given by

$$a \equiv \bar{\gamma}^{-1}\bar{a}, \tag{3.20}$$

where $\bar{a}$ is the bare or volume-average scale factor and $\bar{\gamma}$ is the phenomenological lapse function. These have simple analytic forms in terms of the volume-average time parameter, t, namely

$$\bar{a} = \frac{\bar{a}_0\big(3\bar{H}_0 t\big)^{2/3}}{2+f_{\rm v0}}\Big[3f_{\rm v0}\bar{H}_0 t + (1-f_{\rm v0})(2+f_{\rm v0})\Big]^{1/3} \tag{3.21}$$

and

$$\bar{\gamma} = \tfrac{1}{2}(2+f_{\rm v}) = \frac{3(t+b)}{(2t+3b)} \tag{3.22}$$

respectively [96, 97]. The bare Hubble parameter, $\bar{H} \equiv \partial_t\bar{a}/\bar{a}$, and dressed Hubble parameter, $H \equiv \partial_\tau a/a$, are given respectively by $\bar{H} = (2+f_{\rm v})/(3t)$ and $H = \big(4{f_{\rm v}}^2 + f_{\rm v} + 4\big)\,\bar{H}/[2(2+f_{\rm v})]$. The bare deceleration parameter, $\bar{q} \equiv -\bar{a}^{-1}\bar{H}^{-2}\partial_t^2\bar{a}$, is always positive. However, on account of the different time parameters (3.18) the dressed deceleration parameter inferred by observers in bound systems, $q \equiv -a^{-1}H^{-2}\partial_\tau^2 a$, may

change sign from positive to negative, indicating apparent acceleration. The dressed deceleration parameter is given by

$$q = \frac{-\left(1-f_{\rm v}\right)\left(8{f_{\rm v}}^3+39{f_{\rm v}}^2-12f_{\rm v}-8\right)}{\left(4+f_{\rm v}+4{f_{\rm v}}^2\right)^2}\,. \tag{3.23}$$

The onset of apparent acceleration is determined by a root of the cubic in $f_{\rm v}$ in the numerator of (3.23), and begins when $f_{\rm v} \simeq 0.587$.

One may substitute (3.13)–(3.15) in (3.1) and then invert (3.16) as a series in z using an algebraic computing package to arrive at a low redshift Taylor series for the distance modulus, $\mu_{\rm TS}$, equivalent to (3.11) for the FLRW model. The first terms are given below, along with equivalent expressions for the spatially flat ΛCDM and empty universe models as determined from (3.11):

$$\mu_{\rm TS} = \mu_0(z) + \frac{5}{\ln 10}\left\{\left[\frac{24\,f_{\rm v0}^4-23\,f_{\rm v0}^3+99\,f_{\rm v0}^2+8}{2\left(4\,f_{\rm v0}^2+f_{\rm v0}+4\right)^2}\right]z-\left[\frac{F_8}{24\left(4f_{\rm v0}^2+f_{\rm v0}+4\right)^4}\right]z^2+\ldots\right\} \tag{3.24}$$

$$\mu_{\Lambda{\rm CDM}} = \mu_0(z) + \tfrac{5}{\ln 10}\Big\{(1-\tfrac{3}{4}\Omega_{M0})z-\left[\tfrac{1}{2}+\tfrac{1}{2}\Omega_{M0}-\tfrac{27}{32}\Omega_{M0}^2\right]z^2 + \left[\tfrac{1}{3}-\tfrac{1}{8}\Omega_{M0}+\tfrac{21}{16}\Omega_{M0}^2-\tfrac{45}{32}\Omega_{M0}^3\right]z^3+\ldots\Big\} \tag{3.25}$$

$$\mu_{\rm empty} = \mu_0(z) + \tfrac{5}{\ln 10}\left\{\tfrac{1}{2}z-\tfrac{1}{8}z^2+\tfrac{1}{24}z^3+\ldots\right\}\,, \tag{3.26}$$

where

$$F_8 \equiv 1984\,f_{\rm v0}^8-4352\,f_{\rm v0}^7+16515f_{\rm v0}^6+14770\,f_{\rm v0}^5+7819\,f_{\rm v0}^4-11328f_{\rm v0}^3+32080\,f_{\rm v0}^2-128\,f_{\rm v0}+960\,. \tag{3.27}$$

Here the term $\mu_0(z) \equiv 25+5\log_{10}[{\rm c}z/(H_0\,{\rm Mpc})] = 25+5\log_{10}(2997.9\,h^{-1})+5\log_{10}z$ is common to all models, the Hubble constant being $H_0 = 100\,h\,{\rm km\ sec^{-1}\,Mpc^{-1}}$.

Appendix 3.B Implementation of the SALT2 method

The SALT relation (3.2) refers to the actual emitter (em) and observer (obs), but the luminosity distance relations (3.12) and (3.14) refer to ideal observers who determine an isotropic distance–redshift relation. Consequently, the theoretical relations (3.12) and (3.14) must be transformed to the frame involving the actually measured redshift $\hat{z} = (\lambda_{\rm obs}-\lambda_{\rm em})/\lambda_{\rm em}$ before the SALT relation is applied. The luminosity distance

entering (3.1) is then

$$\hat{d_L}(\hat{z}) = \frac{1+\hat{z}}{1+z} d_L(z) = (1+\hat{z}) D(z), \tag{3.28}$$

where for each cosmological model, $D(z) = d_L/(1+z) = (1+z)d_A$ is the (effective) comoving distance, and

$$1+\hat{z} = (1+z)(1+z^{\rm pec}_{\rm obs})(1+z^{\phi}_{\rm obs})(1+z^{\rm pec}_{\rm em})(1+z^{\phi}_{\rm em}) \tag{3.29}$$

gives the measured redshift, $\hat{z}$, in terms of the cosmological redshift, z, the local Doppler redshifts of observer, $z^{\rm pec}_{\rm obs}$, and emitter, $z^{\rm pec}_{\rm em}$, and gravitational redshifts at the two locations, $z^{\phi}_{\rm obs}$ and $z^{\phi}_{\rm em}$.

For our observations, $\hat{z}$, is the heliocentric redshift as the Earth's annual motion is averaged to the rest frame of the Sun. In the standard cosmology gravitational potential effects are assumed to be small, and the only relevant terms on the r.h.s. of (3.29) are assumed to be local boosts of order $v/c \sim 10^{-3}$. This leads to 0.1% corrections to the luminosity distance which are often neglected. However, as noted by [157] differences of 0.1% in d_L lead to order 1% corrections to cosmological parameters, which we have confirmed in our analysis.

In the timescape model, as in any inhomogeneous cosmology, expansion below the $\sim 100\,h^{-1}$Mpc SHS will generally differ from that of a global average geometry plus local boosts. Equivalently, very slowly varying time-dependent gravitational potentials also make a contribution to (3.29). Such terms encode non-kinematic differential expansion [158] from inhomogeneities below the SHS. Spatial variations in the term $z^{\phi}_{\rm em}$ may have significant consequences for interpreting the local "peculiar velocity field" for sources within $\lesssim 100\,h^{-1}$Mpc of our location [159, 160] but any net anisotropy on SNIa redshifts on larger scales should only make a small correction to the standard boost between the heliocentric and CMB frames. Indeed, it could be a source for a small systematic redshift uncertainty of the type considered by [157]. However, we do not investigate that possibility in the present chapter as the RH16 empirical light-curve models we study are already very complex. The peculiar velocity and gravitational potential terms in (3.29) that we are unable to determine will be assumed to contribute to statistical uncertainties in measured redshifts only.

We therefore compute cosmological luminosity distances is the CMB rest frame,

exclude data below the SHS, and study the effect of different choices for this cutoff.[11] Furthermore, we apply the SALT2 relation in the heliocentric frame using the values tabulated in the JLA catalogue [123], and calculate the corresponding CMB rest frame redshifts ourselves.[12]

We *do not* use the JLA tabulated CMB frame redshifts [123] since in addition to our $z_{\rm obs}^{\rm pec}$ correction, these values also already include a correction, $z_{\rm em}^{\rm pec}$, for the peculiar velocity field [164, 165] of galaxies up to $z = 0.071$, implicitly assuming the FLRW model.

Appendix 3.C Model comparison

3.C.1 Frequentist approach

We are interested in the dependence of the likelihood (3.7) on the model parameters, Θ. We write $\mathcal{L}(\Theta) \equiv \mathcal{L}(\text{Data}|\Theta, \text{M})$. We are interested in a subset of parameter-space $\Theta_1 \subset \Theta$, for which we construct a profile likelihood $\mathcal{L}_p(\Theta_1) \equiv \max_{\Theta_2}[\mathcal{L}(\Theta)]$, where maximization is over the nuisance parameters $\Theta_2 = \Theta \setminus \Theta_1$. In our case Θ_1 is usually the free parameter(s) of the cosmological model, and Θ_2 the intrinsic supernovae parameters and the empirical parameters, α, β, of the light-curve fitter.

Confidence regions for the parameters of interest are estimated from the coverage probability $p_{\rm cov}$ of a region in the k-dimensional slice of parameter space, $k \equiv \dim \Theta_1$, given asymptotically by the integral

$$p_{\rm cov}(\text{region}) = \int_0^{-2\ln(\mathcal{L}_p(\Theta_1)/\mathcal{L}_{\max})} f_{\chi^2}(\Theta_1', k)\mathrm{d}\Theta_1' \tag{3.30}$$

where $\mathcal{L}_{\max} \equiv \max_{\Theta_1}[\mathcal{L}_p(\Theta_1)]$, and $f_{\chi^2}(x, k)$ is the probability density function of a χ^2 distributed variable with k degrees of freedom. Having constructed confidence intervals from (3.30), one can compare nested models.

[11] Since we do not constrain H_0, we do not specifically investigate the relationship between light-curve parameters and determinations of the local Hubble constant, which have been discussed in the past [134, 161, 162, 125, 159, 160]. In the timescape model higher average values of H_0 are expected below the SHS.

[12] We use the NASA/IPAC Extragalactic Database standard, 371 km sec^{-1} in the direction $(\ell, b) = (264.14°, 48.26°)$ [163].

Since we wish to compare independent non-nested models,[13] we need to go beyond the procedure of (3.30). The Akaike Information Criterion (AIC) [166] and Bayesian Information Criterion (BIC) [167] are two widely used measures of the relative information loss for non-nested models, given respectively by

$$\mathrm{AIC} = 2k - 2\ln\left(\mathcal{L}_{\max}\right) \tag{3.31}$$

$$\mathrm{BIC} = k\ln N - 2\ln\left(\mathcal{L}_{\max}\right) \tag{3.32}$$

where k is the number of independent model parameters, and N the number of data points fit. The AIC estimate of relative probability of minimal information loss for two models is $P_{AIC} \equiv \exp\left[-\frac{1}{2}\left(\mathrm{AIC}_1 - \mathrm{AIC}_2\right)\right]$, and similarly for BIC. The BIC gives a greater penalty for introducing additional parameters than AIC if $N \geq 8$. Differences of at least 2, 6 and 10 are considered to be respectively 'positive', 'strong' and 'very strong' evidence [168] for the model with the lower IC value. Both tests reduce to a maximum likelihood comparison when $k_1 = k_2$, as is the case for the timescape and spatially flat ΛCDM models.

3.C.2 Bayesian approach

The frequentist methods place emphasis on the maximum likelihood, which is of limited use. We therefore perform a fully Bayesian analysis of the JLA data set to determine the relative statistical support for each cosmological model, as well as for the introduction of additional redshift dependent light curve parameters.

Given data, D, and a model, M, determined by a set of n parameters $\Theta = (\theta_1, \theta_2, \ldots, \theta_n)$, by Bayes theorem the *posterior* probability distribution, $p(\Theta|D, M)$, is given by

$$p(\Theta|D, \mathrm{M}) = \frac{\mathcal{L}(\Theta)\pi(\Theta|\mathrm{M})}{p(D|\mathrm{M})}, \tag{3.33}$$

where $\mathcal{L}(\Theta) \equiv p(D|\Theta, \mathrm{M})$ is the likelihood, $\pi(\Theta|\mathrm{M})$ is the *prior* distribution and $p(D|\mathrm{M})$ is the *Bayesian evidence*. The prior represents a subjective initial state of belief in the parameters based on external information or previous experiments, while the evidence

[13] We note that only models II, IV, VI are extensions of the 9 parameter base model, i.e., model I is nested in II, IV and VI, while II and IV are nested models of VI. Model V is nested in model VIII.

is a normalization constant,

$$E \equiv p(D|\mathrm{M}) = \int \mathcal{L}(\Theta)\pi(\Theta|\mathrm{M})\,\mathrm{d}\Theta, \tag{3.34}$$

to ensure the posterior is a probability distribution. It is independent of parameters and as such does not play a role in parameter estimation, but becomes important for model comparison.

Given two models, M_1 and M_2, for the same data D, the Bayes factor [168]

$$B \equiv \frac{E_1}{E_2} = \frac{p(D|\mathrm{M}_1)}{p(D|\mathrm{M}_2)}, \tag{3.35}$$

gives a measure for which model is more probable in view of the data. The Bayes factor implicitly applies the principle of Occam's razor[14] with a penalty for adding extra parameters. This makes model selection natural in the Bayesian framework. Values of $B > 1$ indicate preference for model 1, $B < 1$ for model 2. On a standard scale, evidence with $|\ln B| < 1$ is 'not worth more than a bare mention' [168] or 'inconclusive' [169], while $1 \leq |\ln B| < 3$, $3 \leq |\ln B| < 5$ and $|\ln B| \geq 5$ indicate 'positive', 'strong' and 'very strong' evidences respectively [168].

In the Bayesian approach the nuisance parameters are *marginalized* over, i.e., integrated out from the posterior $p(\Theta|D, \mathrm{M})$. E.g., the *marginal posterior* of θ_1 is obtained from the n-dimensional posterior by

$$p(\theta_1|D, \mathrm{M}) = \int p(\theta|D, \mathrm{M})\,\mathrm{d}\theta_2\,\mathrm{d}\theta_3 \ldots \mathrm{d}\theta_n, \tag{3.36}$$

and from this 1-dimensional distribution parameter inferences can be made. The posterior mean value is given by

$$\bar{\theta}_1 = \int \theta_1\, p(\theta_1|D, \mathrm{M})\,\mathrm{d}\theta_1, \tag{3.37}$$

and more generally

$$\bar{f} = \int f(\theta_1)\, p(\theta_1|D, \mathrm{M})\,\mathrm{d}\theta_1, \tag{3.38}$$

[14] The AIC and BIC statistics also include a penalty using simple approximations to Bayesian methods which derive from different assumptions about the priors. The factor of two difference in the IC evidence scale [168] reflects the factor of 2 multiplying $\ln(\mathcal{L}_{\max})$ in the definitions (3.31), (3.32).

for some parameter dependent quantity f. Credible intervals, or uncertainties in parameters, can also be obtained from the marginal posterior. E.g., a 68% equal-tailed credible interval is defined in such a way that $(1 - 0.68)/2 = 0.16$ of the probability lies on either side of the interval.

In cases where the Bayes factor is close to unity giving no clear preference for either model, the *Bayesian complexity* [170] can provide a secondary measure to the model selection process. It is defined as

$$C_b \equiv -2\left(D_{\mathrm{KL}}(p,\pi) - \widehat{D_{\mathrm{KL}}}\right), \tag{3.39}$$

where

$$D_{\mathrm{KL}}(p,\pi) \equiv \int p(\Theta|D,\mathrm{M}) \ln\left[\frac{p(\Theta|D,\mathrm{M})}{\pi(\Theta|\mathrm{M})}\right] \mathrm{d}\Theta, \tag{3.40}$$

is the *Kullback-Leibler divergence* measuring the information gain of the inference, and $\widehat{D_{\mathrm{KL}}}$ is a point estimator evaluated at the posterior mean $\bar{\Theta}$ measuring the expected information gain:

$$\widehat{D_{\mathrm{KL}}} \equiv p(\bar{\Theta}|D,\mathrm{M}) \ln\left[\frac{p(\bar{\Theta}|D,\mathrm{M})}{\pi(\bar{\Theta}|\mathrm{M})}\right] = \ln\mathcal{L}(\bar{\Theta}) - \ln p(D|\mathrm{M}), \tag{3.41}$$

where we have used Bayes theorem in the second equality. As the data may not be able to constrain all parameters, the Bayesian complexity determines the effective number of parameters supported by the data. Thus for models with $|\ln B| < 1$, the model with the lower C_b indicates the simpler model and is therefore preferred. By defining the *effective chi-squared* $\chi^2(\Theta) \equiv -2\ln\mathcal{L}$ and invoking Bayes theorem (3.33), we can rewrite (3.39) as

$$C_b = \overline{\chi^2(\Theta)} - \chi^2(\bar{\Theta}), \tag{3.42}$$

with $\overline{\chi^2}$ being the posterior mean of χ^2.

Appendix 3.D Cosmological model priors

We construct priors for the timescape model [95, 96, 97, 98] based on CMB and BAO observations, to the best of our knowledge. We will also construct equivalent priors for the ΛCDM model based on the same assumptions. The resulting priors are wider than in conventionally assumed, but do not unfairly weight a Bayesian comparison by

integrating the ΛCDM model likelihood function over a narrow parameter range as compared to the timescape case.[15]

3.D.1 CMB acoustic scale constraint

In the case of the CMB, a cosmology independent analysis of the angular scale and heights of the acoustic peaks has been undertaken by [146] from the Planck data. We use the information resulting from the angular scale of the acoustic peaks alone. The angular scale depends on the angular diameter distance of the sound horizon alone, which is constrained in the timescape model. By contrast, the relative peak heights are related to the baryon–to–photon ratio, $\eta_{B\gamma}$, and the spectral index, n_s, which are parameters with the largest systematic uncertainties in the timescape case.

A non-parametric fit of the acoustic scale alone gives $286 \leq \ell_{\rm A} \leq 305$ at 95% confidence [146]. Our CMB prior is then determined by demanding that the angular diameter distance of the sound horizon at decoupling matches the corresponding angular scale $\theta_{\rm A} = \pi/\ell_{\rm A}$; i.e., $0.01030 \leq \theta_{\rm A} \leq 0.01098$. In earlier work [124, 125, 98], given that non-parametric fits had not been performed, we had demanded a match to the FLRW parametric estimate of the acoustic scale $\theta_{\rm A} = 0.01041$ to within 2%, 4% or 6%. The non-parametric fit represents a considerable improvement, particularly since the FLRW model value is not in the mid-range of the non-parametric 95% confidence interval.

To constrain the angular diameter distance of the sound horizon $d_{\rm A\,dec} = \bar{D}_s(z_{\rm dec})/\theta_{\rm A}$ in the timescape model, we determine the redshift of decoupling, $z_{\rm dec}$, and the comoving distance of the sound horizon $\bar{D}_s$ at that epoch [98, 127], which require the baryon–to–photon ratio to be specified. In the FLRW model this ratio is very tightly constrained by the ratio of CMB peak heights, as first measured by WMAP [43]. However, to achieve a similarly precise constraint in the timescape model we would need to include backreaction in the primordial plasma [127], which is beyond the scope of current investigations. In previous work [98, 124, 125] we used a range of pre-WMAP baryon–to–photon ratios [171], $4.6 < 10^{10}\eta_{B\gamma} < 5.6$, for which all light element

[15] If we were to use conventional narrower priors for ΛCDM then the timescape model is either unfairly advantaged or disadvantaged, depending on whether the maximum likelihood lies within the range of the narrower prior or not. For the NGS16 model, for example, this is not the case for the spatially flat ΛCDM model, and the timescape model is unfairly advantaged. For model VIII the situation is reversed.

abundance measurements are within 2σ, i.e., with no primordial lithium abundance anomaly. In the present analysis, we wish to use the same priors on $\eta_{B\gamma}$ for both the timescape and ΛCDM models, and thus need to include the standard model value $\eta_{B\gamma} = 2.736 \times 10^{-8}\Omega_{M0}h^2 = (6.08 \pm 0.07) \times 10^{-10}$ for which the primordial lithium abundance is problematic. We therefore adopt the more conservative pre-WMAP range given by [172], namely $4.2 < 10^{10}\eta_{B\gamma} < 6.3$.

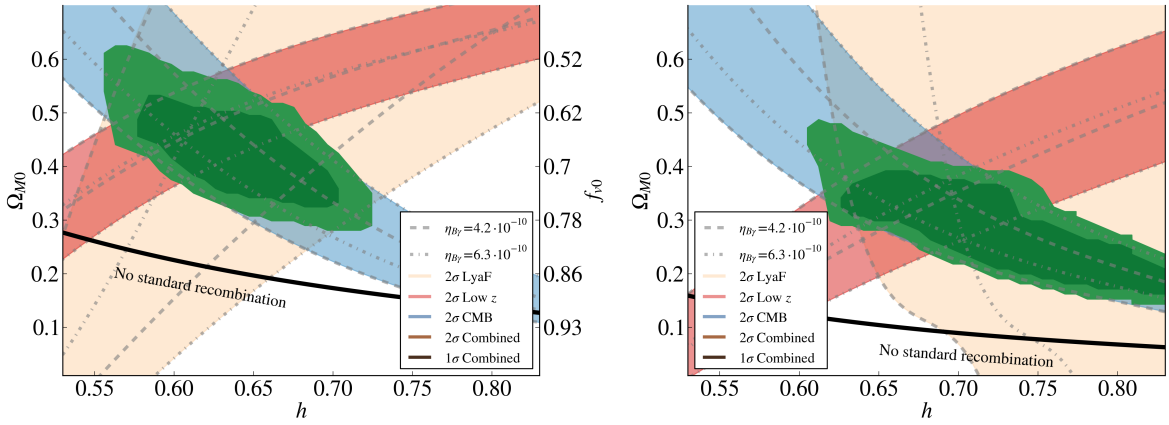

Figure 3.7: Cosmological parameter constraint priors from on the timescape model (left panel) and the spatially flat ΛCDM model (right panel). Independent 2σ constraints are determined for: (i) the angular scale of sound horizon in the CMB (contours from top left to bottom right); (ii) the fit of the angular BAO scale from BOSS galaxies at low redshift (contours from bottom left to top right); (iii) the angular BAO scale from one measurement of the Lyman-α forest at $z = 2.34$ (wide contours). A range of possible baryon–to–photon ratios are allowed, with the extremes indicated. The joint confidence region is determined by applying the CMB constraint and allowing one or other BAO constraint.

3.D.2 Baryon Acoustic Oscillation constraints

Determinations of the BAO scale from galaxy clustering at low redshifts and Lyman alpha forest statistics at $z = 2.34$ provide complementary constraints on the expansion history. In previous work [98, 124, 125] we simply demanded that the timescape effective comoving BAO scale match a single estimate determined from the FLRW cosmology to within ±2%, ±4% or ±6%, which was a crude method but the best available given the earlier precision of measurements. The number and precision of measurements has now improved.

For the present investigation, we have considered estimates of the BAO scale at different redshifts [61, 145, 59] using the best available data from the BOSS survey. Unfortunately the standard FLRW cosmology plays an implicit role in the data reduction, and limits the extent to which bounds can be placed on non-FLRW models. The systematic issues can be most directly understood by noting that the BAO scale is determined separately in the angular and radial directions, by converting angular separations and redshift separations in the galaxy–galaxy correlation function into the displacements

$$\alpha_\perp = \frac{[d_A(z)/r_d]}{[d_A(z)/r_d]_{\rm fid}} \qquad \text{and} \qquad \alpha_\parallel = \frac{[d_H(z)/r_d]}{[d_H(z)/r_d]_{\rm fid}} \tag{3.43}$$

where r_d is the present comoving scale of the sound horizon at the baryon drag epoch, $d_H(z) \equiv c/H(z)$, and the subscript "fid" refers to quantities computed in a fiducial FLRW model that is used to convert the raw angular and redshift displacements into 3-dimensional comoving space. (Here we neglect the effect of redshift–space distortions which are also often modelled with N-body Newtonian simulations based on the ΛCDM model.)

The conversion to 3-dimensional comoving space can be problematic for a non-FLRW model. While use of purely angular results should pose no problems for the timescape cosmology, the conversion of redshift increments to a radial comoving distance involves different assumptions about spatial curvature in the FLRW and timescape models. One could in principle use the values determined by a fiducial ΛCDM model [61, 145, 59] to recompute the radial comoving distance except for an additional problem: in particular redshift ranges the relative Alcock–Paczyński factor $\left[\alpha_\perp/\alpha_\parallel\right]_{\Lambda\rm CDM} / \left[\alpha_\perp/\alpha_\parallel\right]_{\rm TS} = \left[H(z)d_A(z)\right]_{\Lambda\rm CDM} / \left[H(z)d_A(z)\right]_{\rm TS}$ between a fiducial ΛCDM model and the timescape model varies over the redshift slices $\Delta z \sim 0.2$ used in the BOSS survey [59] by an amount similar in magnitude to the uncertainty. Consequently, to have any confidence in radial measurements, one really needs to recompute the radial BAO scale from the raw data assuming a fiducial timescape model. That is beyond the scope of the present chapter.

For the present analysis we will consequently restrict constraints on the BAO scale to 2σ bounds obtained from the angular estimates of BOSS data [59] at low redshifts $0.38 \lesssim z \lesssim 0.61$ and in the Lyman-α forest [61] at $z = 2.34$. In the former case, the radial and angular measurements are actually also somewhat correlated. Consequently,

and also in view of the fact that the measurements at low and high redshifts are in tension in the ΛCDM model, we will take bounds that result from the union of the constraints at low and high redshifts, rather than their intersection. In practice, the bounds are mostly set by the Lyman-α measurement since it has a much larger uncertainty.

3.D.3 Joint constraints

The joint 2σ confidence regions from applying the CMB constraint and either the low-z or $z = 2.34$ BAO constraint is shown in Fig. 3.7. Since a range of possible baryon–to–photon ratios are admitted, with no information from the relative heights of the acoustic peaks used in either model, the width of the allowed regions is larger than in conventional analyses for ΛCDM.

For timescape the confidence regions are $f_{\rm v0} \in (0.588, 0.765)$ at 1σ, $f_{\rm v0} \in (0.500, 0.799)$ at 2σ, $f_{\rm v0} \in (0.378, 0.826)$ at 3σ. The corresponding effective dressed $\Omega_{M0} = \frac{1}{2}(1 - f_{\rm v0})(2 + f_{\rm v0})$ is $\Omega_{M0} \in (0.325, 0.534)$ at 1σ, $\Omega_{M0} \in (0.281, 0.625)$ at 2σ, and $\Omega_{M0} \in (0.245, 0.740)$ at 3σ. For spatially flat ΛCDM the corresponding confidence regions are $\Omega_{M0} \in (0.162, 0.392)$ at 1σ, $\Omega_{M0} \in (0.143, 0.487)$ at 2σ, and $\Omega_{M0} \in (0.124, 0.665)$ at 3σ. We adopt the 2σ bounds as priors.

CHAPTER 4

Dynamical spatial curvature as a fit to type Ia supernovae

In this chapter we consider a class of 'scaling solutions' [173, 131, 174], which forms a closure condition for the system of averaged cosmological equations of Buchert's scheme [87, 88]. These solutions have average spatial curvature evolution which is fundamentally different from that of the FLRW class of space-times. We test this class of models on the Joint Light-curve Analysis (JLA)[123] catalogue of type Ia supernovae. Some observational tests have already been made with these scaling solutions in Ref. [131], using CMB data and a sparse SNIa sample, and in Ref. [175], using BAO measurements and the differential age method.

Another model built from the same scalar averaging scheme as the scaling solutions, the 'timescape model',[1] has been tested on the JLA catalogue of type Ia supernovae and showed an equally good fit to that of the spatially flat ΛCDM model. The successful fit of the timescape model suggests that spatial curvature evolution has the potential of mimicking dark energy in the late epoch Universe. Curvature evolution in the late epoch Universe has first been applied to supernova data by Kasai [176] by dividing the supernova sample into early- and late-type subsamples and fitting these two subsamples with different FLRW models, treating the respective FLRW curvature parameters as free parameters in the analysis. While it is known that the FLRW model with negative constant curvature does not successfully fit cosmological data, nothing in this result prevents non-FLRW curvature evolution towards present-epoch negative curvature—as expected from general considerations of averaged inhomogeneous universe models [115].

In this chapter we use the JLA catalogue to test a family of scaling solutions for the average variables entering in the scalar averaging scheme using the Spectral Adaptive

[1] For a review of the timescape model see Ref. [97].

Lightcurve Template 2 (SALT2) relation. We will compare the resulting fit to that of the ΛCDM model, the empty universe model,[2] and the timescape model.

In Sec. 4.1 we review the scalar averaging scheme and the scaling solutions employed in this chapter, and we provide the distance modulus–redshift relation for the scaling solutions. In Sec. 4.2 we briefly describe the SALT2 method for standardising supernovae, and we review the likelihood-function used in the statistical analysis of the JLA catalogue. In Sec. 4.3 we present the results of our analysis: constraints on model parameters of the investigated scaling solutions, and the quality of fit as compared to that of the ΛCDM model, the empty Milne model (i.e. the FLRW model without sources, but negative constant curvature), and the timescape model. In Sec. 4.4 we examine a FLRW curvature consistency measure, compute the analogous measure for the best-fit results for the scaling solutions, and discuss the potential use of this measure for the discrimination between FLRW models and backreaction models with emerging deviations from the FLRW constant curvature geometry in future surveys. We conclude in Sec. 4.5.

4.1 The scalar averaging scheme and scaling solutions

We now recall the class of scaling solutions of the scalar averaging scheme and provide an associated distance modulus–redshift relation, which we are going to test in this chapter.

We base our analysis on a scheme for averaging of scalar variables in a self-gravitating dust-fluid, recalled in Sec. 4.1.1, and formulated in terms of effective cosmological parameters in Sec. 4.1.2. In Sec. 4.1.3 we introduce the scaling solutions, and in Sec. 4.1.4 we describe our procedure for constructing an effective metric, a so-called template metric, to match an effective light cone structure to the large-scale model defined in the averaging scheme. From this prescribed metric we finally obtain the expressions for the distance modulus–redshift relation in Sec. 4.1.5.

[2] While the empty universe model is unphysical and ruled out by combined constraints from CMB, SNIa, and BAO data, it is an interesting idealization for the *late-epoch Universe* in which matter is highly clustered within tiny volumes and photons primarily propagate in large, empty void-regions.

4.1.1 Irrotational dust averages

We consider a Lorentzian manifold with a self-gravitating irrotational dust fluid as the energy-momentum source in the Einstein equations. The aim is to describe average dynamical properties of this system, and to determine an effective description of light propagation on cosmological scales without knowing the metric of the lumpy space-time in detail.

We employ the Buchert averaging scheme [87] as a method for obtaining global dynamical equations for such a space-time, without knowledge of its 'micro state'. The averaging scheme as detailed in sections 2.1, 2.2, and 2.3 is a generalisation of the averaging scheme described in this section, where the matter content is restricted to that of dust and where volume averaging is performed in the frame orthogonal to the matter flow with the unweigted Riemannian volume element as volume measure. Here we provide the relevant dynamical equations for this analysis with a short explanation of the relevant variables. Precise definitions of the variables and the averaging operation, and the full derivation of the below equations can be found in Ref. [87]. Throughout this chapter we work in units of $c = 1$, c being the speed of light in vacuum.

Let $\boldsymbol{u} = -\boldsymbol{\nabla} t$ be the 4−velocity field of the fluid source, with t being a proper time function of the fluid, and let ϱ be its rest mass density. From averaging the local Raychaudhuri equation in the fluid rest frame over a spatial domain $\mathcal{D}$ comoving with the fluid (no net-flux of particle world-lines through the boundaries of the averaging domain), we obtain the *averaged Raychaudhuri equation*,

$$3\,\frac{\ddot{a}_{\mathcal{D}}}{a_{\mathcal{D}}} \;+\; 4\pi G\,\langle \varrho \rangle_{\mathcal{D}} \;-\; \Lambda \;=\; \mathcal{Q}_{\mathcal{D}}\,, \tag{4.1}$$

where $a_{\mathcal{D}}$ is the volume scale factor, $\langle . \rangle_{\mathcal{D}}$ denotes covariant averaging in the fluid frame over the comoving spatial domain $\mathcal{D}$, Λ is the cosmological constant,[3] and the overdot denotes the covariant time-derivative: $\dot{} \equiv \frac{\mathrm{d}}{\mathrm{d}t}$.

Note that in general $\langle S \rangle^{\cdot}_{\mathcal{D}} \neq \langle \dot{S} \rangle_{\mathcal{D}}$, where $\langle S \rangle^{\cdot}_{\mathcal{D}}$ is the time-derivative of the averaged variable $\langle S \rangle_{\mathcal{D}}$, and $\langle \dot{S} \rangle_{\mathcal{D}}$ is the average of the time-derived local scalar $\dot{S} = u^{\mu}\nabla_{\mu} S$. For details on the averaging operation and the non-commutativity of averaging and time-derivative, see Ref. [87].

[3] We set $\Lambda = 0$ in the investigations of this chapter, as we investigate averaged models without dark energy, but keep Λ in the equations of this section for completeness.

$\mathcal{Q}_\mathcal{D}$ is the 'kinematical backreaction' which is defined from the variance of the rate of expansion of the fluid congruence and the averaged shear of the fluid congruence over the domain $\mathcal{D}$.

The local energy constraint equation can be averaged in a similar way to obtain the averaged energy constraint equation,

$$3\left(\frac{\dot{a}_\mathcal{D}}{a_\mathcal{D}}\right)^2 - 8\pi G\,\langle\varrho\rangle_\mathcal{D} - \Lambda = -\frac{\langle\mathcal{R}\rangle_\mathcal{D} + \mathcal{Q}_\mathcal{D}}{2}\,, \tag{4.2}$$

where $\langle\mathcal{R}\rangle_\mathcal{D}$ is the averaged spatial scalar curvature. Finally, we have the average of the local energy-momentum conservation equation,

$$\langle\varrho\rangle^{\cdot}_\mathcal{D} + 3\,\frac{\dot{a}_\mathcal{D}}{a_\mathcal{D}}\,\langle\varrho\rangle_\mathcal{D} = 0\,. \tag{4.3}$$

All of the global variables $a_\mathcal{D}$, $\langle\varrho\rangle_\mathcal{D}$, $\mathcal{Q}_\mathcal{D}$, and $\langle\mathcal{R}\rangle_\mathcal{D}$ entering in the averaged equations depend on the proper time slice parameterized by t and the spatial domain of integration $\mathcal{D}$.

Note that when positive, $\mathcal{Q}_\mathcal{D}$ can act as an effective source for global acceleration in (4.1). $\mathcal{Q}_\mathcal{D}$ will in general depend on cosmic time t, and on spatial scale through the dependence on the domain of averaging.

Combining (4.1), (4.2), and (4.3), the variables have to obey the following *integrability condition*:

$$\frac{1}{a_\mathcal{D}^6}\,(\,\mathcal{Q}_\mathcal{D}\;a_\mathcal{D}^6\,)^{\cdot} + \frac{1}{a_\mathcal{D}^2}\,(\,\langle\mathcal{R}\rangle_\mathcal{D}\,a_\mathcal{D}^2\,)^{\cdot} = 0\,, \tag{4.4}$$

where the notation $(.)^{\cdot}$ means differentiation with respect to t of the entire content of the parenthesis. Eq. (4.4) shows that kinematical backreaction and the averaged spatial curvature are coupled. This equation is key to understanding the evolution of global curvature as a consequence of structure formation. Note that by demanding $\mathcal{Q}_\mathcal{D} \propto 1/a_\mathcal{D}^6$ (including the trivial case $\mathcal{Q}_\mathcal{D} = 0$), the averaged curvature obeys a separate (scale-dependent) conservation equation corresponding to the FLRW curvature constraint $(\,\langle\mathcal{R}\rangle_\mathcal{D}\,a_\mathcal{D}^2\,)^{\cdot} = 0$.

4.1.2 Cosmological parameters

It shall be convenient to write the averaged energy constraint equation (4.2) in terms of effective cosmological parameters [177]. Dividing (4.2) by $(3\,H_\mathcal{D}^2)$, where we call the

functional $H_{\mathcal{D}} \equiv \dot{a}_{\mathcal{D}}/a_{\mathcal{D}}$ 'the global Hubble parameter', we have:

$$\Omega_m^{\mathcal{D}} \,+\, \Omega_\Lambda^{\mathcal{D}} \,+\, \Omega_{\mathcal{R}}^{\mathcal{D}} \,+\, \Omega_{\mathcal{Q}}^{\mathcal{D}} \;=\; 1 \;, \tag{4.5}$$

where the four cosmological 'parameters' $\Omega_m^{\mathcal{D}}, \Omega_\Lambda^{\mathcal{D}}, \Omega_{\mathcal{R}}^{\mathcal{D}}$, and $\Omega_{\mathcal{Q}}^{\mathcal{D}}$ constitute the 'cosmic quartet' and are defined by:

$$\Omega_m^{\mathcal{D}} \;\equiv\; \frac{8\pi G}{3H_{\mathcal{D}}^2}\,\langle \varrho \rangle_{\mathcal{D}} \;; \qquad \Omega_\Lambda^{\mathcal{D}} \;\equiv\; \frac{\Lambda}{3H_{\mathcal{D}}^2} \;; \tag{4.6}$$

$$\Omega_{\mathcal{R}}^{\mathcal{D}} \;\equiv\; -\,\frac{\langle \mathcal{R} \rangle_{\mathcal{D}}}{6H_{\mathcal{D}}^2} \;; \qquad \Omega_{\mathcal{Q}}^{\mathcal{D}} \;\equiv\; -\,\frac{\mathcal{Q}_{\mathcal{D}}}{6H_{\mathcal{D}}^2} \;. \tag{4.7}$$

As we wish to see whether the averaged spatial curvature $\Omega_{\mathcal{R}}^{\mathcal{D}}$ and backreaction $\Omega_{\mathcal{Q}}^{\mathcal{D}}$ cosmological parameters can mimic dark energy without a local energy component violating the strong energy condition, we set $\Omega_\Lambda^{\mathcal{D}} = 0$. We can further rewrite (4.5) in terms of deviations from a spatially flat Friedmannian parametrization,

$$\Omega_m^{\mathcal{D}} \,+\, \Omega_{\mathcal{X}}^{\mathcal{D}} \;=\; 1 \;\; ; \qquad \Omega_{\mathcal{X}}^{\mathcal{D}} \;\equiv\; \Omega_{\mathcal{R}}^{\mathcal{D}} \,+\, \Omega_{\mathcal{Q}}^{\mathcal{D}} \;, \tag{4.8}$$

where $\mathcal{X}$ stands for '$\mathcal{X}-$matter': an effective 'matter' cosmological component that has the potential to mimic dark energy and/or dark matter signatures as they appear in the standard ΛCDM model.

4.1.3 Scaling solutions to the averaged Einstein equations

In order to uniquely determine the solutions to the four unknown functions $a_{\mathcal{D}}$, $\langle \varrho \rangle_{\mathcal{D}}$, $\langle \mathcal{R} \rangle_{\mathcal{D}}$, and $\mathcal{Q}_{\mathcal{D}}$ satisfying the equations (4.1)–(4.4) (where one of the equations in the set is redundant), we must specify one additional equation as a closure condition.

We shall consider space-times which are consistent with the exact scaling solutions for the averaged spatial curvature and kinematical backreaction variables as formulated in Ref. [173, 131],

$$\langle \mathcal{R} \rangle_{\mathcal{D}} \;=\; \langle \mathcal{R} \rangle_{\mathcal{D}_{\mathbf{i}}}\, a_{\mathcal{D}}^n \;; \qquad \mathcal{Q}_{\mathcal{D}} \;=\; \mathcal{Q}_{\mathcal{D}_{\mathbf{i}}}\, a_{\mathcal{D}}^p \;, \tag{4.9}$$

as an ansatz for the needed closure condition, with n and p being real numbers, and $\mathcal{D}_{\mathbf{i}}$ denoting an initial domain for which the definition $a_{\mathcal{D}_{\mathbf{i}}} \equiv 1$ is imposed. Plugging

the ansatz (4.9) into the integrability condition (4.4) we have that either $n = -2$ and $p = -6$ or $n = p$ must be satisfied.

The solution $n = -2$ and $p = -6$ leads to a quasi-Friedmannian model in which the backreaction variable $\mathcal{Q}_{\mathcal{D}}$ is negligible today (due to its rapid fall-off as a function of volume), and which is the only case where structure formation, encoded in $\mathcal{Q}_{\mathcal{D}}$, is decoupled from the averaged spatial curvature, such that the quasi-FLRW curvature constraint $(\langle \mathcal{R} \rangle_{\mathcal{D}} \, a_{\mathcal{D}}^2)^{\cdot} = 0$ is satisfied.

In the present analysis we will consider the class of solutions $n = p$, which implies coupling of structure formation and averaged scalar curvature. For this class of solutions we have the proportionality relation

$$Q_{\mathcal{D}} \;=\; -\frac{n \,+\, 2}{n \,+\, 6} \, \langle \mathcal{R} \rangle_{\mathcal{D}} \tag{4.10}$$

between kinematical backreaction and averaged spatial curvature. Thus, positive kinematical backreaction (dominance of the variance in the fluid expansion rate over shear[87]) implies negative spatial curvature when $n > -2$.

It is convenient to introduce the following effective deceleration parameter for characterizing the different possible scaling solutions in terms of their acceleration:[4]

$$q_{\mathcal{D}} \;\equiv\; -\frac{\ddot{a}_{\mathcal{D}} \, a_{\mathcal{D}}}{\dot{a}_{\mathcal{D}}^2} \;=\; \frac{\Omega_m^{\mathcal{D}} \,-\, (n+2)\, \Omega_{\mathcal{X}}^{\mathcal{D}}}{2} \;=\; \frac{\Omega_m^{\mathcal{D}_0} \,-\, (n+2)\, \Omega_{\mathcal{X}}^{\mathcal{D}_0} \left(\frac{a_{\mathcal{D}}}{a_{\mathcal{D}_0}} \right)^{n+3}}{2\, \Omega_m^{\mathcal{D}_0} \,+\, 2\, \Omega_{\mathcal{X}}^{\mathcal{D}_0} \left(\frac{a_{\mathcal{D}}}{a_{\mathcal{D}_0}} \right)^{n+3}} \;, \tag{4.11}$$

analogous to the definition of the FLRW deceleration parameter. The second equality follows from combining (4.1) and (4.2), and using the definitions of the cosmological parameters given in Sec. 4.1.2. The last equality follows from the scaling conditions (4.9) with $n = p$, and from (4.8). From (4.11), we can formulate the following acceleration condition:

$$q_{\mathcal{D}} \,<\, 0 \quad \Leftrightarrow \quad (n+2) \left(\frac{a_{\mathcal{D}}}{a_{\mathcal{D}_0}} \right)^{n+3} \,>\, \frac{\Omega_m^{\mathcal{D}_0}}{1 \,-\, \Omega_m^{\mathcal{D}_0}} \;, \tag{4.12}$$

valid for $0 < \Omega_m^{\mathcal{D}_0} < 1$. Thus, for $n \leq -2$, volume acceleration does not occur at any epoch, as the kinematical backreaction $Q_{\mathcal{D}}$ is negative in this case. For $n > -2$, acceleration might be reached depending on the value of $\Omega_m^{\mathcal{D}_0}$. We note that $n = 0$ results in an acceleration condition formally similar to the flat FLRW model ($\Omega_\Lambda =$

[4] Parameters evaluated at the present epoch are indexed with $\mathcal{D}_0$ throughout this chapter.

$1-\Omega_m$) acceleration condition: $2\,(a/a_0)^3 > \Omega_{m0}/(1-\Omega_{m0})$, where a is the FLRW scale factor. This is expected, since the backreaction term $Q_{\mathcal{D}}$ is constant in this case, and thus acts as an effective cosmological constant in the averaged Raychaudhuri equation (4.1) (*cf.* Ref. [177] [Sec. 3.3.2]).

We note that the timescape model, which we also investigate in this analysis, is not part of the scaling solutions discussed here (even though it is solution to the set of averaged equations discussed in Sec. 4.1.1). Rather it is a two-scale model with volume partitioning into over-dense flat regions and under-dense 'void regions'. For details about the formulation of the timescape model, see Ref. [97].

4.1.4 The template metric

In order to translate physical observables of redshift and photon flux into 'measurements' of the free parameters n and $\Omega_m^{\mathcal{D}_0}$ of the scaling solutions outlined in Sec. 4.1.3, we must parameterize predictions of the observables in terms of n and $\Omega_m^{\mathcal{D}_0}$.

With knowledge of the entire hierarchy of structure in the Universe and the corresponding inhomogeneous metric, one would in principle be able to do general relativistic ray-tracing, and properly describe the measurements of an observer at a given location without the need for an averaging scheme. In practice we do not have access to such information, and the aim here is to formulate an effective model for light propagation over cosmic scales $\mathcal{D} \gtrsim 100\,\mathrm{Mpc/h}$ given knowledge of the functions $a_{\mathcal{D}}$, $\langle\varrho\rangle_{\mathcal{D}}$, $\langle\mathcal{R}\rangle_{\mathcal{D}}$, and $\mathcal{Q}_{\mathcal{D}}$ describing the Universe on such scales. These global parameters are built from averages of local space-time variables fulfilling the Einstein equations, but are not themselves solutions to any 'global Einstein equations' valid on the scale $\mathcal{D}$. Rather, they are solutions to the set of equations (4.1), (4.2), and (4.3). Thus, $a_{\mathcal{D}}$ is *not* to be thought of as a scale factor in a local metric, and $\langle\mathcal{R}\rangle_{\mathcal{D}}$ is *not* to be thought of as the spatial Ricci curvature built from such a metric. We can nevertheless conjecture that light sampling the Universe in a volume averaged sense is, on average, propagating according to null-geodesics of an *effective* metric which reduces to an FLRW 3−metric described with spatial curvature $\langle\mathcal{R}\rangle_{\mathcal{D}}$ at each leaf of the space-time normal to the fluid flow, but which has non-trivial union between such leaves due to the non-commutativity of the averaging and time-evolution operations.

Based on this conjecture, we introduce a template metric for describing light propagation on cosmic scales as a constant-curvature metric but which, unlike the FLRW

solution, allows for curvature evolution in 'cosmic time'. We stress that the introduction of such a template metric, which is not a solution to Einstein's equations, is not a violation of general relativity. On the contrary, in a general relativistic universe model, any metric theory describing average light propagation on large scales must be effective.[5]

The form of the effective metric follows the proposal of Ref. [131]:

$$ {}^4g^{\mathcal{D}} \;\equiv\; -\,\mathrm{d}t^2 \,+\, L^2_{H_{\mathcal{D}_0}}\, a^2_{\mathcal{D}} \left(\frac{\mathrm{d}r^2_{\mathcal{D}}}{1 \,-\, \kappa_{\mathcal{D}}(t)\, r^2_{\mathcal{D}}} \,+\, r^2_{\mathcal{D}}\, \mathrm{d}\Omega^2 \right) , \tag{4.13} $$

with t being the proper time function of the dust fluid, such that $t = \text{const.}$ selects hypersurfaces orthogonal to the fluid flow, and $r_{\mathcal{D}}$ is a dimensionless radial coordinate, which also has the interpretation as a comoving distance; $a_{\mathcal{D}}$ is the dimensionless volume scale factor governed by (4.1)–(4.4), and $a_{\mathcal{D}_0} L_{H_{\mathcal{D}_0}} \equiv H^{-1}_{\mathcal{D}_0}$ is the present-day Hubble horizon; $\mathrm{d}\Omega^2 \equiv (\mathrm{d}\theta^2 + \sin(\theta)^2\, \mathrm{d}\phi^2)$ is the angular element on the unit sphere, and $\kappa_{\mathcal{D}}$ is a dimensionless spatial constant-curvature function related to the averaged spatial Ricci scalar through

$$ \kappa_{\mathcal{D}}(t) \;\equiv\; \frac{\langle \mathcal{R} \rangle_{\mathcal{D}}\,(t)}{|\langle \mathcal{R} \rangle_{\mathcal{D}_0}|}\, \frac{a^2_{\mathcal{D}}(t)}{{a_{\mathcal{D}_0}}^2} \,. \tag{4.14} $$

For the class of scaling solutions described in Sec. 4.1.3, with $n = p$, one can rewrite $\kappa_{\mathcal{D}}$ using (4.8) and (4.10):

$$ \kappa_{\mathcal{D}}(a_{\mathcal{D}}) \;=\; -\,\frac{(n+6)\,\Omega^{\mathcal{D}_0}_{\mathcal{X}}}{|(n+6)\,\Omega^{\mathcal{D}_0}_{\mathcal{X}}|}\, \frac{a^{(n+2)}_{\mathcal{D}}}{a^{(n+2)}_{\mathcal{D}_0}} \,. \tag{4.15} $$

In what follows we advance the idealizing conjecture that light propagation over cosmological scales is effectively described by null geodesics in the template metric (4.13). This is an assumption that follows the homogeneous-geometry approximation of the standard model, but corrects for the evolution of curvature to comply with the exact average properties. We also note that more insight and work is needed to improve on

[5] We refer the reader to Ref. [131] for further motivations for introducing the template metric, where it is discussed how constant-curvature metrics can be obtained via Ricci flow smoothing of Riemannian hypersurfaces[115]. Even though the template metric described in this section is not solution to Einstein's equations, local metrics of the same form have been studied as solutions to the Einstein equations (see the recent paper by Stichel [178] and references therein).

this first-step template metric.

4.1.5 Distance modulus

In order to constrain the scaling solutions with supernova data we must make a prediction for the distance modulus within this class of models. We will compute the distance modulus as a function of redshift in the template metric of Sec. 4.1.4.

The distance modulus is defined in terms of the luminosity distance d_L in the following way:

$$\mu(z_{\mathcal{D}}) \;=\; 5\,\log_{10}\left(\frac{d_L(z_{\mathcal{D}})}{10\,\mathrm{Mpc}}\right)\,, \tag{4.16}$$

where $z_{\mathcal{D}}$ is the redshift as inferred from the domain-dependent scale factor (see the below equation (4.19)). By Etherington's theorem (see Ref. [106] and references therein),

$$d_L(z_{\mathcal{D}}) \;=\; (1\,+\,z_{\mathcal{D}})^2\,d_A(z_{\mathcal{D}})\,, \tag{4.17}$$

where d_A is the angular diameter distance. The angular diameter distance is given via the metric (4.13) as

$$d_A(z_{\mathcal{D}}) \;=\; \frac{1}{H_{\mathcal{D}_0}}\,a_{\mathcal{D}}(z_{\mathcal{D}})\,r_{\mathcal{D}}(z_{\mathcal{D}})\,. \tag{4.18}$$

From the geodesic equation of (4.13) we have that light emitted and absorbed by observers comoving with the dust, and propagating radially with respect to the central observer, is redshifted by[6]

$$z_{\mathcal{D}}(a_{\mathcal{D}}) \;=\; \frac{\hat{k}^0(a_{\mathcal{D}})}{a_{\mathcal{D}}}\;-\;1\,, \tag{4.19}$$

with $\hat{k}^0$ given by

$$\frac{\mathrm{d}\ln(\hat{k}^0)}{\mathrm{d}a_{\mathcal{D}}} \;=\; -\,\frac{r^2_{\mathcal{D}}(a_{\mathcal{D}})}{2\,(1\,-\,\kappa_{\mathcal{D}}(a_{\mathcal{D}})r^2_{\mathcal{D}}(a_{\mathcal{D}}))}\,\frac{\mathrm{d}\kappa_{\mathcal{D}}(a_{\mathcal{D}})}{\mathrm{d}a_{\mathcal{D}}}\,. \tag{4.20}$$

The dimensionless coordinate distance $r_{\mathcal{D}}$ along the null rays is

$$\frac{\mathrm{d}r_{\mathcal{D}}}{\mathrm{d}a_{\mathcal{D}}} \;=\; -\,\frac{1}{a^2_{\mathcal{D}}}\sqrt{\frac{1\,-\,\kappa_{\mathcal{D}}(a_{\mathcal{D}})\,r^2_{\mathcal{D}}(a_{\mathcal{D}})}{\Omega_m^{\mathcal{D}_0}\,a_{\mathcal{D}}^{-3}\,+\,\Omega_{\mathcal{X}}^{\mathcal{D}_0}\,a_{\mathcal{D}}^{n}}}\,,\qquad r_{\mathcal{D}}\,(a_{\mathcal{D}}=1)\;\equiv\;0\,, \tag{4.21}$$

[6] We henceforth drop the domain index for the redshift.

where the expression for $\kappa_{\mathcal{D}}$ (4.15) has been used.[7]

4.2 Methods

As in chapter 3 we use the Joint Light-curve Analysis (JLA) sample[123] containing 740 supernovae to test the scaling solutions described in Sec. 4.1. The JLA catalogue gathers data from four independent studies: SuperNovae Legacy Survey (SNLS), Sloan Digital Sky Survey (SDSS), nearby supernovae (Low–z), and Hubble Space Telescope (HST).

We follow the methods discussed in chapter 3 for standardising supernovae and model testing. In this section we briefly review the SALT2 method and the likelihood function used. For details we refer to section 3.1 and section 3.2.1.

4.2.1 The SALT2 method

The Spectral Adaptive Lightcurve Template 2 (SALT2) method for making supernovae standard candles consists in fitting the supernovae light-curves to an empirical template, and subsequently using the parameters of the light-curve fit in the empirical model for band correction:

$$\mu_{SN} \;=\; m_B^* \;-\; M_B \;+\; \alpha\, x_1 \;-\; \beta\, c\,, \tag{4.22}$$

where m_B^* is the peak of the apparent magnitude in the B-band, M_B is the intrinsic magnitude in the rest frame of the supernova, x_1 is the light-curve stretch parameter, and c is the colour correction parameter for each supernova in the sample. m_B^*, x_1, and c are obtained from template fitting of the supernovae light-curves[123]; α and β are global regression parameters that are determined in the fit.

4.2.2 The Likelihood function

We now briefly review the likelihood function $\mathcal{L}(\hat{X}\,|\,\theta)$ used in this analysis, where $\hat{X} = \{\hat{m}^*_{B,1}\,, \hat{x}_{1,1},\, \hat{c}_1, ..., \hat{m}^*_{B,N}\,, \hat{x}_{1,N},\, \hat{c}_N\}$ are the 'observed' parameters for the supernovae

[7] The expression (4.21) for $\mathrm{d}r_{\mathcal{D}}/\mathrm{d}a_{\mathcal{D}}$ is different from that in Eq. (41) of Ref. [131], which is due to minor typos in Ref. [131]; see also the remarks in Ref. [175].

labelled $1, ..., N$, and θ is short for all model assumptions (cosmological model, model for band correction, etc.).

The hats over the parameters in $\hat{X}$ indicate that these parameters are inferred from data, whereas the corresponding parameters without hats represent the 'true' underlying (or intrinsic) parameters.

We use the likelihood function as formulated in Ref. [138] and discussed in section 3.2.1 of this thesis, with the model for the distribution of intrinsic supernovae parameters proposed in Ref. [137], where the intrinsic parameters M_B, x_1, c of each supernova are assumed to be drawn from identical and independent Gaussian distributions with means $M_0, x_{1,0}, c_0$ and standard deviations $\sigma_{M_0}, \sigma_{x_{1,0}}, \sigma_{c_0}$. Using the SALT2 relation (4.22) and the assumptions presented in Ref. [137], the final expression of the likelihood function is

$$\begin{aligned} \mathcal{L} \;=\; & |\, 2\pi \,(\Sigma_{\mathrm{d}} \;\; + A^T \Sigma_{\mathrm{l}} A)\,|^{-1/2} \\ & \times \exp \;\; \Big[-\,(\hat{Z} \;-\; Y_0 A)\,(\Sigma_{\mathrm{d}} \;+\; A^T \Sigma_{\mathrm{l}} A)^{-1}\,(\hat{Z} \;-\; Y_0 A)^T / 2 \Big] \;, \end{aligned} \tag{4.23}$$

where $|\,.\,|$ denotes the determinant of a matrix, Σ_{d} is the estimated experimental covariance matrix (including statistical and systematic errors), and Σ_{l} is the 'intrinsic covariance matrix' $\mathrm{diag}(\sigma^2_{M_0}, \sigma^2_{x_{1,0}}, \sigma^2_{c_0}, \sigma^2_{M_0}, \sigma^2_{x_{1,0}}, \sigma^2_{c_0}, ...)$ of dimension $3N \times 3N$; $\hat{Z} \equiv \{\hat{m}^*_{B,1} \;-\; \mu_1, \hat{x}_{1,1},\, \hat{c}_1, ..., \hat{m}^*_{B,N} \;-\; \mu_1, \hat{x}_{1,N},\, \hat{c}_N\}$, where $\mu_1, ..., \mu_N$ are the distance moduli evaluated at the measured redshifts $\hat{z}_1, ..., \hat{z}_N$ of the supernovae, and $Y_0 \equiv \{M_0, x_{1,0}, c_0, M_0, x_{1,0}, c_0, ...\}$; A is the blog diagonal matrix

$$A \;=\; \begin{pmatrix} 1 & 0 & 0 & 0 \\ -\,\alpha & 1 & 0 & 0 \\ \beta & 0 & 1 & 0 \\ 0 & 0 & 0 & \ddots \end{pmatrix} . \tag{4.24}$$

The final likelihood thus contains the following eight free parameters: α, β, M_0, $x_{1,0}$, c_0, σ_{M_0}, $\sigma_{x_{1,0}}$, and σ_{c_0} in addition to the cosmological parameters entering the expression for the distance modulus μ.

In chapter 3 we discussed the introduction of empirical parameters for modelling redshift-dependence in the intrinsic supernovae parameters and observational biases. In this chapter we stick to the likelihood function (4.23) based on a minimal number of

empirical parameters. We focus on the constraint of cosmological parameters and on the relative quality of fit provided by different cosmological models. For an assessment of the fit of the likelihood function (4.23) to data, and in particular of the ability to fit the distributions of the measured supernovae parameters $\hat{x}_1$ and $\hat{c}$, see Ref. [138].

4.3 Data analysis

We now constrain the parameter space of the scaling solutions with the JLA catalogue using the SALT2 relation and the likelihood model specified in Sec. 4.2.2. We then compare the quality of fit to that of the ΛCDM model, the Milne universe model with no sources and a negative constant curvature (henceforth named the 'empty universe model'), and the timescape model. We discuss the scales of application of the scaling solutions in relation to the application of a redshift cut in the data in Sec. 4.3.1. In Sec. 4.3.2 we present our results.

4.3.1 Statistical homogeneity scale and cut-off in redshift

Any model describing light propagation on a given scale should, for the sake of self-consistency, only be applied to light-rays propagating over at least that scale.

Since all the models tested in this analysis have, per construction, structureless geometry and are designed to hold above an approximate statistical homogeneity scale, it is natural (or even mandatory) to impose a cut-off in radius relative to the observer corresponding to the approximate homogeneity scale. Light emitted by supernovae below such a radius is probing scales below which the cosmological averaged metric description applies.

The largest scales of second-order correlations between structures (applying a cut-off of $\sim 1\%$ in the two-point correlation function)[148] is estimated to be $\sim 70-120$ Mpc/h in ΛCDM.[8] Following Ref. [180] we apply a cut-off at a redshift radius in the CMB frame $z_{\rm CMB,min} = 0.033$ relative to a central observer, corresponding to a comoving distance of ~ 100 Mpc/h, when computing parameter constraints. This choice is a bit more conservative than that imposed in Ref. [149] of $z_{\rm CMB,min} = 0.024$, corresponding

[8] Note that higher-order correlations are still significant on Gpc scales. Probed through Minkowski functionals containing all orders of correlation functions, the analysis of SDSS LRG samples revealed more than $2\,\sigma$ deviations from ΛCDM mock catalogues on scales beyond 600 Mpc/h [179].

to ~ 70 Mpc/h. The slight difference in choice of cut-off does not strongly affect the parameter estimates. We shall examine a few different choices of redshift cut-off when comparing the quality of fit of the tested models, in order to establish the degree of robustness of the results to the subsetting of data.

4.3.2 Results

We use the likelihood function given in Sec. 4.2.2 and the equation for the distance modulus (4.16) to constrain the scaling solutions.

The $1\,\sigma$ confidence bounds on the cosmological parameters of the scaling solution (with fixed scaling index $n = -1$ and free scaling index respectively) are shown in Table 4.1, together with the corresponding results for the ΛCDM model (with imposed spatial flatness and free curvature parameter Ω_k respectively), the empty universe model, and the timescape model (see Table 2 of Ref. [180]). It should be noted that the matter cosmological parameters $\Omega_m^{\mathcal{D}_0}$ of all the models cannot be directly compared (even though they are represented by the same symbol to ease the notation). The scaling solutions, the ΛCDM model, and the timescape model are non-nested (i.e. none of the models can be obtained from any of the other models by parameter space constraints), and their expansion history depend on $\Omega_m^{\mathcal{D}_0}$ in different ways.

The constrained versions of the scaling solution and the ΛCDM model, with $n = -1$ and $\Omega_k = 0$ respectively, are associated with much less uncertainty in the $\Omega_m^{\mathcal{D}_0}$ parameter than the corresponding unconstrained models. This is due to the coupling of the cosmological parameters in the likelihood function.

In addition to the cosmological parameters, we quote the best-fit 'nuisance parameters' α, β, M_0, $x_{1,0}$, c_0, σ_{M_0}, $\sigma_{x_{1,0}}$, and σ_{c_0}, described in Sec. 4.2.2. Our best-fit findings are similar to those found in Ref. [138, 180], and typical differences between the parameters inferred when assuming the respective cosmological models are within a few percent. For typical $1\,\sigma$ constraints on the regression coefficients α and β of the SALT2 relation (4.22) and on the mean M_0 and width σ_{M_0} of the distribution of intrinsic magnitudes, see Ref. [123].

The frequentist $1\,\sigma$ and $2\,\sigma$ confidence contours for the scaling solutions are shown in Fig. 4.1. Our results are consistent with positive present-epoch volume acceleration, ruling out deceleration at the $> 2\,\sigma$ level, for the class of scaling solutions tested.

A striking result is that the best-fit scaling index $n = -1.0^{+0.7\,(1\sigma)}_{-0.6\,(1\sigma)}$ is consistent with

Table 4.1: Best-fit parameters with a redshift cut-off at $z_{\mathrm{CMB,min}} = 0.033$. For the cosmological parameters we also quote '$1\,\sigma$'= 68.27...% confidence bounds. Note that $x_{1,0}$, c_0, $M_{B,0}$, $\sigma_{x_{1,0}}$, σ_{c_0}, and $\sigma_{M_{B,0}}$ are the mean and width parameters of the assumed Gaussian distributions from which the intrinsic parameters of each supernova are assumed to be drawn (see Sec. 4.2.2). Thus, the numbers quoted for $\sigma_{x_{1,0}}$, σ_{c_0}, and $\sigma_{M_{B,0}}$ are best-fit values of the widths of these Gaussian distributions and *not* error bars on the best-fit determinations of $x_{1,0}$, c_0, and $M_{B,0}$.

Models	Scaling solution	Scaling solution $n = -1$	ΛCDM	ΛCDM $\Omega_k = 0$	Empty Universe	Timescape
$\Omega_m^{\mathcal{D}_0}$ or Ω_{m_0}	$0.24^{+0.13}_{-0.24}$	$0.25^{+0.04}_{-0.04}$	$0.30^{+0.10}_{-0.11}$	$0.37^{+0.03}_{-0.03}$	0	$0.31^{+0.07}_{-0.09}$
n	$-1.0^{+0.7}_{-0.6}$	-1	-	-	-	-
Ω_k	-	-	$0.17^{+0.28}_{-0.26}$	-	-	-
α	0.13	0.13	0.13	0.13	0.13	0.13
$x_{1,0}$	0.11	0.11	0.11	0.11	0.10	0.11
$\sigma_{x_{1,0}}$	0.90	0.90	0.90	0.90	0.90	0.90
β	3.1	3.1	3.1	3.1	3.1	3.1
c_0	-0.021	-0.021	-0.021	-0.022	-0.020	-0.021
σ_{c_0}	0.069	0.069	0.068	0.069	0.069	0.069
$M_{B,0}$	-19	-19	-19	-19	-19	-19
$\sigma_{M_{B,0}}$	0.10	0.10	0.10	0.10	0.11	0.10

the results obtained in Ref. [181] in a perturbative framework around an Einstein-de Sitter background[9], where the leading-order (or largest-scale) backreaction was found to obey the scaling law $\mathcal{Q}_{\mathcal{D}} \propto a_{\mathrm{EdS}}^{-1}$. The best-fit scaling index is thus compatible with a perturbative evaluation of backreaction (extrapolating the perturbative scaling law). Notice also that the best-fit scaling index is consistent with $n = 0$ at the $2\,\sigma$ level (but not at the $1\,\sigma$ level). For this value of n, backreaction is mimicking a cosmological constant, *cf.* Ref. [177] [Sect. 3.3.2].

Comparing Fig. 4.1 with the contour plot of Ref. [131] showing the constraints of the scaling solutions from CMB data from WMAP3-yr data and 71 SNIa from the SNLS Collaboration, there is a significant amount of overlap of the $2\,\sigma$ contours.

[9] Einstein-de Sitter (flat 'matter only' FLRW model with $\Omega_m = 1$ and $\Omega_\Lambda = 0$) exhibits volume deceleration, and constitutes an interesting background model for studying the possible emergence of spatial curvature and volume acceleration from an initially decelerating and (almost) spatially flat universe model.

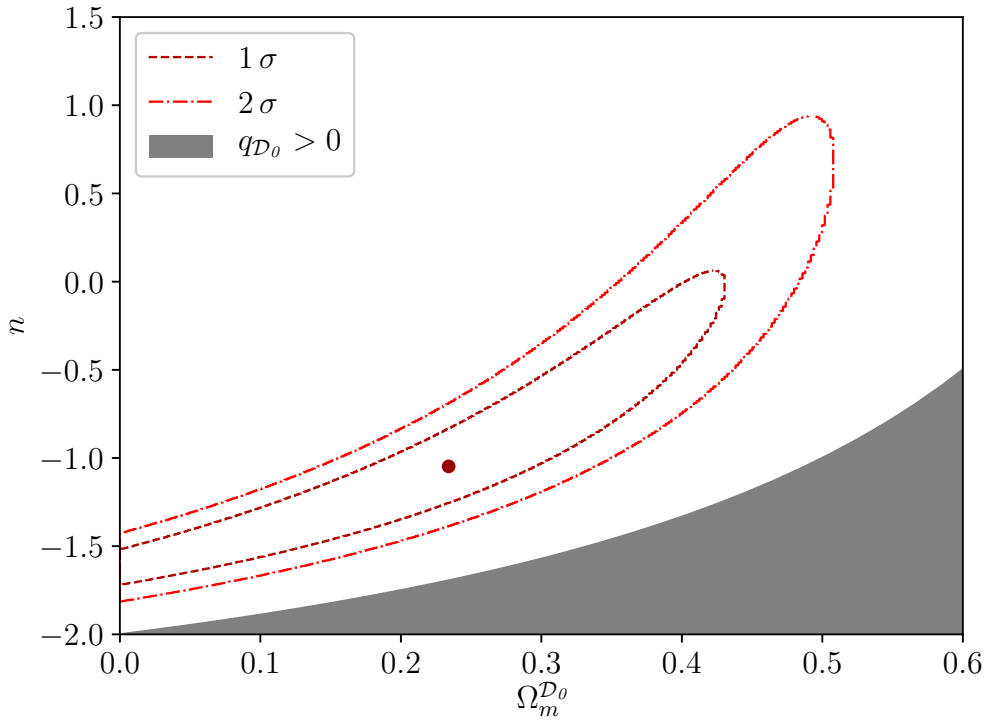

Figure 4.1: $1\,\sigma$ and $2\,\sigma$ confidence contours of the parameters $\Omega_m^{\mathcal{D}_0}$ and n of the scaling solutions. The best-fit, $\{\Omega_m^{\mathcal{D}_0} = 0.24\,,\, n = -1.0\}$, is marked by a dot. The shaded area represents models with present-epoch volume deceleration $q_{\mathcal{D}_0} > 0$, and the remaining area of the parameter space has positive present-epoch volume acceleration. Thus, deceleration is ruled out at the $> 2\,\sigma$ level for the class of scaling solutions tested.

However, the volume of the likelihood in the present analysis is shifted towards lower values of $\Omega_m^{\mathcal{D}_0}$ and n as compared to Ref. [131].[10]

Comparing the results of Table 4.1 with the constraints on the scaling solutions from Ref. [175], obtained from measurements of the Hubble parameter from the differential age method and radial baryon acoustic oscillation data, we find agreement within $1\,\sigma$ of both the scaling index n and the matter cosmological parameter $\Omega_m^{\mathcal{D}_0}$.

We compare the quality of fit of the scaling solutions with that of the ΛCDM model,

[10] It is difficult to compare with the results of Ref. [131] because of the sparse supernova sample used and since the best-fit is obtained from a combination of the supernova and CMB data. Moreover, the error-bars on the best-fit parameters are not quoted. Generally, we refer to Ref. [131] with respect to the theoretical foundations and methods, the results obtained therein are by now outdated.

the empty universe model, and the timescape model using the *Akaike Information Criterion*[11] (AIC)[166]. As discussed in appendix 3.C.1, the AIC is a measure of the relative probability of minimal information loss between two models:

$$\frac{p_1}{p_2} \;=\; \frac{\exp(-\,\mathrm{AIC}_1\,/\,2)}{\exp(-\,\mathrm{AIC}_2\,/\,2)}\;; \qquad \mathrm{AIC}_i \;\equiv\; 2\,q_i \;-\; 2\,\ln(\mathcal{L}_i)\;, \tag{4.25}$$

where q_i is the number of parameters and $\mathcal{L}_i$ is the maximum likelihood of model i, where p_i is the probability that model i minimizes the (estimated) information loss, and where the two models are labelled $i = 1, 2$, respectively. The AIC relative likelihood measure (4.25) can be viewed as a generalization of the likelihood ratio to non-nested models.

The interpretation of the relative numerical estimates of the AIC measure for different models is context-dependent. As a rough guideline, differences in AIC between two models of at least 2, 6, and 10 (corresponding to the AIC relative likelihood with the most likely model in the denominator not exceeding 0.4, 0.05, and 0.007, respectively) are characterized as providing 'positive', 'strong', and 'very strong' evidence, respectively, in favour of the model with minimal AIC[168].[12]

We show the results of the AIC values and the AIC relative likelihood measure in Table 4.2. We use both the spatially flat ΛCDM model and the ΛCDM model with free curvature parameter Ω_k as references, and quote $p_{\rm model}/p^{\Omega_k=0}_{\Lambda\rm CDM}$ and $p_{\rm model}/p_{\Lambda\rm CDM}$ for each of the models. The results are shown for data excluded below redshift cuts, $z_{\rm CMB,min}$, of 0.024, 0.033, 0.07, and 0.15, respectively, to examine the robustness of the AIC results to different redshift cuts in data. The values of $z_{\rm CMB,min}$ of 0.024 and 0.033 are two different estimates of the statistical homogeneity scale as discussed in Sec. 4.3.1. $z_{\rm CMB,min} = 0.07$ and $z_{\rm CMB,min} = 0.15$ correspond to ~ 200 Mpc/h and ~ 500 Mpc/h, respectively, in the concordance ΛCDM model. These scales might be motivated as conservative homogeneity scale estimates based on the studies of convergence of bulk flow [183] and of higher order correlation functions [179].

In addition to the scaling solution with two free cosmological parameters, n and

[11] The Akaike Information Criterion is one of many methods valid for model selection. For an overview of some common methods and their interpretations see Ref. [182].

[12] When the AIC likelihood is bigger than one – i.e. the most likely model is in the numerator – the interpretation reverses such that models with AIC relative likelihood *not smaller* than 1/0.4, 1/0.05, and 1/0.007 are characterized as providing 'positive', 'strong', and 'very strong' evidence, respectively, in favour of the model with minimal AIC.

$\Omega_m^{\mathcal{D}_0}$, the AIC is also computed for the nested solution within this class with the scaling index n fixed to its large-scale theoretical expectation, $n = -1$, from Lagrangian perturbation theory studies.[13]

From Table 4.2 we see that all tested models are relatively close in AIC probability. No model has 'strong' evidence (i.e. AIC relative likelihood of ≤ 0.05) over another from an AIC perspective for any given redshift cut. Some models are weakly preferred over others. For example, the spatially flat ΛCDM model, the scaling solution with $n = -1$ and the timescape model are all weakly preferred (AIC relative likelihood of ≤ 0.4) over the empty universe model.

For the values $z_{\rm CMB,min} = 0.033$ and $z_{\rm CMB,min} = 0.15$, the spatially flat ΛCDM is weakly preferred (AIC relative likelihood of ≤ 0.4) over the scaling solution. However, this conclusion is not robust to the choice of redshift cut, as can be seen in Table 4.2. Furthermore, these weak preferences vanish when we instead compare the scaling solution to the ΛCDM model with curvature, which is perhaps the more natural choice, since the models compared in this case have the same number of free parameters and a 'curvature' parameter each (n and Ω_k respectively).

The AIC relative likelihoods are in general smaller when quoted with the spatially flat ΛCDM model as reference than for the ΛCDM model with curvature as reference, since the likelihood does not increase sufficiently in ΛCDM by adding the curvature parameter to account for the AIC punishment factor for adding an additional parameter. We note, however, that the best-fit ΛCDM model has negative curvature (see Table 4.1), which is also a feature of the scaling solution.

We conclude that the ΛCDM model, the scaling solution, and the timescape model provide adequate fits to data. The spatially flat ΛCDM model, the scaling solution with $n = -1$ and the timescape model overall have the highest AIC likelihoods. The empty universe model is mildly disfavoured as compared to the other models.

It is important to point out, that the comments made here on the quality of fit are valid for the luminosity distance probed at $z \lesssim 1$ only. For example, the empty universe model is not viable as a cosmological model (for physical reasons and from a

[13] We refer here to Lagrangian perturbations on an Einstein-de Sitter background investigated in Ref. [181], as discussed above in this section, where $n = -1$ was found to describe the large-scale behaviour of kinematical backreaction and averaged scalar curvature. In this study, the backreaction functionals were derived using the averaged Einstein equations without restricting assumptions together with a closure condition for the averaged system in terms of a first-order Lagrangian perturbation scheme as a realistic model for structure formation.

quality of fit perspective) for describing CMB physics.

Our findings align with the conclusions in the recent investigation of Ref. [184] in which it is found that the Pantheon sample probing the $z \lesssim 1$ range is little constraining, allowing for possibly large deviations from ΛCDM, and with the results of Ref. [137] reporting marginal evidence for acceleration from supernovae alone within the FLRW framework.

We emphasize that neither the scaling solutions, the timescape model, nor the empty universe model have any local energy-momentum component violating the strong energy condition.

4.3.3 Discussion

Further studies are needed in order to assess the quality of fit of the scaling solutions to a broader range of cosmological data probing different regimes of the expansion history.

A comment is in order in relation to the combined analysis of cosmological data probing a hierarchy of scales for models that include backreaction. Within the standard model it is relatively straightforward to constrain the 'background' FLRW model with data on various scales: by assumption, the Universe — apart from in the immediate vicinity of compact objects with $GM/(rc^2) \gtrsim 1$, where M is the mass of the object, and r is its proper physical radius — is described by a single FLRW background solution with Newtonian potentials, even in the regime where typical density contrasts are highly non-linear.

In inhomogeneous cosmology, such assumptions are not made. Rather, it is considered a possibility that non-linear structure, through its coupling to the inhomogeneous geometry, can significantly impact the appropriate averaged model for describing collective dynamics of a given space-time domain.[14]

Because of the failure of one simple global metric to serve as a 'background' cosmological solution for all structure with $GM/(rc^2) \ll 1$ in inhomogeneous cosmology, a coherent scaling solution framework for interpreting physics on a hierarchy of scales is

[14] Note that the hierarchical structure of our space-time can lead to non-trivial general relativistic phenomena, even though each level of the hierarchy is well described as a 'weak field' perturbation of the previous level [185]. Note also, that even though regions containing general relativistic compact sources are negligible in terms of volume measure as compared to the total volume of a given spatial domain, the domain can exhibit non-trivial general relativistic behaviour [186].

not within immediate reach. For space-times with a notion of *statistical* homogeneity and isotropy, we might nevertheless expect convergence of the scaling solutions on the largest scales, such that the cosmological parameters (4.6) and the associated template metric (4.13) are effectively independent of the spatial scale $\mathcal{D}$ above an appropriate cutoff in physical size of the domain $\mathcal{D}$. Thus, the scaling solution being valid on the largest scales might be constrained with complementary cosmological data such as supernovae, galaxy surveys, and CMB data, as long as the given survey probes large enough spatial domains.

As is well-known, joint fits of the FLRW model with perturbations face the problem of 'tensions', e.g. with respect to different values of the Hubble parameter, a problem that we trace back to naive extrapolation of the model from high to low redshifts and from large to small scales. In particular, insufficient modelling of differential expansion of space might be the cause of the 'tension' related to the Hubble parameter, *cf.* Refs. [68, 181, 93, 187, 188].

4.4 Testing curvature dynamics with upcoming surveys

It is of observational interest to investigate possible signatures distinguishing between models with dynamical spatial curvature and FLRW models (with rigid spatial curvature).

To test the FLRW constant spatial curvature hypothesis, we can consider the useful curvature statistic:[129]

$$k_H \;=\; \frac{1}{D^2}\left(1-\left(\frac{\mathrm{d}D}{\mathrm{d}z}\frac{H}{H_0}\right)^2\right)\;, \tag{4.26}$$

where D is the dimensionless FLRW comoving transverse distance related to the angular diameter distance d_A by

$$D = H_0/c\,(1+z)d_A$$

, and where H is the FLRW Hubble parameter. From the expression for the FLRW comoving distance $D = 1/\sqrt{\Omega_{k_0}}\,\sinh(\sqrt{\Omega_{k_0}}\int_0^z dz'\frac{H_0}{H(z')})$ it follows that $k_H = -\Omega_{k_0}$

per construction. Note that the equality $k_H = -\Omega_{k_0}$ is based purely on geometrical identities valid for the FLRW class of models, and thus does not depend on details of the matter content, dark matter equation of state, or other tuneable features within FLRW cosmology.

For any other model with a prediction of angular diameter distance and volume expansion as a function of redshift, we might also construct the function k_H (4.26). In general, k_H is not interpreted as a spatial curvature density parameter, but simply as the combination of distance measures given by the right-hand side of (4.26), and it is in principle allowed to vary arbitrarily with redshift.

The function $k_H(z)$ is derivable from $H(z)$ and $D(z)$, and thus, it contains no new information with respect to these two functions. However, $k_H(z)$ is a particularly powerful combination of distance measures, as a $k_H(z) \neq \text{const.}$ detection would be a 'smoking gun' for FLRW geometry violation.

Computing $r_{\mathcal{D}}$ and $H_{\mathcal{D}}$ for the best-fit scaling solution, $\{\Omega_m^{\mathcal{D}_0} = 0.24\,,\, n = -1.0\}$, and substituting $D = H_{\mathcal{D}_0}/c\,(1+z)d_A = H_{\mathcal{D}_0}/c\,\hat{k}^0\,r_{\mathcal{D}}$ and $H = H_{\mathcal{D}}$ in (4.26), we obtain k_H and $\mathrm{d}k_H/\mathrm{d}z$ as a function of redshift as shown in Fig. 4.2. We also show the $1\,\sigma$ confidence bounds on n while keeping $\Omega_m^{\mathcal{D}_0}$ fixed. (The functions k_H and $\mathrm{d}k_H/\mathrm{d}z$ are relatively robust to varying $\Omega_m^{\mathcal{D}_0}$ within its $1\,\sigma$ confidence bounds.) Note that the JLA sample contains supernovae at redshifts $z \lesssim 1.3$. We nevertheless show the prediction of k_H for higher redshifts.

The evolution of k_H of the best-fit scaling solution is far from the constant-k_H signature of an FLRW model. The effective curvature parameter k_H tends to increasingly negative values when approaching the present epoch $z \to 0$, and tends to a constant close to zero in the early universe limit.

The deceleration parameter (4.11) decreases with decreasing redshift and becomes negative at $z \sim 0.7$ for the best-fit scaling solution, $\{\Omega_m^{\mathcal{D}_0} = 0.24\,,\, n = -1.0\}$, marking the transition between volume deceleration to volume acceleration in the best-fit model. This redshift of transition is comparable to that predicted by the best-fit ΛCDM model.

Interestingly, our results for the scaling solutions show tendencies similar to those of Ref. [189] (see their Fig. 6) where model-independent fitting functions are used to determine the best-fit shape of k_H from the JLA sample, SDSS-III BOSS BAO measurements, and differential age measurements of galaxies. In the model-independent determination of k_H in Ref. [189], negative values of k_H are favoured towards lower redshifts as shown in their Fig. 6, consistent with our Fig. 4.2a. Despite these best-fit

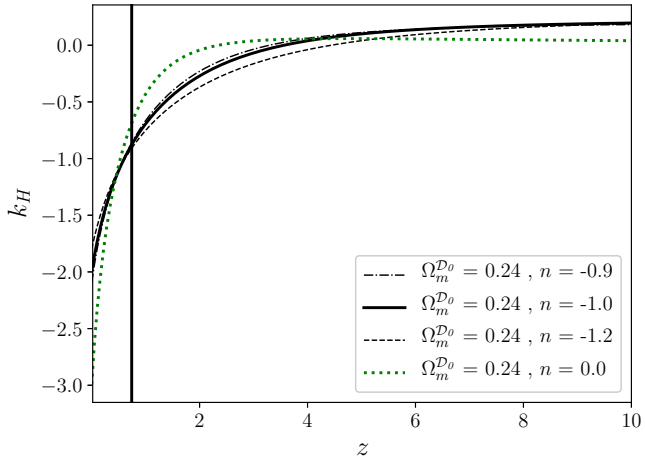

(a) The function k_H, equation (4.26), predicted by the best-fit scaling solution found in this chapter. For a FLRW model universe $k_H = -\Omega_{k_0}$, where Ω_{k_0} is the spatial curvature density parameter evaluated at the present epoch.

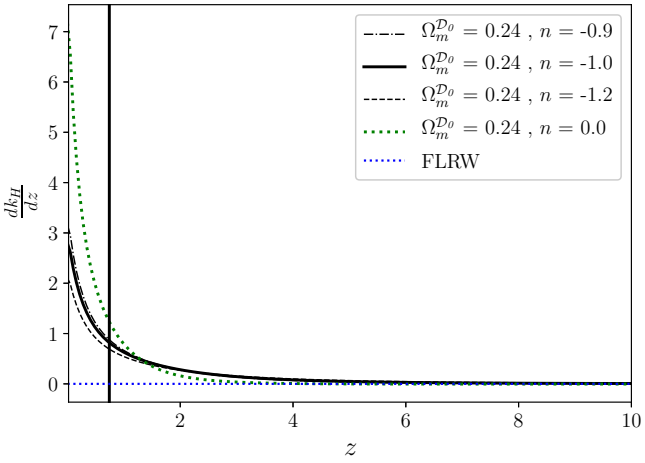

(b) $\mathrm{d}k_H/\mathrm{d}z$ as predicted by the best-fit scaling solution found in this chapter. In a FLRW model universe $\mathrm{d}k_H/\mathrm{d}z = -\mathrm{d}\Omega_{k_0}/\mathrm{d}z = 0$.

Figure 4.2: k_H and $\mathrm{d}k_H/\mathrm{d}z$ as a function of redshift for the best-fit scaling solution, $\{\Omega_m^{\mathcal{D}_0} = 0.24, n = -1.0\}$. The scaling index upper and lower $1\,\sigma$ confidence bounds, $n = -1.0^{+0.7}_{-0.6}$, are shown for fixed $\Omega_m^{\mathcal{D}_0}$. The solution for $\{\Omega_m^{\mathcal{D}_0} = 0.24, n = 0\}$ is shown as well as a reference. The vertical grey line marks the redshift of transition from volume deceleration to volume acceleration as predicted by the best-fit model.

tendencies in Ref. [189], the ΛCDM $k_H = 0$ curvature constraint is still satisfied within

the $2\,\sigma$ confidence intervals of their analysis using present data.

We emphasize that the best-fit scaling index $n = -1.0$ is obtained when assuming the model to be a single-scaling solution. More refined modeling of inhomogeneities, e.g. in terms of two-scale volume partitioning into overdense and underdense regions [190, 191], feature an additional effect due to the expansion variance between the two regions that adds volume acceleration. This feature tends to push the best-fit overall scaling index to values closer to 0, at which backreaction acts as a cosmological constant in the averaged Raychaudhuri equation (4.1).

Although the distance modulus–redshift relation of multi-scale models is different, and thus these refined models cannot be directly compared with the single-scaling solution, we show the reference line $n = 0$ in Fig. 4.2 to illustrate that the $n = 0$ solution closely resembles the solution upper limit of the $1\,\sigma$ confidence interval $n = -0.3$ found in this analysis.

The transition from zero FLRW curvature signature $k_H \sim 0$ to negative FLRW curvature signature $k_H \lesssim -1$ becomes sharper when n tends to zero; it may therefore be easier to observationally distinguish this case from the constant k_H signature of a FLRW model.

One might estimate $k_H(z)$ cosmology-independently by fitting an empirical function, such as a polynomial truncated at some order, with sufficient freedom for luminosity-distance measurements (from e.g. supernova light-curves) and expansion rate measurements (from e.g. BAO analysis and differential age data), respectively, as done in Ref. [189]. It is especially important for this consistency test that the distance and expansion measurements are indeed cosmology-independent and do not rely on fiducial FLRW assumptions, as the procedure might otherwise circularly confirm the FLRW consistency relation.

With next generation data (such as upcoming surveys from LSST and Euclid [15]) the predictions of Fig. 4.2 and complementary distance combinations will be useful for discriminating between the ΛCDM model, the scaling solutions, as well as other models with non-trivial curvature evolution.

[15] See Ref. [192] for performance forecasts for the Euclid satellite and for a discussion of testable alternative frameworks, hereunder backreaction models, to that of the ΛCDM model.

4.5 Discussion

We have investigated the fit of the scaling solutions, which are a class of solutions for the evolution of averaged cosmological variables, constrained by the exact average properties of Einstein's equations and supplemented with a compatible but idealized template metric, to the Joint Light-curve Analysis (JLA) sample of 740 SNIa.

We find constraints that are in good agreement with previously found constraints for the scaling solutions based on SNIa, CMB, the differential age method, and baryon acoustic oscillation measurements in Ref. [131, 175]. Thus, the scaling solutions provide a self-consistent fit to current and complementary cosmological data.

Our result for the scaling index n is consistent with theoretical expectations on the large-scale behaviour of backreaction within an averaged Lagrangian perturbation approach, Ref. [181].

Comparing the quality of fit of the scaling solutions, the ΛCDM model and the timescape model, we find no significant preference of one model over the other from an Akaike Information Criterion (AIC) perspective. The empty universe model is mildly disfavoured when compared to the fit of the other models. This suggests that a broad variety of models of the recent epoch expansion history can match currently available supernova data. More work is needed in order to assess the quality of fit of the scaling solutions relative to that of ΛCDM for complementary cosmological data to that of supernovae.

Backreaction models, exemplified by scaling solutions that match JLA data, predict a clear signature in terms of a particular FLRW curvature consistency measure if compared with the FLRW class of space-times. This indicates that one might be able to significantly discriminate between models with evolving curvature and models with constant-curvature geometry with upcoming surveys using this measure.

Table 4.2: Number of parameters, AIC value, and the AIC relative likelihood for the cosmological models tested, quoted for four different redshift cuts of data. The AIC relative likelihood is shown with the spatially flat ΛCDM model as reference and with the ΛCDM model with free curvature parameter Ω_k as reference respectively. For each redshift cut, the corresponding approximate ΛCDM comoving distance to that redshift is shown in parenthesis. The number of supernovae left in the sample after each redshift cut is also shown.

Models	Scaling solution	Scaling solution $n = -1$	ΛCDM	ΛCDM $\Omega_k = 0$	Empty Universe	Timescape
Number of parameters	10	9	10	9	8	9
	Redshift cut: 0.024 ($\sim$ 70 Mpc/h) - 687 SNIa					
AIC	-213	-215	-214	-216	-217	-215
$p_{\rm model}/p^{\Omega_k=0}_{\Lambda\rm CDM}$	0.5	1.3	0.6	1.0	0.1	1.3
$p_{\rm model}/p_{\Lambda\rm CDM}$	0.8	2.3	1.0	1.8	0.2	2.4
	Redshift cut: 0.033 ($\sim$ 100 Mpc/h) - 655 SNIa					
AIC	-225	-227	-226	-228	-229	-227
$p_{\rm model}/p^{\Omega_k=0}_{\Lambda\rm CDM}$	0.4	1.0	0.5	1.0	0.1	1.0
$p_{\rm model}/p_{\Lambda\rm CDM}$	0.8	2.1	1.0	2.2	0.2	2.1
	Redshift cut: 0.07 ($\sim$ 200 Mpc/h) - 613 SNIa					
AIC	-233	-235	-233	-235	-236	-235
$p_{\rm model}/p^{\Omega_k=0}_{\Lambda\rm CDM}$	0.5	1.4	0.6	1.0	0.4	1.5
$p_{\rm model}/p_{\Lambda\rm CDM}$	0.9	2.5	1.0	1.8	0.7	2.6
	Redshift cut: 0.15 ($\sim$ 500 Mpc/h) - 514 SNIa					
AIC	-197	-199	-197	-199	-195	-199
$p_{\rm model}/p^{\Omega_k=0}_{\Lambda\rm CDM}$	0.3	0.8	0.4	1.0	0.1	0.7
$p_{\rm model}/p_{\Lambda\rm CDM}$	0.8	2.1	1.0	2.7	0.3	1.8

CHAPTER 5

Baryon acoustic oscillation methods for generic curvature: Application to the SDSS-III Baryon Oscillation Spectroscopic Survey

BAO analysis is usually performed assuming a fiducial spatially flat ΛCDM cosmology to transform data into a 'comoving grid', from which the galaxy 2-point correlation function can be estimated and the BAO scale extracted by fitting a fiducial ΛCDM power spectrum [193, 194]. Additional fiducial cosmology analysis steps, such as ΛCDM density-field reconstruction [195], are also often applied. *A priori*, results based on fiducial data-reduction procedures are not valid beyond the given fiducial model, and any extension of such results must be carefully examined for the particular class of models of interest. The extent to which the fiducial ΛCDM results can be applied when considering models with non-trivial spatial curvature is not clear, as the regime of application is usually investigated for FLRW models close to the original fiducial cosmology.

In this chapter we develop methods for using generic metrics to transform galaxy data into a correlation function. Furthermore, we propose and test an empirical fitting procedure with no model assumptions to extract a characteristic scale in the 2-point correlation function. Our fitting procedure can be applied to a large class of cosmological models. We focus on probing a statistical volume-averaged BAO feature. This does not mean that local environmental effects in the BAO feature are unexpected (see, e.g., [196, 197, 198]), but in this chapter we probe the volume-averaged BAO scale for which local effects are marginalised.

We apply our new methods to the CMASS and LOWZ galaxy surveys of the Baryon

Oscillation Spectroscopic Survey 12th Data Release (BOSS DR12). Testing our empirical procedure on ΛCDM BOSS mocks, we recover the BAO scale as the characteristic scale in our empirical fitting function. Our fits to the data using a ΛCDM fiducial cosmology also agree with the results of previous fiducial ΛCDM analyses [193, 194]. We then demonstrate our new methods by self-consistently re-analysing the BOSS dataset assuming the timescape cosmological model.

We summarize the structure of our chapter as follows. In section 5.1.1 we extend the notion of FLRW comoving distances to geodesic distances on preferred spatial hypersurfaces in generic globally hyperbolic space-times in order to calculate the spatial 2-point correlation function for generic models. A restriction to spherical symmetry is then made in order to be able to split small spatial distances into angular and transverse parts, and to associate the redshift with a radial coordinate. The class of models we investigate is detailed in section 5.1.2, and in section 5.1.3 we define an Alcock-Paczyński scaling equivalent to that used in standard BAO analyses for FLRW models (see e.g., [199]). This allows us to parameterise the model cosmology in terms of an underlying 'true' spherically-symmetric metric. The accuracy of the Alcock-Paczyński scaling depends on the models tested and the size of the survey domain. In section 5.2 we present the DR12 CMASS and LOWZ galaxy surveys, random catalogues and simulated mocks used in this analysis. In section 5.3.1 we propose an empirical fitting function for BAO analysis, and in section 5.3.2 we use the ΛCDM mocks to test that we recover the BAO scale for a ΛCDM fiducial cosmology. In section 5.4 we analyse the BOSS DR12 LOWZ and CMASS surveys in both the timescape and ΛCDM cosmologies. We discuss our results and possible extensions in section 5.5.

5.1 Theory

5.1.1 Generalising the comoving distance definition to non-FLRW space-times

In BAO analysis we consider the spatial 2-point correlation function, which describes the excess probability of two galaxies being a certain spatial distance apart as compared to a Poisson point process. We are thus concerned with the *spatial* separation of galaxies, even though we are observing galaxies from a wide range of 'cosmic times' when creating our galaxy catalogues.

However, if we know the (statistical) extension of the galaxy world-lines from the cosmic time of observation, we can map the galaxy distribution on our null cone to a spatial hypersurface of reference. In FLRW cosmology this is done by tracking the galaxies through their comoving coordinates. One can then define spatial comoving distances between the galaxies at the present epoch, and recover the distances at any other reference hypersurface via multiplication by the homogeneous scale factor. For general globally hyperbolic space-times we can also track the galaxy distribution in comoving coordinates to a reference hypersurface, on which we can compute the shortest spatial distances between galaxy pairs that are analogous to FLRW comoving separations.

We consider a globally hyperbolic space-time, and assume that the vorticity of the matter distribution in this space-time can be ignored[1], and that caustics in the matter distribution can be ignored at the coarse-graining level and over the timescale considered. The metric can then in general be written in Gaussian normal coordinates, $x^\mu = (t, x^i)$,

$$ds^2 = -\alpha^2 c^2\, dt^2 + g_{ij}\, dx^i\, dx^j \tag{5.1}$$

where x^i are comoving coordinates labelling the fluid elements of the matter distribution, t labels the hypersurfaces normal to the fluid flow,[2] g_{ij} is the metric adapted to the hypersurfaces defined by $t =$ constant, and $\alpha\, dt$ is the proper time measure on the particle worldlines.

Consider two particles (galaxies) at space-time events P_1 and P_2 with coordinates $x_1^\mu(P_1) = (t_1, x_1^i)$ and $x_2^\mu(P_2) = (t_2, x_2^i)$. We would like to define the shortest spatial distance between the two particles on a reference hypersurface $t = T$. Since the particles are by construction moving on lines of constant comoving coordinates, we can extend the particles to the reference hypersurface $t = T$. We keep the comoving coordinates x_1^i and x_2^i fixed, and consider the new space-time events $P_{1,T}$ and $P_{2,T}$ with

[1] This assumption is made in order to define reference hypersurfaces orthogonal to the fluid frame. However, nothing prevents us from mapping the galaxy distribution to generic spatial hypersurfaces of the given space-time, allowing for a generalisation of the present procedure to the case of vorticity in the matter distribution.

[2] For simplicity we consider model universes where all relevant matter is in the same rest frame. This is never entirely true. The present procedure can easily be generalised to handle multicomponent fluids by simply choosing one of the fluids as a reference fluid for constructing hypersurfaces of reference.

coordinates $x^{\mu}_{1,T}(P_{1,T}) = (T, x^i_1)$ and $x^{\mu}_{2,T}(P_{2,T}) = (T, x^i_2)$. From the metric eq. (5.1) we can compute the shortest spatial distance between $P_{1,T}$ and $P_{2,T}$ on the surface $t = T$ from the geodesic equation of the adapted metric

$$ds^2_T = g_{ij}(t = T, x^k)dx^i dx^j. \tag{5.2}$$

We denote the resulting shortest distance, $D_T(P_1, P_2)$, the Lagrangian distance between P_1 and P_2 at the reference surface $t = T$. This Lagrangian distance definition reduces to the comoving distance definition in FLRW cosmology, when the matter frame coincides with the surfaces of homogeneity and isotropy.

5.1.2 Models under investigation

In this section we outline the assumptions regarding the class of cosmological models for which the procedures outlined in sections 5.1.3 and 5.3.1 apply. The motivation for restricting the class of models is to be able to parameterise different cosmological models in terms of each other through an Alcock-Paczyński scaling, as outlined in section 5.1.3 (see e.g., [199]). We note that the results of the data analysis in the present chapter can be applied *only* to the class of models discussed here.[3]

As in section 5.1.1, we consider globally hyperbolic average space-times, in which vorticity and caustics of the matter distribution can be neglected. We can write the metric in such a space-time as in eq. (5.1). We are interested in using this metric to describe the distances between galaxies within a given survey in a statistical sense. Thus, we need to write the metric in terms of coordinates (z, θ, ϕ) of the average model to which the observed redshifts, and angular positions of galaxies are mapped.

Suppose that we have a set of comoving coordinates (r, θ, ϕ), where θ and ϕ are mapped to the observed angles, and where r is a radial coordinate. For simplicity we shall assume spherical symmetry in (θ, ϕ) such that the adapted metric eq. (5.1) can be written

$$ds^2 = -\alpha(t, r)^2 c^2 dt^2 + g_{rr}(t, r)\, dr^2 + g_{\theta\theta}(t, r)\left(d\theta^2 + \cos^2(\theta) d\phi^2\right) \tag{5.3}$$

where $\cos^2(\theta)$ comes from the convention in the definition of the declination angle. The

[3] The standard BAO results such as [194, 193] are also limited by the regime of applicability of the AP-scaling.

redshift z of radially propagating null rays, $\alpha(t,r)^2dt^2 = g_{rr}(t,r)dr^2$, can therefore be considered as a function of either t or r (since t and r are monotonic functions of each other on radial null lines). Note that since the metric (5.3) only applies to average light propagation over large cosmic distances, z is an *average* model parameter. Although z is not directly observable, it is assumed to be a good approximation for the *mean* observed redshift. We consider universes that are overall expanding, and neglect the small scale collapse of structures that can cause the redshift to be multivalued along the null rays[4]. In such model-universes it is reasonable to assume that z is a strict monotonic function in t (and therefore also in r)[5]. In this case, we can treat z as a radial coordinate on the spatial sections $t = T$ and write the adapted metric (5.2) as[6]

$$ds_T^2 = g_{zz}(t = T, r)dz^2 + g_{\theta\theta}(t = T, r)\left(d\theta^2 + \cos^2(\theta)d\phi^2\right), \tag{5.4}$$

where[7]

$$g_{zz}(t = T, r) \equiv g_{rr}(t = T, r)\left(\frac{dr}{dz}\right)^2. \tag{5.5}$$

The BAO scale is a statistical standard ruler, and in practice the 2-point correlation function probing the BAO scale is obtained by summing over many galaxy pairs. Thus, it is reasonable to consider models with large smoothing scale compared to galaxy pair separations of order the BAO scale $\sim$ 100Mpc/h. In particular, we only discuss models in which the typical pair separation of galaxies surveyed is small compared to variations of the adapted spatial metric (5.2), as detailed in appendix 5.A. In these cases we can approximate the Lagrangian distance $D_T(P_1, P_2)$ for two galaxies with coordinates

[4] See section 3 of [200] for relevant calculations of mean redshift in statistically homogeneous and isotropic space-times, and section 3.2 in particular for a discussion of multivaluedness of redshift along light cones in relation to statistical homogeneity and isotropy.

[5] The monotonicity assumption is independent of the exact parameterisation, t, of the fluid-adapted foliation. Since t labels surfaces normal to the averaged fluid flow, we have $\boldsymbol{u} \propto \boldsymbol{\nabla} t$, where $\boldsymbol{u}$ is the averaged fluid 4-velocity, and t is unique up to transformations $t \to f(t)$ by a monotonic function f. Any function z that is monotonic in t will be monotonic in $f(t)$.

[6] Since the redshift, z, is only defined along the radial null geodesics it is important to realise that (5.4), (5.5) is a *projection* from the null cones onto fiducial spatial hypersurfaces, *not* a global coordinate transformation in the original space-time (5.3).

[7] In any spatially flat FLRW model, with $t = T$ corresponding to the 'present time' hypersurface, we have $g_{rr}(t = T, r) = a(t = T)^2 = 1$ and $g_{zz}(t = T, r) = \left(\frac{dr}{dz}\right)^2 = (c/H)^2$, where $a(t)$ is the scale factor, and we have used the convention $a(t = T) = 1$.

(z_1, θ_1, ϕ_1) and (z_2, θ_2, ϕ_2) separated by redshift $\delta z = z_2 - z_1$ and angle $\delta\Theta$

$$\begin{aligned} \delta\Theta &= \arccos\left[\sin(\theta_1)\sin(\theta_2) + \cos(\theta_1)\cos(\theta_2)\cos(\phi_2 - \phi_1)\right] \\ &\approx \sqrt{(\theta_2 - \theta_1)^2 + \cos^2(\bar{\theta})(\phi_2 - \phi_1)^2}, \qquad \bar{\theta} = (\theta_1 + \theta_2)/2 \end{aligned} \tag{5.6}$$

as

$$D_T^2(P_1, P_2) \approx g_{zz}(t = T, \bar{z})(\delta z)^2 + g_{\theta\theta}(t = T, \bar{z})(\delta\Theta)^2, \tag{5.7}$$

where $\bar{z} = (z_1 + z_2)/2$ is the intermediate redshift.

The validity of the approximation of eq. (5.7) is cosmology-dependent[8], and must be assessed for the particular class of model cosmologies of interest. In appendix 5.A we give the explicit expansion of the geodesic path integral up to third order, and in appendix 5.A.1 we apply our results to spherically-symmetric metrics. For the FLRW and timescape models with reasonable model parameters, we find that higher-order corrections to eq. (5.7) are of order $\lesssim 10^{-3}$ for Lagrangian galaxy separations of order 100 Mpc/h.

It will be convenient to define

$$\mu_T(P_1, P_2) = \frac{\sqrt{g_{zz}(t = T, \bar{z})(\delta z)^2}}{D_T(P_1, P_2)} \tag{5.8}$$

as the 'radial fraction' of the separation. Note that such a splitting into the radial and transverse components of a geodesic distance is not meaningful for general metrics. However, when the approximation of eq. (5.6) is valid, such an Euclidean notion still applies.

Conventionally, the surface of evaluation $t = T$ is taken to be the present day. Whenever we refer to evaluation at the present day we shall omit the T subscript on eq. (5.7) and (5.8). For ease of notation the dependence on the points of the galaxies

[8] The validity of the approximation relies on second order variations of the metric (curvature degrees of freedom) being small as compared to the metric and its first order variations in the adapted coordinate-system (z, θ, ϕ) over scales of the galaxy pair separations of interest (see appendix 5.A). Examples of models with significant spatial curvature for which eq. (5.7) apply to a good approximation for galaxy pair separations of order $\sim$ 100Mpc/h are the empty Milne universe (FLRW with $\Omega_M = \Omega_\Lambda = 0$, $\Omega_k = 1$) and the timescape model, which have significant metric variations only on scales ${}^3\mathcal{R}^{-1/2} \sim c/H_0 \sim 3$ Gpc/h at the present epoch, where ${}^3\mathcal{R}$ is the spatial Ricci scalar of the given model.

will also be implicit, and we will just write D and μ respectively.

5.1.3 Alcock-Paczyński scaling

In the later analysis it will be convenient to parameterise the model cosmology in terms of an unknown 'true' cosmology. We will assume that the universe is well-described by a 'true' metric of the form in section 5.1.2, and that we have a model cosmology also of the form outlined in section 5.1.2, but not necessarily with the same adapted metric.

We can write the model Lagrangian distance between two galaxies eq. (5.7) at mean redshift $\bar{z}_i$ and separation δz_i, $\delta\Theta_i$ on the sky in terms of the 'true' distance measures

$$\begin{aligned}(D_{T,i})^2 &\approx g_{zz}(t=T,\bar{z}_i)(\delta z_i)^2 + g_{\theta\theta}(t=T,\bar{z}_i)(\delta\Theta_i)^2 \\ &= \frac{1}{\alpha_{\parallel,i}^2} g^{\rm tr}_{zz}(t^{\rm tr}=T^{\rm tr},\bar{z}_i)(\delta z_i)^2 + \frac{1}{\alpha_{\perp,i}^2} g^{\rm tr}_{\theta\theta}(t^{\rm tr}=T^{\rm tr},\bar{z}_i)(\delta\Theta_i)^2\end{aligned} \tag{5.9}$$

where 'tr' stands for the 'true' cosmology, the index i labels the galaxy pair, and

$$\alpha_{\parallel,i} \equiv \sqrt{\frac{g^{\rm tr}_{zz}(t^{\rm tr}=T^{\rm tr},\bar{z}_i)}{g_{zz}(t=T,\bar{z}_i)}}, \qquad \alpha_{\perp,i} \equiv \sqrt{\frac{g^{\rm tr}_{\theta\theta}(t^{\rm tr}=T^{\rm tr},\bar{z}_i)}{g_{\theta\theta}(t=T,\bar{z}_i)}} \tag{5.10}$$

are the Alcock-Paczyński (AP) scaling parameters. Note that we are comparing a reference hypersurface of the 'true' cosmology $t^{\rm tr}=T^{\rm tr}$ to the reference hypersurface $t=T$ of the model cosmology, by associating points of the same observational coordinates (z,θ,ϕ).

Each galaxy pair will be associated with its own unique scalings of eq. (5.10). For sufficiently small volume of the galaxy survey considered, we might approximate the individual distortion parameters by one global scaling $\alpha_\parallel$, $\alpha_\perp$ to lowest order. This is a reasonable approximation if the survey volume has a relatively narrow redshift distribution, and if both the 'true' and the model metric are slowly changing in redshift. As a rule of thumb, the narrower the redshift distribution, and the larger the curvature scales of the models of interest, the better the global scaling approximation is. In the present chapter we use the global AP-scaling as a rough tool for testing consistency of the investigated fiducial cosmologies, keeping in mind the limitations of this approximation.

We can define the 'isotropic scaling' α and the 'anisotropic scaling' ϵ

$$\alpha \equiv (\alpha_\perp^2 \alpha_\parallel)^{1/3}, \qquad (1+\epsilon)^3 \equiv \frac{\alpha_\parallel}{\alpha_\perp}. \tag{5.11}$$

Such a decomposition will be useful in the following analysis, since in an isotropically-sampled galaxy distribution we expect the BAO feature to be degenerate with α and not ϵ. (See section 5.3.1 for explicit expressions in the context of the particular fitting function used in this analysis.) We note that α and ϵ as defined in eq. (5.11) are analogous to the AP-scaling parameters outlined in, e.g., [199], when associating g_{zz} with the inverse Hubble parameter multiplied by the speed of light c/H and $g_{\theta\theta}$ with the angular diameter distance D_A.

The isotropic scaling α describes how the volume measure of a small coordinate volume $\delta z\, \cos(\theta)\, \delta\theta\, \delta\phi$ differs to lowest order between the 'true' and the model cosmology,

$$\alpha \approx \left(\frac{\delta V_i^{\rm tr}(t^{\rm tr} = T^{\rm tr}, \bar{z}_i)}{\delta V_i(t = T, \bar{z}_i)} \right)^{1/3} = \left(\frac{g_{zz}^{\rm tr}(t^{\rm tr} = T^{\rm tr}, \bar{z}_i)\, (g_{\theta\theta}^{\rm tr}(t^{\rm tr} = T^{\rm tr}, \bar{z}_i))^2}{g_{zz}(t = T, \bar{z}_i)\, (g_{\theta\theta}(t = T, \bar{z}_i))^2} \right)^{1/6} \tag{5.12}$$

with

$$\delta V_i(t = T, \bar{z}_i) \equiv \sqrt{\det(g)(t = T, \bar{z}_i)}\, \delta z\, \delta\theta\, \delta\phi, \tag{5.13}$$

where $\det(g)$ is the determinant of the spatial metric (5.4) in the coordinate basis (z, θ, ϕ).

It will prove convenient to parameterise α and ϵ of two model cosmologies in terms of the relative transverse and radial distance measures of the models

$$\begin{aligned} \alpha_1 &= \alpha_2 \left(\frac{g_{2,zz}(t_2 = T_2, \bar{z})}{g_{1,zz}(t_1 = T_1, \bar{z})} \right)^{1/6} \left(\frac{g_{2,\theta\theta}(t_2 = T_2, \bar{z})}{g_{1,\theta\theta}(t_1 = T_1, \bar{z})} \right)^{1/3} \\ \epsilon_1 &= (1+\epsilon_2) \left(\frac{g_{2,zz}(t_2 = T_2, \bar{z})}{g_{1,zz}(t_1 = T_1, \bar{z})} \right)^{1/6} \left(\frac{g_{2,\theta\theta}(t_2 = T_2, \bar{z})}{g_{1,\theta\theta}(t_1 = T_1, \bar{z})} \right)^{-1/6} - 1. \end{aligned} \tag{5.14}$$

Knowing α (ϵ) within a reference/fiducial cosmology, we can calculate α (ϵ) within a different cosmology from the known model distance measures using the identity in eq. (5.14).

From the assumption of slowly varying $\alpha_\perp$ and $\alpha_\parallel$ over the survey volume we can

approximate

$$(D_{T,i})^2 \approx \frac{1}{\alpha_\parallel^2} g_{zz}^{\rm tr}(t^{\rm tr} = T^{\rm tr}, \bar{z}_i)(\delta z_i)^2 + \frac{1}{\alpha_\perp^2} g_{\theta\theta}^{\rm tr}(t^{\rm tr} = T^{\rm tr}, \bar{z}_i)(\delta\Theta_i)^2, \tag{5.15}$$

which we can invert to $D^{\rm tr}_{T^{\rm tr}}$ approximated in terms of D_T, μ_T, and the global Alcock-Paczyński scaling parameters $\alpha_\parallel$, $\alpha_\perp$.

$$\begin{aligned}(D^{\rm tr}_{T^{\rm tr},i})^2 &\approx g_{zz}^{\rm tr}(t^{\rm tr} = T^{\rm tr}, \bar{z}_i)(\delta z_i)^2 + g_{\theta\theta}^{\rm tr}(t^{\rm tr} = T^{\rm tr}, \bar{z}_i)(\delta\Theta_i)^2 \\ &\approx \alpha_\parallel^2 g_{zz}(t = T, \bar{z}_i)(\delta z_i)^2 + \alpha_\perp^2 g_{\theta\theta}(t = T, \bar{z}_i)(\delta\Theta_i)^2 \\ &= \alpha_\perp^2 (D_{T,i})^2 \left(1 + \left(\frac{\alpha_\parallel^2}{\alpha_\perp^2} - 1\right)\mu_{T,i}\right) \\ &= \alpha^2 (D_{T,i})^2 \left(\frac{\alpha_\perp}{\alpha_\parallel}\right)^{2/3} \left(1 + \left(\frac{\alpha_\parallel^2}{\alpha_\perp^2} - 1\right)\mu_{T,i}^2\right),\end{aligned} \tag{5.16}$$

where the definition of μ_T in eq. (5.8) has been used. Similarly we have for $\mu^{\rm tr}$

$$\mu^{\rm tr}_{T^{\rm tr},i} = \frac{\sqrt{g_{zz}^{\rm tr}(t^{\rm tr} = T^{\rm tr}, \bar{z}_i)(\delta z_i)^2}}{D^{\rm tr}_{T,i}} \approx \frac{\alpha_\parallel}{\alpha_\perp}\mu_{T,i}\frac{1}{\sqrt{1 + \left(\frac{\alpha_\parallel^2}{\alpha_\perp^2} - 1\right)\mu_{T,i}^2}}. \tag{5.17}$$

5.1.4 Overview of the timescape model

In the present analysis we apply our methods to the spatially flat ΛCDM and the timescape cosmologies. Both models are part of the class described in section 5.1.2, and we can therefore test them with the procedures outlined in this chapter.

The relevant distance measures in the ΛCDM model and the timescape model are given in appendix 3.A. Here we wish to illustrate these distance measures for the parameter values used in this analysis.

In the present chapter we aim to demonstrate feasibility of the method, by making just one choice of the timescape dressed present epoch matter density parameter (see 3.19) and the ΛCDM present epoch matter density parameter respectively. We denote both parameters by the symbol Ω_{M0} and choose the value of investigation to be $\Omega_{M0} = 0.3$. It should be stressed that the matter density parameters of timescape and ΛCDM do not have identical interpretation, and the common symbol is for convenience in the notation. For instance, the dressed matter parameter in the timescape case does

not enter any Friedmann-like Hamiltonian constraint equation. The value $\Omega_{M0} = 0.3$ chosen for this analysis is a reasonable one in the timescape case [98, 127], but not singled out as a best fit in other tests [180].

Figure 5.1 shows $\sqrt{g_{\theta\theta}}$ and $\sqrt{g_{zz}}$ of eq. (5.4) for the timescape and ΛCDM models with $\Omega_{M0} = 0.3$ relative to the empty universe. The same global Hubble parameter H_0 is assumed for all three models. Since $d_A \equiv \sqrt{g_{\theta\theta}(t = t_0, r(t))}/(1+z)$ is the angular diameter distance, while $d_H \equiv \sqrt{g_{zz}(t = t_0, r(t))}/(1+z)$ represents the projected radial proper distance between two particles separated by a small distance δz in redshift (in FLRW cosmology known as the 'Hubble distance'), these quantities represent the standard angular and radial distance measures.

The timescape model redshift–distance relation is closer to that of the empty universe than to ΛCDM for redshifts $z \lesssim 1$. While the timescape model distance measures are within $\sim 2\%$ of the empty universe case, the ΛCDM model differs from the empty universe by up to $\sim 15\%$ in the redshift range $0.15 \leq z \leq 0.7$.[9] The low-redshift proximity of the timescape model expansion history to that of the empty universe reflects the late-epoch volume dominance of voids relative to gravitationally-bound structures, which in the timescape model gives rise to a present-day on average negatively-curved universe. Given this comparison, BOSS large-scale structure data has the potential to distinguish between these scenarios.

The timescape model is currently much less experimentally constrained than the ΛCDM model [98, 127], since a perturbation theory describing structure formation within the timescape model has yet to be developed. As a consequence CMB constraints on the BAO scale are much less precise for timescape as compared to ΛCDM. (One can fit the angular positions of the acoustic peaks CMB using conservative priors for the baryon-to-photon ratio, following an equivalent procedure to that described in appendix D of [180].) This makes the ϵ parameter the most powerful discriminator between the timescape model and ΛCDM, in the context of the present analysis.

[9] These percentage estimates would in general change for distances measured in units of Mpc (rather than units of Mpc/h) for reasonable values of H_0 of the individual models. Typical values of H_0 for the timescape model are around 10% smaller than for the ΛCDM model.

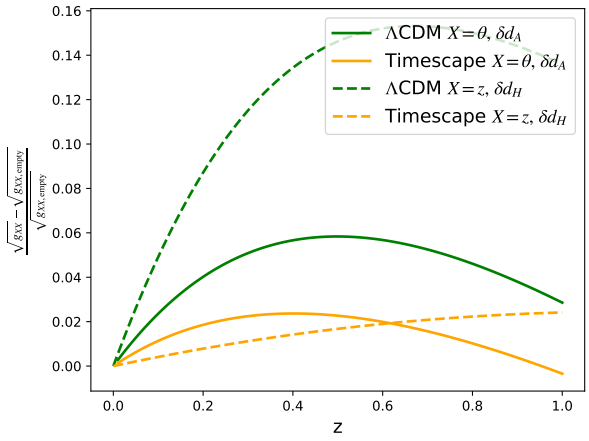

Figure 5.1: ΛCDM $\Omega_{M0} = 0.3$ and timescape dressed $\Omega_{M0} = 0.3$ radial and transverse distance measures, relative to the empty universe distance measures, as a function of redshift z. The axis $(\sqrt{g_{XX}} - \sqrt{g_{XX,\mathrm{empty}}})/\sqrt{g_{XX,\mathrm{empty}}}$ represents the fractional difference of the angular diameter distance and radial Hubble distances for ΛCDM and timescape relative to an empty universe for an observer at the present epoch, assuming the same value of the Hubble parameter for all three models. I.e., when $X = \theta$ it corresponds to $\delta d_A \equiv (d_A - d_{A,\mathrm{empty}})/d_{A,\mathrm{empty}}$ and when $X = z$ it corresponds to $\delta d_H \equiv (H^{-1} - H^{-1}_{\mathrm{empty}})/H^{-1}_{\mathrm{empty}}$.

5.1.5 The Landy-Szalay estimators

The 2-point correlation function in cosmology (see for example [52]) describes the excess in correlation between structure in a spatial section of the universe, relative to the case in which matter is distributed according to an uncorrelated Poisson process. Thus the 2-point correlation function describes characteristic scales in the matter distribution.

The spatial 2-point correlation function is defined as

$$\xi(X,Y) = \frac{f(X,Y)}{f(X)f(Y)} - 1 \tag{5.18}$$

where $f(X,Y)$ is the ensemble probability density of finding two galaxies at points X and Y, and $f(X)$ is the uncorrelated probability density of finding a galaxy at point X. By assuming that the galaxy distribution is well-described by a homogeneous and

isotropic point process, eq. (5.18) reduces to

$$\xi(D) = \frac{f(D)}{f_{\text{Poisson}}(D)} - 1, \tag{5.19}$$

where D is the Lagrangian distance of the 'true' underlying metric between the points X, Y defined in section 5.1.1, $f(D)$ represents the probability density of finding two objects with the mutual distance D, and $f_{\text{Poisson}}(D)$ represents the analogous probability density in the uncorrelated case. Note that we can define a correlation function with a similar form to eq. (5.19) for an inhomogeneous and anisotropic point process by marginalising over the position and direction degrees of freedom in $f(X, Y)$ (see appendix 5.B). For a given spherically-symmetric metric, where in addition to the Lagrangian distance D we can define the radial fraction of the separation μ (see section 5.1.2), it will be convenient to define the correlation function analogous to eq. (5.19),

$$\xi(D, \mu) = \frac{f(D, \mu)}{f_{\text{Poisson}}(D, \mu)} - 1, \tag{5.20}$$

parameterised by μ and D. (See appendix 5.B for details.)

Various estimators of the 2-point correlation function have been tested within ΛCDM [201]. An efficient estimator is found to be the Landy-Szalay (LS) estimator [202]

$$\hat{\xi}_{LS}(D, \mu) = \frac{DD(D, \mu) + RR(D, \mu) - 2DR(D, \mu)}{RR(D, \mu)}, \tag{5.21}$$

where DD is the binned normalised number count

$$DD(D, \mu) = \frac{1}{N_D(N_D - 1)} \sum_{a,b}^{N_D} \mathbb{1}_{D \pm \Delta D}(D(x_a^i, x_b^i)) \mathbb{1}_{\mu \pm \Delta\mu}(\mu(x_a^i, x_b^i)) \tag{5.22}$$

over galaxies in the survey, where N_D is the total number of galaxies, and ΔD and $\Delta\mu$ are the binning size, and $\mathbb{1}_A(y)$ is the indicator function, having the value 1 for $y \in A$ and 0 for $y \notin A$. RR is defined in the same way

$$RR(D, \mu) = \frac{1}{N_R(N_R - 1)} \sum_{a,b}^{N_R} \mathbb{1}_{D \pm \Delta D}(D(x_a^i, x_b^i)) \mathbb{1}_{\mu \pm \Delta\mu}(\mu(x_a^i, x_b^i)), \tag{5.23}$$

except that the sum is now over N_R artificial galaxies in a random Poisson catalogue, designed to match the galaxy density of the galaxy survey. We also define DR, the normalised cross pair-count between the galaxy catalogue and the random sample, by

$$DR(D,\mu) = \frac{1}{N_D N_R} \sum_a^{N_D} \sum_b^{N_R} \mathbb{1}_{D\pm\Delta D}(D(x_a^i, x_b^i)) \mathbb{1}_{\mu\pm\Delta\mu}(\mu(x_a^i, x_b^i)) \tag{5.24}$$

We will use the LS estimator (5.21) to estimate the underlying 2-point correlation function in this chapter. It will be convenient to average this estimator in μ to obtain the wedge LS estimator,

$$\hat{\xi}_{LS[\mu_1,\mu_2]}(D) = \frac{1}{\mu_2 - \mu_1} \int_{\mu_1}^{\mu_2} d\mu\, \hat{\xi}_{LS}(D,\mu). \tag{5.25}$$

We define the isotropic wedge $\hat{\xi}(D)$, the transverse wedge $\hat{\xi}_\perp(D)$ and radial wedge $\hat{\xi}_\parallel(D)$ estimator as respectively

$$\hat{\xi}(D) \equiv \hat{\xi}_{LS[0,1]}(D), \qquad \hat{\xi}_\perp(D) \equiv \hat{\xi}_{LS[0,0.5]}(D), \qquad \hat{\xi}_\parallel(D) \equiv \hat{\xi}_{LS[0.5,1]}(D) \tag{5.26}$$

where we have dropped the subscript LS.

5.2 Galaxy surveys, random catalogues, and mocks

In this section we describe the datasets (observed and simulated) used in this analysis. Since the 2-point correlation function is defined as an excess probability of the correlation of galaxies compared to an unclustered Poisson distribution, we also use a random catalogue to construct the Landy-Szalay estimators (5.26). We use mock catalogues to test our analysis methods in a fiducial ΛCDM cosmology, and to estimate the covariance of our measurements.

5.2.1 The galaxy surveys

The Sloan Digital Sky Survey (SDSS) III [203] is a large spectroscopic redshift survey performed at the Apache Point Observatory in New Mexico. SDSS contains the Baryon Oscillation Spectroscopic Survey (BOSS) [204] of Luminous Red Galaxies (LRGs), which constitutes the current largest-volume map of large-scale structure, spanning

the approximate redshift range $0.1 \leq z \leq 0.7$ across 10,000 deg^2 of sky. Different colour and magnitude cuts are used to select homogeneous galaxy types across redshift ranges $0.15 \leq z \leq 0.43$ (the LOWZ sample) and $0.43 \leq z \leq 0.7$ (the CMASS sample). The samples are split into disconnected sub-surveys containing the galaxies from the North Galactic Cap (NGC) and South Galactic Cap (SGC).

We use the BOSS Data Release 12 (DR12) [205] in this analysis. Each of the galaxies is labelled by observed coordinates (z, θ, ϕ), where z is the observed redshift, θ is the angle of declination and ϕ is the angle of right ascension. The redshift distribution of the surveys is shown in figure 5.2. The total number of galaxies contained in our selected redshift intervals is 361,762 for LOWZ and 777,202 for CMASS.

We do *not* use a reconstruction procedure of peculiar motions of galaxies such as the one described in [195]. Such a procedure reconstructs the displacements of galaxies relative to a ΛCDM background based on the density field of the survey, using the relation between the linear density field and velocity fields in ΛCDM perturbation theory. Such a perturbation theory has not yet been developed for the timescape cosmology, so we do not apply it in our analysis.

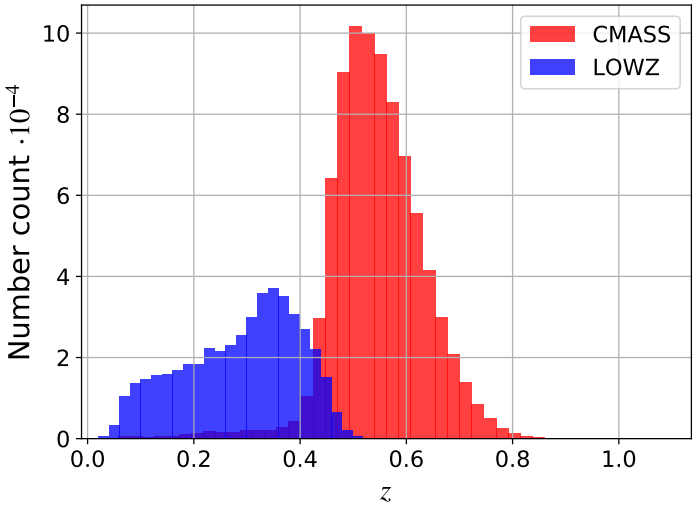

Figure 5.2: Redshift distribution of CMASS (red) and LOWZ (blue).

In computing the spatial 2-point correlation function, we make use of the cosmology-independent 'total galaxy weights' (or completeness weights) described by [206]. These weights are designed to account for observational biases, in order to make the observed

galaxy distribution an unbiased estimate of the underlying galaxy distribution. For example, neighbours to galaxies for which redshift determination failed are up-weighted in order to compensate for the missing galaxy in the sample. We do not use Feldman, Kaiser & Peacock (FKP) weights (see [207, 206]), since they are derived in the context of a fiducial cosmological model. However, the application of FKP weights does not significantly affect acoustic peak measurements in BOSS.

5.2.2 The random catalogues

We use random catalogues generated from the CMASS and LOWZ galaxy distributions as described by [206]. The random catalogues are generated independently of a cosmological model and are based solely on the distribution of the galaxies in observed coordinates (z, θ, ϕ). The random catalogue uniformly samples the angular coverage of the data, and random redshifts are assigned from the redshift probability distribution of the survey. We use a random catalogue 10 times the size of the given galaxy catalogue or mock.

5.2.3 The mocks

The errors in the correlation function used in BAO analysis can be estimated in the context of a fiducial ΛCDM cosmology using theory or simulations. Alternatively, non-parametric methods such as jack-knife estimation can be applied.

The assumption of a fiducial cosmology in error analysis is not satisfying from the point of view of investigating a broader class of models than the fiducial cosmology. However, in practice non-parametric methods are hard to implement, as the assumptions underlying them cannot be satisfied for current galaxy surveys. To apply jack-knife variance estimation we must be able to divide our sample into a (large) number of subsamples that are well approximated as resulting from identical and independent probability distributions, i.e., we must be able to view the regions as realisations of an ensemble. Furthermore, jack-knife regions must be sufficiently large to contain enough galaxy pairs separated by the relevant scales, which conflicts with the requirement that the number of jack-knife regions must be sufficiently large to allow an accurate inverse covariance matrix to be constructed.

We instead use the Quick Particle Mesh (QPM) mocks as described in detail in [208] for error analysis. These mocks are based on ΛCDM N-body simulations, and

are generated specifically for the BOSS clustering analysis. The number density in the mock catalogues is designed to match the observed galaxy number density of the BOSS catalogues, and to follow the radial and angular selection functions of BOSS. The fiducial ΛCDM cosmology of the QPM simulations is

$$\Omega_{M0} = 0.29, \quad \Omega_{\Lambda 0} = 0.71, \quad \Omega_{b0} = 0.048, \quad \sigma_8 = 0.8, \quad h = 0.7, \tag{5.27}$$

where Ω_{M0}, $\Omega_{\Lambda 0}$ and Ω_{b0} are the present epoch matter density parameter, dark energy density parameter, and baryonic matter density parameter respectively, σ_8 is the root mean square of the linear mass fluctuations at the present epoch averaged at scales 8 Mpc/h given by the integral over the ΛCDM power spectrum, and $H_0 = 100\,h$ km/s/Mpc is the Hubble parameter evaluated at the present epoch. The sound horizon at the drag epoch within this model is $r_s = 103.05$ Mpc/h.

There are 1000 QPM mocks available. We use all of these to construct an approximate covariance matrix of the measured galaxy correlation function. Furthermore, we use these mocks to test how well our empirical procedure can recover the input acoustic scale and the anisotropic distortion in the fiducial ΛCDM cosmology with parameters (5.27).

5.3 Empirical model for the correlation function, and extraction of the BAO characteristic scale

Conventional ΛCDM BAO fitting procedures [194, 193] involve the construction of a template power spectrum model motivated by ΛCDM perturbation theory. We cannot necessarily apply these techniques in more general cosmological models. In this section we therefore develop an empirical approach for fitting the baryon acoustic oscillation feature in models with non-trivial curvature, where we do not have a model for the shape of the correlation function, but where we nevertheless expect a characteristic scale in the matter distribution to be sourced from early-universe oscillations of the baryonic plasma.

In our analysis we will leave the Hubble constant free to vary and extract the BAO scale in units Mpc/h, rather than fixing h independently to some particular value. Our key fitted parameter, ϵ, is dimensionless and independent of H_0. In future analysis we

aim to obtain independent constraints on both Ω_{M0} and H_0 from joint BAO and CMB observations; Ω_{M0} is just fixed in the present chapter to develop the methodology.

5.3.1 The fitting function

The simplest model-independent form we might consider for the BAO correlation function is the superposition of a Gaussian and a featureless (e.g., polynomial) fitting function. Such empirical models have been considered in e.g., [209, 210, 211]. For a universe with statistical homogeneity and isotropy, we expect the BAO characteristic scale to be statistically independent of the direction of separation of the galaxies relative to our position, up to observational biases such as redshift-space distortions and non-representative sampling of the underlying galaxy distribution. These considerations motivate the following empirical model as a function of the Lagrangian separation D and radial fraction μ:

$$\xi_{Fit}(D^{\rm tr},\mu^{\rm tr}) = (D^{\rm tr})^2 A \exp\left[\frac{-\left(D^{\rm tr}-r_{\rm BAO}\right)^2}{2\sigma^2}\right] + C_0(\mu^{\rm tr}) + \frac{C_1(\mu^{\rm tr})}{D^{\rm tr}} + \frac{C_2(\mu^{\rm tr})}{(D^{\rm tr})^2} \quad (5.28)$$

where the superscript 'tr' refers to the underlying 'true' cosmology. The polynomial terms model the underlying featureless shape of the correlation function without the BAO feature and are equivalent in form to those of [193]. The scaled Gaussian empirically models the BAO feature, and replaces the ΛCDM power spectrum model of [193].

We note that the local maximum of the 2-point correlation function at the BAO peak does not in general correspond to the BAO scale in a particular cosmological model (for example, these two characteristic scales differ by $\sim 2-3\%$ in ΛCDM cosmology, a systematic difference which is significantly larger than the statistical measurement error in the scale). This is a significant issue for empirical modelling, if we wish to incorporate predictions of the underlying BAO scale.

To partially address this issue, we include a factor $(D^{\rm tr})^2$ multiplying the Gaussian term in eq. (5.28), which changes the position of the local maximum in order to produce a closer match to the expected fiducial characteristic scale $r_{\rm BAO}$ of the ΛCDM mock catalogues, within the current level of statistical precision. This calibration would need

to be re-assessed in the context of other cosmological models.[10] Furthermore, we do not assume any calibration of $r_{\rm BAO}$ in this study, instead quoting results for $r_{\rm BAO}/\alpha$, and focus our investigation on the significance of the BAO feature and the self-consistency of the radial and transverse wedges.

We allow for $\mu^{\rm tr}$ dependence in the polynomial terms of the fitting function (5.28) since observational biases such as redshift-space distortions can depend on the separation of the galaxies relative to the line of sight. We assume that the BAO feature is independent of $\mu^{\rm tr}$, although asymmetric biases might enter here as well. However, from our mock investigations (see section 5.3.2) we find that we successfully recover the BAO scale and the distortion parameter ϵ with the fitting function (5.28), justifying this form at least for the ΛCDM model.

We can approximate eq. (5.28) in terms of the model cosmology through the Alcock-Paczyński scaling explained in section 5.1.3. Substituting $D^{\rm tr}$ with the approximation (5.16) and $\mu^{\rm tr}$ with the approximation (5.17), the empirical model (5.28) can be written

$$\begin{aligned}\xi_{Fit}(D^{\rm tr},\mu^{\rm tr}) &\approx \xi_{Fit}\left(\tilde{D}^{\rm tr}(D,\mu;\alpha_\parallel,\alpha_\perp),\tilde{\mu}^{\rm tr}(D,\mu;\alpha_\parallel,\alpha_\perp)\right) \\ &= (D)^2\alpha_\perp^2\left(1+\psi\mu^2\right)A\,\mathrm{e}^{-\left(D\alpha_\perp\sqrt{1+\psi\mu^2}-r_{\rm BAO}\right)^2/(2\sigma^2)}+C_0(\mu)+\frac{C_1(\mu)}{D}+\frac{C_2(\mu)}{(D)^2},\end{aligned} \tag{5.29}$$

with

$$\psi \equiv \left(\frac{\alpha_\parallel}{\alpha_\perp}\right)^2 - 1 = (1+\epsilon)^6 - 1, \tag{5.30}$$

and where $\tilde{D}^{\rm tr}(D,\mu;\alpha_\parallel,\alpha_\perp)$ is the approximation of $D^{\rm tr}$ given by (5.16) and $\tilde{\mu}^{\rm tr}(D,\mu;\alpha_\parallel,\alpha_\perp)$ is the approximation of $\mu^{\rm tr}$ given by (5.17). Thus, when $\xi_{Fit}(D^{\rm tr},\mu^{\rm tr})$ is expressed in terms of D and μ through the approximation of the Alcock-Paczyński scaling, it has the form of a Gaussian in D scaled by D^2 plus first and second order polynomial terms in D^{-1}. The coefficients of the Gaussian in the basis of the model cosmology eq. (5.29) are now dependent on μ.

As discussed in section 5.1.5, we construct two wedge correlation functions and the angle-averaged correlation function, by averaging eq. (5.29) over μ-ranges. For current

[10] Models that are not developed with respect to perturbation theory cannot be tested against the full information in the CMB anisotropies, and are consequently more weakly constrained than ΛCDM scenarios.

galaxy surveys, it is in practice not useful to consider finer binning in μ, as the noise in the 2-point correlation function increases with decreasing bin-size, and two wedges already capture the information on α and ϵ.

In the regime of $\psi D/\sigma \ll 1$, we may expand the Gaussian part of the fitting function (5.29) to linear order in $\psi D/\sigma$ before performing the averaging in μ. This has the advantage of providing an analytic expression for the average. Expanding the Gaussian part of $\xi_{Fit,\mathcal{N}}$ (5.29) to linear order in $\psi D/\sigma$ we have

$$\begin{aligned}\xi_{Fit,\mathcal{N}}(D,\mu) &\approx (D)^2\alpha_\perp^2\left(1+\psi\mu^2\right)A\,\mathrm{e}^{-(D\alpha_\perp-r_{\mathrm{BAO}})^2/(2\sigma^2)-\psi\mu^2 D\alpha_\perp(D\alpha_\perp-r_{\mathrm{BAO}})/(2\sigma^2)} \\ &\approx (D)^2\alpha_\perp^2 A\,\mathrm{e}^{-(D\alpha_\perp-r_{\mathrm{BAO}})^2/(2\sigma^2)}\left(1-\frac{\psi\mu^2 D\alpha_\perp\left(D\alpha_\perp-r_{\mathrm{BAO}}\right)}{2\sigma^2}+\psi\mu^2\right),\end{aligned} \tag{5.31}$$

and taking the average in μ over the range $[\mu_1,\mu_2]$ we have

$$\begin{aligned}&\frac{1}{\mu_2-\mu_1}\int_{\mu_1}^{\mu_2} d\mu\,\xi_{Fit,\mathcal{N}}(D,\mu) \\ &\approx (D)^2\alpha_\perp^2 A\,\mathrm{e}^{-(D\alpha_\perp-r_{\mathrm{BAO}})^2/(2\sigma^2)}\left[1+\frac{1}{3}\psi\frac{\mu_2^3-\mu_1^3}{\mu_2-\mu_1}\left(1-\frac{D\alpha_\perp\left(D\alpha_\perp-r_{\mathrm{BAO}}\right)}{2\sigma^2}\right)\right] \\ &\approx (D)^2\alpha_\perp^2\left(1+\kappa\right)A\,\mathrm{e}^{-\left[D\alpha_\perp\left(1+\frac{1}{2}\kappa\right)-r_{\mathrm{BAO}}\right]^2/(2\sigma^2)} \\ &\approx (D)^2\widetilde{A}\,\mathrm{e}^{-(D-\tilde{r}_{BAO})^2/(2\tilde{\sigma}^2)},\end{aligned} \tag{5.32}$$

where

$$\kappa \equiv \frac{1}{3}\psi\frac{\mu_2^3-\mu_1^3}{\mu_2-\mu_1}, \tag{5.33}$$

we have neglected terms $\mathcal{O}(\kappa^2)$ at each step, and in the final line the distorted Gaussian parameters are defined by

$$\tilde{r}_{BAO} \equiv \frac{1-\frac{1}{2}\kappa}{\alpha_\perp}r_{\mathrm{BAO}}, \qquad \tilde{\sigma} \equiv \frac{1-\frac{1}{2}\kappa}{\alpha_\perp}\sigma, \qquad \widetilde{A} \equiv \alpha_\perp^2(1+\kappa)A. \tag{5.34}$$

The final wedge fitting function thus yields

$$\xi_{Fit,[\mu_1,\mu_2]}(D) = (D)^2\widetilde{A}\,\mathrm{e}^{-(D-\tilde{r}_{BAO})^2/(2\tilde{\sigma}^2)} + \bar{C}_0 + \frac{\bar{C}_1}{D} + \frac{\bar{C}_2}{(D)^2}, \tag{5.35}$$

where $\bar{C}_0$, $\bar{C}_1$, and $\bar{C}_2$ are unspecified coefficients depending on the interval $[\mu_1,\mu_2]$. In

the following, we investigate some limits of the wedge fitting function eq. (5.35).

We emphasise that the applicability of the expansion in eq. (5.31) and the resulting expression for the wedge fitting function (5.35) must be checked for a given application. When $\psi D/\sigma \ll 1$ is not satisfied over the fitting range in D, one must average the full expression (5.29) over μ in order to obtain the exact expression for the empirical wedge fitting function. We use the approximation (5.35) in our analysis, and confirm its validity by repeating our analysis using the exact expression. (See section 5.4.2 for a discussion of this point.)

The ideal wedge limit. Let us consider the ideal wedge limit $\mu_2 \to \mu_1$, in which the bin width is reduced to zero. In this limit we have

$$\kappa = \psi\mu_1^2 = \psi\mu_2^2. \tag{5.36}$$

Working to linear order in the anisotropic distortion parameter, so that by (5.30) $\alpha_\parallel/\alpha_\perp \simeq 1 + 3\epsilon$, the distorted Gaussian parameters (5.34) in this case read

$$\tilde{r}_{BAO} = \frac{r_{\rm BAO}}{\alpha_\perp^{1-\mu_1^2}\alpha_\parallel^{\mu_1^2}}, \qquad \tilde{\sigma} \equiv \frac{\sigma}{\alpha_\perp^{1-\mu_1^2}\alpha_\parallel^{\mu_1^2}}, \qquad \widetilde{A} \equiv \alpha_\perp^{2-2\mu_1^2}\alpha_\parallel^{2\mu_1^2}A, \tag{5.37}$$

e.g., for the pure transverse wedge ($\mu_1^2 = \mu_2^2 = 0$) and pure radial wedge ($\mu_1^2 = \mu_2^2 = 1$), one can check that this expression reduces to the expected scaling by $\alpha_\perp$ and $\alpha_\parallel$ respectively. For $\mu_1^2 = \mu_2^2 = \frac{1}{2}$, eq. (5.37) is symmetric in $\alpha_\perp$ and $\alpha_\parallel$, as expected.

The observational wedges. In practice we need to make a crude binning in μ in order to increase the galaxy counts for each bin. Thus in the further analysis we shall work with two μ-bins and denote $\mu_1 = 0, \mu_2 = \frac{1}{2}$ the transverse wedge, and $\mu_1 = \frac{1}{2}, \mu_2 = 1$ the radial wedge. For the transverse and radial wedges we find respectively for κ

$$\kappa_\perp = \frac{1}{12}\psi, \qquad \kappa_\parallel = \frac{7}{12}\psi, \tag{5.38}$$

which on substitution in eq. (5.34), to linear order in ϵ, yield the distorted Gaussian

parameters

$$\tilde{r}_{BAO\perp} = \frac{r_{\rm BAO}}{\alpha_\perp^{11/12}\alpha_\parallel^{1/12}}, \qquad \tilde{\sigma}_\perp \equiv \frac{\sigma}{\alpha_\perp^{11/12}\alpha_\parallel^{1/12}}, \qquad \widetilde{A}_\perp \equiv \alpha_\perp^{11/6}\alpha_\parallel^{1/6}A, \tag{5.39}$$

and

$$\tilde{r}_{BAO\parallel} = \frac{r_{\rm BAO}}{\alpha_\perp^{5/12}\alpha_\parallel^{7/12}}, \qquad \tilde{\sigma}_\perp \equiv \frac{\sigma}{\alpha_\perp^{5/12}\alpha_\parallel^{7/12}}, \qquad \widetilde{A}_\perp \equiv \alpha_\perp^{5/6}\alpha_\parallel^{7/6}A, \tag{5.40}$$

for the transverse and radial wedges, respectively. Note that eq. (5.39) and (5.40) are not symmetric under interchange $\alpha_\perp \leftrightarrow \alpha_\parallel$. This asymmetry between the radial and transverse wedges comes from the fact that we have defined the wedge as an unweighted average in μ.

The isotropic wedge. For the isotropic wedge ($\mu_1 = 0, \mu_2 = 1$) we have $\kappa = \psi/3$ which to linear order in ϵ leads to the 'isotropically distorted' Gaussian parameters

$$\tilde{r}_{BAO} = \frac{r_{\rm BAO}}{\alpha}, \qquad \tilde{\sigma} \equiv \frac{\sigma}{\alpha}, \qquad \widetilde{A} \equiv \alpha^2 A. \tag{5.41}$$

Note that only the isotropic scaling parameter α enters here, and not the anisotropic distortion parameter ϵ.

5.3.2 Testing on ΛCDM mocks

We now apply the fitting function (5.35) to ΛCDM mocks, to test if we recover the fiducial BAO scale and distortion parameter. To do this we perform fits to the mean correlation function of the QPM mocks based on the CMASS NGC and LOWZ NGC galaxy distributions, assuming a fiducial flat ΛCDM model with $\Omega_{M0} = 0.3$. First we perform a fit to the isotropic correlation function $\xi(D)$ with the fitting function discussed in section 5.3.1. Next we perform a joint fit to estimates of the radial wedge $\xi_\parallel(D)$ and transverse wedge $\xi_\perp(D)$ functions. We fit to correlation function measurements in the range $D \in [50; 150]$ Mpc/h with a bin size of 5 Mpc/h.

For the likelihood function $\mathcal{L}$ of the data given the model, we assume a Gaussian

distribution $\xi_{\rm Fit}$

$$\mathcal{L}\left(\bar{\hat{\xi}}\,\middle|\,\xi_{\rm Fit}\right) \propto \exp(-\chi^2/2), \tag{5.42}$$

with

$$\chi^2 = Z^{\intercal}\underline{\underline{C}}^{-1}_{\bar{\hat{\xi}}}Z, \qquad Z = \bar{\hat{\xi}} - \xi_{\rm Fit}, \tag{5.43}$$

where $\hat{\xi}$ is the binned estimate of the (isotropic or wedge) 2-point correlation function, and $\bar{\hat{\xi}}$ is its average over the mocks. For the wedge analysis, the transverse and radial estimates are combined into a single vector $\hat{\xi}$ in order to perform a combined fit, taking into account the covariance between the wedges. $\xi_{\rm Fit}$ is the fitting function prescribed in eq. (5.35). The covariance matrix of $\bar{\hat{\xi}}$ is given by the covariance of the individual measurements $\hat{\xi}$ scaled by the number of mocks over which we take the mean, $N_{\rm mean}$

$$\underline{\underline{C}}_{\bar{\hat{\xi}}} = \frac{1}{N_{\rm mean}}\underline{\underline{C}}_{\hat{\xi}}, \qquad \underline{\underline{C}}_{\hat{\xi}} = \overline{(\hat{\xi} - \bar{\hat{\xi}})(\hat{\xi} - \bar{\hat{\xi}})^{\intercal}}, \tag{5.44}$$

where the overbar represents the averages over the number of mocks, $N_{\rm mocks}$. In this analysis we have $N_{\rm mocks} = 1000$ for both CMASS and LOWZ. $N_{\rm mean}$ is chosen such that $\chi^2/N_{\rm dof} \sim 1$ in order to not to go beyond the regime of applicability of the empirical fitting function ($N_{\rm mean} = 40$ for CMASS and $N_{\rm mean} = 80$ for LOWZ), where $N_{\rm dof}$ is the number of independent degrees of freedom.

We determine the parameters of $\xi_{\rm Fit}$ in both a frequentist and Bayesian setting: that is, we find frequentist best fit parameters as well as Bayesian median parameters with conservative priors. The results of the fit to the isotropic correlation function for the CMASS and LOWZ QPM mock mean are shown in figure 5.3, and the results of the fit to the wedges are shown in figure 5.4. The estimates of the parameters describing the isotropic BAO feature $\left(\frac{r_{\rm BAO}}{\alpha}, \frac{\sigma}{\alpha}, A\alpha^2\right)$ are in good agreement between the isotropic and wedge analyses. The results for the estimated isotropic BAO scale are $\frac{r_{\rm BAO}}{\alpha} = 102.1 \pm 0.4$ Mpc/h for CMASS and $\frac{r_{\rm BAO}}{\alpha} = 101.8 \pm 0.5$ Mpc/h for LOWZ, and the results for the estimated anisotropic distortion parameter are $\epsilon = 0.0005 \pm 0.0035$ for CMASS and $\epsilon = 0.0008 \pm 0.0043$ for LOWZ.

As noted in section 5.2.3, the acoustic scale of the model underlying the QPM mocks is $r_s = 103.05$ Mpc/h. Since the QPM mocks are generated using $\Omega_{M0} = 0.29$, and our

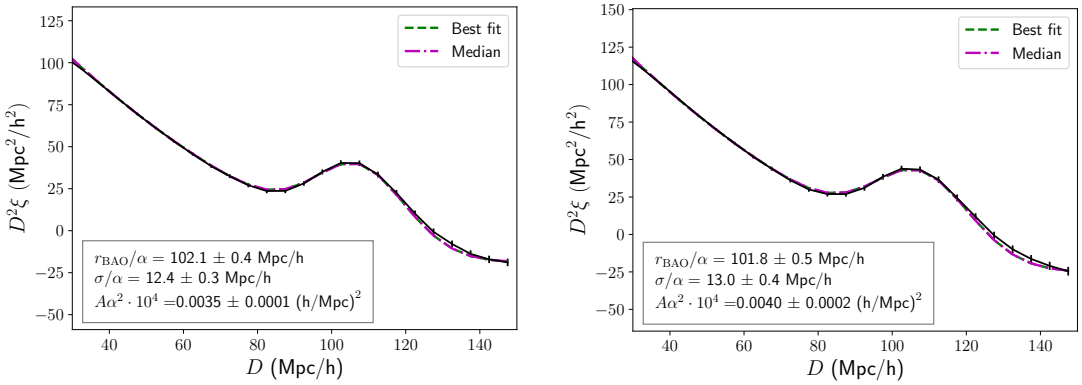

(a) $\xi(D_{\Lambda\rm CDM})$ CMASS

(b) $\xi(D_{\Lambda\rm CDM})$ LOWZ

Figure 5.3: Fit to the isotropic wedge $\xi(D_{\Lambda\rm CDM})$ of the mean of the CMASS NGC and LOWZ NGC QPM mocks respectively. $D_{\Lambda\rm CDM}$ is the Lagrangian distance evaluated at present times for ΛCDM with $\Omega_{M0} = 0.3$. The model fit includes 6 parameters $\left(\frac{r_{\rm BAO}}{\alpha}, \frac{\sigma}{\alpha}, A\alpha^2, C_0, C_1, C_2\right)$. The best fit (green line) is the fit that maximises the likelihood function. The median fit (purple line) is based on the 50% quantiles of the Bayesian posterior, resulting from conservative priors (meaning priors that span the significant volume of the likelihood). Mean values of $\frac{r_{\rm BAO}}{\alpha}$, $\frac{\sigma}{\alpha}$, and $A\alpha^2$ with 1σ equal tail credible intervals are superimposed on the plots.

fiducial model has $\Omega_{M0} = 0.30$, we have $\alpha(\bar{z} = 0.55) = 1.005$, and $\alpha(\bar{z} = 0.32) = 1.003$. We thus compute expected fiducial values

$$\frac{r_s}{\alpha(\bar{z} = 0.55)} = 102.5 \text{ Mpc}/h, \qquad \frac{r_s}{\alpha(\bar{z} = 0.32)} = 102.7 \text{ Mpc}/h \tag{5.45}$$

$$\epsilon(\bar{z} = 0.55) = 0.0013, \qquad \epsilon(\bar{z} = 0.32) = 0.0008 \tag{5.46}$$

As seen in the isotropic results in figure 5.3, the BAO scale is recovered to a precision of $0.4\% \pm 0.4\%$ for CMASS and $0.9\% \pm 0.5\%$ for LOWZ. The difference between the measured and the model ϵ-parameter is $|\Delta\epsilon| \lesssim 0.0008$, which is much smaller than typical errors in ϵ in the context of ΛCDM template-fitting approaches to BAO.

We note that $\sim 1\%$ systematic error is significant in standard BAO template-fitting approaches, where the statistical errors in the BAO scale measurement from the latest galaxy redshift surveys are around 1%, and the contribution from systematic errors in a ΛCDM model universe are significantly less than 1% [212]. Systematic errors in a empirical fitting procedure will inevitably be larger, and dependent on the cosmological

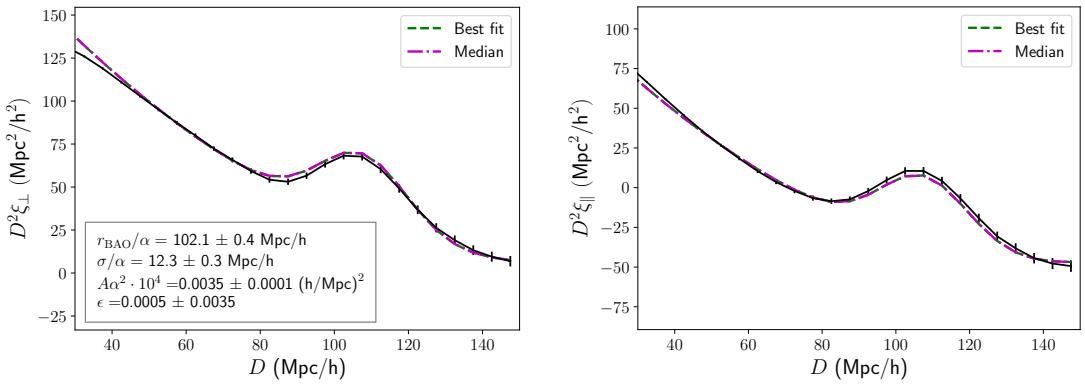

(a) $\xi_\perp(D_{\Lambda\rm CDM})$ CMASS NGC

(b) $\xi_\parallel(D_{\Lambda\rm CDM})$ CMASS NGC

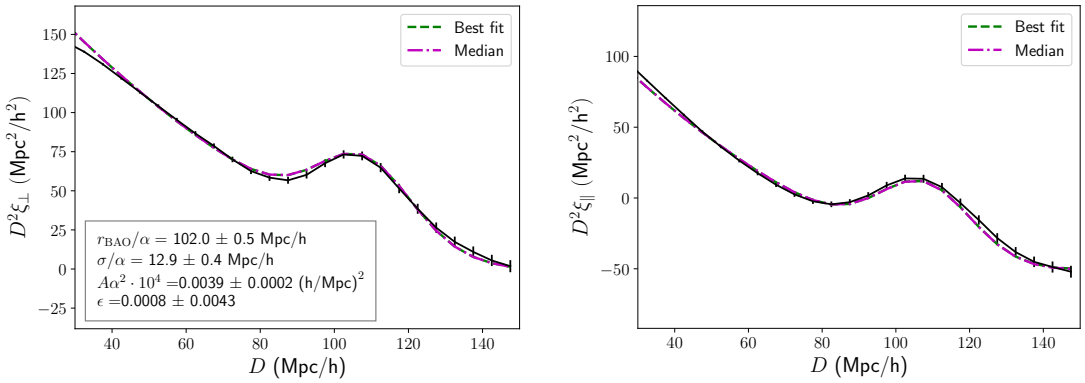

(c) $\xi_\perp(D_{\Lambda\rm CDM})$ LOWZ NGC

(d) $\xi_\parallel(D_{\Lambda\rm CDM})$ LOWZ NGC

Figure 5.4: Combined fit to the transverse wedge $\xi_\perp(D_{\Lambda\rm CDM})$ and radial wedge $\xi_\parallel(D_{\Lambda\rm CDM})$ of the mean of the CMASS NGC and LOWZ NGC QPM mocks respectively, where $D_{\Lambda\rm CDM}$ is the Lagrangian distance evaluated at present times for ΛCDM with $\Omega_{M0} = 0.3$. The model fit includes 10 parameters $\left(\frac{r_{\rm BAO}}{\alpha}, \frac{\sigma}{\alpha}, A\alpha^2, \epsilon, \bar{C}_{0\perp}, \bar{C}_{1\perp}, \bar{C}_{2\perp}, \bar{C}_{0\parallel}, \bar{C}_{1\parallel}, \bar{C}_{2\parallel}\right)$. The best fit (green line) is the fit that maximises the likelihood function. The median fit (purple line) is based on the 50% quantiles of the Bayesian posterior, resulting from conservative priors (meaning priors that span the significant volume of the likelihood). The numerical values superimposed on the plot of $\xi_\perp$ are the mean values with 1σ equal tail credible intervals.

model.[11] However, the errors in the underlying calibration of the BAO scale from the

[11] A fiducial ΛCDM fitting function per construction gives back the correct BAO scale when fitted to mocks generated from that same fiducial ΛCDM model. Any empirical fitting model, aiming at analysing BAO features for a broader class of models will yield larger systematics in the context of ΛCDM model simulations than the fitting procedure adapted specifically to ΛCDM. The price to

CMB are also larger in models with greater uncertainities in the underlying physical parameters. In this chapter, we will mainly be interested in the ϵ parameter as a consistency check of the tested fiducial cosmologies, and in comparing the significance of the BAO feature between the tested models, and do not include a calibration of the underlying BAO scale.

We experimented with modifications of eq. (5.35), allowing for a relative scaling of the wedge amplitudes, wedge widths, or both. The resulting fits were of similar quality to that of eq. (5.35) from an Akaike Information Criterion perspective. Thus we had no ΛCDM-based motivation for introducing additional parameters in the analysis of the galaxy survey. We note, however, that for models with more complicated curvature evolution than ΛCDM, there might be physical effects equivalent to the ΛCDM redshift-space distortions but possibly with stronger magnitude, distorting the relative amplitude and width of the BAO feature in the two wedges.[12]

We also experimented with different scaling behaviour of the Lagrangian distance D^{tr} in eq. (5.28) – for example, changing the scaling $(D^{\mathrm{tr}})^2$ of the Gaussian function to $(D^{\mathrm{tr}})^n$ with different values of n. The inferred peak of the Gaussian changed as expected, in some cases being significantly different from the BAO scale. However, ϵ was consistent with the expected values in eq. (5.46) for all investigated modifications of the fitting function.

5.4 Data analysis

The empirical procedure developed in this chapter can be applied to a wide class of cosmological models. In this analysis, we consider two fiducial model frameworks – the timescape model and the spatially flat ΛCDM model, with $\Omega_{M0} = 0.3$ in both cases.

pay for introducing a flexible fitting function adaptable to a large range of cosmologies, is exactly that it is not adapted to a particular cosmology.

[12] There is no obvious reason for this to be the case in the timescape model, however, since it implements a "uniform quasilocal Hubble flow condition" [95, 97]. Calculations of the amplitude of redshift-space distortions require the development of a framework analogous to standard cosmological perturbation theory, which is yet to be done for the timescape cosmology. Estimates of the amplitude of non-kinematic differential expansion [158] have been made using the Lemaître-Tolman-Bondi models for local structures on scales of order 10–60 Mpc [213], with the result that differences from the standard model expectation are smaller than current measurement uncertainties in peculiar velocities. Thus we would not expect substantial differences from the amplitude of the standard Kaiser effect [214], at least within this class of models.

We note that both the ΛCDM and timescape models have a spherically symmetric effective adapted geometry with a large curvature scale proportional to the Hubble distance $\sim c/H_0$, which is in both models of order 3 Gpc/h. Thus the curvature scale is of order the survey diameter. The Lagrangian distance introduced in section 5.1.1 between two galaxies separated around ~ 100 Mpc/h is thus well approximated by eq. (5.7) with correction terms[13] of order $\lesssim 10^{-3}$. We caution that our results may not be suitable for extrapolation to other model cosmologies, depending on the Alcock-Paczyński scaling.

We estimate the 2-point correlation function in each fiducial model for the CMASS and LOWZ NGC and SGC regions using the LS estimator described in section 5.1.5. We compute the isotropic correlation function estimator $\hat{\xi}(D)$, along with the radial and transverse wedge correlation function estimators, $\hat{\xi}_\parallel(D)$ and $\hat{\xi}_\perp(D)$, defined in eq. (5.26). We use the covariance matrix $\underline{\underline{C}}_{\hat{\xi}}$ formulated in eq. (5.44), computed from the QPM mocks described in section 5.2.3, to estimate the variance of the correlation function over realisations of an imagined ensemble of galaxy catalogues, of which our galaxy catalogue is a single realisation. We expect different models to ΛCDM, with different models for structure formation and global geometry, to give rise to a different random process underlying our measured galaxy catalogue. However, we shall assume that the ΛCDM estimate provides a reasonable lowest-order approximation of the covariance.

We combine the estimated correlation functions for the NGC and SGC regions using the inverse covariance weighting [58, 215]

$$\hat{\xi}_{\rm comb} = \underline{\underline{C}}_{\rm comb} \left(\underline{\underline{C}}^{-1}_{\rm NGC}\, \hat{\xi}_{\rm NGC} + \underline{\underline{C}}^{-1}_{\rm SGC}\, \hat{\xi}_{\rm SGC} \right), \tag{5.47}$$

where

$$\underline{\underline{C}}^{-1}_{\rm comb} = \underline{\underline{C}}^{-1}_{\rm NGC} + \underline{\underline{C}}^{-1}_{\rm SGC}, \tag{5.48}$$

is the inverse covariance of the combined measurement, and where ξ represents either the isotropic correlation functions $\xi(D)$ or the combined wedge correlation function $(\xi_\parallel(D), \xi_\perp(D))$. We experimented with different methods of combining the NGC and SGC measurements, and found that our results were robust to the exact weighting

[13] See appendix 5.A for an explicit derivation of the correction terms.

scheme used.

5.4.1 Isotropic fitting analysis

The estimated isotropic correlation function and best fit and median models are displayed in figure 5.5 for ΛCDM and in figure 5.6 for the timescape cosmology, and the results of the fits are summarised in table 5.1. The Gaussian peak component is significant in the CMASS isotropic correlation function at the 4.6σ level for ΛCDM and at the 3.8σ level for timescape. We quantify the significance of the peak as the posterior probability of having $\alpha^2 A > 0$.[14] For the LOWZ correlation function, the peak is significant at the 2.4σ level for ΛCDM and at the 1.9σ level for timescape.

We have used conservative priors for our fits to both timescape and ΛCDM, meaning (log-)uniform priors that span all regions of parameter space of significant likelihood volume. For the sake of comparing our ΛCDM results with the standard fiducial ΛCDM analysis of [193] and [194], we have repeated the fit with narrow Gaussian error bars on $\sigma_{\rm BAO}/\alpha$ with mean and standard deviation as determined by the isotropic mock fit of section 5.3.2. For both models, using this prior increases the significance of the BAO feature and decreases the errors in $r_{\rm BAO}/\alpha$. We only compare model fits when the priors are equally restrictive for both models and, unless otherwise stated, we comment on the analysis with conservative priors.

The results for $r_{\rm BAO}/\alpha$ and $\sigma_{\rm BAO}/\alpha$ are consistent between the LOWZ and CMASS samples for both timescape and ΛCDM. The results for the CMASS BAO peak positions for the conservative prior analysis are $r_{BAO}/\alpha = 102.0\pm1.7$ Mpc$/h$ for ΛCDM and 95.4 ± 1.8 Mpc$/h$ for timescape. The equivalent results for LOWZ are 99.9 ± 4.3 Mpc$/h$ for ΛCDM and 93.4 ± 4.9 Mpc$/h$ for timescape. The sign and magnitude of the relative peak positions of timescape and ΛCDM are consistent with figure 5.1 within the statistical error bars of the analysis. This can be realised by computing the relative isotropic AP-scaling α (5.14) between ΛCDM and timescape based on figure 5.1 and comparing it to the ratio of the measured peak positions r_{BAO}/α of the models.

Values of the Hubble constant for the timescape model obtained from CMB constraints can be up to 10% smaller than for the ΛCDM model [98]. Thus for typical

[14] We note that this is different to the typical way of quantifying BAO significance in ΛCDM-based fitting, where a reference power spectrum with no BAO feature is used to assess the increase of quality in fit when introducing the BAO feature [216].

values of H_0 the estimated isotropic peak position in units Mpc may in fact be slightly *larger* for timescape than the analogous peak position for ΛCDM.

The fits are reasonably good, all with a minimum χ^2 value of reasonable probability. The most extreme value is $\chi^2 = 22$ for the timescape LOWZ fit, the probability of $\chi^2 > 22$ being 8% for 14 degrees of freedom.

When we include a prior in σ, our ΛCDM results for the isotropic peak position $r_{\rm BAO}/\alpha$ are in $\lesssim 1\%$ agreement with those found in the fiducial ΛCDM analysis considered in e.g., [193] and [194]. The magnitude of the error bars are also comparable to those found in standard analyses. As an example, we compare our results with the isotropic pre-reconstruction DR12 results of table 8 in [194], derived assuming the fiducial cosmology $\Omega_{M0,\rm fid} = 0.29$ and $r_{{\rm BAO},fid} = 103.0$ Mpc/h. The isotropic CMASS measurement yields $\tilde{\alpha} = \alpha(\Omega_{M0} = 0.29)\,\frac{r_{{\rm BAO},fid}}{r_{\rm BAO}} = 1.015 \pm 0.013$, which together with the value of $r_{{\rm BAO},fid}$ yields $\frac{r_{\rm BAO}}{\alpha(\Omega_{M0}=0.29)} = 101.4 \pm 1.3$ Mpc/h, and finally scaling the result with the α-ratio of ΛCDM fiducial $\Omega_{M0,\rm fid} = 0.29$ and $\Omega_{M0} = 0.3$ we have $\frac{r_{\rm BAO}}{\alpha(\Omega_{M0}=0.30)} = 100.9 \pm 1.3$ Mpc/h. This result is within 1σ agreement with the ΛCDM results in table 5.1 for both the conservative prior analysis and for the analysis with a narrow Gaussian prior in $\sigma_{\rm BAO}/\alpha$. The analogous isotropic LOWZ result from table 8 in [194] reads $\tilde{\alpha} = \alpha(\Omega_{M0} = 0.29)\,\frac{r_{{\rm BAO},fid}}{r_{\rm BAO}} = 1.009 \pm 0.030$, which gives $\frac{r_{\rm BAO}}{\alpha(\Omega_{M0}=0.30)} = 101.7 \pm 3.1$ Mpc/h, in agreement with the ΛCDM results in table 5.1 for the conservative prior analysis and for the narrow Gaussian prior in $\sigma_{\rm BAO}/\alpha$.

Isotropic fit $\boldsymbol{\xi}$	$\alpha^2 A \cdot 10^4$	$r_{\rm BAO}/\alpha$	$\sigma_{\rm BAO}/\alpha$	$\chi^2/N_{\rm dof}$
ΛCDM CMASS	0.0032 ± 0.0007	102.0 ± 1.7	9.7 ± 1.8	17/14
ΛCDM LOWZ	0.0034 ± 0.0014	99.9 ± 4.3	13.1 ± 3.3	19/14
Timescape CMASS	0.0034 ± 0.0009	95.4 ± 1.8	9.8 ± 2.8	21/14
Timescape LOWZ	0.0035 ± 0.0018	93.4 ± 4.9	13.1 ± 4.2	22/14
ΛCDM CMASS $\mathcal{N}_{\sigma_{\rm BAO}/\alpha}$	0.0037 ± 0.0007	100.4 ± 1.5	12.2 ± 0.3	17/14
ΛCDM LOWZ $\mathcal{N}_{\sigma_{\rm BAO}/\alpha}$	0.0035 ± 0.0011	100.6 ± 3.0	12.2 ± 0.3	19/14

Table 5.1: Results of fitting the isotropic correlation function of CMASS and LOWZ. The parameter estimates shown are the Bayesian median with 1σ equal tail credible intervals. Conservative priors (meaning priors that span the significant volume of the likelihood) are used for all parameters in all fits, except for the ΛCDM fits labelled $\mathcal{N}_{\sigma_{\rm BAO}/\alpha}$, which use a narrow Gaussian prior with mean and width as determined in the mock analysis of section 5.3.2. The minimum χ^2 value divided by number of degrees of freedom $N_{\rm dof}$ is also quoted. $r_{\rm BAO}/\alpha$ and $\sigma_{\rm BAO}/\alpha$ are in units of Mpc/h. A is in units of (Mpc/h)^2.

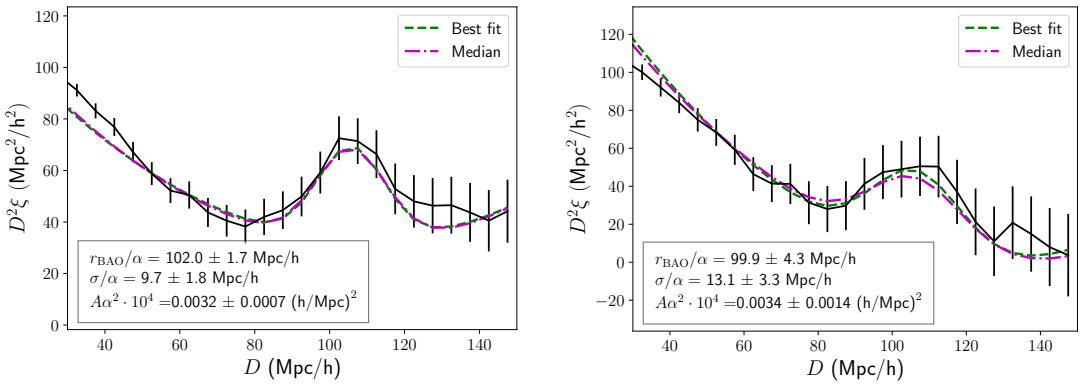

(a) $\xi(D_{\Lambda\rm CDM})$ CMASS

(b) $\xi(D_{\Lambda\rm CDM})$ LOWZ

Figure 5.5: Fit to the isotropic wedge $\xi(D_{\Lambda\rm CDM})$ of the CMASS and LOWZ survey respectively, where $D_{\Lambda\rm CDM}$ is the Lagrangian distance evaluated at present times for ΛCDM with $\Omega_{M0} = 0.3$. The model fit includes 6 parameters $\left(\frac{r_{\rm BAO}}{\alpha}, \frac{\sigma}{\alpha}, A\alpha^2, C_0, C_1, C_2\right)$. The best fit (green line) is the fit that maximises the likelihood function. The median fit (purple line) is based on the 50% quantiles of the Bayesian posterior, resulting from conservative priors (meaning priors that span the significant volume of the likelihood). Mean values of $\frac{r_{\rm BAO}}{\alpha}$, $\frac{\sigma}{\alpha}$, and $A\alpha^2$ with 1σ equal tail credible intervals are superimposed on the plots.

5.4.2 Anisotropic fitting analysis

We now turn to the wedge analysis, which is useful for examining the consistency of the BAO feature in the transverse and radial separation of galaxy pairs. The results of fitting the empirical parameters describing the BAO feature are shown in table 5.2. The measurements of the anisotropic distortion parameter in CMASS are $\epsilon = -0.021 \pm 0.017$ for ΛCDM and $\epsilon = 0.021 \pm 0.017$ for timescape, and the LOWZ results are $\epsilon = -0.022 \pm 0.084$ for ΛCDM and $\epsilon = 0.013 \pm 0.110$ for timescape. The CMASS and LOWZ results for the peak position $r_{\rm BAO}/\alpha$ and the width $\sigma_{\rm BAO}/\alpha$ are consistent within 1σ for both ΛCDM and the timescape model.

The Gaussian peak in the CMASS wedge correlation functions has a significance of $\sim 4.8\sigma$ for ΛCDM and $\sim 3.9\sigma$ for timescape. For LOWZ, the peak has a significance of $\sim 1.4\sigma$ and $\sim 1.3\sigma$ for ΛCDM and timescape respectively. As above, the significance of the peak is quantified as the posterior probability of having $\alpha^2 A > 0$.

We note that the values of epsilon gives $\psi \approx 0.1$, for which the expansion in eq. (5.31) is not guaranteed to hold for the fitting range $D \in [50; 150]$ Mpc/h. We

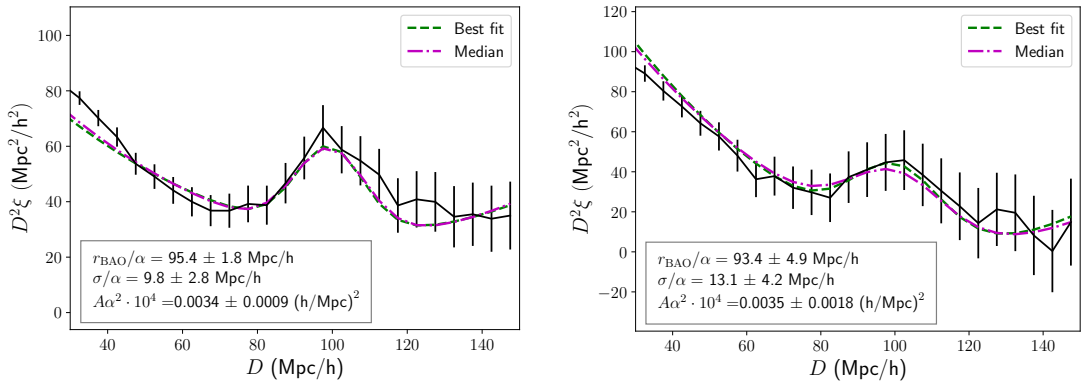

(a) $\xi(D_{\rm timescape})$ CMASS

(b) $\xi(D_{\rm timescape})$ LOWZ

Figure 5.6: Fit to the isotropic wedge $\xi(D_{\rm timescape})$ of the CMASS and LOWZ survey respectively, where $D_{\rm timescape}$ is the Lagrangian distance evaluated at present times for the timescape model with $\Omega_{M0} = 0.3$. The model fit includes 6 parameters $\left(\frac{r_{\rm BAO}}{\alpha}, \frac{\sigma}{\alpha}, A\alpha^2, C_0, C_1, C_2\right)$. The best fit (green line) is the fit that maximises the likelihood function. The median fit (purple line) is based on the 50% quantiles of the Bayesian posterior, resulting from conservative priors (meaning priors that span the significant volume of the likelihood). Mean values of $\frac{r_{\rm BAO}}{\alpha}$, $\frac{\sigma}{\alpha}$, and $A\alpha^2$ with 1σ equal tail credible intervals are superimposed on the plots.

checked the validity of the approximate fitting model eq. (5.35) by comparing to the exact wedge fitting functions calculated from the average of eq. (5.29) over μ, and found that best fit parameter results derived in our linearised analysis receive corrections of order $\sim 10\%$ of the error bars on the same parameters. Since the corrections are an order of magnitude smaller than the error bars, we ignore these corrections here and quote the results from the linearised analysis.

The best fit and median models of eq. (5.35) are shown superimposed on the $\xi_\perp$ and $\xi_\parallel$ measurements for the spatially flat ΛCDM fiducial cosmology in figure 5.7 and for the timescape fiducial cosmology in figure 5.8. The most extreme χ^2 value is for the timescape CMASS fit with $\chi^2 = 49$, with 2% probability of $\chi^2 > 49$ for 30 degrees of freedom.

The significance and precision of the acoustic peak in the LOWZ sample is significantly increased by imposing a prior in $\sigma_{\rm BAO}/\alpha$, which is illustrated for the ΛCDM case in table 5.2. Using narrow Gaussian priors with mean and width determined by the mock analysis of section 5.3.2, the significance of the peak goes up to 2σ and the

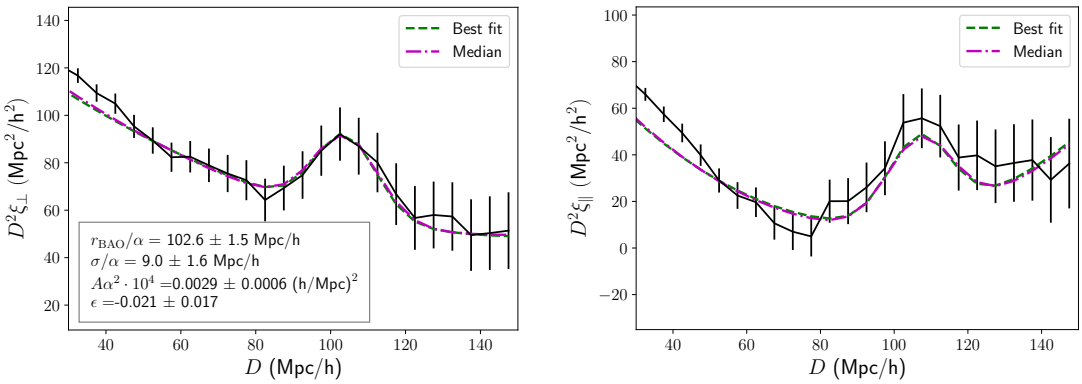

(a) $\xi_\perp(D_{\Lambda\rm CDM})$ CMASS

(b) $\xi_\parallel(D_{\Lambda\rm CDM})$ CMASS

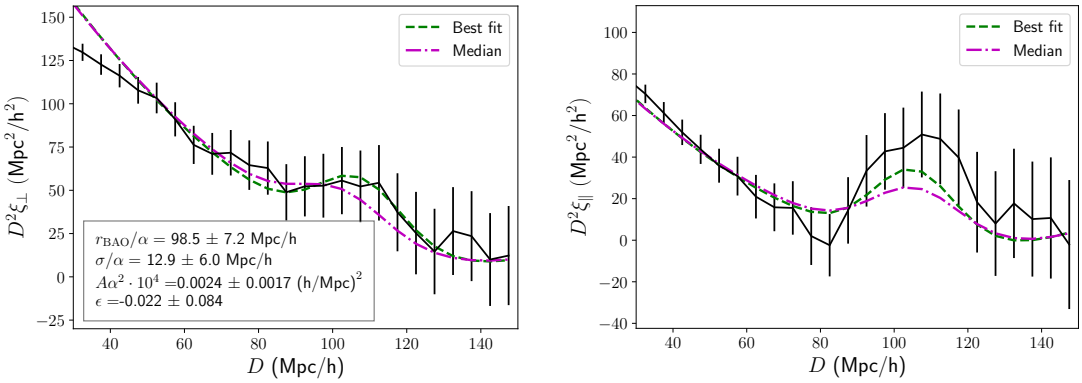

(c) $\xi_\perp(D_{\Lambda\rm CDM})$ LOWZ

(d) $\xi_\parallel(D_{\Lambda\rm CDM})$ LOWZ

Figure 5.7: Combined fit to the transverse wedge $\xi_\perp(D_{\Lambda\rm CDM})$ and radial wedge $\xi_\parallel(D_{\Lambda\rm CDM})$ of the CMASS and LOWZ survey respectively, where $D_{\Lambda\rm CDM}$ is the Lagrangian distance evaluated at present times for ΛCDM with $\Omega_{M0} = 0.3$. The model fit includes 10 parameters $\left(\frac{r_{\rm BAO}}{\alpha}, \frac{\sigma}{\alpha}, A\alpha^2, \epsilon, \bar{C}_{0\perp}, \bar{C}_{1\perp}, \bar{C}_{2\perp}, \bar{C}_{0\parallel}, \bar{C}_{1\parallel}, \bar{C}_{2\parallel}\right)$. The best fit (green line) is the fit that maximises the likelihood function. The median fit (purple line) is based on the 50% quantiles of the Bayesian posterior, resulting from conservative priors (meaning priors that span the significant volume of the likelihood). The numerical values superimposed on the plot of $\xi_\perp$ are the mean values with 1σ equal tail credible intervals.

errors in $r_{\rm BAO}/\alpha$ decrease by $\sim 30\%$. The measurements of $\alpha^2 A$, $r_{\rm BAO}/\alpha$, and $\sigma_{\rm BAO}/\alpha$ for the wedge analysis are in good agreement with those of the isotropic analysis in table 5.1 for both timescape and ΛCDM. We note that the errors on $\alpha^2 A$, $r_{\rm BAO}/\alpha$, and $\sigma_{\rm BAO}/\alpha$ all decrease when going from the isotropic analysis to the anisotropic analysis

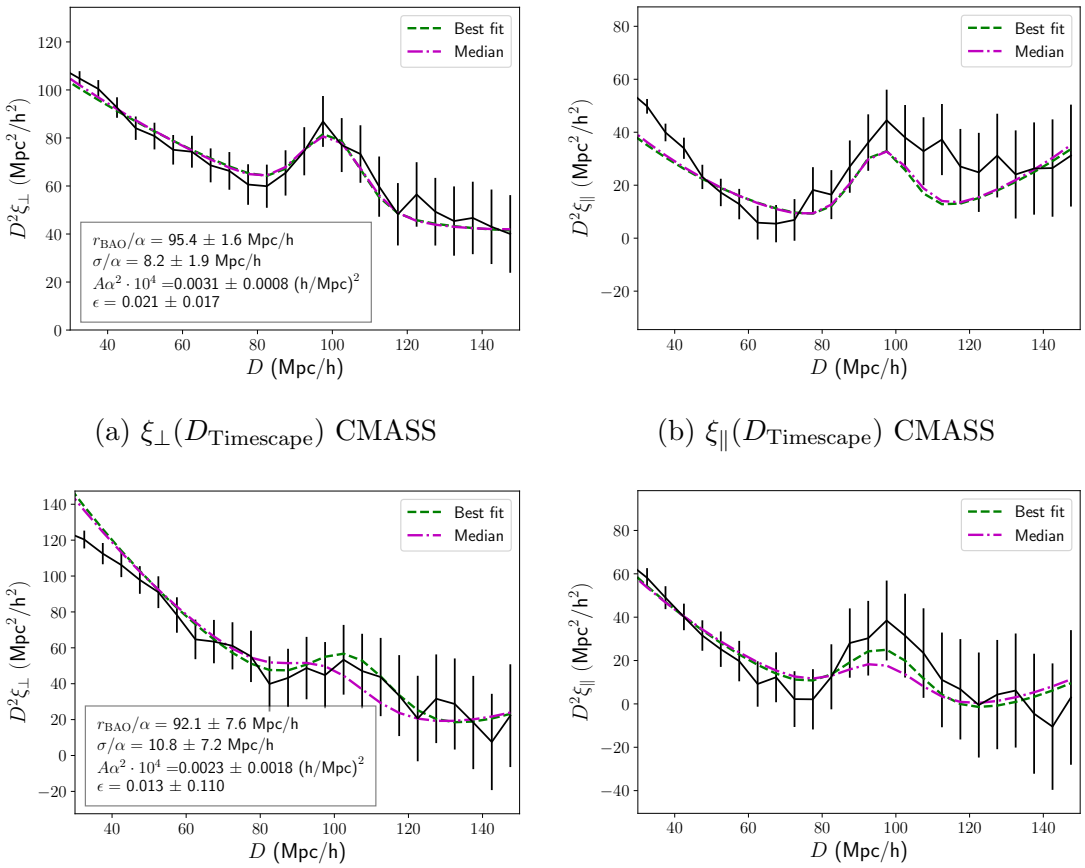

(a) $\xi_\perp(D_{\mathrm{Timescape}})$ CMASS

(b) $\xi_\parallel(D_{\mathrm{Timescape}})$ CMASS

(c) $\xi_\perp(D_{\mathrm{Timescape}})$ LOWZ

(d) $\xi_\parallel(D_{\mathrm{Timescape}})$ LOWZ

Figure 5.8: Combined fit to the transverse wedge $\xi_\perp(D_{\mathrm{Timescape}})$ and radial wedge $\xi_\parallel(D_{\mathrm{Timescape}})$ of the CMASS and LOWZ survey respectively, where $D_{\mathrm{Timescape}}$ is the Lagrangian distance evaluated at present times for the timescape model with $\Omega_{M0} = 0.3$. The model fit includes 10 parameters $\left(\frac{r_{\mathrm{BAO}}}{\alpha}, \frac{\sigma}{\alpha}, A\alpha^2, \epsilon, \bar{C}_{0\perp}, \bar{C}_{1\perp}, \bar{C}_{2\perp}, \bar{C}_{0\parallel}, \bar{C}_{1\parallel}, \bar{C}_{2\parallel}\right)$. The best fit (green line) is the fit that maximises the likelihood function. The median fit (purple line) is based on the 50% quantiles of the Bayesian posterior, resulting from conservative priors (meaning priors that span the significant volume of the likelihood). The numerical values superimposed on the plot of $\xi_\perp$ are the mean values with 1σ equal tail credible intervals.

for CMASS, whereas they all increase for LOWZ. This might be because of the strong correlation between $\sigma_{\mathrm{BAO}}/\alpha$ and the remaining parameters of the analysis: a posterior which widens in σ/α is likely to widen in the other parameters as well.

The results of our fiducial ΛCDM analysis displayed in table 5.2 are in good agree-

ment with previous measurements reported by [193] and [194]. For example, table 8 of [194] reports $\epsilon = -0.016 \pm 0.020$ for a DR12 CMASS pre-reconstruction wedge analysis which, when transformed through AP-scaling eq. (5.14) from the fiducial model $\Omega_{M0} = 0.29$ of [194] to the fiducial model $\Omega_{M0} = 0.3$ of this chapter, produces $\epsilon = -0.015 \pm 0.020$. This is in agreement well within 1σ of our results listed in table 5.2. The analogous result for the LOWZ sample in table 8 of [194] is 0.026 ± 0.041, which AP-scaled gives $\epsilon = 0.025 \pm 0.041$, which is in agreement with our ΛCDM results for LOWZ in table 5.2 at the 1σ level.

Wedge fit $\boldsymbol{\xi}_\perp$, $\boldsymbol{\xi}_\parallel$	$\alpha^2 A \cdot 10^4$	$r_{\rm BAO}/\alpha$	$\sigma_{\rm BAO}/\alpha$	ϵ	$\chi^2/N_{\rm dof}$
ΛCDM CMASS	0.0029 ± 0.0006	102.6 ± 1.5	9.0 ± 1.6	-0.021 ± 0.017	48/30
ΛCDM LOWZ	0.0024 ± 0.0017	98.5 ± 7.2	12.9 ± 6.0	-0.022 ± 0.084	40/30
Timescape CMASS	0.0031 ± 0.0008	95.4 ± 1.6	8.2 ± 1.9	0.021 ± 0.017	49/30
Timescape LOWZ	0.0023 ± 0.0018	92.1 ± 7.6	10.8 ± 7.2	0.013 ± 0.110	38/30
ΛCDM CMASS $\mathcal{N}_{\sigma_{\rm BAO}/\alpha}$	0.0035 ± 0.0006	100.9 ± 1.8	12.3 ± 0.2	-0.022 ± 0.023	48/30
ΛCDM LOWZ $\mathcal{N}_{\sigma_{\rm BAO}/\alpha}$	0.0027 ± 0.0012	100.3 ± 4.6	12.3 ± 0.3	-0.008 ± 0.060	40/30

Table 5.2: Results of the combined fit to the transverse and radial wedge for CMASS and LOWZ. The parameter estimates shown are the Bayesian median with 1σ equal tail credible intervals. Conservative priors (meaning priors that span the significant volume of the likelihood) are used for all parameters in all fits, except for the ΛCDM fits labelled $\mathcal{N}_{\sigma_{\rm BAO}/\alpha}$, where a narrow Gaussian prior is used with mean and width as determined in the mock analysis of section 5.3.2. The minimum χ^2 value divided by number of degrees of freedom $N_{\rm dof}$ is also quoted. $r_{\rm BAO}/\alpha$ and $\sigma_{\rm BAO}/\alpha$ are in units of Mpc/h. A is in units of $(\text{Mpc}/h)^2$.

The anisotropic distortion parameter ϵ describes how the fiducial model is distorted in a relative angular and radial sense compared to the 'true' underlying cosmology, to lowest order. Since ϵ is consistent with zero at the $< 2\sigma$ level for both timescape and ΛCDM in the above data analysis, both models are in agreement with no anisotropic distortion. We can formulate the $\epsilon = 0$ consistency test in terms of the effective metric combination $g_{\theta\theta}^{1/2}/g_{zz}^{1/2}$ (equal to $d_A H/c$ in ΛCDM, where d_A is the angular diameter distance, and H is the Hubble parameter), which from the AP-scaling of our results can be formulated as

$$\frac{g_{\theta\theta}^{1/2}}{g_{zz}^{1/2}} \approx \frac{\alpha_\perp}{\alpha_\parallel} \frac{g_{{\rm fid},\theta\theta}^{1/2}}{g_{{\rm fid},zz}^{1/2}} = (1+\epsilon)^{-3} \frac{g_{{\rm fid},\theta\theta}^{1/2}}{g_{{\rm fid},zz}^{1/2}} \tag{5.49}$$

where $g_{\rm fid}$ corresponds to the fiducial adapted metric of either ΛCDM or timescape,

and where ϵ is the estimate quoted in table 5.2 for the respective fiducial cosmologies. The results of the effective measurement of the metric combinations (5.49) for CMASS and LOWZ are shown in figure 5.9. We see that that both effective measurements are consistent with the respective fiducial lines, as expected since the estimated ϵ-parameter is consistent with zero within both models. The precision in the measurements of the metric combination is comparable to the difference between the fiducial metric combination of the two cosmologies for the CMASS survey, potentially making this metric combination a useful discriminator between the ΛCDM and timescape model for future surveys. We also note that the systematics in the measurement arising from the choice of fiducial cosmology is of order the distance between the cosmologies, indicating that a careful analysis of the regime of application of the AP-scaling is needed.

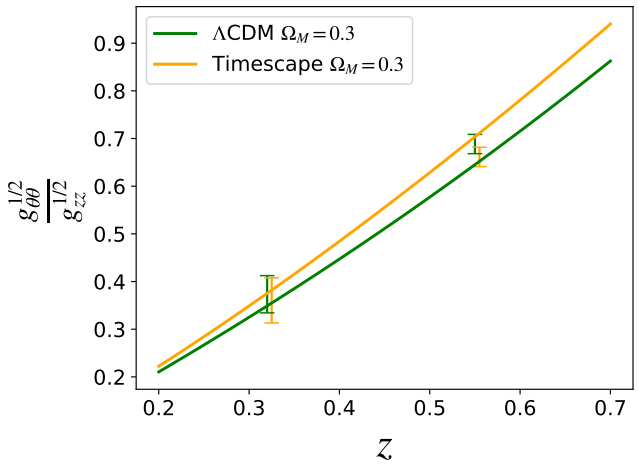

Figure 5.9: Effective measurement of the metric combination $g_{\theta\theta}^{1/2}/g_{zz}^{1/2}$ for LOWZ and CMASS within the timescape model and ΛCDM respectively, with the fiducial ΛCDM and timescape $\Omega_{M0} = 0.3$ predictions superimposed. The timescape measurements are artificially shifted slightly in redshift relative to the mean LOWZ and CMASS redshifts $z = 0.32$ and $z = 0.55$, in order to see the measurements and their comparison more clearly.

5.5 Discussion

In this chapter we have developed methods for examining BAO features in the 2-point correlation function for cosmological models with non-trivial curvature: models that are not necessarily spatially flat, close to spatially flat, nor with constant spatial curvature. The methods outlined in section 5.1 and 5.3.1 are applicable for a broad class of large-scale cosmological models. (see section 5.1.2 for precise statements about the regime of applicability). Our assumptions on the model cosmology can be summarised as follows:

- We assume global hyperbolicity of the average space-time, and that the galaxies can to a good approximation be described as particles in a non-caustic, vorticity-free fluid description. These assumptions are made in order to formulate the reduced 2-point correlation function descriptive statistic in terms of the lagrangian distance definition given in section 5.1.1, generalising the comoving distance definition of FLRW cosmology.

- We further impose the assumptions outlined in section 5.1.2, such that the lagrangian distance definition can be approximated as in eq. (5.7). The approximation (5.7) is needed to: (i) define the 'radial fraction' of the separation μ_T in (5.8); and (ii) make sense of the generalised AP-scalings $\alpha_\parallel, \alpha_\perp$ of the 'radial' and 'transverse' component of the metric introduced in section 5.1.3.

- Finally, we assume that the empirical fitting function described in section 5.3.1 is appropriate for extracting the isotropic BAO characteristic scale and the anisotropic distortion between the radial and transverse scale. (This assumption is tested and confirmed for a fiducial ΛCDM model using mocks catalogues, but is left as an ansatz for other cosmologies.)

Our methods allow us to explicitly formulate the 2-point correlation function in the context of a broad class of cosmologies and hence analyse the clustering statistics for those cosmologies in detail, instead of relying on results extrapolated from ΛCDM. The only ΛCDM estimate used in this chapter enters when estimating errors in the observed 2-point correlation function, where we use mocks generated from a fiducial ΛCDM model to give a rough estimate for the variance over ensembles of our sky.

When testing our methods on ΛCDM mocks we recover the isotropic peak position to within one per cent of the fiducial value. This $\lesssim 1\%$ discrepancy is due to a calibra-

tion issue between the characteristic scale extracted in the fitting procedure and the underlying BAO scale discussed in section 5.3. It should be noted that, while this level of systematic error is somewhat higher than obtained by ΛCDM fitting procedures, it can be considered low in (semi-)model independent analysis. Removing cosmology dependence in data reduction necessarily comes at the price of increasing uncertainties. The systematics related to the BAO scale extraction in the context of other models must be assessed for each cosmology of interest. The anisotropic scaling parameter ϵ is recovered to high precision; the systematics in our mock analysis on the determination of ϵ are much smaller than the usual statistical errors in ΛCDM fitting procedures. The estimation of the ϵ parameter is robust to the exact form of the fitting function assumed, and is not associated with the calibration issues of the statistical BAO scale.

A shortcoming of this analysis is that a fiducial cosmology of choice is still needed in order to reduce data into a 2-point correlation function. Model-independent analysis has been proposed in, e.g., [211] and [210]. While such procedures are certainly relevant for next-generation surveys, the signal strength is greatly reduced due to the split of the fiducial spatial scale to a range of angular and redshift separations.

Another shortcoming of this analysis is the approximations of section 5.1.2, implying that only effective cosmic metric theories which are averaged on scales of the order of the BAO scale can be tested in our framework. While testing more complicated models with a hierarchy of curvature scales, describing different scales of structure in our universe, would be of interest, this is beyond the scope of this analysis.

We apply our fitting methods to the BOSS DR12 CMASS and LOWZ galaxy surveys using two fiducial cosmologies: a spatially flat ΛCDM model and the timescape model, which at the present epoch has a marginal apparent acceleration with a recent expansion history closer to the empty FLRW universe. We recover the pre-reconstruction results for the BAO peak position and the anisotropic distortion parameter ϵ based on ΛCDM template-fitting obtained in [194].

It should be noted, that since the parameter estimates of our empirical procedure and of the standard ΛCDM template-fitting are based on the same datasets, any difference in the results can be attributed to systematic differences in the parameter extraction procedures. For procedures with small systematic differences as compared to the statistical errors, we would thus expect differences in parameter estimates much smaller than 1σ. The systematic differences between the present procedure and the standard ΛCDM procedure are smaller, but of order, the statistical errors. The main

difference between the estimated BAO peak position of the present procedure and of the standard ΛCDM power spectrum fitting procedure can be ascribed to the systematics related to the calibration of the BAO scale in the empirical fit (see discussion in section 5.3). Other examples of systematics between the procedures that can lead to differences in the parameter estimates are: choice of statistical framework, choice of priors, and galaxy weights. For example, the $\sigma_{\rm BAO}/\alpha$ prior in the present analysis has a $\sim 1\%$ effect on the peak position, which is comparable to the differences in our inferred scale as compared to the results of [194].

Based on our empirical model for the shape of the 2-point correlation function, we find that the BAO feature of the models is detected at a similar level of significance in the two cosmologies, and that the distortion between the radial and transverse directions, quantified by the ϵ parameter, is consistent with zero for both fiducial models within 2σ. Thus, both models are consistent with no anisotropic distortion with respect to the 'true' cosmological model, and thus provide self-consistent fits to the BAO-data. This finding is interesting in light of the significant difference between the timescape model and the ΛCDM model distance measures (see figure 5.1).

Our analysis suggests that a wide class of cosmological models can yield a statistically isotropic BAO feature with $\epsilon = 0$, consistent with the expectation of statistical homogeneity and isotropy of our universe. In future work, we will combine these BAO measurements with estimations of the standard ruler scale in timescape cosmology to perform a full model comparison.

Appendix 5.A Taylor expansion of geodesic distances

In the present analysis we make use of a Taylor expansion of the spatial geodesic distance between two points on a spatial hypersurface. Such an expansion is convenient when the spatial geodesic equation (defined on spatial hypersurfaces of interest) of the model under investigation has no analytic solution, and applicable when the curvature scale of the model is much larger than the particle separation of interest.

We consider a metric on the form eq. (5.1)

$$ds^2 = -\alpha^2 c^2 dt^2 + g_{ij} dx^i dx^j, \tag{5.50}$$

where t defines a spatial foliation of interest (in the context of this analysis, $t =$ constant slices are taken to coincide with the matter frame, which can be done in the absence of vorticity).

Consider a geodesic spatial line between two points P_1 and P_2 on the hypersurface $t = T$, such that the line is required to lie in the $t = T$ plane everywhere. The geodesic distance between the points is given by

$$d_T(P_1, P_2) \equiv \int_{l_1}^{l_2} dl \sqrt{g_{ij} \frac{dx^i}{dl} \frac{dx^j}{dl}} = l_2 - l_1 \tag{5.51}$$

where l is the affine parameter along a spatial geodesic connecting P_1 and P_2, $\frac{dx^i}{dl}$ is the tangent to the geodesic with $g_{ij} \frac{dx^i}{dl} \frac{dx^j}{dl} = 1$, $l_1 = l(P_1)$ and $l_2 = l(P_2)$ is the affine parameter evaluated at the endpoints. The function d_T coincides with the Lagrangian distance D_T defined in section (5.1.1), when the points P_1 and P_2 represent the intersection of two particle worldlines with the surface $t = T$.

We expand the coordinate functions on the line in the affine parameter l

$$\begin{aligned} x_2^i &= x_1^i + \left.\frac{dx^i}{dl}\right|_{l=l_1} (l_2 - l_1) + f^i, \\ f^i &= \sum_{n=2}^{\infty} f_n^i, \qquad f_n^i = \frac{1}{n!} \left.\frac{d^n x^i}{dl^n}\right|_{l=l_1} (l_2 - l_1)^n \end{aligned} \tag{5.52}$$

where $x_1^i = x^i(P_1)$ and $x_2^i = x^i(P_2)$ are the coordinate labels of the end points. The higher-order terms f_n^i can be expressed in terms of $\Delta x^i = x_2^i - x_1^i$ up to a given order. Here we shall keep terms up to $\mathcal{O}\left(f_3^i\right)$, where we assume $\Delta x^j f_2^k \sim \mathcal{O}\left(f_3^i\right)$ etc. The second order term yields

$$\begin{aligned} f_2^i &= \frac{1}{2}\frac{d^2x^i}{dl^2}(l_2-l_1)^2 = -\frac{1}{2}\Gamma^i{}_{jk}\frac{dx^j}{dl}\frac{dx^k}{dl}(l_2-l_1)^2 \\ &= -\frac{1}{2}\Gamma^i{}_{jk}(\Delta x^j - f^j)(\Delta x^k - f^k) = -\frac{1}{2}\Gamma^i{}_{jk}\,\Delta x^j\,\Delta x^k + \Gamma^i{}_{jk}\,\Delta x^j\,f_2^k + \mathcal{O}\left(f_4^i\right) \\ &= -\frac{1}{2}\Gamma^i{}_{jk}\,\Delta x^j\,\Delta x^k - \frac{1}{2}\Gamma^i{}_{jk}\Gamma^k{}_{st}\,\Delta x^j\,\Delta x^s\,\Delta x^t + \mathcal{O}\left(f_4^i\right), \end{aligned} \tag{5.53}$$

where the first line follows from the affine geodesic equation, the second line follows from applying (5.52) and keeping terms up to $\mathcal{O}\left(f_3^i\right)$. The third line comes from recursively plugging (5.53) into itself and again keeping terms up to $\mathcal{O}\left(f_3^i\right)$. The evaluation at $l = l_1$ is implicit.

With a similar derivation, the third-order term of the expansion eq. (5.52) yields

$$f_3^i = \left(\frac{1}{3}\Gamma^i{}_{jk}\Gamma^k{}_{st} - \frac{1}{6}\partial_s\Gamma^i{}_{jt}\right)\Delta x^j\Delta x^s\Delta x^t + \mathcal{O}\left(f_4^i\right). \tag{5.54}$$

We can now expand the geodesic distance (5.51) in an adapted coordinate system x^i of choice. Keeping terms up to $\mathcal{O}\left(f_4^i\right)$ we have

$$\begin{aligned} d_T(P_1,P_2) = l_2 - l_1 &= \sqrt{g_{ij}\frac{dx^i}{dl}\frac{dx^j}{dl}(l_2-l_1)^2} \\ &= \sqrt{g_{ij}(\Delta x^i - f^i)(\Delta x^j - f^j)} \\ &= \sqrt{g_{ij}\Delta x^i\Delta x^j - 2g_{ij}\Delta x^i(f_2^j + f_3^j) + g_{ij}f_2^i f_2^j + \mathcal{O}\left(f_5^i\right)} \\ &= \sqrt{{}^{(0)}g + {}^{(1)}g + {}^{(2)}g + \mathcal{O}\left(f_5^i\right)}, \end{aligned} \tag{5.55}$$

where all terms are evaluated at $l = l_1$. The first line follows from a convenient multiplication by $1 = \sqrt{g_{ij}\frac{dx^i}{dl}\frac{dx^j}{dl}}$. The following lines comes from applying the expansion (5.52) and truncating the resulting terms at $\mathcal{O}\left(f_4^i\right)$. In the last line we have used the

definitions

$$
\begin{aligned}
{}^{(0)}g &\equiv g_{ij}\,\Delta x^i \Delta x^j, \qquad {}^{(1)}g \equiv g_{ij}\,\Gamma^j_{\ st}\,\Delta x^i \Delta x^s \Delta x^t \\
{}^{(2)}g &\equiv \left[\frac{1}{3} g_{ij}\left(\partial_s \Gamma^j_{\ tb} + \Gamma^j_{\ ab}\Gamma^a_{\ st}\right) + \frac{1}{4} g_{kj}\,\Gamma^k_{\ st}\Gamma^j_{\ ib}\right] \Delta x^i \Delta x^s \Delta x^t \Delta x^b
\end{aligned}
\tag{5.56}
$$

The extent to which the coordinate expansion (5.55) is accurate at a given truncation of the series depends on the space-time metric and the chosen events P_1 and P_2, but also on the adapted coordinates used in the expansion. The convergence of the expansion (5.55) must be examined for the particular problem at hand.

5.A.1 Spherically symmetric metrics

As a special case relevant for this chapter we consider the spherically-symmetric metric (5.3) of section 5.1.2. The adapted metric on the spatial hypersurfaces given by eq. (5.4)

$$
ds^2_T = g_{rr}(t=T,r)dr^2 + g_{\theta\theta}(t=T,r)\left(d\theta^2 + \cos^2(\theta)d\phi^2\right). \tag{5.57}
$$

In this case we have for the lowest-order term of eq. (5.55)

$$
{}^{(0)}g = g_{rr}(\Delta r)^2 + g_{\theta\theta}\left((\Delta\theta)^2 + \cos^2(\theta)(\Delta\phi)^2\right). \tag{5.58}
$$

The first order correction yields

$$
\begin{aligned}
{}^{(1)}g &= \frac{1}{2}\frac{\partial}{\partial x^k}(g_{sm})\Delta x^m \Delta x^k \Delta x^s \\
&= \frac{1}{2}\Delta g_{rr}(\Delta r)^2 + \frac{1}{2}\Delta g_{\theta\theta}\left((\Delta\theta)^2 + \cos^2(\theta)(\Delta\phi)^2\right) + \frac{1}{2} g_{\theta\theta}[\Delta\cos^2(\theta)](\Delta\phi)^2,
\end{aligned}
\tag{5.59}
$$

where we have defined

$$
\Delta g_{rr} \equiv \frac{dg_{rr}}{dr}\Delta r, \qquad \Delta g_{\theta\theta} \equiv \frac{dg_{\theta\theta}}{dr}\Delta r, \qquad \Delta\cos^2(\theta) \equiv \frac{d(\cos^2(\theta))}{d\theta}\Delta\theta. \tag{5.60}
$$

Combining the lowest order term and the first order correction we thus have for eq. (5.55) up to $\mathcal{O}\left({}^{(2)}g\right)$

$$
d_T(P_1,P_2) = \sqrt{\overline{g}_{rr}(\Delta r)^2 + \overline{g}_{\theta\theta}\left((\Delta\theta)^2 + \overline{\cos^2(\theta)}(\Delta\phi)^2\right) + \mathcal{O}\left({}^{(2)}g\right)}, \tag{5.61}
$$

where we have used the definition

$$\overline{g}_{rr} \equiv g_{rr} + \tfrac{1}{2}\Delta g_{rr}, \qquad \overline{g}_{\theta\theta} \equiv g_{\theta\theta} + \tfrac{1}{2}\Delta g_{\theta\theta}, \qquad \overline{\cos^2(\theta)} \equiv \cos^2(\theta) + \tfrac{1}{2}\Delta\cos^2(\theta), \quad (5.62)$$

and a term $-\frac{1}{2}\Delta g_{\theta\theta}[\Delta\cos^2(\theta)](\Delta\phi)^2$ is subsumed in the $\mathcal{O}\left({}^{(2)}g\right)$ terms in (5.61). Hence the first order correction represents a shift of evaluation at x^i_1 to the mean coordinate point $\bar{x}^i = x^i_1 + \frac{1}{2}\Delta x^i$.

We can examine the accuracy of the approximation (5.61), truncated at first order, by evaluating the second order correction terms of ${}^{(2)}g$, which will contain terms of order $\sim \frac{\left({}^{(1)}g\right)^2}{{}^{(0)}g}$ and terms involving the second derivatives of the metric. All of these terms should be evaluated in the model of interest and in the desired coordinate system, in order to examine the approximation (5.61). For observational coordinates (z, θ, ϕ) in both the FLRW and timescape model with realistic model parameters, we find $\frac{{}^{(2)}g}{{}^{(0)}g} \lesssim 10^{-3}$, for separation distances Δz, $\Delta\theta$, $\Delta\phi$ around the BAO scale.

Appendix 5.B The 2-point correlation function

The spatial 2-point correlation function ξ describes the excess probability of finding two galaxies at two given points on a spatial surface, relative to an uncorrelated sample. The typical formulation of the 2-point correlation function in standard cosmology is tightly linked to the assumption of symmetries of the 'background' FLRW space-time, and the ergodic assumptions on the density perturbation field on top of the background, which leads to the modelling of the galaxy distribution as a stationary and ergodic point process.

Thus if we revisit the 'background' cosmology, or do cosmology without imposing a background, we should also revisit the theory underlying the 2-point correlation function. Here we seek to provide a more general introduction to the 2-point correlation function, valid for models with no exact symmetries in the pointwise ensemble average of the galaxy counts.

Consider a spatial domain of a hypersurface $\mathcal{D}$. We view the position of the galaxies within this domain as random variables, and fix the total number of galaxies N within the domain $\mathcal{D}$. We use adapted coordinates x^i on the hypersurface, and denote the random position of the a'th particle x^i_a. The scaled probability (ensemble average number count) of finding two galaxies located in the infinitesimal volume elements

dV_X and dV_Y centred at the points $x^i = X^i$ and $x^i = Y^i$ can be written as

$$f(X,Y)dV_X\,dV_Y \equiv \langle N(dV_X)N(dV_Y)\rangle\,, \tag{5.63}$$

where $f(X,Y)$ is the number count density and where

$$N(dV_X) \equiv \sum_a^N \mathbb{1}_{dV_X}(x_a^i). \tag{5.64}$$

is the number count in the volume element dV_X in a given realisation, where

$$\mathbb{1}_{dV_X}(x_a^i) = \begin{cases} 1, & x_a^i \in dV_X, \\ 0, & x_a^i \notin dV_X, \end{cases} \tag{5.65}$$

is the indicator function. (If the volume dV_X is made small enough, this is zero or one in practice.) The spatial volume elements dV are given by[15] the adapted metric (5.1)

$$dV = \sqrt{\det(g_{ij})}dx^1 \wedge dx^2 \wedge dx^3. \tag{5.66}$$

The integral of (5.63) over two arbitrary domains $\mathcal{D}_X \in \mathcal{D}$ and $\mathcal{D}_Y \in \mathcal{D}$ is

$$\int_{X\in\mathcal{D}_X}\int_{Y\in\mathcal{D}_Y} f(X,Y)dV_X\,dV_Y = \langle N(\mathcal{D}_X)N(\mathcal{D}_Y)\rangle \tag{5.67}$$

following from the property $\mathbb{1}_{A\cup B}(y) = \mathbb{1}_A(y) + \mathbb{1}_B(y)$ of the indicator function, where A and B are disjoint sets.

The scaled probability of finding a galaxy in the small volume dV_X (ensemble average number count) can be expressed as an integral over (5.67)

$$f(X)dV_X \equiv \langle N(dV_X)\rangle = \frac{1}{N}\int_{Y\in\mathcal{D}} f(X,Y)dV_X\,dV_Y. \tag{5.68}$$

We shall be interested in writing the probability (5.63) in terms of the excess probability

[15] We could alternatively absorb any non-zero function into the number count density $f(X,Y)$ and make the redefinition $f(X,Y) \to \det(g_{ij})f(X,Y)$, $\quad dV \to dV/\sqrt{\det(g_{ij})} = dx^1 \wedge dx^2 \wedge dx^3$ if we prefer to work in terms of coordinate volumes instead of physical volumes.

of the uncorrelated process

$$f_{\rm Poisson}(X,Y) = f(X)f(Y), \qquad X \neq Y. \tag{5.69}$$

Assuming that $f(X) \neq 0$ over the domain $\mathcal{D}$ we can write

$$f(X,Y)\, dV_X\, dV_Y = f(X)f(Y)\,(1+\xi(X,Y))\, dV_X\, dV_Y \tag{5.70}$$

where we have defined

$$\xi(X,Y) = \frac{f(X,Y)}{f(X)f(Y)} - 1. \tag{5.71}$$

This correlation function, ξ, is zero for $X \neq Y$ for a Poisson point process per construction, and measures the departure from an uncorrelated distribution of galaxies.

The correlation function (5.71) is a function of all 6 variables (X^i, Y^i) in a general inhomogeneous universe. In practice, in BAO analysis, we are interested in integrating out some of these degrees of freedom, to isolate a characteristic statistical scale. We can make the substitution $(X^i, Y^i) \to (X^i, \hat{n}^i_X, D)$ in (5.63), where $\hat{n}^i_X$ is a unit vector at X^i defining a geodesic starting at X^i and intersecting Y^i and D is the geodesic distance from X^i to Y^i

$$f(X,Y)\, dV_X\, dV_Y = f(X,\hat{n}_X,D)\, dV_X\, d\hat{n}_X\, dD = f(X,\hat{n}_X,D)\, J\, dV_X\, dV_Y \tag{5.72}$$

with

$$J \equiv \det\left(\frac{\partial(X,\hat{n}_X,D)}{\partial(X,Y)}\right) \tag{5.73}$$

being the Jacobian of the transformation. It follows that (5.71) reads

$$\xi(X,\hat{n}_X,D) = \frac{f(X,\hat{n}_X,D)}{f_{\rm Poisson}(X,\hat{n}_X,D)} - 1, \tag{5.74}$$

where the Jacobian J of the transformation $(X^i, Y^i) \to (X^i, \hat{n}^i_X, D)$ cancels in (5.71), since f and $f_{\rm Poisson}$ have identical transformations. We denote the random process underlying the ensemble homogeneous and isotropic if $f_{HI}(X+\alpha) = f_{HI}(X)$, $f_{HI}(X+\alpha, R\hat{n}_X, D) = f_{HI}(X,\hat{n}_X,D)$ are satisfied, where α is an arbitrary translation, R is

an arbitrary rotation of the unit vector $\hat{n}_X$, and where the subscript HI stands for homogenous and isotropic. In this case (5.74) becomes the so-called reduced 2-point correlation function

$$\xi_{HI}(D) = \frac{f_{HI}(D)}{f_{HI\,\text{Poisson}}(D)} - 1. \tag{5.75}$$

In the general case where the random process underlying the ensemble is not associated with any exact symmetries, we can still create a reduced version of the correlation function (5.74) by marginalising over the direction and position degrees of freedom $\hat{n}_X$, X. This can be done as follows. We define the marginalised number count density over a subdomain $\mathcal{D}_S \in \mathcal{D}$ as

$$f(D, \mathcal{D}_S) \equiv \int_{X \in \mathcal{D}_S} dV_X \int dn_X f(X, \hat{n}_X, D). \tag{5.76}$$

The marginalised ensemble number count in a small range of affine distance dD is given by

$$f(D, \mathcal{D}_S) dD = \left\langle \sum_{a,b}^{N} \mathbb{1}_{[D,D+dD]}(D(x_a^i, x_b^i)) \mathbb{1}_{\mathcal{D}_S}(x_a^i) \right\rangle, \tag{5.77}$$

where we have used the fact that we can rewrite the number count in terms of the new coordinates $X, \hat{n}_X, D$,

$$\begin{aligned} N(dV_X)N(dV_Y) &= \sum_{a,b}^{N} \mathbb{1}_{dV_X}(x_a^i) \mathbb{1}_{dV_Y}(x_b^i) \\ &= \sum_{a,b}^{N} \mathbb{1}_{dV_X}(x_a^i) \mathbb{1}_{[\hat{n}_X, \hat{n}_X + d\hat{n}_X]}(\hat{n}_X(x_a^i, x_b^i)) \, \mathbb{1}_{[D,D+dD]}(D(x_a^i, x_b^i)), \end{aligned} \tag{5.78}$$

and that by (5.72) $f(X, \hat{n}_X, D)\, dV_X\, d\hat{n}_X\, dD = \langle N(dV_X)N(dV_Y) \rangle$. We can write (5.76) in terms of $f_{\text{Poisson}}(D, \mathcal{D}_S)$ defined through the integral over $f_{\text{Poisson}}(X, \hat{n}_X, D)$ analogue to (5.76).

$$f(D, \mathcal{D}_S)\, dD = f_{\text{Poisson}}(D, \mathcal{D}_S)\, (1 + \xi(D, \mathcal{D}_S))\, dD, \tag{5.79}$$

with

$$\xi(D, \mathcal{D}_S) = \frac{f(D, \mathcal{D}_S)}{f_{\text{Poisson}}(D, \mathcal{D}_S)} - 1, \tag{5.80}$$

which we denote the 'marginalised' two point correlation function.

Note that eq. (5.80) has the form of the conventional reduced 2-point correlation function of a homogenous and isotropic cosmology. However, the interpretation is different here, as the reduction does not follow from symmetry assumptions on the probability distribution of the density field, but rather follows from marginalisation over the position and direction degrees of freedom (and hence depends on scale through $\mathcal{D}_S$). Eq. (5.80) coincides with the conventional 2-point correlation function (5.75) when the galaxy distribution is assumed to be represented by a homogeneous and isotropic point process. We can thus view eq. (5.80) as a generalisation of the 2-point correlation function to inhomogeneous space-times.

For models of the form outlined in section 5.1.2 we can decompose $\hat{n}_X$ into μ, $\text{sgn}(\delta z)$, and the normalised angular separation vector $\delta\hat{\Theta} = \frac{1}{|\delta\Theta|}(\delta\theta, \cos(\theta)\delta\phi)$. In this case we can write

$$f(X, Y) dV_X\, dV_Y = f(X, \mu, \text{sgn}(\delta z), \delta\hat{\Theta}, D) dV_X\, d\mu\, d\delta\hat{\Theta}\, dD \tag{5.81}$$

and we can construct a marginalised number count density in D analogue to (5.76) by marginalising over the remaining variables. We shall sometimes be interested in keeping μ as a variable, and construct the following marginalised number count density

$$f(D, \mu, \mathcal{D}_S) \equiv \sum_{\text{sgn}(\delta z)=\pm 1} \int_{X \in \mathcal{D}_S} dV_X \int d\delta\hat{\Theta}\; f(X, \mu, \text{sgn}(\delta z), \delta\hat{\Theta}, D), \tag{5.82}$$

for which we can define the marginalised μ-dependent 2-point correlation function

$$\xi(D, \mu, \mathcal{D}_S) = \frac{f(D, \mu, \mathcal{D}_S)}{f_{\text{Poisson}}(D, \mu, \mathcal{D}_S)} - 1. \tag{5.83}$$

Integrating out the μ-dependence in (5.82) we arrive at the marginalised isotropic number count density $f(D, \mathcal{D}_S)$ from which we can construct the isotropic marginalised 2-point correlation function of (5.80).[16]

[16] For the estimate of (5.83) or (5.80) based on number counts in a subdomain $\mathcal{D}_{S'}$ of a single realisa-

We define the 'wedge' as the mean of eq. (5.83) over a given μ range $[\mu_1, \mu_2]$.

$$\xi_{[\mu_1,\mu_2]}(D) \equiv \frac{1}{\mu_2 - \mu_1} \int_{\mu_1}^{\mu_2} d\mu\, \xi(D,\mu), \tag{5.84}$$

where the dependence on $\mathcal{D}_S$ is implicit in (5.84) and in the following. It can be viewed as the mean excess of probability of finding two galaxies a distance D apart over the given μ range. We define the transverse and the radial wedge as respectively

$$\xi_\perp(D) \equiv \xi_{[0,0.5]}(D), \qquad \xi_\parallel(D) \equiv \xi_{[0.5,1]}(D). \tag{5.85}$$

When $f(D,\mu)$ is mainly depending on D such that

$$\begin{aligned} f(D,\mu) &= f(D)(1 + h(D,\mu)), \qquad h(D,\mu) \ll 1 \\ f_{\rm Poisson}(D,\mu) &= f_{\rm Poisson}(D)(1 + h_{\rm Poisson}(D,\mu)), \qquad h_{\rm Poisson}(D,\mu) \ll 1, \end{aligned} \tag{5.86}$$

we have the useful approximation

$$\begin{aligned} \int_0^1 d\mu\, \xi(D,\mu) &= \int_0^1 d\mu \frac{f(D)(1 + h(D,\mu))}{f_{\rm Poisson}(D)(1 + h_{\rm Poisson}(D,\mu))} - 1 \\ &\approx \int_0^1 d\mu \frac{f(D)}{f_{\rm Poisson}(D)}(1 + h(D,\mu) - h_{\rm Poisson}(D,\mu)) - 1 \\ &= \frac{f(D)}{f_{\rm Poisson}(D)} - 1 = \xi(D) \end{aligned} \tag{5.87}$$

where we have used $\int_0^1 d\mu\, h(D,\mu) = 0$ and $\int_0^1 d\mu\, h_{\rm Poisson}(D,\mu) = 0$ by construction. Note that corrections to eq. (5.87) are *second order* in h and $h_{\rm Poisson}$. A similar approximation can be formulated for the wedges (5.84)

$$\xi_{[\mu_1,\mu_2]}(D) \approx \xi(D, \mu_1 \le \mu \le \mu_2) \equiv \frac{f(D, \mu_1 \le \mu \le \mu_2)}{f_{\rm Poisson}(D, \mu_1 \le \mu \le \mu_2)} - 1. \tag{5.88}$$

---

tion of the ensemble to be representative for the ensemble average, we must invoke the approximate convergence condition $\hat{\xi}(D, \mathcal{D}'_S)_{\lim V(\mathcal{D}_{S'}) \to \infty} \approx \xi(D, \mathcal{D}_S)$ for some choice of scale $V(\mathcal{D}_S)$, with fast enough convergence of the estimate. In practice $\mathcal{D}_{S'}$ will correspond to a given survey domain.

CHAPTER 6

Quantifying the accuracy of the Alcock-Paczyński scaling of baryon acoustic oscillation measurements

Most work on the 2-point correlation function (theoretical and observational) has been done assuming homogeneous spatially-flat FLRW models. While cosmological data, when interpreted within the ΛCDM cosmology, suggests that the universe is spatially flat on large scales, there is nothing preventing significant large-scale spatial curvature if the universe is more accurately described by a model outside the class of the conventionally studied FLRW models which may still be consistent with the data. This is the case, e.g., in the timescape model [95, 96, 97] which is used as a test-case in this analysis.

In large-scale structure analysis there are strong motivations for assuming a fiducial cosmological model in data reduction such as the use of of N-body mocks to investigate non-linear effects. In the context of BAOs, applying a fiducial cosmological model allows the computation of an accurate template for the BAO peak and all galaxy pairs to be binned by their estimated co-moving spatial separation. Reconstruction methods [195] based on ΛCDM perturbation theory can further enhance the signal. An obvious draw-back of imposing fiducial model cosmologies in data reduction is that the assumptions of a model cosmology are then implicitly present in the conclusions drawn. This may in some cases bias the results, lead to an underestimation of the error budget, and will in a worst-case scenario lead to circular verification of the assumed fiducial cosmological model.

Alcock and Paczyński [217] introduced a geometric test to compare radial and transverse distance measures for a spherical region that is expanding with the Hubble flow in a FLRW model. This provided the means to distinguish FLRW models with a cosmological constant from those with $\Lambda = 0$. Recent analyses of the BAO scale

build on the ideas of Alcock and Paczyński [217] and its early applications [218, 219], and are now described as AP scaling methods. In modern analysis these methods are applied to parametrise a FLRW trial cosmology in terms of a different fiducial FLRW cosmology to 'first order' [220, 199].

The AP scaling used in BAO analysis, (see, e.g., [194, 193]), makes use of this reparametrisation in order to test cosmological models different to the fiducial model. The extent to which the AP scaling methods, which rely on the scaling of a fiducial template-metric by two constant 'AP scaling parameters', can be thought of as independent of the fiducial model cosmology has not been thoroughly tested in the literature. This question is important for the range of validity of the distance measurements inferred from such procedures, and for constraining alternative cosmological models to that of the fiducial template-metric used to extract them.

While the systematic errors related to the AP-distortion of conventional BAO analysis have been quantified by some studies such as [208, 221], such analyses usually only examine the cases of a few ΛCDM models which are close in terms of model parameters. In this chapter we will test the extent to which this underestimates the error for constraining models which are outside the narrow space of cosmological models assessed for systematics, using the framework developed in chapter 5 to study the 2-point correlation function and the BAO feature in spherically-symmetric template metrics.

In section 6.1 we outline some theoretical results and definitions on which the analysis of this work is built. In section 6.2 we provide general results for the effect of the AP scaling on the 2-point correlation function as viewed in the fiducial cosmological model as compared to the 'true' underlying cosmological model, and we propose a new and improved AP scaling approximation. In section 6.3 we apply our results to a concrete model of the 2-point correlation function, and investigate how the BAO feature depends on the redshift-dependent AP scaling. In section 6.4 we test our predictions by applying them to the 2-point correlation function based on ΛCDM mock catalogues and formulated in a selection of fiducial model cosmologies, some of which are 'physical' cosmological models built from general relativistic modelling and some of which are 'artificial' models. We assess systematic errors associated with the AP scaling approximations and additional systematic errors. We discuss our results in section 6.5.

6.1 The framework

6.1.1 Models under investigation

We follow chapter 5 and consider the observer-adapted spherically-symmetric template metrics[1]

$$ds^2 = -\alpha(t,r)^2 c^2 dt^2 + g_{rr}(t,r)\, dr^2 + g_{\theta\theta}(t,r)\left(d\theta^2 + \cos^2(\theta) d\phi^2\right), \tag{6.1}$$

where θ and ϕ are angular coordinates on the observer's sky, r is a radial coordinate, and t is a time-coordinate labelling surfaces orthogonal to the 'matter frame' with which the galaxies of the survey are (statistically) comoving. We shall further assume that the model-redshift z of radially propagating null rays is monotonic in the radial coordinate r, in which case the adapted metric on a given 3-surface selected by $t = T$ can be written

$$ds_T^2 = g_{zz}(t = T, r) dz^2 + g_{\theta\theta}(t = T, r)\left(d\theta^2 + \cos^2(\theta) d\phi^2\right), \tag{6.2}$$

where

$$g_{zz}(t = T, r) \equiv g_{rr}(t = T, r)\left(\frac{dr}{dz}\right)^2. \tag{6.3}$$

As outlined in appendix 5.A, for small separations of points P_1 and P_2 on the $t = T$ hypersurface as compared to variations of the adapted spatial metric (6.2), the geodesic distance $D_T(P_1, P_2)$ between the points P_1 and P_2 represented by coordinates (z_1, θ_1, ϕ_1) and (z_2, θ_2, ϕ_2) is

$$D_T^2(P_1, P_2) \approx g_{zz}(t = T, \bar{z})(\delta z)^2 + g_{\theta\theta}(t = T, \bar{z})(\delta\Theta)^2, \tag{6.4}$$

[1] The metric considered might be an exact solution to the Einstein equations (e.g., a Lemaître-Tolman-Bondi space-time metric), a solution to other specified field equations from modified gravity theories, or an effective metric which is not necessarily a space-time metric substituted into the Einstein equations or any set of local field equations. The spherically-symmetric metrics allow for defining the Alcock-Paczyński (AP) scaling in section 6.1.2.

where $\bar{z} = (z_1 + z_2)/2$ is the intermediate redshift, $\delta z = z_2 - z_1$ is the separation in redshift, and $\delta\Theta$ is the separation in angle

$$\begin{aligned}\delta\Theta &= \arccos\left[\sin(\theta_1)\sin(\theta_2) + \cos(\theta_1)\cos(\theta_2)\cos(\phi_2 - \phi_1)\right] \\ &\approx \sqrt{(\theta_2 - \theta_1)^2 + \cos^2(\bar{\theta})(\phi_2 - \phi_1)^2}, \qquad \bar{\theta} = (\theta_1 + \theta_2)/2\end{aligned} \tag{6.5}$$

As an example, for the FLRW and timescape [97, 128, 98] models with reasonable model parameters, we find that higher-order corrections to eq. (6.4) are of order $\lesssim 10^{-3}$ for galaxy separations of order 100 Mpc/h.

From the approximation (6.4) it is natural to define the 'radial fraction' of the separation as

$$\mu_T(P_1, P_2) = \frac{\sqrt{g_{zz}(t = T, \bar{z})(\delta z)^2}}{D_T(P_1, P_2)}. \tag{6.6}$$

It is conventional to take the surface of evaluation $t = T$ to be that of the 'present epoch'. When we refer to evaluation at the present epoch we shall omit the T subscript on eq. (6.4) and (6.6). We shall also sometimes omit the reference to the points P_1,P_2 for ease of notation, and refer to $D_T(P_1, P_2)$ and $\mu_T(P_1, P_2)$ as D and μ respectively.

6.1.2 Alcock-Paczyński scaling

The conventional Alcock-Paczyński (AP) scaling as outlined in [220, 199] exploits the fact that a geodesic distance between two points in a spherically-symmetric large-scale metric can be approximated by (6.4), as long as second-order metric variations within the distance spanned between the points are negligible.

The geodesic distance between 'closely separated' points in a model cosmology of the type described in section 6.1.1 can be parametrised in terms of an unknown 'true' model cosmology of the same type, by associating points of the same observational coordinates (z, θ, ϕ), as

$$\begin{aligned}D^2 &\approx g_{zz}(t = T_0, z)(\delta z)^2 + g_{\theta\theta}(t = T_0, z)(\delta\Theta)^2 \\ &= \frac{1}{\alpha_\parallel^2(z)} g^{\rm tr}_{zz}(t^{\rm tr} = T_0^{\rm tr}, z)(\delta z)^2 + \frac{1}{\alpha_\perp^2(z)} g^{\rm tr}_{\theta\theta}(t^{\rm tr} = T_0^{\rm tr}, z)(\delta\Theta)^2\end{aligned} \tag{6.7}$$

where 'tr' stands for the 'true' cosmology, $t = T_0$ and $t^{\rm tr} = T_0^{\rm tr}$ are the 'present epoch'

hypersurfaces of the trial model cosmology and the 'true' model cosmology respectively, and the redshift of evaluation z is the mean redshift of the points. The AP scaling functions

$$\alpha_{\parallel}(z) \equiv \sqrt{\frac{g^{\mathrm{tr}}_{zz}(t^{\mathrm{tr}} = T^{\mathrm{tr}}_0, z)}{g_{zz}(t = T_0, z)}}, \qquad \alpha_{\perp}(z) \equiv \sqrt{\frac{g^{\mathrm{tr}}_{\theta\theta}(t^{\mathrm{tr}} = T^{\mathrm{tr}}_0, z)}{g_{\theta\theta}(t = T_0, z)}}, \tag{6.8}$$

describe the relative radial and transverse distortion between the 'true' cosmology and the trial cosmology. We can re-express the information of $\alpha_{\parallel}(z)$ and $\alpha_{\perp}(z)$ in terms of the isotropic scaling function $\alpha(z)$ and the anisotropic scaling function $\epsilon(z)$

$$\alpha(z) \equiv (\alpha^2_{\perp}(z)\alpha_{\parallel}(z))^{1/3}, \qquad (1 + \epsilon(z))^3 \equiv \frac{\alpha_{\parallel}(z)}{\alpha_{\perp}(z)}. \tag{6.9}$$

The definitions (6.9) are analogous to those presented in [220], except that we keep the redshift dependence instead of assuming $\alpha(z)$ and $\epsilon(z)$ to be constant. The function $\alpha(z)$ describes how the volume measure of a small coordinate volume $\delta z\, \cos(\theta)\, \delta\theta\, \delta\phi$ centred at z differs between the 'true' and the model cosmology, while $\epsilon(z)$ quantifies the relative scaling of the angular and transverse metric components between the 'true' and the model cosmologies.

Using the definitions (6.6) and (6.9), we can rewrite the approximation (6.7) for points with mean redshift z as (see chapter 5)

$$(D^{\mathrm{tr}})^2 \approx \alpha^2(z) D^2 \frac{1 + \psi(z)\mu^2}{(1 + \epsilon(z))^2}\,, \qquad \psi(z) \equiv (1 + \epsilon(z))^6 - 1. \tag{6.10}$$

Similarly, using the definitions (6.6) and (6.9), and the result (6.10), we have the relation

$$(\mu^{\mathrm{tr}})^2 \approx \mu^2 \frac{(1 + \epsilon(z))^6}{1 + \psi(z)\mu^2}. \tag{6.11}$$

When the AP scaling is applied in standard analysis it is assumed that $\alpha(z)$ and $\epsilon(z)$ can be considered constant and equal to their evaluation at the effective redshift of the survey, i.e., that the replacement $\alpha(z) \mapsto \alpha(\bar{z})\,, \epsilon(z) \mapsto \epsilon(\bar{z})$ is accurate. This replacement is expected to be a reasonable approximation if the survey volume has a relatively narrow redshift distribution, and if both the 'true' and the model metric are slowly changing in redshift.

In the present analysis we will investigate the correction terms that arise when we take into account the variation of $\alpha(z)$ and $\epsilon(z)$ over the survey volume, and quantify the accuracy of the usual constant AP scaling approximation $\alpha(z) \mapsto \alpha(\bar{z})$, $\epsilon(z) \mapsto \epsilon(\bar{z})$ when applied in the 2-point correlation function to extract the parameters of the BAO feature.

6.1.3 Empirical model for the correlation function

In this section we introduce the empirical fitting function we use for examining the BAO feature of the two-point correlation function, its dependence on the fiducial cosmology, and the accuracy of the constant AP scaling approximation. We could have used the fiducial ΛCDM template fitting function outlined, e.g., in [193], where the BAO feature is derived from a model power spectrum. However, we expect the conclusions about the accuracy of the constant AP scaling approximation to be similar between the two fitting functions. The advantage of considering the simple empirical fitting function is that it does not assume a particular cosmological model. Specifically, for non-FLRW models where no well-defined perturbation theory exists, but where we nevertheless expect a statistical standard ruler to be present in form of a BAO scale, we must rely on empirical extraction methods of the BAO characteristic scale. Furthermore, the simple form of the empirical fitting function presented here allows us to obtain useful analytical results.

We follow chapter 5 and consider the model for the 2-point correlation function (6.57)

$$\xi^{\rm tr}(D^{\rm tr},\mu^{\rm tr},z) = (D^{\rm tr})^2 A(z)\, \mathrm{e}^{\frac{-\left(D^{\rm tr}-r\right)^2}{2\sigma^2(z)}} + C_0^{\rm tr}(\mu^{\rm tr},z) + \frac{C_1^{\rm tr}(\mu^{\rm tr},z)}{D^{\rm tr}} + \frac{C_2^{\rm tr}(\mu^{\rm tr},z)}{(D^{\rm tr})^2}\,, \quad (6.12)$$

as formulated in the underlying 'true' cosmology, where r denotes the BAO scale or a characteristic scale shifted with respect to the BAO scale. (See the discussion below on calibration of the BAO scale.) The polynomial terms account for the 'background' shape of the correlation function without the BAO feature and are equivalent in form to those of [193]. The scaled Gaussian models the BAO feature, and replaces the ΛCDM power spectrum model of [193]. Empirical models of similar form to (6.12) have been considered in, e.g., [209, 210, 211].

Note that in contrast to previous analyses we are modelling the redshift-dependent

2-point correlation function $\xi^{\rm tr}(D^{\rm tr}, \mu^{\rm tr}, z)$ (6.57). This is done to examine the impact of the redshift dependence of the generalised AP-scaling functions (6.9). For simplicity we assume a model where A and σ are constant for the numerical investigations in this chapter, while no assumption is made on the redshift dependence of the polynomial coefficients.

We assume the peak of the BAO feature r to be a 'standard ruler' independent of redshift. This approximation is good in ΛCDM cosmology as confirmed with ΛCDM mock catalogues in [212] using standard ΛCDM template procedures and in chapter 5 using the empirical model presented here. From the results in [212] and chapter 5 we can expect shifts of the BAO scale of $\lesssim 0.5\%$ in a ΛCDM universe at redshifts $\gtrsim 0.3$. The approximation is less obviously good in non-ΛCDM cosmology, where environmental dependence of the BAO peak is expected [197]. However, as long as: (i) data is not binned according to environmental factors such as density, and (ii) each redshift slice represents the volume average for the corresponding approximate cosmic epoch, then we might make the ansatz that r is an approximate statistical standard ruler for volume measures.

The scaling of the Gaussian part of the model 2-point correlation function in (6.12) is an approximation that accounts for calibration issues in BAO physics: that the local maximum of the 2-point correlation function does not in general correspond to the BAO scale. (In ΛCDM cosmology these two scales differ by roughly $\sim 2-3\%$.) The scaling by the factor $(D^{\rm tr})^2$ of the Gaussian feature allows us to interpret the mean of the Gaussian r as the BAO scale with a precision of $< 1\%$ within the ΛCDM concordance cosmology, as verified with ΛCDM mock catalogues in chapter 5. Note that the degree to which r can be interpreted as a BAO scale for other models must be assessed for each particular case, or simply be posed as an ansatz of the analysis.[2]

[2] For models where perturbation theory has yet to be developed, we cannot predict how the sound horizon scale of the drag epoch will appear in the galaxy distribution, and an ansatz is needed in order to constrain the sound horizon scale at the drag epoch with galaxy catalogues.

6.2 Theoretical investigation of the redshift-dependent Alcock-Paczyński scaling

In this section we investigate how the redshift-dependent Alcock-Paczyński scaling enters in the 2-point correlation function. We quantify the accuracy of the conventional constant Alcock-Paczyński (AP) scaling approximation $\alpha(z) \mapsto \alpha(\bar{z})$, $\epsilon(z) \mapsto \epsilon(\bar{z})$ over the survey volume. Based on our investigations, we propose a new and improved version of the constant Alcock-Paczyński (AP) scaling.

In standard BAO analysis, as described in, e.g., [220, 199] for ΛCDM cosmology, and in the generalisation of such analyses to generic geometries (see chapter 5), the fitting procedure is based on making an ansatz for the form of the 2-point correlation function as formulated in the unknown 'true' cosmological model. Furthermore, the assumed function is parameterised in a given fiducial cosmology using AP scaling methods as outlined in section 6.1.2.

6.2.1 Re-parametrisation of the 2-point correlation function

Suppose that the 2-point correlation function (6.57) in D, μ, and z has the form

$$\xi^{\mathrm{tr}}(D^{\mathrm{tr}}, \mu^{\mathrm{tr}}, z) = \frac{f^{\mathrm{tr}}(D^{\mathrm{tr}}, \mu^{\mathrm{tr}}, z)}{f^{\mathrm{tr}}_{\mathrm{Poisson}}(D^{\mathrm{tr}}, \mu^{\mathrm{tr}}, z)} - 1, \tag{6.13}$$

in the 'true' spherically-symmetric cosmology, where $f^{\mathrm{tr}}(D^{\mathrm{tr}}, \mu^{\mathrm{tr}}, z)$ and $f^{\mathrm{tr}}_{\mathrm{Poisson}}(D^{\mathrm{tr}}, \mu^{\mathrm{tr}}, z)$ are the probability densities of finding a pair of galaxies separated by D^{tr} and μ^{tr} with one of the galaxies centred at z, in the catalogue and random catalogue respectively. We can express $\xi(D, \mu, z)$ of any other given spherically-symmetric model in terms of $\xi^{\mathrm{tr}}(D^{\mathrm{tr}}, \mu^{\mathrm{tr}}, z)$ in the following way

$$\begin{aligned}\xi(D, \mu, z) &= \frac{f(D, \mu, z)}{f_{\mathrm{Poisson}}(D, \mu, z)} - 1 = \frac{J\, f^{\mathrm{tr}}\left(D^{\mathrm{tr}}\left(D, \mu, \alpha(z), \epsilon(z)\right), \mu^{\mathrm{tr}}(\mu, \epsilon(z)), z\right)}{J\, f^{\mathrm{tr}}_{\mathrm{Poisson}}\left(D^{\mathrm{tr}}(D, \mu, \alpha(z), \epsilon(z)), \mu^{\mathrm{tr}}(\mu, \epsilon(z)), z\right)} - 1 \\ &= \xi^{\mathrm{tr}}\left(D^{\mathrm{tr}}(D, \mu, \alpha(z), \epsilon(z)), \mu^{\mathrm{tr}}(\mu, \epsilon(z)), z\right),\end{aligned} \tag{6.14}$$

where J is the determinant of the Jacobian of the transformation $(D^{\mathrm{tr}}, \mu^{\mathrm{tr}}) \mapsto (D, \mu)$ which can be derived from (6.10) and (6.11). The first line follows from the transformation of a density under a change of variables by the determinant of the Jacobian of the transformation, and the second line follows from the cancellation of J in the nu-

merator and denominator of the expression. Note that $D^{\rm tr}$ and $\mu^{\rm tr}$ introduce redshift dependence in $\xi(D,\mu,z)$ through $\alpha(z)$ and $\epsilon(z)$. We shall sometimes be interested in evaluating the right hand side of (6.14) for parameters α and ϵ which do not necessarily correspond to the redshift dependent AP scaling functions $\alpha(z)$ and $\epsilon(z)$. In such cases we simply write $\xi^{\rm tr}\left(D^{\rm tr}(D,\mu,\alpha,\epsilon),\mu^{\rm tr}(\mu,\epsilon),z\right)$ for evaluation for any given point z,α,ϵ.

As outlined in appendix 6.A, $\xi(D,\mu)$ (6.59) can be obtained as a weighted integral in redshift over $\xi(D,\mu,z)$ if the condition of almost multiplicative separability (6.63) is satisfied. If this is the case the result in (6.66) holds, and to first order in the non-multiplicatively separable functions $\delta(D,\mu,z)$ and $\delta_{\rm Poisson}(D,\mu,z)$ defined in (6.63), we have

$$\xi(D,\mu) \approx \int dz\, P(z)\, \xi(D,\mu,z), \tag{6.15}$$

where $P(z)$ is the normalised galaxy distribution in redshift (6.62). We might further expand $\xi(D,\mu,z) = \xi^{\rm tr}\left(D^{\rm tr}(D,\mu,\alpha,\epsilon),\mu^{\rm tr}(\mu,\epsilon),z\right)$ to first order in z, α, and ϵ, (leaving α and ϵ as exact functions in z, rather than their approximations in terms of expansions in z), around some appropriate point $z=\mathring{z}$ to obtain

$$\begin{aligned}
\xi(D,\mu) &\approx \int dz\, P(z)\, \xi(D,\mu,z) = \\
&\approx \int dz\, P(z) \left(\xi^{\rm tr}\big|_{\mathring{z},\mathring{\alpha},\mathring{\epsilon}} + \left.\frac{\partial \xi^{\rm tr}}{\partial z}\right|_{\mathring{z},\mathring{\alpha},\mathring{\epsilon}} (z-\mathring{z}) + \left.\frac{\partial \xi^{\rm tr}}{\partial \alpha}\right|_{\mathring{z},\mathring{\alpha},\mathring{\epsilon}} (\alpha-\mathring{\alpha}) + \left.\frac{\partial \xi^{\rm tr}}{\partial \epsilon}\right|_{\mathring{z},\mathring{\alpha},\mathring{\epsilon}} (\epsilon-\mathring{\epsilon}) \right) \\
&= \xi^{\rm tr}\big|_{\mathring{z},\mathring{\alpha},\mathring{\epsilon}} + \left.\frac{\partial \xi^{\rm tr}}{\partial z}\right|_{\mathring{z},\mathring{\alpha},\mathring{\epsilon}} (\bar{z}-\mathring{z}) + \left.\frac{\partial \xi^{\rm tr}}{\partial \alpha}\right|_{\mathring{z},\mathring{\alpha},\mathring{\epsilon}} (\bar{\alpha}-\mathring{\alpha}) + \left.\frac{\partial \xi^{\rm tr}}{\partial \epsilon}\right|_{\mathring{z},\mathring{\alpha},\mathring{\epsilon}} (\bar{\epsilon}-\mathring{\epsilon}) \\
&\approx \xi^{\rm tr}\big|_{\bar{z},\bar{\alpha},\bar{\epsilon}}\,,
\end{aligned} \tag{6.16}$$

where $\{\mathring{z},\mathring{\alpha},\mathring{\epsilon}\} = \{\mathring{z},\alpha(\mathring{z}),\epsilon(\mathring{z})\}$, and where we use the short hand notation $\xi^{\rm tr}|_{z,\alpha,\epsilon} \equiv \xi^{\rm tr}\left(D^{\rm tr}(D,\mu,\alpha,\epsilon),\mu^{\rm tr}(\mu,\epsilon),z\right)$ where the dependence on D,μ is implicit. In the third line of (6.16) we have used the short-hand notation for the averages in redshift

$$\bar{z} \equiv \int dz\, P(z)\, z\,, \qquad \bar{\alpha} \equiv \int dz\, P(z)\, \alpha(z)\,, \qquad \bar{\epsilon} \equiv \int dz\, P(z)\, \epsilon(z)\,, \tag{6.17}$$

which we use throughout this analysis. The accuracy of the expansion (6.16) depends

on the magnitude of the deviations of z, α, ϵ over the survey and on the function $\xi(D,\mu,z) = \xi^{\rm tr}\left(D^{\rm tr}(D,\mu,\alpha,\epsilon), \mu^{\rm tr}(\mu,\epsilon), z\right)$.

The result in (6.16) *suggests that the re-parametrising of a given physical 2-point correlation function in terms of a distorted fiducial cosmology is more accurately described by the survey averages $\bar{\alpha}$ and $\bar{\epsilon}$ of the AP-scaling functions, rather than by the same AP-scaling functions evaluated at the mean redshift of the survey $\alpha(\bar{z})$ and $\epsilon(\bar{z})$. This conjecture is substantiated in appendix 6.B. We shall examine this hypothesis for a set of concrete empirical models for the 2-point correlation function of mock catalogues in section 6.4.*

We will denote the replacement $\alpha(z) \mapsto \bar{\alpha}$, $\epsilon(z) \mapsto \bar{\epsilon}$ the *modified* constant AP scaling approximation, in order to distinguish it from the standard constant AP scaling approximation $\alpha(z) \mapsto \alpha(\bar{z})$, $\epsilon(z) \mapsto \epsilon(\bar{z})$. The modified constant AP scaling approximation is intuitive, and formalises that statistical estimators built from a survey probe *averaged* distance scales over the survey volume.

6.2.2 Bounding the difference between the constant AP scaling approximations

We now quantify the difference between the modified constant AP scaling approximation $\alpha(z) \mapsto \bar{\alpha}$, $\epsilon(z) \mapsto \bar{\epsilon}$ and the standard constant AP scaling approximation $\alpha(z) \mapsto \alpha(\bar{z})$, $\epsilon(z) \mapsto \epsilon(\bar{z})$. In the ideal case, where the modified constant AP scaling approximation $\alpha(z) \mapsto \bar{\alpha}$, $\epsilon(z) \mapsto \bar{\epsilon}$ can be made with no error in the approximation (6.16), we can view the difference between the two AP approximations as quantifying the error in the conventional AP approximation $\alpha(z) \mapsto \alpha(\bar{z})$, $\epsilon(z) \mapsto \epsilon(\bar{z})$.[3]

Assuming that $\alpha(z)$ and $\epsilon(z)$ are both twice differentiable over the redshift range of the survey we can use the following approximations

$$\alpha(z) = \alpha(\bar{z}) + \frac{\partial\alpha}{\partial z}(\bar{z})\,(z-\bar{z}) + \mathcal{R}_1^{\alpha}(z)\,, \qquad \epsilon(z) = \epsilon(\bar{z}) + \frac{\partial\epsilon}{\partial z}(\bar{z})\,(z-\bar{z}) + \mathcal{R}_1^{\epsilon}(z)\,, \tag{6.18}$$

where $\mathcal{R}_1^{\alpha}(z)$ and $\mathcal{R}_1^{\epsilon}(z)$ are the remainder terms of the first order expansions in α and

[3] Indeed, the modified constant AP scaling approximation $\alpha(z) \mapsto \bar{\alpha}$, $\epsilon(z) \mapsto \bar{\epsilon}$ turns out to be very accurate for the broad sample of tested models in section 6.4.

ϵ respectively. Let us first consider the α parameter. Its integral reads

$$\bar{\alpha} = \int dz\, P(z)\, \alpha(z) = \alpha(\bar{z})\,(1 + \Delta_\alpha)\ , \tag{6.19}$$

where we define the 'error term' as

$$\Delta_\alpha \equiv \frac{1}{\alpha(\bar{z})} \int dz\, P(z)\, \mathcal{R}_1^\alpha(z)\,, \tag{6.20}$$

where it has been used that the first order term in (6.18) vanishes by construction, since $\overline{(z-\bar{z})} \equiv \int dz\, P(z)\,(z-\bar{z}) = 0$. We can bound the error term (6.20) by bounding the remainder $\mathcal{R}_1^\alpha(z)$ of the first order expansion (6.18). The detailed derivations of a bound on the error term (6.20) and the corresponding error term for ϵ are given in appendix 6.C. We obtain the following bound, derived in appendix 6.C.1:

$$|\Delta_\alpha| \;\leq\; \frac{1}{2}\frac{M_{L\,0}^{\max}}{M_{L\,0}^{\min}} \left(\beta_{L\,2} M_{L\,2} + 2\beta_{L\,1}^2 M_{L\,1}\right) \overline{(z-\bar{z})^2}, \tag{6.21}$$

where $M_{L\,0}^{\min}$, $M_{L\,0}^{\max}$, $M_{L\,1}$, $M_{L\,2}$, $\beta_{L\,1}$, and $\beta_{L\,2}$ are all positive dimensionless constants bounding the metric combinations $L \equiv (g_{\theta\theta}^2 g_{zz})^{\frac{1}{6}}$, $L^{\mathrm{tr}} \equiv ((g_{\theta\theta}^{\mathrm{tr}})^2 g_{zz}^{\mathrm{tr}})^{\frac{1}{6}}$ and their derivatives in the following way

$$M_{L\,0}^{\min} \leq \frac{L^{\mathrm{tr}}}{L} \leq M_{L\,0}^{\max}, \qquad \left| \frac{\left(\frac{\partial L^{\mathrm{tr}}/\partial z}{L^{\mathrm{tr}}}\right)}{\left(\frac{\partial L/\partial z}{L}\right)} - 1 \right| \leq M_{L\,1}\,, \qquad \left| \frac{\left(\frac{\partial^2 L^{\mathrm{tr}}/\partial z^2}{L^{\mathrm{tr}}}\right)}{\left(\frac{\partial^2 L/\partial z^2}{L}\right)} - 1 \right| \leq M_{L\,2}\,, \tag{6.22}$$

$$\left| \frac{\frac{\partial L}{\partial z}}{L} \right| \leq \beta_{L\,1}\,, \qquad \left| \frac{\frac{\partial^2 L}{\partial z^2}}{L} \right| \leq \beta_{L\,2}. \tag{6.23}$$

We note that it is possible to have order of magnitude ~ 1 deviations between the models such that $M_{L\,0}^{\max} \sim 1/M_{L\,0}^{\min} \sim 2$ and $M_{L\,1} \sim M_{L\,2} \sim 1$ while still having $\Delta_\alpha \lesssim$ a few percent, depending on the survey and of the first and second-order derivatives of L. We shall investigate bounds for various choices of trial cosmologies in subsection

6.2.3 below. Let us next consider the corresponding integral for ϵ,

$$\bar{\epsilon} = \int dz\, P(z)\, \epsilon(z) = \epsilon(\bar{z}) + \Delta_\epsilon\,, \tag{6.24}$$

where we define the error term,

$$\Delta_\epsilon \equiv \int dz\, P(z)\, \mathcal{R}_1^\epsilon(z) \tag{6.25}$$

which is obtained in a similar way as the error term Δ_α in (6.20). Note that, as opposed to α which is strictly larger than zero since it describes the ratio of two positive distance scales, ϵ can be zero, and thus, Δ_ϵ is defined as an absolute error rather than a relative error. We obtain the following bound on Δ_ϵ, derived in appendix 6.C.2:

$$|\Delta_\epsilon| \;\leq\; \frac{1}{6} M_{R0}^{\max} \left(\beta_{R2} M_{R2} + 2\beta_{R1}^2 \left(M_{R1} + \frac{1}{3} M_{R1}^2 \right) \right) \overline{(z-\bar{z})^2}\,, \tag{6.26}$$

where $M_{R0}^{\max}$, M_{R1}, M_{R2}, β_{R1}, and β_{R2} are all positive dimensionless constants bounding the metric combinations $R \equiv (g_{zz}/g_{\theta\theta})^{1/2}$ and $R^{\rm tr} \equiv (g_{zz}^{\rm tr}/g_{\theta\theta}^{\rm tr})^{1/2}$ in the following way

$$\left(\frac{R^{\rm tr}}{R}\right)^{\frac{1}{3}} \leq M_{R0}^{\max}, \qquad \left| \frac{\left(\frac{\partial R^{\rm tr}/\partial z}{R^{\rm tr}}\right)}{\left(\frac{\partial R/\partial z}{R}\right)} - 1 \right| \leq M_{R1}\,, \qquad \left| \frac{\left(\frac{\partial^2 R^{\rm tr}/\partial z^2}{R^{\rm tr}}\right)}{\left(\frac{\partial^2 R/\partial z^2}{R}\right)} - 1 \right| \leq M_{R2}\,, \tag{6.27}$$

$$\left| \frac{\frac{\partial R}{\partial z}}{R} \right| \leq \beta_{R1}\,, \qquad \left| \frac{\frac{\partial^2 R}{\partial z^2}}{R} \right| \leq \beta_{R2}\,. \tag{6.28}$$

The bound in (6.26) shows that it is possible to have order of magnitude ~ 1 deviations between the models such that $M_{R0}^{\max} \sim 2$ and $M_{R1} \sim M_{R2} \sim 1$ while still having $\Delta_\alpha \lesssim$ a few percent, depending on the survey and of the first and second-order derivatives of R.

Assuming that the modified constant AP approximation is accurate – which is indeed the case for the broad sample of tested models in section 6.4 – the bounds in (6.21) and (6.26) are useful for quantifying which models are expected to be well-approximated by the usual constant AP scaling approximation: $\alpha \mapsto \alpha(\bar{z})$, $\epsilon \mapsto \epsilon(\bar{z})$.

For models that have metric combinations L and R with derivatives up to second order within order ~ 1 from the corresponding derivatives of the 'true' metric combinations L^{tr} and R^{tr}, we expect the usual constant AP scaling approximation to be reasonable for typical galaxy surveys.

For example, the CMASS NGC catalogue [204] has $\overline{(z-\bar{z})^2} = 4.0 \times 10^{-3}$ when including galaxies in the interval $0.43 < z < 0.7$, and the LOWZ NGC catalogue has $\overline{(z-\bar{z})^2} = 5.7 \times 10^{-3}$ when including galaxies in the interval $0.15 < z < 0.43$. Thus the terms multiplying (6.21) and (6.26) must be larger than 1 in order to facilitate a correction of more than 1% to the standard constant AP scaling approximation for these surveys. Such large terms can only be obtained if one considers models with large bounding coefficients in (6.22), (6.23), (6.27), and (6.28). This could for instance happen for a 'true' model differing by more than order ~ 1 from the fiducial model – e.g., if the fiducial model is 'smooth' in its distance measures while the 'true' model is rapidly oscillating.

6.2.3 Quantitative results for selected models

We now consider a few model cosmologies for which we will compute the error terms Δ_α and Δ_ϵ and their corresponding bounds as given by the results in section 6.2.2. The models investigated are the spatially-flat ΛCDM model with $\Omega_M = 0.99$, the Milne universe model, the spatially-flat FLRW model with[4] $\Omega_M = 0$ and with phantom energy equation of state $w = -4/3$, and the timescape cosmological model with $\Omega_M = 0.3$. In addition we consider a class of unphysical models which are bounded with respect to a fiducial ΛCDM model but which allows for large metric gradients.

We consider the typical redshift range used for the LOWZ catalogue $0.15 < z < 0.43$ and the CMASS catalogue $0.43 < z < 0.7$ respectively.

We imagine that the given model cosmology is the 'true' underlying cosmology, and take the spatially-flat ΛCDM model with $\Omega_M = 0.3$, $\Omega_\Lambda = 0.7$ to be the fiducial cosmological model. The derivations below could easily be reversed in terms of 'true'

[4] Here Ω_M refers to the present epoch value of the "dressed matter density parameter" in the timescape model. It is *not* related to the Friedmann equation in the usual way and is not a fundamental parameter of the model. Rather it is defined for convenience to take numerical values of similar order to those of the matter density parameter in the ΛCDM model. At late epochs it is related to fundamental parameter of the model, the void fraction f_{v}, according to $\Omega_M = \frac{1}{2}(1-f_{\mathrm{v}})(2+f_{\mathrm{v}})$.

and fiducial cosmology, by making the replacements $L \leftrightarrow L^{\rm tr}$ and $R \leftrightarrow R^{\rm tr}$ in all expressions of section 6.2.2.

For a given underlying 'true' cosmological model and for a given redshift distribution of a survey, we can compute Δ_α (6.20) and Δ_ϵ (6.25). We might also compute the associated bounds on $|\Delta_\alpha|$ (6.21) and $|\Delta_\epsilon|$ (6.26), assuming knowledge only on the realised bounds (6.22), (6.23), (6.27), and (6.28), but no additional knowledge of the functions $\alpha(z)$ and $\epsilon(z)$.

For convenience, we model the redshift distributions of the galaxy catalogues as truncated Gaussian distributions

$$P(z) \equiv \begin{cases} \frac{1}{\mathcal{N}} \frac{1}{\sqrt{2\pi}\sigma} e^{\frac{-(z-\mu)^2}{2\sigma^2}} & z \in [z_1, z_2]\,, \\ 0 & \text{otherwise}\,, \end{cases} \qquad \mathcal{N} \equiv \int_{z_1}^{z_2} \frac{1}{\sqrt{2\pi}\sigma} e^{\frac{-(z-\mu)^2}{2\sigma^2}}\,, \tag{6.29}$$

noting that using the exact redshift distributions produce nearly identical results. The normalised redshift distributions of CMASS and LOWZ are shown with superimposed Gaussian models with suitable parameters μ and σ in figure 6.1.

We compute $\bar{\alpha}$ and $\bar{\epsilon}$ and compare these to α and ϵ evaluated at the mean redshifts of the truncated artificial distributions $P(z)_{\rm CMASS}$ and $P(z)_{\rm LOWZ}$ in order to compute Δ_α (6.20) and Δ_ϵ (6.25).

The exact results for the error terms Δ_α, Δ_ϵ and their upper bounds – assuming knowledge only of the bounds on the distance combinations (6.22), (6.23), (6.27), and (6.28) over the surveys and using the inequalities (6.21) and (6.26) – are shown in table 6.1 for four cosmological test-models which are all far from the fiducial spatially-flat ΛCDM model with $\Omega_M = 0.3$, $\Omega_\Lambda = 0.7$. All of these models have error terms Δ_α of order 0.2% or smaller when compared to the fiducial spatially-flat FLRW model with $\Omega_M = 0.3$, $\Omega_\Lambda = 0.7$. The corresponding upper bounds on $|\Delta_\alpha|$ are of order 5% or smaller. The value of Δ_ϵ for the models tested is of order 0.0005 or smaller. The bounds on $|\Delta_\epsilon|$ are of order 0.02 or smaller.

We note that even though the models investigated in table 6.1 are significantly different to the spatially-flat ΛCDM model with $\Omega_M = 0.3$, $\Omega_\Lambda = 0.7$ used as an example of a fiducial cosmological model, Δ_α and Δ_ϵ – of order $\lesssim 0.002$ and $\lesssim 0.0005$ respectively – are much smaller than typical statistical errors in α and ϵ of order $\sim$1% and $\sim$0.02 respectively inferred from existing galaxy catalogues [194, 193].

The upper bounds on $|\Delta_\alpha|$ and $|\Delta_\epsilon|$ – valid for all models which obey the same

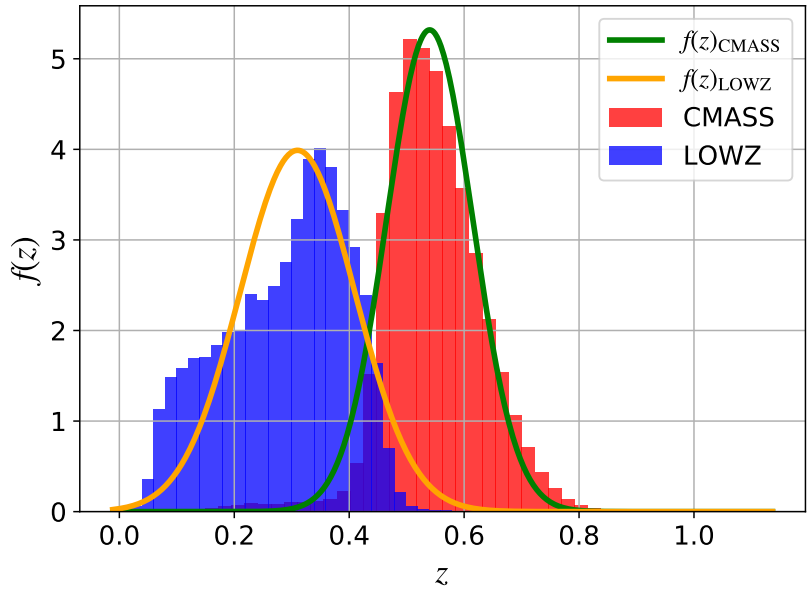

Figure 6.1: Normalised redshift distributions of CMASS (red) and LOWZ (blue) along with superimposed Gaussian probability density distributions $f(z)_{\mathrm{CMASS}}$ and $f(z)_{\mathrm{LOWZ}}$ which roughly sample the redshift distributions. $f(z)_{\mathrm{CMASS}}$ has mean $\mu_{\mathrm{CMASS}} = 0.54$ and standard deviation $\sigma_{\mathrm{CMASS}} = 0.075$, and $f(z)_{\mathrm{LOWZ}}$ has $\mu_{\mathrm{LOWZ}} = 0.31$ and standard deviation $\sigma_{\mathrm{LOWZ}} = 0.10$.

constraints (6.22) and (6.27) as the tested models over the redshift range – are of order $\lesssim 0.04$ and $\lesssim 0.01$ respectively, and are in most cases comparable or smaller than typical statistical errors in α and ϵ when inferred from existing galaxy catalogues. Note that the bounds on $|\Delta_\alpha|$ and $|\Delta_\epsilon|$ quoted represent worst case scenarios, which are never realised in practice.

We conclude that in order to have a large difference between the two constant AP approximations, we must have models ('true' and fiducial) which differ more extremely in their distance measures (and derivatives of these) than is the case for the models presented in table 6.1. This can happen, for example, if the 'true' underlying cosmological model has structure on a hierarchy of scales, with resulting small/intermediate scale wiggles in the distance-redshift relations $g_{\theta\theta}(z)$ and $g_{zz}(z)$.

We now consider a simple class of model cosmologies which can illustrate what might happen when gradients in the metric components become large. We consider a

	$\Lambda\text{CDM}_{\Omega_M=0.99}$		Milne		$\text{FLRW}^{w=-4/3}_{\Omega_M=0.3}$		$\text{Timescape}_{\Omega_M=0.3}$	
	LOWZ	**CMASS**	**LOWZ**	**CMASS**	**LOWZ**	**CMASS**	**LOWZ**	**CMASS**
$\lvert\Delta_\alpha\rvert$ bound	0.036	0.0028	0.010	0.0016	0.0059	0.00061	0.0071	0.00094
Δ_α	0.0022	0.00097	0.0015	0.00066	-0.00087	-0.00032	0.0010	0.00043
$\lvert\Delta_\epsilon\rvert$ bound	0.010	0.00076	0.0032	0.00049	0.0021	0.00022	0.0022	0.00029
Δ_ϵ	0.00052	0.00022	0.00029	0.00012	-0.00029	-0.000067	0.00048	0.00019

Table 6.1: The AP scaling error terms Δ_α and Δ_ϵ computed from the artificial truncated Gaussian distributions $P(z)_{\text{CMASS}}$ and $P(z)_{\text{LOWZ}}$. The corresponding upper bounds on $|\Delta_\alpha|$ and $|\Delta_\epsilon|$ obtained from (6.21) and (6.26) respectively are also shown.

simple three-parameter family of spatially flat unphysical models with metrics

$$ds^2 = -c^2dt^2 + \tilde{a}(t)^2(d\tilde{D}^2 + \tilde{D}^2 d\Omega^2)\,, \tag{6.30}$$

in coordinates adapted to a central observer. The models are constructed by distorting the comoving distance–redshift relation $D(z)$ of a reference ΛCDM model with $\Omega_M = 0.3$ in the following way

$$\tilde{D}(\tilde{z}) = D(\tilde{z})\ (1 + A\cos(f\,\tilde{z} + \Phi))\ , \tag{6.31}$$

where A, f, and Φ are the amplitude, frequency and phase of the trigonometric distortion respectively. This form is chosen as a simple case of a bounded distance redshift relation around the reference model relation $D(\tilde{z})$, but with the possibility of significant gradients of $\tilde{D}(\tilde{z})$ in redshift. The Hubble distance function then reads

$$\frac{c}{\tilde{H}} \equiv -\frac{c}{\tilde{a}}\frac{dt}{d\tilde{z}} = \frac{d\tilde{D}(\tilde{z})}{d\tilde{z}} = \frac{dD(\tilde{z})}{d\tilde{z}}\,(1 + A\cos(f\,\tilde{z} + \Phi)) - D(\tilde{z})\,f\,A\sin(f\,\tilde{z} + \Phi)\,, \tag{6.32}$$

where $\tilde{z} \equiv 1/\tilde{a}$, and where the second equality follows from considering radially propagating null rays in the metric (6.30). We note that even though differences in the comoving distance scales $\tilde{D}(\tilde{z})$ and $D(\tilde{z})$ might be small, differences between the derivatives of the comoving distance scales in redshift can be large, if the frequency f of the perturbation (6.31) is large.

The results for the tested unphysical models are shown in table 6.2. The error terms Δ_α, Δ_ϵ and their bounds are in general significantly larger than for the model cosmologies in table 6.1 – especially for the large frequencies, f. The error terms Δ_α

are of order 1% for the two models with $f = 30$ and $f = 50$, and the error terms Δ_ϵ are of order 0.01 - which is similar in order to typical statistical errors in BAO analysis with current galaxy surveys. The upper bounds on $|\Delta_\alpha|$ and $|\Delta_\epsilon|$ are as high as $\sim$30% and ~ 0.1 respectively.

These results are intuitive; the more rapidly the 'true' and fiducial models are varying with respect to each other, the more we expect evaluation at a single redshift and an average of α and ϵ to differ. We expect the same tendencies to be present in models which are more complicated than the simple class of distorted models (6.30)–(6.32), but which possess the same features in terms of allowed gradients of the relevant metric components.

	FLRW $^{A=0.01}_{f=10}$ $^{}_{\Phi=-0.3}$		FLRW $^{A=0.005}_{f=15}$ $^{}_{\Phi=-0.3}$		FLRW $^{A=0.005}_{f=30}$ $^{}_{\Phi=-0.3}$		FLRW $^{A=0.001}_{f=50}$ $^{}_{\Phi=-0.6}$	
	LOWZ	**CMASS**	**LOWZ**	**CMASS**	**LOWZ**	**CMASS**	**LOWZ**	**CMASS**
$\lvert\Delta_\alpha\rvert$ bound	0.037	0.014	0.054	0.018	0.32	0.21	0.31	0.15
Δ_α	0.0046	-0.0047	-0.0012	0.0064	0.016	-0.0085	0.0052	0.011
$\lvert\Delta_\epsilon\rvert$ bound	0.012	0.0047	0.018	0.0061	0.11	0.070	0.10	0.049
Δ_ϵ	0.0026	-0.0039	-0.0024	0.0061	0.012	-0.013	0.0049	0.010

Table 6.2: The AP scaling error terms Δ_α and Δ_ϵ computed from the artificial truncated Gaussian distributions $P(z)_{\rm CMASS}$ and $P(z)_{\rm LOWZ}$. The corresponding upper bounds on $|\Delta_\alpha|$ and $|\Delta_\epsilon|$ obtained from (6.21) and (6.26) respectively are also shown.

6.3 The Alcock-Paczyński scaling and the BAO feature

In order to quantify the impact of the redshift-dependent AP-scaling investigated in section 6.2 on the BAO feature as viewed in a fiducial cosmology, we must specify a model for the BAO feature.

Let us investigate the example of the empirical model for the correlation function $\xi^{\rm tr}(D^{\rm tr}, \mu^{\rm tr}, z)$ as proposed in section 6.1.3, with a Gaussian function describing the BAO feature and polynomial terms describing the 'background' featureless correlation function. Using the identity derived in (6.14) together with the form of the empirical

model of the correlation function (6.12) we can write

$$\begin{aligned}\xi(D,\mu,z) &= \xi^{\rm tr}\left(D^{\rm tr}(D,\mu,\alpha,\epsilon),\mu^{\rm tr}(\mu,\epsilon),z\right)\\ &\approx (D)^2\alpha^2\frac{1+\psi(\epsilon)\mu^2}{(1+\epsilon)^2}A\,\mathrm{e}^{-\left(D\alpha\sqrt{1+\psi(\epsilon)\mu^2}/(1+\epsilon)-r\right)^2/(2\sigma^2)}+C_0(\mu)+\frac{C_1(\mu)}{D}+\frac{C_2(\mu)}{(D)^2}\,,\end{aligned} \tag{6.33}$$

where the redshift dependence of α, ϵ, A, σ, and the polynomial coefficients $C_0(\mu)$, $C_1(\mu)$, and $C_2(\mu)$ is implicit, and where $\psi(\epsilon)$ is given by the second equation of (6.10). The approximation in (6.33) follows from the approximations (6.10) and (6.11) for $D^{\rm tr}(D,\mu,\alpha,\epsilon)$ and $\mu^{\rm tr}(\mu,\epsilon)$ respectively. We note that (6.33) has the same form as (6.12) (Gaussian in D plus a second-order polynomial function in $1/D$ for fixed μ and z), but the coefficients for each value of μ, z are redefined by the AP-scaling.

We might further obtain $\xi(D,\mu)$ from (6.33) by applying the approximation (6.15), neglecting the second-order corrections from the non-multiplicatively separable parts $\delta(D,\mu,z)$ and $\delta_{\rm Poisson}(D,\mu,z)$ of $f(D,\mu,z)$ and $f_{\rm Poisson}(D,\mu,z)$ respectively.

$$\begin{aligned}\xi(D,\mu) &\approx \int dzP(z)\xi(D,\mu,z)\\ &= \int dzP(z)\left((D)^2\alpha^2\frac{1+\psi(\epsilon)\mu^2}{(1+\epsilon)^2}A\,\mathrm{e}^{-\left(D\alpha\sqrt{1+\psi(\epsilon)\mu^2}/(1+\epsilon)-r\right)^2/(2\sigma^2)}\right)\\ &\qquad +\overline{C}_0(\mu)+\frac{\overline{C}_1(\mu)}{D}+\frac{\overline{C}_2(\mu)}{(D)^2}\,,\end{aligned} \tag{6.34}$$

where the overbar refers to the averaging operation in redshift $\overline{S}\equiv\int dzP(z)S(z)$. For α and ϵ for which deviations remain small ($\ll 1$) over the survey, we can use the approximation (6.16), to simplify the Gaussian integral in (6.34)

$$\begin{aligned}\xi(D,\mu) &\approx \int dzP(z)\xi(D,\mu,z)\\ &\approx (D)^2\bar{\alpha}^2\frac{1+\psi(\bar{\epsilon})\mu^2}{(1+\bar{\epsilon})^2}A\,\mathrm{e}^{-\left(D\bar{\alpha}\sqrt{1+\psi(\bar{\epsilon})\mu^2}/(1+\bar{\epsilon})-r\right)^2/(2\sigma^2)}+\overline{C}_0(\mu)+\frac{\overline{C}_1(\mu)}{D}+\frac{\overline{C}_2(\mu)}{(D)^2}\,,\end{aligned} \tag{6.35}$$

where the Gaussian parameters $A(z)$, $\sigma(z)$ are now evaluated at the mean redshift of the survey $\bar{z}$. Note that the standard constant AP approximation $\alpha(z)\mapsto\alpha(\bar{z})$, $\epsilon(z)\mapsto\epsilon(\bar{z})$ yields the same form as the expression in (6.35) but with $\bar{\alpha},\bar{\epsilon}$ replaced by $\alpha(\bar{z}),\epsilon(\bar{z})$.

Assuming that the conditions are met for the form (6.35) to be accurate, we can analyse the change of the Gaussian feature in the wedges (6.74) as a function of the AP-scaling, by replacing the constant α, ϵ parameters in the results of section 5.3.1 by $\bar{\alpha}, \bar{\epsilon}$.

From the definition of the wedge functions (6.60) we find that the wedges corresponding to the 2-point correlation function (6.35) read

$$\xi_{[\mu_1,\mu_2]}(D) = \frac{1}{\mu_2-\mu_1}\int_{\mu_1}^{\mu_2} d\mu\, \xi(D,\mu) \approx$$
$$\frac{\int_{\mu_1}^{\mu_2} d\mu\, (D)^2\bar{\alpha}^2 \frac{1+\psi(\bar{\epsilon})\mu^2}{(1+\bar{\epsilon})^2} A\, \mathrm{e}^{-\left(D\bar{\alpha}\sqrt{1+\psi(\bar{\epsilon})\mu^2}/(1+\bar{\epsilon})-r\right)^2/(2\sigma^2)}}{\mu_2-\mu_1} + \overset{\mu_1,\mu_2}{C}_0 + \frac{\overset{\mu_1,\mu_2}{C}_1}{D} + \frac{\overset{\mu_1,\mu_2}{C}_2}{(D)^2}, \quad (6.36)$$

with

$$\overset{\mu_1,\mu_2}{C}_0 \equiv \frac{\int_{\mu_1}^{\mu_2} d\mu\, \overline{C}_0(\mu)}{\mu_2-\mu_1}, \qquad \overset{\mu_1,\mu_2}{C}_1 \equiv \frac{\int_{\mu_1}^{\mu_2} d\mu\, \overline{C}_1(\mu)}{\mu_2-\mu_1}, \qquad \overset{\mu_1,\mu_2}{C}_2 \equiv \frac{\int_{\mu_1}^{\mu_2} d\mu\, \overline{C}_2(\mu)}{\mu_2-\mu_1}. \quad (6.37)$$

For sufficiently small $\bar{\epsilon}$, the Gaussian part of (6.36) can be expanded in $\psi \ll 1$ and $\psi(\bar{\epsilon})D/\sigma \ll 1$ to first order for relevant distance scales D[5], such that (6.36) reads

$$\xi_{[\mu_1,\mu_2]}(D) \approx (D)^2\bar{\alpha}^2\frac{1+\psi(\bar{\epsilon})\kappa^{\mu_2}_{\mu_1}}{(1+\bar{\epsilon})^2} A\, \mathrm{e}^{-\left(D\bar{\alpha}\sqrt{1+\psi(\bar{\epsilon})\kappa^{\mu_2}_{\mu_1}}/(1+\bar{\epsilon})-r\right)^2/(2\sigma^2)} + \overset{\mu_1,\mu_2}{C}_0 + \frac{\overset{\mu_1,\mu_2}{C}_1}{D} + \frac{\overset{\mu_1,\mu_2}{C}_2}{(D)^2}$$
$$\approx (D)^2\tilde{A}\, \mathrm{e}^{-(D-\tilde{r})^2/(2\tilde{\sigma}^2)} + \overset{\mu_1,\mu_2}{C}_0 + \frac{\overset{\mu_1,\mu_2}{C}_1}{D} + \frac{\overset{\mu_1,\mu_2}{C}_2}{(D)^2}, \quad (6.38)$$

where

$$\kappa^{\mu_2}_{\mu_1} \equiv \frac{1}{\mu_2-\mu_1}\int_{\mu_1}^{\mu_2} d\mu\, \mu^2 = \frac{1}{3}\frac{\mu_2^3-\mu_1^3}{\mu_2-\mu_1}, \quad (6.39)$$

and where the Gaussian parameters in the final line are kept to first order in $\psi(\bar{\epsilon})$ are given by

$$\tilde{r} \equiv \frac{1-\frac{1}{2}\kappa^{\mu_2}_{\mu_1}\psi(\bar{\epsilon})}{\bar{\alpha}\,/\,(1+\bar{\epsilon})} r, \qquad \tilde{\sigma} \equiv \frac{1-\frac{1}{2}\kappa^{\mu_2}_{\mu_1}\psi(\bar{\epsilon})}{\bar{\alpha}\,/\,(1+\bar{\epsilon})}\sigma, \qquad \widetilde{A} \equiv \frac{\bar{\alpha}^2}{(1+\bar{\epsilon})^2}(1+\kappa^{\mu_2}_{\mu_1}\psi(\bar{\epsilon}))A. \quad (6.40)$$

[5] See section 5.3.1 for details.

This can be obtained from the first line of (6.38), by expanding to first order $\sqrt{1+\psi(\bar{\epsilon})\kappa_{\mu_1}^{\mu_2}} \approx 1+\psi(\bar{\epsilon})\kappa_{\mu_1}^{\mu_2}/2$, and absorbing the coefficient multiplying D in the exponential into a rescaling of r and σ.

For the isotropic, transverse, and radial wedges (6.61) we can thus compute the scaled Gaussian parameters ($\tilde{r}$, $\tilde{\sigma}$, $\tilde{A}$) (6.40) relative to the undistorted parameters (r, σ, A) as a function of $\bar{\alpha}$ and $\bar{\epsilon}$ by substituting the value of $\kappa_{\mu_1}^{\mu_2}$ corresponding to the given wedge

$$\kappa_0^1 = \frac{1}{3}\,, \qquad \kappa_0^{0.5} = \frac{1}{12}\,, \qquad \kappa_{0.5}^1 = \frac{7}{12}\,. \tag{6.41}$$

We note that for the 'isotropic wedge' ($\mu_1 = 0$, $\mu_2 = 1$), (6.40) reduces to $\tilde{r} = r/\bar{\alpha}\,, \sigma/\bar{\alpha}\,, \widetilde{A} = \bar{\alpha}^2 A$, since from the definition of ψ (6.10) $\psi(\epsilon) \approx 1 + 6\epsilon$ to first order in ϵ (or first order in ψ). Thus, to lowest order, the isotropic wedge contains information on the isotropic scaling α only.

The exact result for the Gaussian parameter distortions (6.40) is useful for gaining intuition about the appearance of the BAO feature in a cosmology which is distorted from the true one according to AP-scaling factors $\alpha(z)$ and $\epsilon(z)$. If the conditions for the expansions (6.38) and (6.36) are not met, then the exact integrals in μ over (6.34) must be performed numerically.

6.4 Testing the predicted shift of the BAO feature with mock catalogues

In this section we test the predictions of section 6.2 and section 6.3 for the reparametrisation effects on the BAO feature using CMASS NGC mock catalogues. The advantage of using mock catalogues is that by averaging many mocks we can obtain arbitrarily small statistical variance in our correlation function estimators, meaning that we can detect small systematics which would otherwise be difficult to disentangle from noise. A further advantage is that we know the true underlying cosmology of the mock catalogues.

By fitting the empirical Gaussian correlation function model described in section 6.3 to the mock data, we test the accuracy of the BAO scale recovered when using the standard constant AP scaling approximation $\alpha(z) \mapsto \alpha(\bar{z})$, $\epsilon(z) \mapsto \epsilon(\bar{z})$, the modified

constant AP scaling approximation $\alpha(z) \mapsto \bar{\alpha}$, $\epsilon(z) \mapsto \bar{\epsilon}$, and the exact AP redshift-dependent scalings $\alpha(z)$ and $\epsilon(z)$ with no approximation respectively. We calibrate the BAO scale against that measured in a reference cosmology in order to calibrate for any systematic offsets that might occur between the peak of the empirical gaussian and the BAO scale.

6.4.1 The mocks

In this analysis we use the Quick Particle Mesh (QPM) mock catalogues as described in detail in [208]. The QPM mock catalogues are generated from ΛCDM N-body simulations, and are designed for the BOSS clustering analysis. The number density in the mock catalogues match the observed galaxy number density of the BOSS catalogues, and follow the same radial and angular selection functions. The QPM simulations are generated from the fiducial ΛCDM cosmology

$$\Omega_{M0} = 0.29, \quad \Omega_{\Lambda 0} = 0.71, \quad \Omega_{b0} = 0.048, \quad \sigma_8 = 0.8, \quad h = 0.7, \tag{6.42}$$

where Ω_{M0}, $\Omega_{\Lambda 0}$ and Ω_{b0} are the present epoch matter density parameter, dark energy density parameter, and baryonic matter density parameter respectively, σ_8 is the root mean square of the linear mass fluctuations at the present epoch averaged at scales 8 Mpc/h given by the integral over the ΛCDM power spectrum, and $H_0 = 100\,h$ km/s/Mpc is the Hubble parameter evaluated at the present epoch. The sound horizon at the drag epoch within this model is $r_s = 103.05$ Mpc/h.

In this analysis we focus on the CMASS NGC catalogue. There are 1000 QPM mock catalogues available for the CMASS NGC catalogue. We use all 1000 QPM mock catalogues in calculating the correlation function of our chosen 'reference model' used to calibrate the BAO peak position (see section 6.4.2). For the remaining trial cosmologies we use 200 mock catalogues. We use these, along with the associated random catalogues as described in [206], to construct the 2-point correlation in a number of different trial cosmologies.

6.4.2 The likelihood function and the fitting procedure

We assume the likelihood function $\mathcal{L}$ of data given the empirical fitting model (6.12) $\xi_{\rm Fit}$

$$\mathcal{L}\left(\bar{\hat{\xi}}\,\middle|\,\xi_{\rm Fit}\right) \propto \exp(-\chi^2/2), \tag{6.43}$$

with

$$\chi^2 = Z^{\intercal}\underline{\underline{C}}^{-1}_{\bar{\hat{\xi}}}Z, \qquad Z = \bar{\hat{\xi}} - \xi_{\rm Fit}, \tag{6.44}$$

where $\hat{\xi}$ is the binned estimate of the (isotropic or wedge) 2-point correlation function computed for each mock, and where $\bar{\hat{\xi}}$ is the unweighted average over the mock catalogues. In the anisotropic wedge analysis, the transverse and radial estimates are combined into a single vector $\hat{\xi}$ in order to perform a combined fit. $\xi_{\rm Fit}$ is the fitting function, which in this analysis is taken to be the model described in section 6.3. The covariance matrix of $\bar{\hat{\xi}}$ is given by the covariance of the individual measurements $\hat{\xi}$ scaled by the inverse of the number of mock catalogues used, $N_{\rm mocks}$

$$\underline{\underline{C}}_{\bar{\hat{\xi}}} = \frac{1}{N_{\rm mocks}}\underline{\underline{C}}_{\hat{\xi}}, \qquad \underline{\underline{C}}_{\hat{\xi}} = \overline{(\hat{\xi}-\bar{\hat{\xi}})(\hat{\xi}-\bar{\hat{\xi}})^{\intercal}}, \tag{6.45}$$

where the overbar represents the averages over the mock catalogues.

As discussed in chapter 5 and in section 6.1.3 of this chapter, the calibration of the BAO scale to the peak of the Gaussian model (6.12), r, is itself a source of error in empirical BAO investigations. In order to account for the calibration issue, we use the inferred peak position from the 2-point correlation function computed in the spatially-flat ΛCDM reference model with $\Omega_M = 0.3$.

We use the fitting function (6.36) and the likelihood function (6.43) for estimating the best fit of $\tilde{r}_{\rm isotropic} = r/\bar{\alpha}$ and $\bar{\epsilon}$ for the spatially-flat ΛCDM reference model with $\Omega_M = 0.3$ using 1000 CMASS NGC QPM mock catalogues (see section 6.4.1). The fitting range is taken to be $[50, 150]\,{\rm Mpc}/h$.

For the isotropic fit, $\mu_1 = 0, \mu_2 = 1$, we find a best fit value $\hat{\tilde{r}}_{\rm isotropic} = 102.08\,{\rm Mpc}/h$. For the anisotropic analysis, consisting of a combined fit to the transverse wedge $\mu_1 = 0, \mu_2 = 0.5$ and the radial wedge $\mu_1 = 0.5, \mu_2 = 1$, we get best fit values $\hat{\tilde{r}}_{\rm isotropic} = 102.16\,{\rm Mpc}/h$ and $\hat{\bar{\epsilon}} = 0.0006$. The discrepancy between the best fit estimates of the

isotropic peak positions are $0.08\,\mathrm{Mpc}/h$, while the errors in the individual estimates are of order $0.08\,\mathrm{Mpc}/h$. Thus the isotropic and anisotropic peak positions are consistent within the level of uncertainty on the best fit. The error in the best fit epsilon is 0.0007, and $\hat{\bar{\epsilon}}$ is thus consistent with zero at the level of precision of 1000 mock catalogues. These findings are consistent with the reference model (6.12) with $r = 102.08\,\mathrm{Mpc}/h$. We thus use this empirical model as a reference, and consider reparametrisations (6.33) with respect to the reference ΛCDM model with $\Omega_M = 0.3$.

We are now able to quantify the accuracy of the predictions of the constant AP scaling approximations $\alpha(z) \mapsto \alpha(\bar{z})$, $\epsilon(z) \mapsto \epsilon(\bar{z})$ and $\alpha(z) \mapsto \bar{\alpha}$, $\epsilon(z) \mapsto \bar{\epsilon}$ respectively, and the exact integral expression (6.34), under the assumptions of the empirical fitting function. Let us first consider any constant AP-approximation $\alpha(z) \mapsto \mathcal{C}_\alpha$, $\epsilon(z) \mapsto \mathcal{C}_\epsilon$, where $\mathcal{C}_\alpha$ and $\mathcal{C}_\epsilon$ are constants. With this approximation (6.34) reads

$$\begin{aligned}
&\xi(D,\mu) \approx \int dz P(z)\xi(D,\mu,z) \\
&= (D)^2\mathcal{C}_\alpha^2 \frac{1+\psi(\mathcal{C}_\epsilon)\mu^2}{(1+\mathcal{C}_\epsilon)^2} A\,\mathrm{e}^{-\left(D\mathcal{C}_\alpha\sqrt{1+\psi(\mathcal{C}_\epsilon)\mu^2}/(1+\mathcal{C}_\epsilon)-r\right)^2/(2\sigma^2)} + \overline{C}_0(\mu) + \frac{\overline{C}_1(\mu)}{D} + \frac{\overline{C}_2(\mu)}{(D)^2}\,,
\end{aligned} \tag{6.46}$$

which can be substituted into the definition of the wedges (6.60) to obtain

$$\begin{aligned}
\xi_{[\mu_1,\mu_2]}(D) &\equiv \frac{1}{\mu_2-\mu_1}\int_{\mu_1}^{\mu_2} d\mu\,\xi(D,\mu) \\
&\approx \frac{1}{\mu_2-\mu_1}\int_{\mu_1}^{\mu_2} d\mu\,(D)^2\mathcal{C}_\alpha^2 \frac{1+\psi(\mathcal{C}_\epsilon)\mu^2}{(1+\mathcal{C}_\epsilon)^2} A\,\mathrm{e}^{-\left(D\mathcal{C}_\alpha\sqrt{1+\psi(\mathcal{C}_\epsilon)\mu^2}/(1+\mathcal{C}_\epsilon)-r\right)^2/(2\sigma^2)} \\
&\quad + \overset{\mu_1,\mu_2}{C}_0 + \frac{\overset{\mu_1,\mu_2}{C}_1}{D} + \frac{\overset{\mu_1,\mu_2}{C}_2}{(D)^2}\,,
\end{aligned} \tag{6.47}$$

where the polynomial coefficients $\overset{\mu_1,\mu_2}{C}_0$, $\overset{\mu_1,\mu_2}{C}_1$, and $\overset{\mu_1,\mu_2}{C}_2$ are given by (6.37). We perform the exact numerical integral (6.47) for the three wedges $\xi_{[0,1]}$, $\xi_{[0,0.5]}$, $\xi_{[0.5,1]}$ and fit for the independent parameters $r/\mathcal{C}_\alpha$, $\mathcal{C}_\alpha^2 A$, $\sigma/\mathcal{C}_\alpha$, $\mathcal{C}_\epsilon$, $\overset{\mu_1,\mu_2}{C}_0$, $\overset{\mu_1,\mu_2}{C}_1$, $\overset{\mu_1,\mu_2}{C}_2$ for a given model cosmology. Using the calibrated peak position $r = 102.08$ Mpc$/h$ for the reference spatially-flat ΛCDM model with $\Omega_M = 0.3$, we can compare the best fit estimates of $r/\mathcal{C}_\alpha$ and $\mathcal{C}_\epsilon$ with the standard constant AP scaling approximation $\mathcal{C}_\alpha = \alpha(\bar{z})$, $\mathcal{C}_\epsilon = \epsilon(\bar{z})$, and the modified constant AP scaling approximation $\mathcal{C}_\alpha = \bar{\alpha}$, $\mathcal{C}_\epsilon = \bar{\epsilon}$.

We define the fractional error in any given constant AP scaling approximation as

$$\text{APerror}_r = \frac{\widehat{r/\mathcal{C}_\alpha} - (r/\mathcal{C}_\alpha)_{\rm th}}{(r/\mathcal{C}_\alpha)_{\rm th}}\,, \qquad \text{APerror}_\epsilon = \hat{\mathcal{C}}_\epsilon - (\mathcal{C}_\epsilon)_{\rm th} \qquad \text{(const. AP approx.)}\,, \tag{6.48}$$

where $\widehat{r/\mathcal{C}_\alpha}$, $\hat{\mathcal{C}}_\epsilon$ are the best fit estimates of the parameters $r/\mathcal{C}_\alpha$, $\mathcal{C}_\epsilon$, and $(r/\mathcal{C}_\alpha)_{\rm th}$, $(\mathcal{C}_\epsilon)_{\rm th}$ are the corresponding theoretical predictions obtained from the calibration scale $r_{\rm th} = 102.08$ Mpc$/h$, and the choice of constant AP approximation $\mathcal{C}_\alpha$, $\mathcal{C}_\epsilon$.

For $\mathcal{C}_\alpha = \alpha(\bar{z})$, $\mathcal{C}_\epsilon = \epsilon(\bar{z})$, we can compute $(\mathcal{C}_\alpha)_{\rm th}$, $(\mathcal{C}_\epsilon)_{\rm th}$ from the metric components $g_{\theta\theta}$, g_{zz} of the tested model and the reference spatially-flat ΛCDM model with $\Omega_M = 0.3$ respectively evaluated at the mean redshift z of the CMASS NGC catalogue. For $\mathcal{C}_\alpha = \bar{\alpha}$, $\mathcal{C}_\epsilon = \bar{\epsilon}$, we can compute $(\mathcal{C}_\alpha)_{\rm th}$, $(\mathcal{C}_\epsilon)_{\rm th}$ from the metric components $g_{\theta\theta}$, g_{zz} of the tested model cosmology and the reference spatially-flat ΛCDM model with $\Omega_M = 0.3$ respectively and from the model redshift distribution $P(z)$ of the CMASS NGC catalogue.

We also use this redshift distribution to evaluate the exact integral expression (6.34) where no constant AP approximation is made, using the knowledge of the exact AP scaling functions $\alpha(z)$, $\epsilon(z)$ between the tested model cosmology and the reference spatially-flat ΛCDM model with $\Omega_M = 0.3$. Substituting the approximation (6.34) in the definition of the wedge functions (6.60) we find

$$\begin{aligned}\xi_{[\mu_1,\mu_2]}(D) &\equiv \frac{1}{\mu_2-\mu_1}\int_{\mu_1}^{\mu_2} d\mu\, \xi(D,\mu) \\ &\approx \frac{1}{\mu_2-\mu_1}\int_{\mu_1}^{\mu_2} d\mu \int dz P(z) \left((D)^2\alpha^2 \frac{1+\psi(\epsilon)\mu^2}{(1+\epsilon)^2} A\, \mathrm{e}^{-\left(D\alpha\sqrt{1+\psi(\epsilon)\mu^2}/(1+\epsilon)-r\right)^2/(2\sigma^2)} \right) \\ &\qquad + \overset{\mu_1,\mu_2}{C}_0 + \frac{\overset{\mu_1,\mu_2}{C}_1}{D} + \frac{\overset{\mu_1,\mu_2}{C}_2}{(D)^2}\,,\end{aligned} \tag{6.49}$$

where the free parameters are r, A, σ, $\overset{\mu_1,\mu_2}{C}_0$, $\overset{\mu_1,\mu_2}{C}_1$, $\overset{\mu_1,\mu_2}{C}_2$. Note that there is no 'ϵ' fitting parameter describing the anisotropic warping as in the corresponding fitting function (6.47), since the exact AP scaling functions $\alpha(z)$, $\epsilon(z)$ are integrated over in (6.49). We can, however, artificially introduce a 'warping' fitting parameter $\mathcal{K}_\epsilon$ by making the replacement $\epsilon(z) \to \epsilon(z) + \mathcal{K}_\epsilon$ in (6.49). $\mathcal{K}_\epsilon = 0$ gives back the exact expression (6.49), and a non-zero $\mathcal{K}_\epsilon$ quantifies constant warping not accounted for in the expression

(6.49). We thus arrive at the 7 independent parameters r, A, σ, $\mathcal{K}_\epsilon$, $\overset{\mu_1,\mu_2}{C_0}$, $\overset{\mu_1,\mu_2}{C_1}$, $\overset{\mu_1,\mu_2}{C_2}$.

We define fractional errors analogous to those of the constant AP approximation fitting function (6.48) for the 'exact' fitting function (6.49) as

$$\text{APerror}_r = \frac{\hat{r} - r_{\text{th}}}{r_{\text{th}}}, \qquad \text{APerror}_\epsilon = \hat{\mathcal{K}}_\epsilon \qquad \text{(exact } \alpha(z) \text{ and } \epsilon(z)\text{)} \tag{6.50}$$

where $\hat{r}$ and $\hat{\mathcal{K}}_\epsilon$ are best fit estimates of the parameters r and $\mathcal{K}_\epsilon$, and where $r_{\text{th}} = 102.08$ Mpc$/h$ is the calibration scale of the reference spatially-flat ΛCDM model with $\Omega_M = 0.3$.

6.4.3 Large-scale model cosmologies

First, we test the recovery of the BAO characteristic scale when using various large-scale cosmological models which differ substantially from the reference spatially-flat ΛCDM cosmological model with $\Omega_M = 0.3$. We are interested in testing models which are far from the reference ΛCDM model, rather than necessarily being candidates for accurately describing cosmological data.

We consider the two-parameter family of spatially-flat FLRW models parameterised by the matter cosmological parameter Ω_M and the constant dark energy equation of state parameter w for which we consider the values $\{-0.333, -1, -1.333\}$. The dark energy cosmological parameter is given by $\Omega_{d.e.} = 1 - \Omega_M$, and all other cosmological parameters are zero. In addition, we consider three curved models: the Milne universe, the positively-curved ΛCDM universe with $\Omega_M = 1$ and $\Omega_K = -1$ and the timescape model with $\Omega_M = 0.3$.

For each test model we compute the mean of the (isotropic and wedge) 2-point correlation function of 200 mock catalogues $\bar{\hat{\xi}}$, and the associated covariance matrix (6.45). For most models, the correlation function is calculated for the range of distances $[0, 150]$ Mpc$/h$, however for models with $\bar{\alpha} < 1$ the correlation function is calculated out to values of 200 Mpc$/h$. This is done in order to ensure that the full BAO feature lies within the calculated range, and to facilitate a broad enough physical fitting range.

The mean isotropic 2-point correlation function is shown in figure 6.2 for each model. Each correlation function has been normalised by a constant in order to align the local peaks of the correlation functions, to make the shift of the peak position more visible. As expected, the isotropic BAO feature shifts according to the magnitude of

the isotropic scaling of the distance measures relative to the reference model α. We shall investigate the shift of the peak in detail below.

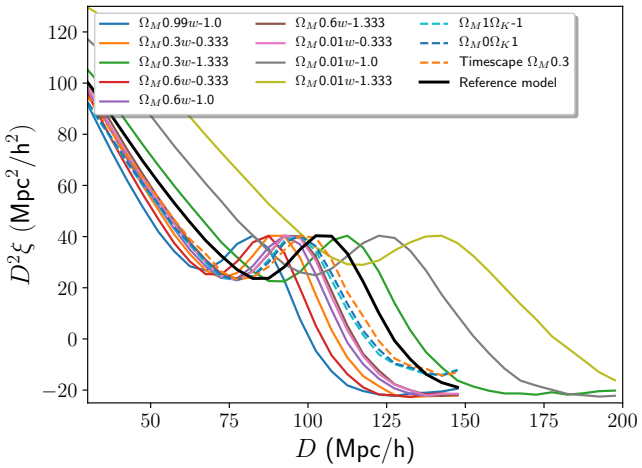

Figure 6.2: The mean of the isotropic 2-point correlation function of 200 mock catalogues for each tested model. The reference spatially-flat ΛCDM cosmological model with $\Omega_M = 0.3$ is shown in black. In order to visualise the shift of the acoustic scale, the correlation function for each model has been normalised by a constant such that the local maxima are aligned with that of the reference ΛCDM model.

For 200 mock catalogues, the $1\,\sigma$ error in the estimate of isotropic BAO scale r is of order ~ 0.2 Mpc$/h$ corresponding to a 0.2% error, and the error in the estimate of the warping parameter is of order ~ 0.002.[6] For perfect accuracy of any applied AP approximation and for perfect modelling assumptions in general, we expect recovery of the isotropic BAO scale and the warping parameter respectively at this level of accuracy.

In order to minimise systematic errors involved with the choices made in the fitting procedure, we fit to the range of distances $[50/\bar{\alpha}, 150/\bar{\alpha}]$ Mpc$/h$, where α is the AP-scaling between the reference ΛCDM model and the model tested. In this way, we are approximately fitting to the same physical distance scale for all models involved, irrespective of the ruler with which we measure the distance between galaxies.

For the isotropic fits, we fix the constant warping parameters $\mathcal{C}_\epsilon$ and $\mathcal{K}_\epsilon$ in (6.47) and (6.49) respectively, in order to avoid the degeneracies introduced by the quadratic

[6] The errors are reasonably robust between the test models and consistent within $\sim 0.1\%$ for the peak position and ~ 0.001 for ϵ.

contributions of ϵ to the isotropic wedge. We fix $\mathcal{C}_\epsilon = \bar{\epsilon}$ in the constant AP scaling approximation analysis [7] and $\mathcal{K}_\epsilon = 0$ in the exact analysis.

The results of the isotropic analysis are shown in figure 6.3 for nine models with different values of Ω_M and w, and for the three curved models described above. The figures show the fractional error in the recovery of the BAO scale for the various models. The labels on the x-axes and y-axes indicate the model used, and under which assumptions. The label '$(\mathcal{C}_\alpha)_{\rm th} = \alpha(\bar{z}) \mid \mathcal{C}_\epsilon = \bar{\epsilon}$' indicates that the constant AP approximation (6.47) has been used in the wedge functions under the assumption that $\mathcal{C}_\alpha = \alpha(\bar{z})$, and that $\mathcal{C}_\epsilon$ has been fixed to the theoretically computed value of $\bar{\epsilon}$. '$(\mathcal{C}_\alpha)_{\rm th} = \bar{\alpha} \mid \mathcal{C}_\epsilon = \bar{\epsilon}$' represents the same situation, only here it is assumed that $\mathcal{C}_\alpha = \bar{\alpha}$. The label 'Exact $\alpha(z), \epsilon(z) \mid \mathcal{K}_\epsilon = 0$' indicates that no constant AP approximation has been used, resulting in the wedge fitting function (6.49). $\mathcal{K}_\epsilon = 0$ in the isotropic analysis,[8] and $\mathcal{K}_\epsilon$ is only introduced as a free parameter in the anisotropic analysis.

In figure 6.3a, APerror_r (6.48) is shown for the standard constant AP scaling approximation analysis with $(\mathcal{C}_\alpha)_{\rm th} = \alpha(\bar{z})$ and the modified constant AP scaling approximation with $(\mathcal{C}_\alpha)_{\rm th} = \bar{\alpha}$. We see that the errors of both constant AP scaling approximations are of order $\lesssim 1\%$. The accuracy of the predictions from $(\mathcal{C}_\alpha)_{\rm th} = \alpha(\bar{z})$ and $(\mathcal{C}_\alpha)_{\rm th} = \bar{\alpha}$ are very close as expected from the results of section 6.2.3. However, the modified constant AP scaling approximation $(\mathcal{C}_\alpha)_{\rm th} = \bar{\alpha}$ is marginally but systematically more accurate. For most models, the errors exceed the 0.2% level which is the magnitude of the 1σ error bars of the individual best fit values of the peak positions. Thus, the instability of the best fits cannot account for the errors, and we conclude that systematic errors are dominating the error budget.

In figure 6.3b the accuracy of the modified constant AP scaling approximation $(\mathcal{C}_\alpha)_{\rm th} = \bar{\alpha}$ is compared to that of the exact AP scaling $\alpha(z)$, $\epsilon(z)$. The plot shows no systematic improvements in accuracy when using the exact expression (6.49) as compared to imposing the constant AP approximation $(\mathcal{C}_\alpha)_{\rm th} = \bar{\alpha}$. The errors thus remain of order $\lesssim 1\%$, with most models exceeding 0.2%. The inaccuracies in the recovery of the isotropic scale must thus be assigned to other systematic errors than those of any AP scaling approximation.

One possible source of systematic error worth investigating is the decrease in the

[7] Changing the fixed value to $\mathcal{C}_\epsilon = \epsilon(\bar{z})$ does not significantly alter the results.

[8] See the motivation for introducing this parameter for the anisotropic analysis in the text below eq. (6.49)

number of bins of the fit, since we are counting galaxy pairs in bins of a constant size of 5 Mpc/h. Keeping the bin size constant in the reference cosmology, and scaling the bin-sizes accordingly by $1/\bar{\alpha}$ for the test models did, however, not improve the accuracy. Other possible sources of systematics might for instance include degeneracies of parameters in the fit or inaccuracies in the approximate integral relation (6.15) used in (6.34).

In order to examine whether the systematic error in the determination of the isotropic scale is an artefact of our fitting procedure, we redid the analysis for the ΛCDM power-spectrum template fitting procedure for a few ΛCDM models with significantly differing Ω_M values. We used the conventionally employed 5-parameter ΛCDM template for the isotropic wedge-function, see e.g., [193]. In each fit we kept the parameters $\Omega_M h^2$ and $\Omega_b h^2$ constant, in order to keep the template function fixed in each case and isolate the distortion due to the AP-scaling[9]. We then measured the value of the constant AP-scaling parameter $\alpha(\bar{z})$ - or interpreted via the modified constant AP scaling approximation[10] $\bar{\alpha}$.

In figure 6.5 the systematic error in the inferred best fit isotropic peak position is shown for both the empirical fitting procedure and the ΛCDM template fitting procedure. The squares represent measurements done within the ΛCDM template fitting procedure, while the remaining measurements are the ones done within the empirical fitting procedure depicted also in figures (6.3). The statistical errors of each measurement are of order 0.2%. The order of magnitude of the errors are similar between the fitting procedures, and are of order $\sim 1\%$ for models with $|\bar{\alpha} - 1| \sim 0.1$. We also note that trends in systematics as a function of $\bar{\alpha}$ are of the same sign between the two fitting procedures. Our results indicate that the level of systematics is robust to the exact choice of fitting procedure.

We now consider the anisotropic fits for the same models as for the isotropic analysis. The recovery of the isotropic peak positions in the anisotropic analysis closely resembles the results for the isotropic analysis shown in figure 6.3, and consequently we omit plots of these results. The recovery of the warping parameters is shown in

[9] Note that the assumed value of h is varying with Ω_M in this setting. However, the value of h assumed does not affect the results of our analysis since distance scales are measured in units of Mpc/h.

[10] As noted several times in this chapter the difference between $\alpha(\bar{z})$ and $\bar{\alpha}$ is negligible when the transformation is between smooth model cosmologies. We thus use $\alpha(\bar{z})$ and $\bar{\alpha}$ interchangeably for the ΛCDM models tested here.

figure 6.4.

The error in the constant AP scaling (6.48) $\text{APerror}_\epsilon = \hat{\mathcal{C}}_\epsilon - (\mathcal{C}_\epsilon)_{\text{th}}$ is shown in figure 6.4a for the standard constant AP scaling approximation analysis with $(\mathcal{C}_\epsilon)_{\text{th}} = \epsilon(\bar{z})$ and the modified constant AP scaling approximation with $(\mathcal{C}_\epsilon)_{\text{th}} = \bar{\epsilon}$. The errors for both constant AP scaling approximations are of order $\lesssim 0.002$. The statistical $1\,\sigma$ error bars on the best fit values of the warping parameters are of order 0.002. We conclude that the level of inaccuracy in the recovery of the warping parameters is consistent with the level of statistical noise expected for ~ 200 mock catalogues. The accuracy of the two constant AP approximations are very close for each model cosmology as expected from the investigations in section 6.2.3. There is no systematic improvement of the accuracy to be seen for the modified constant AP scaling approximation $(\mathcal{C}_\epsilon)_{\text{th}} = \bar{\epsilon}$ as compared to the standard constant AP scaling approximation $(\mathcal{C}_\epsilon)_{\text{th}} = \epsilon(\bar{z})$.

In figure 6.4b the accuracy of the modified constant AP scaling approximation $(\mathcal{C}_\epsilon)_{\text{th}} = \bar{\epsilon}$ is compared to that of the exact AP scaling $\alpha(z)$, $\epsilon(z)$. For each cosmological model, the recovery of the anisotropic warping parameter is almost identical for the constant AP scaling approximation and the exact case. In conclusion, the constant AP approximations tested work extremely well for the tested cosmological models for recovering the anisotropic warping parameter. The more accurate recovery of the warping parameter as compared to the isotropic peak position, suggests that the systematics governing the peak shift are similar between the wedges.

6.4.4 Toy models with large metric gradients

Let us consider a class of unphysical model cosmologies, for which we can expect breakdown of the standard AP scaling approximation with respect to the reference ΛCDM model with $\Omega_M = 0.3$.

As shown in general in section 6.2.2 and detailed for a selection of model cosmologies in section 6.2.3, the standard constant AP approximation $\alpha(z) \mapsto \alpha(\bar{z})$, $\epsilon(z) \mapsto \epsilon(\bar{z})$ is expected to be accurate between cosmologies which are of the same order of magnitude for gradient terms of the adapted metric components $\{g_{\theta\theta}, g_{zz}\}$ up to second order. This condition is fulfilled for essentially all cosmological metric theories designed for modelling the largest scales of our Universe. However, taking into account gradients in the geometry on smaller scales, we might arrive at physical models for which the usual constant AP scaling approximation breaks down when the fiducial cosmology used to

formulate the 2-point correlation function is a large-scale metric. In this section we formulate some toy models which can illustrate how the usual constant AP scaling approximation might break down on account of gradients in the metric components $\{g_{\theta\theta}, g_{zz}\}$.

In this analysis we consider the reference ΛCDM model with $\Omega_M = 0.3$ as the 'true' cosmological model, whereas the toy models with significant metric gradients are fiducial models used to formulate the 2-point correlation function by the observer who does not know about the true cosmological model. Our conclusions are expected to hold for the reversed scenario where the reference ΛCDM model with $\Omega_M = 0.3$ plays the role of the fiducial model.

We consider the simple three parameter family of spatially-flat toy model metrics (6.30)–(6.32), which are perturbations around the spatially flat ΛCDM model with $\Omega_M = 0.3$ with a trigonometric distortion parameterised by an amplitude A, frequency f, and phase Φ.

We repeat the analysis of section 6.4.3 for eight test models of varying A, f, and Φ. The mean isotropic 2-point correlation function is shown in figure 6.6 for each model. The shifts of the BAO feature relative to the reference ΛCDM model are in general much smaller than for the models tested in section 6.4.3. This can be assigned to the fact, that $\bar{\alpha}$ is close to the value 1 for all the models because of the cancellation of the relatively large fluctuation of $\alpha(z)$ by the averaging operation. Even though the mutual distance between many galaxy pairs are shifted significantly by changing from one model to the other, the overall count in each distance bin is largely robust, and the shape of the reference correlation function is largely preserved as seen in figure 6.6a. The zoomed in version of the plot in figure 6.6b visualises the changes around the peak location.

The results of the isotropic analysis are shown in figure 6.7. In figure 6.7a the error in the recovery of the isotropic peak position $\mathrm{APerror}_r$ (6.48) is shown for the standard constant AP scaling approximation analysis with $(\mathcal{C}_\alpha)_{\mathrm{th}} = \alpha(\bar{z})$ and the modified constant AP scaling approximation with $(\mathcal{C}_\alpha)_{\mathrm{th}} = \bar{\alpha}$. The precision obtained with the modified constant AP scaling approximation is generally higher, with typical errors of order ~ 0.5 times those of the standard constant AP scaling approximation. The errors associated with the modified constant AP scaling approximation are $\lesssim 1\%$ and comparable to those of the spatially-flat FLRW models investigated in section 6.4.3. As in the case of the spatially-flat FLRW models, the statistical errors are not

sufficient to account for the errors, and we conclude that systematic uncertainties are dominating the error budget.

In figure 6.3b the accuracy of the modified constant AP scaling approximation $(\mathcal{C}_\alpha)_{\rm th} = \bar{\alpha}$ is compared to the accuracy of the exact AP scaling $\alpha(z)$, $\epsilon(z)$. As for the spatially-flat FLRW models investigated in section 6.4.3, the plot shows no systematic improvements in accuracy when using the 'exact' wedge function (6.49) as compared to imposing the constant AP approximation $(\mathcal{C}_\alpha)_{\rm th} = \bar{\alpha}$.

The recovery of the warping parameters of the anisotropic wedge analysis is shown in figure 6.8. The error term $\text{APerror}_\epsilon = \hat{\mathcal{C}}_\epsilon - (\mathcal{C}_\epsilon)_{\rm th}$ from (6.48) is shown in figure 6.8a for the standard constant AP scaling approximation analysis $(\mathcal{C}_\epsilon)_{\rm th} = \epsilon(\bar{z})$ and the modified constant AP scaling approximation $(\mathcal{C}_\epsilon)_{\rm th} = \bar{\epsilon}$. The precision of the modified constant AP scaling approximation is in general higher than that of the standard constant AP scaling approximation. For the modified constant AP scaling approximation, errors in the inferred warping parameters are of order $\lesssim 0.005$, and typical errors are roughly a factor of two higher than for the spatially-flat FLRW models investigated in section 6.4.3. Typical errors are slightly higher than ~ 0.002 for which we would expect most points to lie within, for the errors to be consistent with statistical noise.

In figure 6.8b the accuracy of the modified constant AP scaling approximation $(\mathcal{C}_\epsilon)_{\rm th} = \bar{\epsilon}$ is compared to that of the exact AP scaling $\alpha(z)$, $\epsilon(z)$. The recovery of the anisotropic warping parameter is almost the same between the modified constant AP scaling approximation and the exact AP scaling.

In conclusion, the modified constant AP approximation works extremely well for the toy models considered here – as well as for the models tested in section 6.4.3, where both constant AP scaling approximations were accurate – and approximate the 'exact' case, where no approximations are made for $\alpha(z), \epsilon(z)$, extremely well. However, additional systematic errors contribute to the error budget in the empirical fitting procedure, as discussed in context of the spatially-flat FLRW models in section 6.4.3.

6.5 Discussion

Since the mid 2000's when the first detections of the BAO scale were made [56, 57], galaxy surveys have increased in terms of sample size and volume coverage, which has led to an increased significance of the measured BAO peak in the concordance ΛCDM cosmology [193, 194, 193] and precisely mapped out the distance-redshift relation.

The increase in data has also facilitated (semi-)model-independent analysis such as [210] and the methods developed in chapter 5. Such analysis allows for determining characteristic scales in the 2-point correlation function without assuming a ΛCDM fiducial model. It is naturally of interest to what extent the measurements performed under the assumptions of conventional ΛCDM BAO analysis can be expected to be accurate for a Universe which might be far from the ΛCDM model in some respects.

In this analysis we have investigated the accuracy of the standard constant AP scaling method, and a theoretically motivated modification of this, for applying BAO distance measurements in different cosmologies. We have quantified the difference between the two methods in section 6.2.2. The two methods agree well when the 'true' underlying cosmological model and the fiducial model have the same order of magnitude metric gradients. However, when large differences in metric gradients emerge – which can happen in the scenario where a smooth fiducial model metric is used to extract information about the galaxy catalogue of a lumpy universe – the methods can differ substantially.

In our mock-based tests in section 6.4 we investigated the BAO peak shifts between different fiducial cosmologies. We avoid calibration issues in the extraction of the BAO feature by considering the shift of the BAO feature relative to a reference model. We find that the standard constant AP method works well for recovering the BAO scale when the fiducial model and the reference (or 'true') cosmological model are close – up to systematics which cannot be ascribed to the constant AP approximation. As expected from the theoretical results of section 6.2.2, the modified constant AP method gives very similar results to those of the standard constant AP method when the fiducial and reference models are not differing substantially in terms of metric gradients. When we introduce large differences in gradients between the fiducial model and the reference cosmological model, the standard constant AP scaling method becomes inaccurate, while our modified constant AP scaling method remains accurate. This is due to the fact the modified constant AP scaling takes into account the volume statistical aspect of the BAO feature, whereas the standard constant AP scaling method is based on evaluation at a single redshift.

Our results can help understand the 'effective distance scales' that we infer in BAO analysis. The conventionally 'measured' AP parameters are better understood as averages $\overline{\alpha(z)}$ and $\overline{\epsilon(z)}$ over the survey. Thus, they do not represent the *ratio of the mean* of the 'true' model and the fiducial model distance scales evaluated a

particular redshift – but are more accurately thought of as the *mean of the ratio* of the 'true' model and the fiducial model distance scales, which vary over the galaxy survey. This difference in interpretation might be important, depending on the exact lumpy geometry that describes our universe.

We find additional systematics in the recovery of the BAO scale of order $\sim 1\%$ for $|\bar{\alpha}-1| \sim 0.1$ in section 6.4 which cannot be assigned to the constant AP approximation. These systematics persists when we use a ΛCDM template fitting procedure instead of our empirical method, which indicate that the level of systematics is robust to the exact choice of fitting procedure. The systematics are in general larger than what is found in other examinations of systematic errors due to choice of fiducial cosmology, see e.g., [208, 221], which we hypothesise is due to the fact that such analysis are concerned with ΛCDM models which are close – typically within a few percent in terms of cosmological parameters. Our analysis reveal that larger systematic errors emerge when the fiducial and 'true' cosmological models are not close in all respects.[11]

Our analysis based on test cases indicate that the error budget in the standard literature is significantly underestimated when interpreting the herein measured distance scales as 'model-independent' and using the results for constraining alternative models. The additional systematics must be included for consistency even in cases where the aim is to constrain the standard FLRW class of cosmologies, and where priors from the cosmic microwave background are employed at a later step in the analysis. Implicit priors in data-reduction must in general be avoided for self-consistency of a statistical analysis and reliability of the error budget. Alternatively, if neglecting the systematic errors associated with the choice of fiducial model, the assumption about closeness of the 'true' cosmological model and the fiducial model $|\bar{\alpha} - 1| \ll 0.1$ must be stated explicitly. However, in this case, the results of the given analysis are primarily useful for consistency testing the fiducial model employed and not suitable for extrapolation to other cosmological models.

Our conclusions are twofold. On one hand, the standard constant AP scaling approximation works surprisingly well for a broad class of pairs of 'true' and fiducial models. The fiducial model can be far from the 'true' model in terms of the relevant

[11] We note that the systematics might be even larger if we omit the precaution of scaling the fitting range by a factor $1/\bar{\alpha}$ in order to approximately fit the tested models over the same physical distance range as the reference model. This is of course only possible to do since we know the 'true' underlying model with respect to which we define α, but is not possible when fitting to actual data where the 'true' underlying model is unknown.

distance measures – as long as these and their gradients are bounded to be of similar order of magnitude to those of the 'true' cosmological model – while the constant AP approximation remains accurate for the purposes of BAO analysis. By reinterpreting the constant AP scaling parameters one can modify the standard constant AP scaling approximation to be accurate for an even larger class of pairs of models. On the other hand, there are systematic uncertainties which are not directly related to the constant AP approximation. These systematic uncertainties of order $\sim 1\%$ for $|\bar{\alpha} - 1| \sim 0.1$ – which are independent of the fitting procedure chosen – are comparable in size to the statistical errors often reported in BAO analysis. Our results indicate that one must re-assess the error budget of standard BAO analysis on account of systematics related to the choice of fiducial cosmology.

A limitation of our analysis is that it applies to spherically-symmetric template geometries only. Even though large-scale average template metrics are usually taken as spherically symmetric, the symmetry is broken at scales below that of statistical isotropy. Systematic effects of the anisotropy from smaller scales – which do not cancel on average in all respects and might feed into the large-scale estimators of the two-point correlation function – might be important for realistic lumpy space-times. One might attempt to generalise our methods to more generic geometries. A challenge of this is that the AP scaling is designed for spherical symmetry. For generic spatial 3-metrics, one would need six generalised AP functions instead of two in order to account for the degrees of freedom involved.

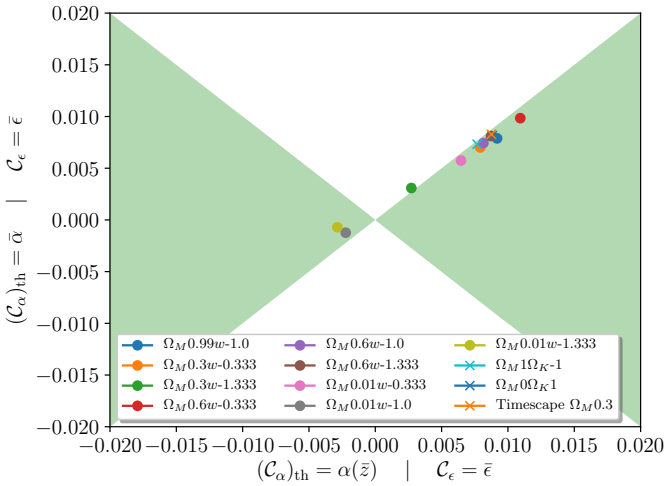

(a) The constant AP scaling approximation error $\text{APerror}_r = \left(\widehat{r/\mathcal{C}_\alpha} - (r/\mathcal{C}_\alpha)_{\rm th}\right) / (r/\mathcal{C}_\alpha)_{\rm th}$ with $(\mathcal{C}_\alpha)_{\rm th} = \alpha(\bar{z})$ (horizontal axis) and $(\mathcal{C}_\alpha)_{\rm th} = \bar{\alpha}$ (vertical axis) respectively.

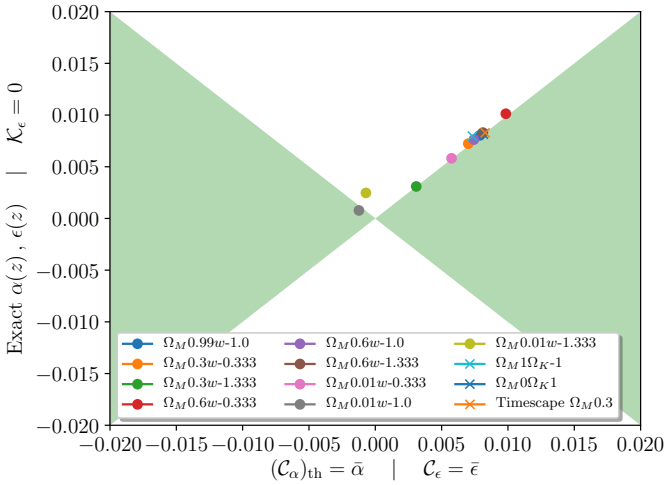

(b) The constant AP scaling error $\text{APerror}_r = \left(\widehat{r/\mathcal{C}_\alpha} - (r/\mathcal{C}_\alpha)_{\rm th}\right) / (r/\mathcal{C}_\alpha)_{\rm th}$ with $(\mathcal{C}_\alpha)_{\rm th} = \bar{\alpha}$ (horizontal axis) and the error in the 'exact' AP scaling $\text{APerror}_r = (\hat{r} - (r)_{\rm th}) / (r)_{\rm th}$ (vertical axis).

Figure 6.3: The accuracy of the inferred isotropic peak position for the constant AP scaling approximations and for the exact AP scaling. For points within the green shaded region, the AP model on the vertical axis is more accurate, and for points in the unshaded region, the AP model on the horizontal axis is more accurate. The warping parameters are fixed such that $\mathcal{C}_\epsilon = \bar{\epsilon}$ in (6.47) and $\mathcal{K}_\epsilon = 0$ in (6.49). Flat test models are represented by a dot, whereas curved models are represented by a cross.

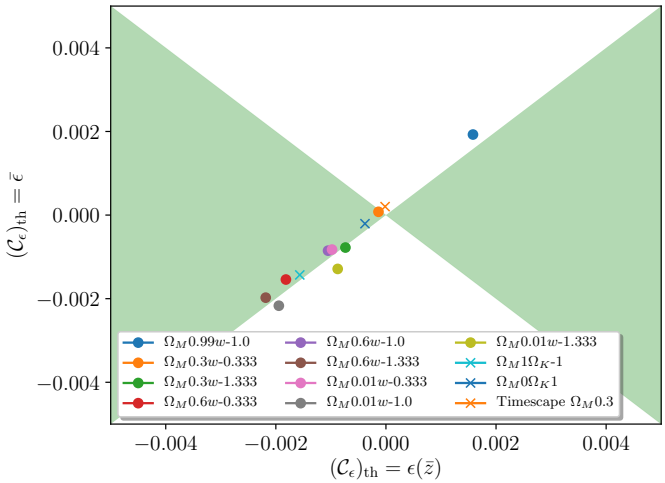

(a) The constant AP scaling approximation error $\text{APerror}_\epsilon = \hat{\mathcal{C}}_\epsilon - (\mathcal{C}_\epsilon)_{\rm th}$ for the constant AP scaling approximation analysis with $(\mathcal{C}_\epsilon)_{\rm th} = \epsilon(\bar{z})$ (horizontal axis) and with $(\mathcal{C}_\epsilon)_{\rm th} = \bar{\epsilon}$ (vertical axis) respectively.

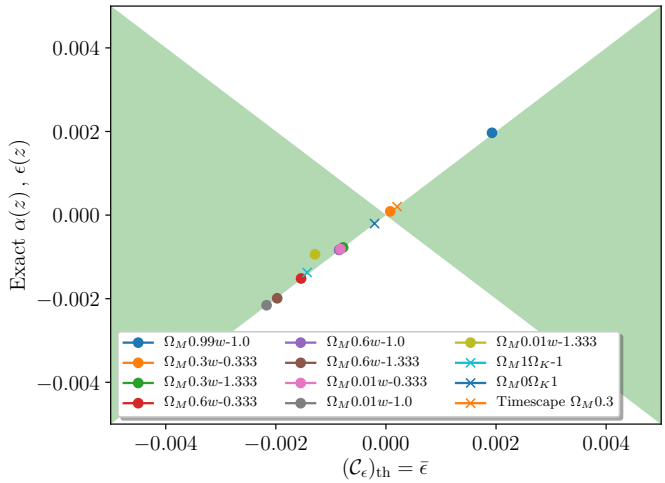

(b) The constant AP scaling approximation error $\text{APerror}_\epsilon = \hat{\mathcal{C}}_\epsilon - (\mathcal{C}_\epsilon)_{\rm th}$ with $(\mathcal{C}_\epsilon)_{\rm th} = \bar{\epsilon}$ (horizontal axis) and the error in the 'exact' AP scaling $\text{APerror}_\epsilon = \hat{\mathcal{K}}_\epsilon$ (vertical axis).

Figure 6.4: The accuracy of the inferred warping parameters of the constant AP scaling approximations and for the exact AP scaling. For points within the green shaded region, the AP model on the vertical axis is more accurate, and for points in the unshaded region, the AP model on the horizontal axis is more accurate. Flat test models are represented by a dot, whereas curved models are represented by a cross.

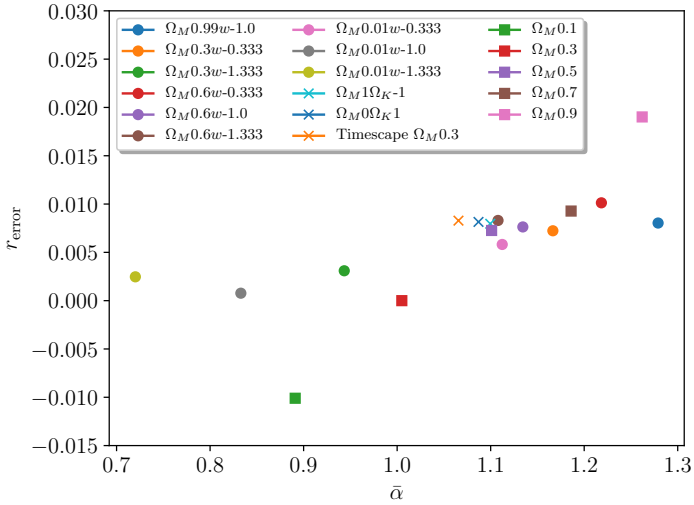

Figure 6.5: The accuracy of the inferred isotropic peak position as a function of the theoretical value of $\bar{\alpha}$. For the empirical fitting procedure, flat test models are represented by a dot, whereas curved models are represented by a cross. For the ΛCDM template fitting procedure, the models are represented by squares. Statistical errors of the individual measurements are of order 0.2%.

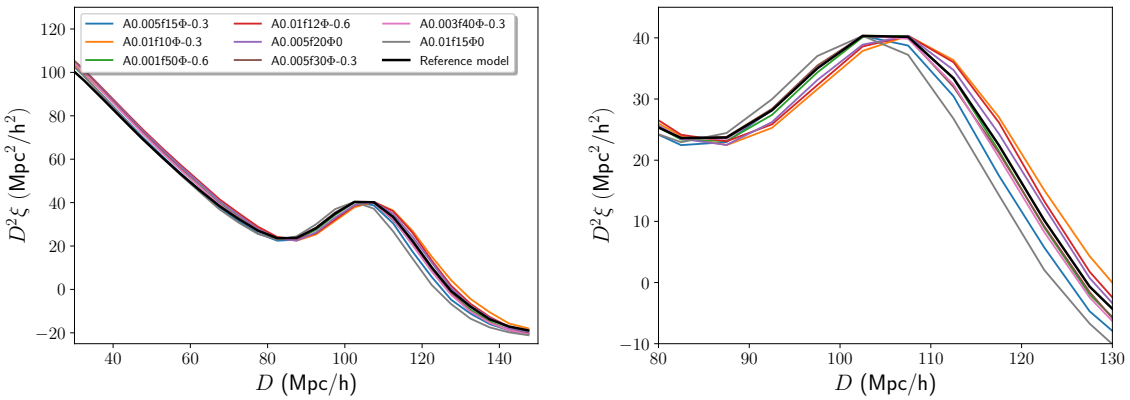

(a) The correlation functions as plotted over the full range.

(b) Zoomed in version around the local maxima of the correlation functions.

Figure 6.6: The mean of the isotropic 2-point correlation function of 200 mock catalogues for each tested toy model. The reference spatially-flat ΛCDM cosmological model with $\Omega_M = 0.3$ is shown in black. In order to visualise the shift of the acoustic scale, the correlation function for each model has been normalised by a constant such that the local maxima are aligned with that of the reference ΛCDM model.

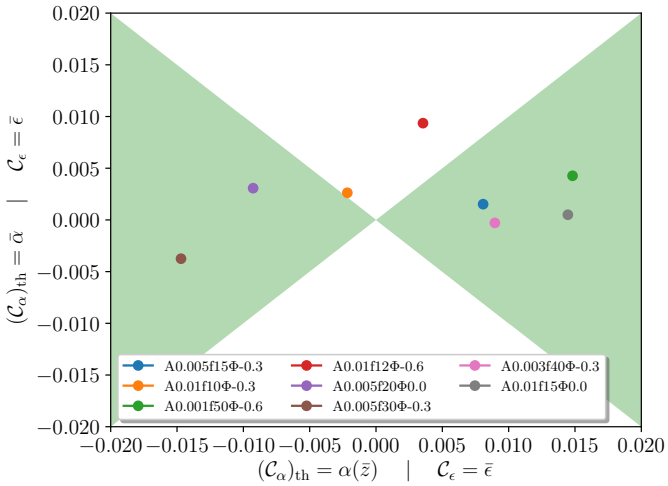

(a) The constant AP scaling approximation error $\text{APerror}_r = \left(\widehat{r/\mathcal{C}_\alpha} - (r/\mathcal{C}_\alpha)_{\text{th}}\right) / (r/\mathcal{C}_\alpha)_{\text{th}}$ with $(\mathcal{C}_\alpha)_{\text{th}} = \alpha(\bar{z})$ (horizontal axis) and $(\mathcal{C}_\alpha)_{\text{th}} = \bar{\alpha}$ (vertical axis) respectively.

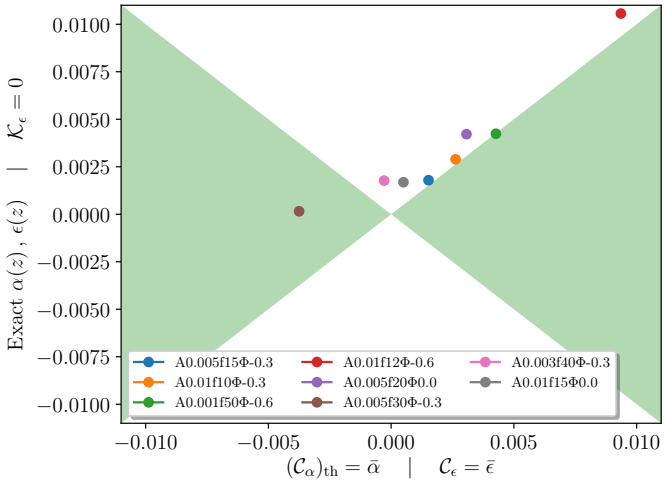

(b) The constant AP scaling error $\text{APerror}_r = \left(\widehat{r/\mathcal{C}_\alpha} - (r/\mathcal{C}_\alpha)_{\text{th}}\right) / (r/\mathcal{C}_\alpha)_{\text{th}}$ with $(\mathcal{C}_\alpha)_{\text{th}} = \bar{\alpha}$ (horizontal axis) and the error in the 'exact' AP scaling $\text{APerror}_r = (\hat{r} - (r)_{\text{th}}) / (r)_{\text{th}}$ (vertical axis).

Figure 6.7: The accuracy of the inferred isotropic peak position for the constant AP scaling approximations and for the exact AP scaling. For points within the green shaded region, the AP model on the vertical axis is more accurate, and for points in the unshaded region, the AP model on the horizontal axis is more accurate. The warping parameters are fixed such that $\mathcal{C}_\epsilon = \bar{\epsilon}$ in (6.47) and $\mathcal{K}_\epsilon = 0$ in (6.49).

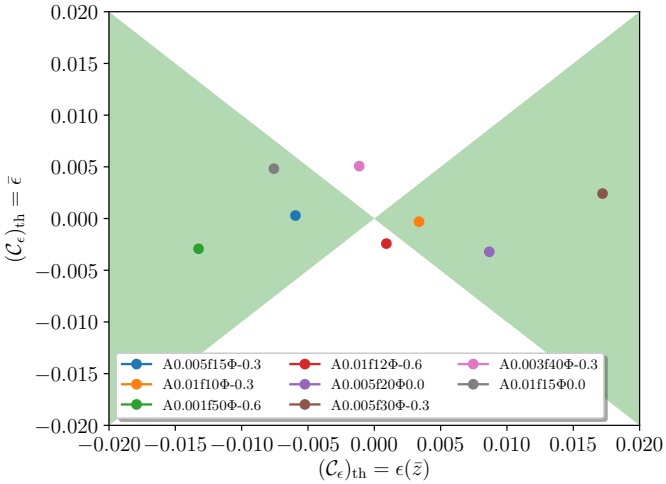

(a) The constant AP scaling approximation error $\text{APerror}_\epsilon = \hat{\mathcal{C}}_\epsilon - (\mathcal{C}_\epsilon)_{\rm th}$ for the constant AP scaling approximation analysis with $(\mathcal{C}_\epsilon)_{\rm th} = \epsilon(\bar{z})$ (horizontal axis) and with $(\mathcal{C}_\epsilon)_{\rm th} = \bar{\epsilon}$ (vertical axis) respectively.

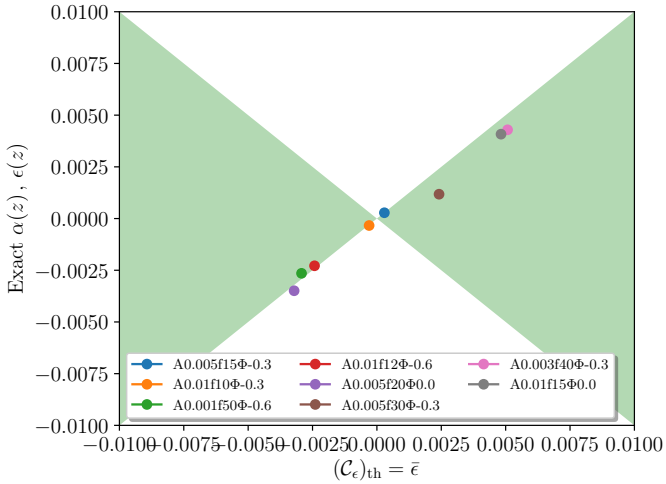

(b) The constant AP scaling approximation error $\text{APerror}_\epsilon = \hat{\mathcal{C}}_\epsilon - (\mathcal{C}_\epsilon)_{\rm th}$ with $(\mathcal{C}_\epsilon)_{\rm th} = \bar{\epsilon}$ (horizontal axis) and the error in the 'exact' AP scaling $\text{APerror}_\epsilon = \hat{\mathcal{K}}_\epsilon$ (vertical axis).

Figure 6.8: The accuracy of the inferred warping parameters of the constant AP scaling approximations and for the exact AP scaling. For points within the green shaded region, the AP model on the vertical axis is more accurate, and for points in the unshaded region, the AP model on the horizontal axis is more accurate.

Appendix 6.A The 2-point correlation function and the Landy-Szalay estimators

The 2-point correlation function in cosmology [52] describes the clustering of matter as a function of scale to lowest order. Here we give a review of the 2-point correlation function, and define a useful 'reduced' form of the correlation function, relevant for the present analysis, and we review the estimators of the 2-point correlation function conventionally used.

6.A.1 The 2-point correlation

The definition of the 2-point correlation function relies on considering ensemble averages of model universes as generated from a random process specified within the given cosmological model.

Let us consider a fixed spatial domain $\mathcal{D}$. We consider the position of the galaxies within this domain random variables, and keep the total number of galaxies N within the domain $\mathcal{D}$ constant over the ensembles. We use adapted coordinates X^i on the spatial domain, and denote the random position of the a'th particle x^i_a. We define the ensemble averaged pair count density $f(X,Y)$ of galaxies as the ensemble average pair count per unit volume squared:

$$f(X,Y)dV_X\, dV_Y \equiv \langle N(dV_X)N(dV_Y)\rangle\,, \tag{6.51}$$

where dV_X and dV_Y are infinitesimal volume elements centred on coordinates X and Y, and the indices on X and Y have been suppressed. (These volume elements need not be 'physical' volume elements but might be conveniently defined as coordinate volumes, absorbing any volume measure into $f(X,Y)$.) The brackets $\langle\rangle$ denote the

average over realisations of the ensemble, and

$$N(dV_X) \equiv \sum_a^N \mathbb{1}_{dV_X}(x_a^i)\,, \qquad \mathbb{1}_{dV_X}(x_a^i) = \begin{cases} 1, & x_a^i \in dV_X, \\ 0, & x_a^i \notin dV_X, \end{cases} \tag{6.52}$$

is the number count in the volume element dV_X in a given realisation, where $\mathbb{1}_{dV_X}$ is the indicator function of the volume dV_X. The ensemble averaged galaxy density function $f(X)$ can be expressed as an integral over (6.51)

$$f(X)dV_X \equiv \langle N(dV_X)\rangle = \frac{1}{N}\left(\int f(X,Y)dV_Y\right) dV_X\,, \tag{6.53}$$

where integration without limits indicate integration over the entire domain $\mathcal{D}$, and where the normalisation $N = N(\mathcal{D})$ is the ensemble-fixed total number of galaxies in the domain $\mathcal{D}$.

The spatial 2-point correlation function is defined as

$$\xi(X,Y) \equiv \frac{f(X,Y)}{f_{\text{Poisson}}(X,Y)} - 1 = \frac{f(X,Y)}{f(X)f(Y)} - 1\,, \tag{6.54}$$

and describes the excess ensemble number count over the ensemble number count in an artificial uncorrelated ensemble with factorising pair count density $f_{\text{Poisson}}(X,Y) = f(X)f(Y)$.

We can define a number of 'reduced' 2-point correlation functions by integrating over $f(X,Y)dV_X\,dV_Y$ and $f_{\text{Poisson}}(X,Y)dV_X\,dV_Y$ subject to a given constraint.[12]

Typically we might consider the geodesic distance to be fixed in the integration. For this purpose, it is useful to perform the change of variables $(X^i, Y^i) \mapsto (X^i, \hat{n}_X^i, D)$, where $\hat{n}_X^i$ is a unit vector defined at X^i representing a geodesic starting at X^i and

[12] It is conventional to assume that the galaxy distribution is described by a homogeneous and isotropic point process, in which case the 2-point correlation function (6.54) automatically reduces to a function of the geodesic distance D between the galaxy pairs, where D is defined within the 'true' cosmological model. However, here we are relaxing the conventional assumptions of homogeneity and isotropy to potentially allow for asymmetric random processes describing the galaxy distribution, and to account for systematic observational effects, such as the redshift depth of the survey or survey-coverage. (The survey might be limited in parts of the sky as compared to others.) Even for the homogeneous and isotropic point process, this new formulation is relevant when the 'wrong' fiducial cosmology is used for constructing the 2-point correlation function.

intersecting Y^i and D is the geodesic distance[13] from X^i to Y^i. Using the Jacobian of the transformation, we can then formulate the pair count density as a function of the new variables $f(X^i, \hat{n}^i_X, D)$.

For the type of spherically-symmetric models specified in section 6.1.1 we can decompose $\hat{n}_X$ into μ, $\mathrm{sgn}(\delta z)$, and the normalised angular separation vector $\hat{\Theta} = \frac{1}{|\delta\Theta|}(\delta\theta, \cos(\theta)\delta\phi)$. Furthermore for this class of models we can use the observer adapted functions (z, θ, ϕ) as convenient coordinates on a spatial domain $\mathcal{D}$ on a hypersurface defined by $t = \text{const.}$, and take $X = (z, \theta, \phi)$. We can then rewrite (6.51) in terms of the new set of variables

$$f(X, Y)dV_X\, dV_Y = f[z, \theta, \phi, \mu, \mathrm{sgn}(\delta z), \hat{\Theta}, D]dz\, d\theta\, d\phi\, d\mu\, d\hat{\Theta}\, dD\,. \tag{6.55}$$

Let us now define the 'reduced' pair count density function in (D, μ, z) by integrating (6.55) over the remaining variables $(\theta, \phi, \hat{\Theta}, \mathrm{sgn}(\delta z))$

$$f(D, \mu, z) \equiv \sum_{\mathrm{sgn}(\delta z)=\pm 1} \int f(z, \theta, \phi, \mu, \mathrm{sgn}(\delta z), \hat{\Theta}, D)d\theta\, d\phi\, d\hat{\Theta}\,, \tag{6.56}$$

and analogously define $f_{\mathrm{Poisson}}(D, \mu, z)$. From the 'reduced' pair count density functions, we can define the 'reduced' 2-point correlation function

$$\xi(D, \mu, z) \equiv \frac{f(D, \mu, z)}{f_{\mathrm{Poisson}}(D, \mu, z)} - 1\,. \tag{6.57}$$

We can further reduce the pair count density functions by defining

$$f(D, \mu) \equiv \int f(D, \mu, z)dz\,, \qquad f_{\mathrm{Poisson}}(D, \mu) \equiv \int f_{\mathrm{Poisson}}(D, \mu, z)dz\,, \tag{6.58}$$

from which we can define the 'reduced' 2-point correlation function in D and μ as

$$\xi(D, \mu) = \frac{f(D, \mu)}{f_{\mathrm{Poisson}}(D, \mu)} - 1\,. \tag{6.59}$$

[13] The transformation $(X^i, Y^i) \mapsto (X^i, \hat{n}^i_X, D)$ is bijective if there is a unique geodesic between the points X^i, Y^i, or if some requirement is imposed to single out a unique geodesic. We assume bijectivity in the following.

From (6.59) we can construct the following 'wedge' 2-point correlation function

$$\xi_{[\mu_1,\mu_2]}(D) = \frac{1}{\mu_2 - \mu_1}\int_{\mu_1}^{\mu_2} d\mu\, \xi(D,\mu), \tag{6.60}$$

where we denote

$$\xi(D) \equiv \xi_{[0,1]}(D), \qquad \xi_{\perp}(D) \equiv \xi_{[0,0.5]}(D), \qquad \xi_{\parallel}(D) \equiv \xi_{[0.5,1]}(D) \tag{6.61}$$

the isotropic wedge, the transverse wedge, and the radial wedge respectively.

It will be useful in the present analysis to approximate (6.59) as an integral over (6.57). We do this by defining the normalised density function in z as

$$P(z) \equiv \frac{\int f(z,\theta,\phi)d\theta\, d\phi}{\int f(z',\theta',\phi')dz'\, d\theta'\, d\phi'} = \frac{\int f(D,\mu,z)d\mu\, dD}{\int f(D',\mu',z')dz'\, d\mu'\, dD'}\,, \tag{6.62}$$

where $f(z,\theta,\phi)dz\, d\theta\, d\phi = f(X)dV_X$, and where the equality follows from (6.53) and (6.56). Suppose that the pair count functions $f(D,\mu,z)$ and $f_{\rm Poisson}(D,\mu,z)$ are almost of a multiplicatively separable form, such that

$$f(D,\mu,z) = f(D,\mu)P(z)(1+\delta(D,\mu,z))\,, \qquad \delta(D,\mu,z) \ll 1, \tag{6.63}$$

$$f_{\rm Poisson}(D,\mu,z) = f_{\rm Poisson}(D,\mu)P(z)(1+\delta(D,\mu,z))\,, \qquad \delta_{\rm Poisson}(D,\mu,z) \ll 1. \tag{6.64}$$

Note that by the definitions (6.58) we have the constraints

$$\int P(z)\delta(D,\mu,z)dz = \int P(z)\delta_{\rm Poisson}(D,\mu,z)dz = 0 \quad \forall\, D,\mu\,. \tag{6.65}$$

We can now use the decomposition (6.63) to write the following integral over (6.57) in

redshift as

$$\begin{aligned}
&\int \xi(D,\mu,z)P(z)dz = \int \frac{f(D,\mu,z)}{f_{\text{Poisson}}(D,\mu,z)}P(z)dz - 1 \\
&\approx \frac{f(D,\mu)}{f_{\text{Poisson}}(D,\mu)} \int \left[1+\delta-\delta_{\text{Poisson}}-\delta_{\text{Poisson}}(\delta-\delta_{\text{Poisson}})\right] P(z)dz - 1 \\
&= \frac{f(D,\mu)}{f_{\text{Poisson}}(D,\mu)} \int \left[1-\delta_{\text{Poisson}}(\delta-\delta_{\text{Poisson}})\right] P(z)dz - 1 \\
&= \xi(D,\mu) - (1+\xi(D,\mu)) \int \delta_{\text{Poisson}}(\delta-\delta_{\text{Poisson}})P(z)dz\,, \qquad (6.66)
\end{aligned}$$

where the second line follows from substituting (6.63) and expanding around $\delta = 0$ to second order, the third line follows from (6.65), and the last equality follows from (6.59) and the condition that the integral of $P(z)$ is normalised to 1. Thus, under the assumptions (6.63), $\int \xi(D,\mu,z)P(z)dz = \xi(D,\mu)$ to first order in δ and δ_{Poisson}.

6.A.2 The Landy-Szalay estimators

Estimators of the 2-point correlation function require (approximate) spatial ergodicity to be satisfied [51]. To this end we write the theoretical 2-point correlation function (6.59) as

$$\xi(D,\mu) = \frac{f(D,\mu)}{f_{\text{Poisson}}(D,\mu)} - 1 = \frac{\langle N(D\pm\delta D,\mu\pm\delta\mu)\rangle}{\langle N_{\text{Poisson}}(D\pm\delta D,\mu\pm\delta\mu)\rangle} - 1\,, \qquad (6.67)$$

where $N(D\pm\delta D,\mu\pm\delta\mu)$ is the number pair count of galaxies separated by a distance $D\pm\delta D$ and 'radial fraction of the separation' $\mu\pm\delta\mu$, where δD and $\delta\mu$ are infinitesimal displacements, and $\langle\rangle$ denotes the average over ensembles. Spatial ergodicity then amounts to the assumption that $\xi(D,\mu)$ can be approximated within a single realisation such that

$$\lim_{V(\mathcal{D})\to\infty} \frac{N(D\pm\delta D,\mu\pm\delta\mu)}{N_{\text{Poisson}}(D\pm\delta D,\mu\pm\delta\mu)} - 1 \approx \xi(D,\mu)\,. \qquad (6.68)$$

Furthermore, we must in practice assume fast enough convergence, such that a finite volume of the size of a typical available catalogues approximates the left hand side of (6.68).

Naturally, we can imagine performing pair counts of galaxies in a universe which is a

realisation of an ensemble that does not satisfy (6.68). In this case, the pair count ratio on the left hand side of (6.68) is merely a descriptive statistic of correlation between structure for a single realisation and has no interpretation in terms of the ensemble average.

Various estimators of the 2-point correlation function have been tested within ΛCDM simulations [201]. The Landy-Szalay (LS) estimator [202] is found to have small variance compared to other estimators of the 2-point correlation function and reads

$$\hat{\xi}(D,\mu) = \frac{DD(D,\mu) + RR(D,\mu) - 2DR(D,\mu)}{RR(D,\mu)}, \tag{6.69}$$

where DD is the normalised number count

$$DD(D,\mu) = \frac{1}{N_D(N_D-1)} \sum_{a,b}^{N_D} \mathbb{1}_{D\pm\Delta D}(D(x_a^i, x_b^i))\mathbb{1}_{\mu\pm\Delta\mu}(\mu(x_a^i, x_b^i)) \tag{6.70}$$

over galaxies in the survey, where N_D is the total number of galaxies, and ΔD and $\Delta\mu$ are bin sizes for the count. $\mathbb{1}_A(y)$ is the indicator function, having the value 1 for $y \in A$ and 0 for $y \notin A$. RR is defined in the same way,

$$RR(D,\mu) = \frac{1}{N_R(N_R-1)} \sum_{a,b}^{N_R} \mathbb{1}_{D\pm\Delta D}(D(x_a^i, x_b^i))\mathbb{1}_{\mu\pm\Delta\mu}(\mu(x_a^i, x_b^i)), \tag{6.71}$$

except that the sum is now over N_R artificial galaxies in a random Poisson catalogue, designed to match the galaxy survey density in redshift and angular position. We also define DR, as the normalised cross pair-count between the galaxy catalogue and the random sample, by

$$DR(D,\mu) = \frac{1}{N_D N_R} \sum_{a}^{N_D}\sum_{b}^{N_R} \mathbb{1}_{D\pm\Delta D}(D(x_a^i, x_b^i))\mathbb{1}_{\mu\pm\Delta\mu}(\mu(x_a^i, x_b^i)) \tag{6.72}$$

It is often useful to average (6.69) over μ to obtain the wedge LS estimator corresponding to the ensemble wedge function (6.60)

$$\hat{\xi}_{[\mu_1,\mu_2]}(D) = \frac{1}{\mu_2-\mu_1}\int_{\mu_1}^{\mu_2} d\mu\, \hat{\xi}(D,\mu). \tag{6.73}$$

We define the estimators of the isotropic wedge $\hat{\xi}(D)$, the transverse wedge $\hat{\xi}_{\perp}(D)$ and radial wedge $\hat{\xi}_{\parallel}(D)$ as respectively

$$\hat{\xi}(D) \equiv \hat{\xi}_{[0,1]}(D), \qquad \hat{\xi}_{\perp}(D) \equiv \hat{\xi}_{[0,0.5]}(D), \qquad \hat{\xi}_{\parallel}(D) \equiv \hat{\xi}_{[0.5,1]}(D). \tag{6.74}$$

Appendix 6.B Conjecture of improved AP scaling

In this section we conjecture that the modified constant AP scaling $\alpha(z) \mapsto \bar{\alpha}$, $\epsilon(z) \mapsto \bar{\epsilon}$ is typically better for extracting characteristic features of a 2-point correlation function as compared to the standard constant AP scaling approximation $\alpha(z) \mapsto \alpha(\bar{z})$, $\epsilon(z) \mapsto \epsilon(\bar{z})$.

Let us consider the function $\Xi : X \subset \mathbb{R}^5 \to Y \subset \mathbb{R}$, such that Ξ assigns a unique real number

$$\Xi(D, \mu, z, \alpha, \epsilon) = \xi^{\rm tr}\left(D^{\rm tr}(D, \mu, \alpha, \epsilon), \mu^{\rm tr}(\mu, \epsilon), z\right) , \tag{6.75}$$

to each point $\{D, \mu, z, \alpha, \epsilon\} \in X$. $\xi^{\rm tr}$ is the 2-point correlation function as given in the 'true' underlying cosmology, and $D^{\rm tr}(D, \mu, \alpha, \epsilon)$ and $\mu^{\rm tr}(\mu, \epsilon)$ are given in (6.10) and (6.11). The parameters α and ϵ might take any values, but we shall often be interested in identifying α and ϵ with the AP scaling functions $\alpha(z)$ and $\epsilon(z)$, given by the 'true' cosmological model and the choice of fiducial model respectively. When identifying α and ϵ with the AP scaling functions $\alpha(z)$ and $\epsilon(z)$, Ξ reduces to the redshift dependent 2-point correlation function ξ in (6.14)

$$\Xi(D, \mu, z, \alpha(z), \epsilon(z)) = \xi(D, \mu, z) = \xi^{\rm tr}\left(D^{\rm tr}(D, \mu, \alpha(z), \epsilon(z)), \mu^{\rm tr}(\mu, \epsilon(z)), z\right) . \tag{6.76}$$

Consider the situation where the condition of almost multiplicative separability (6.63) is satisfied. Then the result (6.66) holds, and we might write

$$\xi(D, \mu) = \overline{\xi(D, \mu, z)} = \overline{\Xi(D, \mu, z, \alpha(z), \epsilon(z))} , \tag{6.77}$$

to first order in the 'non-separability terms' δ, $\delta_{\rm Poisson}$ defined in (6.63). The overbar denotes the averaging operation $\overline{f(z)} \equiv \int dz\, P(z) f(z)$ for an arbitrary function $f(z)$, and the second equality follows from the re-parametrisation (6.76). Let us for simplicity suppose that separability is a good approximation, such that the second order

correction terms are so small that we can for all practical purposes consider the first order approximation in 6.77 exact.

We consider what we denote the standard constant AP approximation of $\xi(D,\mu)$ by performing the mapping $\{z \mapsto \bar{z}, \alpha \mapsto \alpha(\bar{z}), \epsilon \mapsto \epsilon(\bar{z})\}$ in (6.75) to obtain

$$\mathcal{I}_{\text{standard AP}}(D,\mu) \equiv \Xi(D,\mu,\bar{z},\alpha(\bar{z}),\epsilon(\bar{z})) = \xi(D,\mu,\bar{z})\,. \tag{6.78}$$

In addition we consider the analogous modified constant AP approximation $\{z \mapsto \bar{z}, \alpha \mapsto \bar{\alpha}, \epsilon \mapsto \bar{\epsilon}\}$ of $\xi(D,\mu)$

$$\mathcal{I}_{\text{modified AP}}(D,\mu) \equiv \Xi(D,\mu,\bar{z},\bar{\alpha},\bar{\epsilon})\,, \tag{6.79}$$

where we use the short hand notation $\bar{f} = \overline{f(z)}$. We want to estimate which of the functions (6.78) and (6.79) provide the better approximation of $\xi(D,\mu)$.

We assume that $\Xi(D,\mu,z,\alpha,\epsilon)$ is three times differentiable in z,α,ϵ and that α,ϵ are twice differentiable in z. We consider the first order Taylor expansions around $\{z=\bar{z}, \alpha=\alpha(\bar{z}), \epsilon=\epsilon(\bar{z})\}$

$$\begin{aligned} G(D,\mu,z) &\equiv \xi(D,\mu,\bar{z}) + \left.\frac{d\xi(D,\mu,z)}{dz}\right|_{\bar{z}} (z-\bar{z}) \\ &= \xi(D,\mu,\bar{z}) + \left.\left(\frac{\partial\Xi}{\partial z} + \frac{d\alpha}{dz}\frac{\partial\Xi}{\partial\alpha} + \frac{d\epsilon}{dz}\frac{\partial\Xi}{\partial\epsilon}\right)\right|_{\bar{z}} (z-\bar{z})\,, \end{aligned} \tag{6.80}$$

and

$$H(D,\mu,z,\alpha,\epsilon) \equiv \xi(D,\mu,\bar{z}) + \left.\frac{\partial\Xi}{\partial z}\right|_{\bar{z}} (z-\bar{z}) + \left.\frac{\partial\Xi}{\partial\alpha}\right|_{\bar{z}} (\alpha-\alpha(\bar{z})) + \left.\frac{\partial\Xi}{\partial\epsilon}\right|_{\bar{z}} (\epsilon-\epsilon(\bar{z}))\,. \tag{6.81}$$

Let us write the error term associated with (6.81) as an approximation of (6.75) as

$$\Xi(D,\mu,z,\alpha,\epsilon) - H(D,\mu,z,\alpha,\epsilon) = {}^{(2)}\Xi(D,\mu,z,\alpha,\epsilon) + {}^{(2)}\mathcal{R}(D,\mu,z,\alpha,\epsilon)\,, \tag{6.82}$$

where

$$
{}^{(2)}\Xi(D,\mu,z,\alpha,\epsilon) \equiv \frac{1}{2}\left.\frac{\partial^2\Xi}{\partial z^2}\right|_{\bar{z}}(z-\bar{z})^2 + \frac{1}{2}\left.\frac{\partial^2\Xi}{\partial \alpha^2}\right|_{\bar{z}}(\alpha-\alpha(\bar{z}))^2 + \frac{1}{2}\left.\frac{\partial^2\Xi}{\partial \epsilon^2}\right|_{\bar{z}}(\epsilon-\epsilon(\bar{z}))^2 + \\
\left.\frac{\partial^2\Xi}{\partial\alpha\partial z}\right|_{\bar{z}}(z-\bar{z})(\alpha-\alpha(\bar{z})) + \left.\frac{\partial^2\Xi}{\partial\epsilon\partial z}\right|_{\bar{z}}(z-\bar{z})(\epsilon-\epsilon(\bar{z})) + \left.\frac{\partial^2\Xi}{\partial\alpha\partial\epsilon}\right|_{\bar{z}}(\epsilon-\epsilon(\bar{z}))(\alpha-\alpha(\bar{z}))\,, \tag{6.83}
$$

is the second order contribution and ${}^{(2)}\mathcal{R}$ is the remainder at second order.[14] Combining (6.80) and (6.81) we have

$$
\begin{aligned}
&G(D,\mu,z) - H(D,\mu,z,\alpha(z),\epsilon(z)) \\
&= \left(\left.\frac{d\alpha}{dz}\right|_{\bar{z}}(z-\bar{z}) - (\alpha(z)-\alpha(\bar{z}))\right)\left.\frac{\partial\Xi}{\partial\alpha}\right|_{\bar{z}} + \left(\left.\frac{d\epsilon}{dz}\right|_{\bar{z}}(z-\bar{z}) - (\epsilon(z)-\epsilon(\bar{z}))\right)\left.\frac{\partial\Xi}{\partial\epsilon}\right|_{\bar{z}}\,,
\end{aligned} \tag{6.84}
$$

and taking the average we obtain

$$
\overline{G(D,\mu,z)} - \overline{H(D,\mu,z,\alpha(z),\epsilon(z))} = -(\bar{\alpha}-\alpha(\bar{z}))\left.\frac{\partial\Xi}{\partial\alpha}\right|_{\bar{z}} - (\bar{\epsilon}-\epsilon(\bar{z}))\left.\frac{\partial\Xi}{\partial\epsilon}\right|_{\bar{z}}\,. \tag{6.85}
$$

We might now conveniently rewrite (6.78) as

$$
\begin{aligned}
\mathcal{I}_{\text{standard AP}}(D,\mu) &= \overline{G(D,\mu,z)} \\
&= \overline{H(D,\mu,z,\alpha(z),\epsilon(z))} - (\bar{\alpha}-\alpha(\bar{z}))\left.\frac{\partial\Xi}{\partial\alpha}\right|_{\bar{z}} - (\bar{\epsilon}-\epsilon(\bar{z}))\left.\frac{\partial\Xi}{\partial\epsilon}\right|_{\bar{z}}\,,
\end{aligned} \tag{6.86}
$$

where the first equality follows from the definition (6.80) and the last equality follows from (6.85). Similarly we might express (6.79) in terms of the average of (6.81) and its error terms as

$$
\begin{aligned}
\mathcal{I}_{\text{modified AP}}(D,\mu) &= H(D,\mu,\bar{z},\bar{\alpha},\bar{\epsilon}) + {}^{(2)}\Xi(D,\mu,\bar{z},\bar{\alpha},\bar{\epsilon}) + {}^{(2)}\mathcal{R}(D,\mu,\bar{z},\bar{\alpha},\bar{\epsilon}) \\
&= \overline{H(D,\mu,z,\alpha(z),\epsilon(z))} + {}^{(2)}\Xi(D,\mu,\bar{z},\bar{\alpha},\bar{\epsilon}) + {}^{(2)}\mathcal{R}(D,\mu,\bar{z},\bar{\alpha},\bar{\epsilon})\,.
\end{aligned} \tag{6.87}
$$

[14] Following Taylor's theorem one might express ${}^{(2)}\mathcal{R}$ as an integral-expression where the integrand is a linear combination of third order derivatives of Ξ evaluated at $\{z=\bar{z}, \alpha=\alpha(\bar{z}), \epsilon=\epsilon(\bar{z})\}$.

Let us now quantify the accuracy of $\mathcal{I}_{\text{standard AP}}(D,\mu)$ and $\mathcal{I}_{\text{modified AP}}(D,\mu)$ as estimates of $\xi(D,\mu)$. From (6.77), (6.82), and (6.86) we have

$$\begin{aligned}&|\xi(D,\mu) - \mathcal{I}_{\text{standard AP}}(D,\mu)| \\ &= \left| \overline{{}^{(2)}\Xi(D,\mu,z,\alpha(z),\epsilon(z))} + \overline{{}^{(2)}\mathcal{R}(D,\mu,z,\alpha(z),\epsilon(z))} + (\bar{\alpha} - \alpha(\bar{z}))\left.\frac{\partial \Xi}{\partial \alpha}\right|_{\bar{z}} + (\bar{\epsilon} - \epsilon(\bar{z}))\left.\frac{\partial \Xi}{\partial \epsilon}\right|_{\bar{z}} \right|,\end{aligned} \tag{6.88}$$

and from (6.77), (6.82), and (6.87) we have

$$\begin{aligned}&|\xi(D,\mu) - \mathcal{I}_{\text{modified AP}}(D,\mu)| \\ &= \left| \overline{{}^{(2)}\Xi(D,\mu,z,\alpha(z),\epsilon(z))} + \overline{{}^{(2)}\mathcal{R}(D,\mu,z,\alpha(z),\epsilon(z))} - {}^{(2)}\Xi(D,\mu,\bar{z},\bar{\alpha},\bar{\epsilon}) - {}^{(2)}\mathcal{R}(D,\mu,\bar{z},\bar{\alpha},\bar{\epsilon}) \right|.\end{aligned} \tag{6.89}$$

We might note that (6.88) contains terms which are first order in $\alpha(z) - \alpha(\bar{z})$ and $\epsilon(z) - \epsilon(\bar{z})$ respectively, while (6.89) contain only second and higher order terms in these separations.

So far we have made no assumption on $\Xi(D,\mu,z,\alpha,\epsilon)$, $\alpha(z)$, and $\epsilon(z)$ as functions, other than assuming regularity conditions to be fulfilled. Let us suppose that $\alpha(z)$ and $\epsilon(z)$ are sufficiently bounded in terms of size of the variations $\alpha(z) - \alpha(\bar{z})$ and $\epsilon(z) - \epsilon(\bar{z})$ respectively within this redshift interval. Further assume that the third order derivatives of $\Xi(D,\mu,z,\alpha,\epsilon)$ in z, α, and ϵ can be sufficiently bounded within the redshift interval $\mathcal{Z}$ of integration, in such a way that the error term (6.82) is dominated by its second order contribution and that ${}^{(2)}\mathcal{R}$ can be neglected. In this case we have

$$|\xi(D,\mu) - \mathcal{I}_{\text{standard AP}}(D,\mu)| = \left| \overline{{}^{(2)}\Xi(D,\mu,z,\alpha(z),\epsilon(z))} + (\bar{\alpha} - \alpha(\bar{z}))\left.\frac{\partial \Xi}{\partial \alpha}\right|_{\bar{z}} + (\bar{\epsilon} - \epsilon(\bar{z}))\left.\frac{\partial \Xi}{\partial \epsilon}\right|_{\bar{z}} \right|, \tag{6.90}$$

and from (6.77), 6.82, and (6.87) we have

$$|\xi(D,\mu) - \mathcal{I}_{\text{modified AP}}(D,\mu)| = \left| \overline{{}^{(2)}\Xi(D,\mu,z,\alpha(z),\epsilon(z))} - {}^{(2)}\Xi(D,\mu,\bar{z},\bar{\alpha},\bar{\epsilon}) \right|. \tag{6.91}$$

If $\alpha(z)$ and $\epsilon(z)$ are varying sufficiently slowly that the remainder at second order of their expansion can be ignored along with the remainder ${}^{(2)}\mathcal{R}$, then the first or-

der term in $\alpha(z) - \alpha(\bar{z})$ and $\epsilon(z) - \epsilon(\bar{z})$ in (6.90) reduces to the second order term $\frac{1}{2}\frac{\partial^2\alpha}{\partial z^2}\frac{\partial\Xi}{\partial\alpha}\Big|_{\bar{z}}\overline{(z-\bar{z})^2} + \frac{\partial^2\epsilon}{\partial z^2}\frac{\partial\Xi}{\partial\epsilon}\Big|_{\bar{z}}\overline{(z-\bar{z})^2}$. In this case, the competing terms in (6.90) and (6.91) can be considered to be of the same order. As long as there are no chance cancellations we therefore expect the approximations to be accurate at the same order. We will now consider cases where gradients of $\alpha(z)$ and $\epsilon(z)$ are not necessarily small.

Let us consider the case where $\left|\overline{{}^{(2)}\Xi(D,\mu,z,\alpha(z),\epsilon(z))}\right| \neq 0$. In this case we can write $\left|\overline{{}^{(2)}\Xi(D,\mu,z,\alpha(z),\epsilon(z))} - {}^{(2)}\Xi(D,\mu,\bar{z},\bar{\alpha},\bar{\epsilon})\right| \leq \mathcal{K}_{D,\mu}\left|\overline{{}^{(2)}\Xi(D,\mu,z,\alpha(z),\epsilon(z))}\right|$, where $\mathcal{K}_{D,\mu}$ is some positive number which might be chosen differently for different values of D,μ and for each test model. Then the modified AP scaling approximation is guaranteed to be better if $\left|(\bar{\alpha}-\alpha(\bar{z}))\,\frac{\partial\Xi}{\partial\alpha}\big|_{\bar{z}} + (\bar{\epsilon}-\epsilon(\bar{z}))\,\frac{\partial\Xi}{\partial\epsilon}\big|_{\bar{z}}\right| > (\mathcal{K}_{D,\mu}+1)\left|\overline{{}^{(2)}\Xi(D,\mu,z,\alpha(z),\epsilon(z))}\right|$. The left and right hand side of this inequality are just the averages of the first and second order term respectively in the expansion of Ξ (where the latter is scaled by $\mathcal{K}_{D,\mu}+1 \geq 1$). In general we expect the first order term to dominate of a well behaved expansion. We expect $\mathcal{K}_{D,\mu} \lesssim 1$ for most values of D,μ for model 2-point correlation functions which do not have extreme variations with redshift – i.e., where systematics such as galaxy evolution and the distortion due to the choice of trial cosmology are not disturbing the 2-point correlation function by more than order unity.

For a given test model with some set of specified AP functions $\alpha(z)$ and $\epsilon(z)$, we expect that there will be values of D,μ in the physical range of interest for which the second order term of the expansion of Ξ dominates over the first order term, and we might even expect (6.90) to be zero for some region of the domain of negligible measure. However, for most of the domain of D,μ we expect first order terms to dominate over second order terms. In the special case where $\overline{{}^{(2)}\Xi(D,\mu,z,\alpha(z),\epsilon(z))} = 0$ the condition for the modified constant AP scaling approximation to work better than the standard constant AP scaling approximation reduces to $\left|(\bar{\alpha}-\alpha(\bar{z}))\,\frac{\partial\Xi}{\partial\alpha}\big|_{\bar{z}} + (\bar{\epsilon}-\epsilon(\bar{z}))\,\frac{\partial\Xi}{\partial\epsilon}\big|_{\bar{z}}\right| > \left|{}^{(2)}\Xi(D,\mu,\bar{z},\bar{\alpha},\bar{\epsilon})\right|$. This is a direct constraint on the relative size of the first and second order term of the expansion of Ξ as evaluated at $\bar{z},\bar{\alpha},\bar{\epsilon}$. Again we expect the first order term to dominate except for cases where chance cancellations occur.

We conclude without rigorous proof that it is reasonable to assume that the modified constant AP scaling $\alpha(z) \mapsto \bar{\alpha}$, $\epsilon(z) \mapsto \bar{\epsilon}$ approximation is in general better or – in case of sufficiently slowly varying $\alpha(z)$ and $\epsilon(z)$ – equally good, as compared to the standard constant AP scaling approximation $\alpha(z) \mapsto \alpha(\bar{z})$, $\epsilon(z) \mapsto \epsilon(\bar{z})$.

Appendix 6.C Bounds on the AP error terms

In this appendix, we discuss bounds on the magnitude of the error terms Δ_α and Δ_ϵ defined in (6.20) and (6.25) respectively.

6.C.1 Bounds on the magnitude of Δ_α

We shall be interested in bounding Δ_α from above for various situations. Obviously, from its definition in (6.20), Δ_α can be bounded if a bound on $\mathcal{R}_1^\alpha(z)$ of the first order expansion (6.18) is obtained. From Taylor's theorem the remainder term can be written on the form

$$\mathcal{R}_1^\alpha(z) = \frac{1}{2}\frac{\partial^2\alpha}{\partial z^2}(b_{\bar{z}}(z))\,(z-\bar{z})^2 \tag{6.92}$$

for each value of z, where $b_{\bar{z}}(z)$ is a real number between $\bar{z}$ and z.

Bounding the remainder term $\mathcal{R}_1^\alpha(z)$, amounts to bounding the second derivative of α

$$\frac{\partial^2\alpha}{\partial z^2} = \frac{L^{\rm tr}}{L}\left[\frac{\frac{\partial^2 L^{\rm tr}}{\partial z^2}}{L^{\rm tr}} - \frac{\frac{\partial^2 L}{\partial z^2}}{L} - 2\,\frac{\frac{\partial L}{\partial z}}{L}\left(\frac{\frac{\partial L^{\rm tr}}{\partial z}}{L^{\rm tr}} - \frac{\frac{\partial L}{\partial z}}{L}\right)\right], \quad L \equiv \left(g_{\theta\theta}^2 g_{zz}\right)^{\frac{1}{6}},\; L^{\rm tr} \equiv \left((g_{\theta\theta}^{\rm tr})^2 g_{zz}^{\rm tr}\right)^{\frac{1}{6}} \tag{6.93}$$

where $\alpha = L^{\rm tr}/L$ which follows from the definition of α (6.9).

Constraints on L and its derivatives can now be turned into constraints on (6.93). Let us for instance assume that we are considering a class of model cosmologies which are bounded with respect to the 'true' cosmology over the redshift range of the survey in the following sense

$$M_{L\,0}^{\rm min} \leq \frac{L^{\rm tr}}{L} \leq M_{L\,0}^{\rm max}, \qquad \left|\frac{\left(\frac{\partial L^{\rm tr}/\partial z}{L^{\rm tr}}\right)}{\left(\frac{\partial L/\partial z}{L}\right)} - 1\right| \leq M_{L\,1}\,, \qquad \left|\frac{\left(\frac{\partial^2 L^{\rm tr}/\partial z^2}{L^{\rm tr}}\right)}{\left(\frac{\partial^2 L/\partial z^2}{L}\right)} - 1\right| \leq M_{L\,2}\,, \tag{6.94}$$

while L is bounded in its first and second derivatives

$$\left|\frac{\frac{\partial L}{\partial z}}{L}\right| \leq \beta_{L\,1}\,, \qquad \left|\frac{\frac{\partial^2 L}{\partial z^2}}{L}\right| \leq \beta_{L\,2}, \tag{6.95}$$

where $M_{L\,0}^{\min}$, $M_{L\,0}^{\max}$, $M_{L\,1}$, $M_{L\,2}$, $\beta_{L\,1}$, and $\beta_{L\,2}$ are all positive dimensionless constants. We then obtain the following upper bound on (6.93) expressed in terms of these constants

$$\begin{aligned}\left|\frac{\partial^2\alpha}{\partial z^2}\right| &\leq \frac{L^{\mathrm{tr}}}{L}\left(\left|\frac{\frac{\partial^2 L}{\partial z^2}}{L}\left(\frac{\frac{\partial^2 L^{\mathrm{tr}}/\partial z^2}{L^{\mathrm{tr}}}}{\frac{\partial^2 L/\partial z^2}{L}}-1\right)\right| + 2\left(\frac{\frac{\partial L}{\partial z}}{L}\right)^2\left|\frac{\frac{\partial L^{\mathrm{tr}}/\partial z}{L^{\mathrm{tr}}}}{\frac{\partial L/\partial z}{L}}-1\right|\right) \\ &\leq M_{L\,0}^{\max}\left(\beta_{L\,2}M_{L\,2}+2\beta_{L\,1}^2 M_{L\,1}\right). \end{aligned} \tag{6.96}$$

The first inequality follows from the triangle inequality and rearranging of the terms of (6.93), and the second inequality follows from (6.94) and (6.95). The inequality in (6.96) implies the following bound on the remainder $\mathcal{R}_1^\alpha(z)$ in (6.92)

$$|\mathcal{R}_1^\alpha(z)| = \frac{1}{2}\left|\frac{\partial^2\alpha}{\partial z^2}(b_{\bar{z}}(z))\right|(z-\bar{z})^2 \leq \frac{1}{2}M_{L\,0}^{\max}\left(\beta_{L\,2}M_{L\,2}+2\beta_{L\,1}^2M_{L\,1}\right)(z-\bar{z})^2. \tag{6.97}$$

Finally we can use the bound (6.97) to obtain bounds on the error term in (6.20)

$$\begin{aligned}|\Delta_\alpha| &= \frac{1}{\alpha(\bar{z})}\left|\int dz P(z)\mathcal{R}_1^\alpha(z)\right| \leq \frac{1}{\alpha(\bar{z})}\int dz P(z)|\mathcal{R}_1^\alpha(z)| \\ &\leq \frac{1}{2}\frac{M_{L\,0}^{\max}}{M_{L\,0}^{\min}}\left(\beta_{L\,2}M_{L\,2}+2\beta_{L\,1}^2M_{L\,1}\right)\overline{(z-\bar{z})^2}, \end{aligned} \tag{6.98}$$

where the lower bound on $\alpha = L^{\mathrm{tr}}/L$ in (6.94) has been used in the final inequality.

6.C.2 Bounds on the magnitude of Δ_ϵ

We shall now bound the magnitude of the error term Δ_ϵ (6.25) in a similar fashion as done for Δ_α in appendix 6.C.1. We can write the remainder term $\mathcal{R}_1^\epsilon(z)$ (6.18) of the first order expansion

$$\mathcal{R}_1^\epsilon(z) = \frac{1}{2}\frac{\partial^2\epsilon}{\partial z^2}(c_{\bar{z}}(z))(z-\bar{z})^2 \tag{6.99}$$

for each value of z, where $c_{\bar{z}}(z)$ is a real number between $\bar{z}$ and z.

In a similar way to (6.93) we write the second derivative of ϵ in terms of first and

second derivatives of metric combinations of the models

$$\frac{\partial^2\epsilon}{\partial z^2} = \frac{1}{3}\left(\frac{R^{\rm tr}}{R}\right)^{\frac{1}{3}}\left(\frac{\frac{\partial^2 R^{\rm tr}}{\partial z^2}}{R^{\rm tr}} - \frac{\frac{\partial^2 R}{\partial z^2}}{R} - 2\,\frac{\frac{\partial R}{\partial z}}{R}\left(\frac{\frac{\partial R^{\rm tr}}{\partial z}}{R^{\rm tr}} - \frac{\frac{\partial R}{\partial z}}{R}\right) - \frac{2}{3}\left(\frac{\frac{\partial R^{\rm tr}}{\partial z}}{R^{\rm tr}} - \frac{\frac{\partial R}{\partial z}}{R}\right)^2\right), \tag{6.100}$$

where $R \equiv (g_{zz}/g_{\theta\theta})^{1/2}$ and $R^{\rm tr} \equiv (g^{\rm tr}_{zz}/g^{\rm tr}_{\theta\theta})^{1/2}$ are relative distance scales of the models, and where $(1+\epsilon)^3 = \frac{R^{\rm tr}}{R}$ from the definition of epsilon in (6.9).

Similarly to the case of α, the second derivative of ϵ can be bounded as a function of bounds on the metric combination R and its first and second derivatives. Let us consider a class of models which are bounded with respect to the 'true' cosmological model within the redshift interval of the survey in the following way:

$$\left(\frac{R^{\rm tr}}{R}\right)^{\frac{1}{3}} \leq M^{\rm max}_{R0}, \qquad \left|\frac{\left(\frac{\partial R^{\rm tr}/\partial z}{R^{\rm tr}}\right)}{\left(\frac{\partial R/\partial z}{R}\right)} - 1\right| \leq M_{R1}\,, \qquad \left|\frac{\left(\frac{\partial^2 R^{\rm tr}/\partial z^2}{R^{\rm tr}}\right)}{\left(\frac{\partial^2 R/\partial z^2}{R}\right)} - 1\right| \leq M_{R2}\,, \tag{6.101}$$

and where R is bounded in its first and second derivative as

$$\left|\frac{\frac{\partial R}{\partial z}}{R}\right| \leq \beta_{R1}\,, \qquad \left|\frac{\frac{\partial^2 R}{\partial z^2}}{R}\right| \leq \beta_{R2}\,. \tag{6.102}$$

We can now bound the second derivative of ϵ (6.100) based on the above bounds as follows

$$\begin{aligned}\left|\frac{\partial^2\epsilon}{\partial z^2}\right| &\leq \frac{1}{3}\left(\frac{R^{\rm tr}}{R}\right)^{\frac{1}{3}}\left|\frac{\frac{\partial^2 R}{\partial z^2}}{R}\left(\frac{\frac{\partial^2 R^{\rm tr}/\partial z^2}{R^{\rm tr}}}{\frac{\partial^2 R/\partial z^2}{R}} - 1\right)\right| \\ &\qquad + \frac{2}{3}\left(\frac{R^{\rm tr}}{R}\right)^{\frac{1}{3}}\left(\frac{\partial R}{\partial z}\right)^2\left(\left|\frac{\frac{\partial R^{\rm tr}/\partial z}{R^{\rm tr}}}{\frac{\partial R/\partial z}{R}} - 1\right| + \frac{1}{3}\left|\frac{\frac{\partial R^{\rm tr}/\partial z}{R^{\rm tr}}}{\frac{\partial R/\partial z}{R}} - 1\right|^2\right) \\ &\leq \frac{1}{3}M^{\rm max}_{R0}\left(\beta_{R2}M_{R2} + 2\beta^2_{R1}\left(M_{R1} + \frac{1}{3}M^2_{R1}\right)\right), \end{aligned} \tag{6.103}$$

where the first inequality follows from the triangle inequality, and the second inequality follows from (6.101) and (6.102). We can now bound the remainder $\mathcal{R}^{\epsilon}_1(z)$ (6.99) in a similar manner to (6.97), and use the result for bounding the error term Δ_ϵ. The

result reads

$$|\Delta_\epsilon| \leq \int dz P(z) |\mathcal{R}_1^\epsilon(z)| \leq \frac{1}{6} M_{R0}^{\max} \left(\beta_{R2} M_{R2} + 2\beta_{R1}^2 \left(M_{R1} + \frac{1}{3} M_{R1}^2 \right) \right) \overline{(z - \bar{z})^2}\,, \tag{6.104}$$

which follows from the triangle inequality, the bound (6.103), and the definition of the remainder term (6.99).

CHAPTER 7

Conclusion

Inhomogeneities in our Universe are undoubtedly present. However, the significance of inhomogenieties on our perception of overall properties of the Universe is a topic of much controversy in modern cosmology. The main reasons for the inconclusiveness are the richness of possible general relativistic theories which might serve as candidates for modelling our Universe – and the ambiguity in applying general relativity on cosmological scales in the first place – together with the limitation of cosmological data available (and realistically obtainable in the future) to distinguish between various scenarios.

In this thesis we have discussed both theoretical and observational aspects of inhomogeneous cosmology. Common for the frameworks and models discussed is that they are either formulated in Buchert's scheme of averaging or in generalisations thereof.

In chapter 2 we have introduced a generalisation of the covariant scalar averaging scheme of Gasperini, Marozzi and Veneziano (2010) [91], where the integration measure need not coincide with the Riemannian volume element defined on the given spatial hypersurface. The procedure facilitates choosing volume elements of integration which might for some purposes be considered more physical than the usual Riemannian volume element. The scheme makes explicit the role of the foliation scalar in singling out hypersurfaces of integration, and it is thus useful for studying the functional dependence of averaged quantities on the foliation. Such studies are important for quantifying the significance of the choice of the foliation in which averages are defined in Buchert's scheme and its generalisations. Even though some foliation might appear more fundamental or natural in a given space-time, the choice of foliation suitable for averaging is rarely uniquely prescribed or intuitively obvious. In future work we will consider the foliation dependence of scalar averaging schemes [108].

In chapter 3 we have used the JLA SNIa catalogue of supernovae to test the distance–redshift relation of the timescape cosmological model. We found that the timescape model could account for the observed data with the same quality of fit as

ΛCDM, whereas the Milne universe is weakly disfavoured with respect to both the ΛCDM model and the timescape model by current data. We have discussed redshift-dependent biases which have been argued to be present in supernovae analysis, and discussed model-dependence in supernovae data reduction. The future of supernovae analysis for precise cosmological analysis largely depends on being able to independently model systematics in data such as host galaxy properties and observational biases. The degree to which the understanding of such systematic effects can be improved will largely determine the gain in precision for cosmological constraints which can be achieved with future surveys.

In chapter 4 we carried out another analysis on the JLA sample. We examined the fit of a class of scaling solutions formulated in Buchert's averaging scheme combined with a template hypothesis for interpreting observables within Buchert's scheme. We found that the dynamical curvature allowed by the scaling solutions can account for the data of the JLA sample, and that the scaling solutions, the ΛCDM model, and the timescape model are equally preferred from an information-criterion perspective. Future analysis must be carried out to assess whether the scaling solutions can account for complementary data-sets such as CMB and BAO surveys.

In chapter 5 we have developed methods for consistently investigating BAO features in cosmological models with non-trivial curvature. The developed methods include formulating generalisations of comoving distance separations of galaxies to generic spacetimes, generalising the AP scaling methods used in BAO analysis to a non-FLRW setting, and formulating an empirical model for extracting knowledge about characteristic scales in a 2-point correlation function without the assumption of a fiducial cosmological model. We applied our methods to the Baryon Oscillation Spectroscopic Survey (BOSS) dataset, and investigated both the ΛCDM and timescape cosmological models as case studies.

In chapter 6 we have investigated the AP scaling conventionally used in BAO analysis for extracting information about the BAO characteristic scale using a fiducial ΛCDM model. We investigated to which extent such methods might be considered model-independent. We found that the conventionally applied constant AP scaling approximation works surprisingly well for a broad class of pairs of 'true' and fiducial models. We also found that one can modify the standard constant AP scaling approximation to be accurate for an even larger class of pairs of models through a reinterpretation of the constant AP scaling parameters. However, there are systematic

uncertainties which are not caused by the constant AP approximation, which we find to be largely independent of the exact fitting procedure chosen. These systematic uncertainties – which are of order 1% when the fiducial model differs substantially from the 'true' cosmological model – are comparable in size to the statistical errors often reported in BAO analysis. Our results indicate that the error budget of standard BAO analysis must be re-assessed to accurately account for the systematic errors related to the choice of fiducial cosmology, if the results are to be used to consistently test models which are not close to the concordance ΛCDM model in all respects.

Publications related to the PhD

Published Journal Articles

- A. Heinesen, P. Mourier and T. Buchert,
  On the covariance of scalar averaging and backreaction in relativistic inhomogeneous cosmology,
  Class. Quantum Grav. **36** (2019) 075001 [arXiv:1811.01374]

- L.H. Dam, A. Heinesen and D.L. Wiltshire,
  Apparent cosmic acceleration from type Ia supernovae,
  Mon. Not. R. Astr. Soc.472 (2017) 835, [arXiv:1706.07236]

- C. Desgrange, A. Heinesen and T. Buchert,
  Dynamical spatial curvature as a fit to type Ia supernovae,
  (accepted for publication in Int. J. Mod. Phys. D) [arXiv:1902.07915]

- A. Heinesen, C. Blake, Y. Li and D.L. Wiltshire,
  Baryon acoustic oscillation methods for generic curvature: application to the SDSS-III Baryon Oscillation Spectroscopic Survey,
  J. Cosmol. Astropart. Phys. JCAP03 (2019) 003 [arXiv:1811.11963]

Articles in preparation

- A. Heinesen, C. Blake, Y. Li and D.L. Wiltshire,
  Quantifying the accuracy of the Alcock-Paczynski scaling of baryon acoustic oscillation measurements,
  (To be submitted to *J. Cosmol. Astropart. Phys.*)

REFERENCES

[1] A. Einstein. Cosmological Considerations in the General Theory of Relativity. *Sitzungsber. Preuss. Akad. Wiss. Berlin (Math. Phys.)*, (1917):142, 1917.

[2] A. Friedmann. On the curvature of space. *Z. Phys.*, **10**:377, 1922. Republished in *Gen. Rel. Grav.*, **31**:1991, 1999.

[3] A. Friedmann. On the possibility of a world with constant negative curvature of space. *Z. Phys.*, **21**:326, 1924. Republished in *Gen. Rel. Grav.*, **31**:2001, 1999.

[4] G. Lemaître and A. S. Eddington. The expanding universe. *Mon. Not. Roy. Astron. Soc.*, **91**:490, 1931. Republished in *Gen. Rel. Grav.*, **29**:641, 1933.

[5] H. P. Robertson. On the foundations of relativistic cosmology. *Proceedings of the National Academy of Sciences of the United States of America*, **15**:822, 1929.

[6] A. Einstein and W. de Sitter. On the relation between the expansion and the mean density of the universe. *Proceedings of the National Academy of Sciences*, **18**:213, 1932.

[7] E. A. Milne. World structure and the expansion of the universe. *Nature*, **130**:9, 1932.

[8] A. G. Walker. On Milne's theory of world-structure. *Proceedings of the London Mathematical Society*, **s2-42**:90, 1937.

[9] G. Lemaître. Un Univers homogène de masse constante et de rayon croissant rendant compte de la vitesse radiale des nbuleuses extra-galactiques. *Annales de la Société Scientifique de Bruxelles*, **A47**:49, 1927. Republished in English translation: Mon. Not. Roy. Astron. Soc., 91:438, 1931.

[10] E. P. Hubble. A relation between distance and radial velocity among extra-galactic nebulae. *Proceedings of the National Academy of Sciences*, **15**:168, 1929.

[11] E. P. Hubble. Extragalactic nebulae. *Astrophys. J.*, **64**:321, 1926.

[12] E. P. Hubble. The distribution of extra-galactic nebulae. *Astrophys. J.*, **79**:8, 1934.

[13] E. Tempel *et al.* Detecting filamentary pattern in the cosmic web: a catalogue of filaments for the SDSS. *Mon. Not. Roy. Astron. Soc.*, **438**:3465, 2014. [arXiv:1308.2533].

[14] D. S. Aguado *et al.* The Fifteenth Data Release of the Sloan Digital Sky Surveys: First Release of MaNGA Derived Quantities, Data Visualization Tools and Stellar Library. *Astrophysical J. Suppl.*, **240**:23, 2019. [arXiv:1812.02759].

[15] A. A. Penzias and R. W. Wilson. A Measurement of excess antenna temperature at 4080-Mc/s. *Astrophys. J.*, **142**:419, 1965.

[16] H. Bondi. *Cosmology.* Cambridge University Press, 1952.

[17] A. McKellar. Molecular Lines from the Lowest States of Diatomic Molecules Composed of Atoms Probably Present in Interstellar Space. *Publications of the Dominion Astrophysical Observatory Victoria*, **7**:251, 1941.

[18] J. Ehlers, P. Geren, and R. K. Sachs. Isotropic Solutions of the Einstein-Liouville Equations. *J. Math. Phys.*, **9**:1344, 1968.

[19] W. R. Stoeger, R. Maartens, and G. F. R. Ellis. Proving almost homogeneity of the universe: An Almost Ehlers-Geren-Sachs theorem. *Astrophys. J.*, **443**:1, 1995.

[20] S. Räsänen. On the relation between the isotropy of the CMB and the geometry of the universe. *Phys. Rev. D*, **79**:123522, 2009. [arXiv:0903.3013].

[21] E. Lifshitz. On the gravitational stability of the expanding universe. *J. Phys. (USSR)*, **10**:116, 1946.

[22] J. M. Bardeen. Gauge-invariant cosmological perturbations. *Phys. Rev. D*, **22**:1882, 1980.

[23] H. Kodama and M. Sasaki. Cosmological Perturbation Theory. *Prog. Theor. Phys. Suppl.*, **78**:1, 1985.

[24] V. F. Mukhanov, H. A. Feldman, and R. H. Brandenberger. Theory of cosmological perturbations. *Phys. Rept.*, **215**:203, 1992.

[25] V. Springel *et al.* Simulations of the formation, evolution and clustering of galaxies and quasars. *Nature*, **435**:629, 2005. [astro-ph/0504097].

[26] V. R. Bouillot *et al.* Probing dark energy models with extreme pairwise velocities of galaxy clusters from the DEUS–FUR simulations. *Mon. Not. Roy. Astron. Soc.*, **450**:145, 2015.

[27] M. Kuhlen, M. Vogelsberger, and R. Angulo. Numerical simulations of the dark universe: State of the art and the next decade. *Phys. Dark Univ.*, **1**:50, 2012. [arXiv:1209.5745].

[28] R. K. Sachs and A. M. Wolfe. Perturbations of a cosmological model and angular variations of the microwave background. *Astrophys. J.*, **147**:73, 1967.

[29] R. C. Tolman. Thermodynamic treatment of the possible formation of helium from hydrogen. *Journal of the American Chemical Society*, **44**:1902, 1922.

[30] S. Suzuki. On the thermal equilibrium of dissociation of atom-naclei. *Proc. of the Physico-Mathematical Society of Japan*, **10**:166, 1928.

[31] H. C. Urey and C. A. Bradley. On the relative abundances of isotopes. *Phys. Rev.*, **38**:718, 1931.

[32] R. C. Tolman. *Relativity, Thermodynamics and Cosmology.* Clarendon Press, Oxford, 1934.

[33] S. Chandrasekhar and L. R. Henrich. An attempt to interpret the relative abundances of the elements and their isotopes. *Astrophys. J.*, **95**:288, 1942.

[34] G. Gamow. Expanding universe and the origin of elements. *Phys. Rev.*, **70**:572, 1946.

[35] R. A. Alpher,, H. Bethe, and G. Gamow. The origin of chemical elements. *Phys. Rev.*, **73**:803, 1948.

[36] R. A. Alpher,. A neutron-capture theory of the formation and relative abundance of the elements. *Phys. Rev.*, **74**:1577, 1948.

[37] R. A. Alpher, and R. Herman. Evolution of the universe. *Nature*, **162**:774, 1948.

[38] G. Gamow. The evolution of the universe. *Nature*, **162**:680, 1948.

[39] G. F. Smoot *et al.* Structure in the COBE differential microwave radiometer first-year maps. *Astrophys. J.*, **396**:L1, 1992.

[40] D. J. Fixsen *et al.* The cosmic microwave background spectrum from the full COBE FIRAS data set. *Astrophys. J.*, **473**:576, 1996.

[41] P. de Bernardis *et al.* A flat universe from high-resolution maps of the cosmic microwave background radiation. *Nature*, **404**:955, 2000. [astro-ph/0004404].

[42] J. M. Kovac *et al.* Detection of polarization in the cosmic microwave background using DASI. *Nature*, **420**:772, 2002. [astro-ph/0209478].

[43] C. L. Bennett *et al.* First Year Wilkinson Microwave Anisotropy Probe (WMAP) observations: Preliminary maps and basic result. *Astrophys. J. Suppl.*, **148**:1, 2003. [astro-ph/0302207].

[44] N. Aghanim *et al.* Planck 2015 results - xi. cmb power spectra, likelihoods, and robustness of parameters. *Astron. Astrophys*, **594**:A11, 2016. [arXiv:1507.02704].

[45] C. T. Kowal. Absolute magnitudes of supernovae. *Astron. J.*, **73**:1021, 1968.

[46] M. M. Phillips. The absolute magnitudes of Type IA supernovae. *Astrophys. J.*, **413**:L105, 1993.

[47] A. G. Riess *et al.* Observational Evidence from Supernovae for an Accelerating Universe and a Cosmological Constant. Astron. J., **116**:1009, 1998. [astro-ph/9805201].

[48] S. Perlmutter *et al.* Measurements of Omega and Lambda from 42 High-Redshift Supernovae. *Astrophys. J.*, **517**:565, 1999. [astro-ph/9812133].

[49] P. J. E. Peebles and J. T. Yu. Primeval Adiabatic Perturbation in an Expanding Universe. *Astrophys. J.*, **162**:815, 1970.

[50] R. A. Sunyaev and Y. B. Zeldovich. Small-Scale Fluctuations of Relic Radiation. *Ap&SS*, **7**:3, 1970.

[51] F. S. Labini. Inhomogeneities in the universe. *Class. Quantum Grav.*, **28**:164003, 2011. [arXiv:1103.5974v2].

[52] P. J. E. Peebles. Statistical Analysis of Catalogs of Extragalactic Objects. I. Theory. *Astrophys. J.*, **185**:413, 1973.

[53] M. Davis and P. J. E. Peebles. A survey of galaxy redshifts. V - The two-point position and velocity correlations. *Astrophys. J.*, **267**:465, 1983.

[54] D. J. Eisenstein and W. Hu. Baryonic Features in the Matter Transfer Function. *Astrophys. J.*, **496**:605, 1998. [astro-ph/9709112].

[55] T. Matsubara. Correlation Function in Deep Redshift Space as a Cosmological Probe. *Astrophys. J.*, **615**:573, 2004. [astro-ph/0408349].

[56] D. J. Eisenstein *et al.* Detection of the Baryon Acoustic Peak in the Large-Scale Correlation Function of SDSS Luminous Red Galaxies. *Astrophys. J.*, **633**:560, 2005. [astro-ph/0501171].

[57] S. Cole *et al.* The 2dF Galaxy Redshift Survey: Power-spectrum analysis of the final dataset and cosmological implications. *Mon. Not. R. Astr. Soc.*, **362**:505, 2005. [astro-ph/0501174].

[58] C. Blake *et al.* The WiggleZ Dark Energy Survey: mapping the distance-redshift relation with baryon acoustic oscillations. *Mon. Not. R. Astr. Soc.*, **418**:1707, 2011. [arXiv:1108.2635].

[59] S. Alam *et al.* The clustering of galaxies in the completed SDSS-III Baryon Oscillation Spectroscopic Survey: cosmological analysis of the DR12 galaxy sample. *Mon. Not. R. Astr. Soc.*, **470**:2617, 2017. [arXiv:1607.03155].

[60] N. G. Busca *et al.* Baryon acoustic oscillations in the Lyα forest of BOSS quasars. *Astron. Astrophys*, **552**:A96, 2013. [arXiv:1211.2616].

[61] T. Delubac *et al.* Baryon acoustic oscillations in the Lyα forest of BOSS DR11 quasars. *Astron. Astrophys*, **574**:A59, 2015. [arXiv:1404.1801].

[62] N. Aghanim *et al.* Planck 2018 results. VI. Cosmological parameters. *e-Print arXiv:1807.06209*, 2018. [arXiv:1807.06209].

[63] W. L. Freedman. Cosmology at a Crossroads. Nature Astron., **1**:0121, 2017. [arXiv:1706.02739].

[64] P. A. R. Ade *et al.* Planck 2015 results. XXIV. Cosmology from Sunyaev-Zeldovich cluster counts. *Astron. Astrophys*, **594**:A24, 2016. [arXiv:1502.01597].

[65] H. M. Bourboux *et al.* Baryon acoustic oscillations from the complete SDSS-III Lyα-quasar cross-correlation function at z=2.4. *Astron. Astrophys*, **608**:A130, 2017. [arXiv:1708.02225].

[66] B. D. Fields. The primordial lithium problem. Ann. Rev. Nucl. Part. Sci., **61**:47, 2011. [arXiv:1203.3551].

[67] H. Hildebrandt *et al.* KiDS-450: Cosmological parameter constraints from tomographic weak gravitational lensing. *Mon. Not. R. Astr. Soc.*, **465**:1454, 2017. [arXiv:1606.05338].

[68] T. Buchert, A. A. Coley, H. Kleinert, B. F. Roukema, and D. L. Wiltshire. Observational Challenges for the Standard FLRW Model. *Int. J. Mod. Phys. D*, **25**:1630007, 2016. [arXiv:1512.03313].

[69] L. Bianchi. On the three-dimensional spaces which admit a continuous group of motions. *Gen. Rel. Grav.*, **33**:2171, 1898.

[70] A. H. Taub. Empty space-times admitting a three parameter group of motions. *Ann. Math.*, **53**:472, 1951.

[71] O. Heckman and O. Schücking. *Relativistic Cosmology in Gravitation (an introduction to current research).* New York, Wiley, 1962.

[72] G. F. R. Ellis and M. A. H. MacCallum. A class of homogeneous cosmological models. *Communications in Mathematical Physics*, **12**:108, 1969.

[73] R. C. Tolman. Effect of Inhomogeneity on Cosmological Models. *Proc. Nat. Acad. Sci.*, **20**:169, 1934.

[74] H. Bondi. Spherically Symmetrical Models in General Relativity. *Mon. Not. R. Astr. Soc.*, **107**:410, 1947.

[75] A. Einstein and E. G. Straus. The Influence of the Expansion of Space on the Gravitation Fields Surrounding the Individual Stars. *Rev. Mod. Phys.*, **17**:120, 1945. Err. **18**:148, 1946.

[76] P. Szekeres. A class of inhomogeneous cosmological models. *Commun. Math. Phys.*, **41**:55, 1975.

[77] W. Israel. Singular hypersurfaces and thin shells in general relativity. *Nuovo Cim. B*, **44S10**:1, 1966.

[78] W. B. Bonnor and P. A. Vickers. Junction conditions in general relativity. *Gen. Rel. Grav.*, **13**:29, 1981.

[79] R. A. Isaacson. Gravitational Radiation in the Limit of High Frequency. I. The Linear Approximation and Geometrical Optics. *Phys. Rev.*, **166**:1263, 1968.

[80] R. A. Isaacson. Gravitational Radiation in the Limit of High Frequency. II. Nonlinear Terms and the Effective Stress Tensor. *Phys. Rev.*, **166**:1272, 1968.

[81] G. A. Burnett. The High Frequency Limit in General Relativity. *J. Math. Phys.*, **30**:90, 1989.

[82] S. R. Green and R. M. Wald. How well is our universe described by an FLRW model? *Class. Quant. Grav.*, **31**:234003, 2014. [arXiv:1407.8084].

[83] G. F. R. Ellis. Relativistic Cosmology: Its Nature, Aims and Problems. *General Relativity and Gravitation*, **GR10 Conf. Rep.**:215, Reidel, Dordrecht, 1984.

[84] G. F. R. Ellis and W. Stoeger. The fitting problem in cosmology. *Class. Quantum Grav.*, **4**:1697, 1987.

[85] D. L. Wiltshire. Cosmological equivalence principle and the weak–field limit. *Phys. Rev. D*, **78**:084032, 2008. [arXiv:0809.1183].

[86] D. L. Wiltshire. What is dust?—Physical foundations of the averaging problem in cosmology. *Class. Quantum Grav.*, **28**:164006, 2011. [arXiv:1106.1693].

[87] T. Buchert. On average properties of inhomogeneous fluids in general relativity. I: Dust cosmologies. *Gen. Relativ. Grav.*, **32**:105, 2000. [gr-qc/9906015].

[88] T. Buchert. On average properties of inhomogeneous fluids in general relativity. II: Perfect fluid cosmologies. *Gen. Relativ. Grav.*, **33**:1381, 2001. [gr-qc/0102049].

[89] T. Buchert and S. Räsänen. Backreaction in Late–Time Cosmology. *Annu. Rev. Nucl. Part. Sci.*, **62**:57, 2012. [arXiv:1112.5335].

[90] M. Gasperini, G. Marozzi, and G. Veneziano. Gauge invariant averages for the cosmological backreaction. *J. Cosmol. Astropart. Phys.*, (03):011, 2009. [arXiv:0901.1303].

[91] M. Gasperini, G. Marozzi, and G. Veneziano. A covariant and gauge invariant formulation of the cosmological "backreaction". *J. Cosmol. Astropart. Phys.*, (02):009, 2010. [arXiv:0912.3244].

[92] M. Gasperini, G. Marozzi, F. Nugier, and G. Veneziano. Light cone averaging in cosmology: formalism and applications. *J. Cosmol. Astropart. Phys.*, (07):008, 2011. [arXiv:1104.1167].

[93] K. Bolejko. Emerging spatial curvature can resolve the tension between high-redshift CMB and low-redshift distance ladder measurements of the Hubble constant. *Phys. Rev. D*, **97**:103529, 2018. [arXiv:1712.02967].

[94] M. Korzyński. Covariant coarse–graining of inhomogeneous dust flow in General Relativity. *Class. Quantum Grav.*, **27**:105015, 2010.

[95] D. L. Wiltshire. Cosmic clocks, cosmic variance and cosmic averages. *New J. Phys.*, **9**:337, 2007. [arXiv:0702.0732].

[96] D. L. Wiltshire. Exact solution to the averaging problem in cosmology. *Phys. Rev. Lett.*, **99**:251101, 2007. [arXiv:0709.0732].

[97] D. L. Wiltshire. Average observational quantities in the timescape cosmology. *Phys. Rev. D.*, **80**:123512, 2009. [arXiv:0909.0749].

[98] J. A. G. Duley, M. A. Nazer, and D. L. Wiltshire. Timescape cosmology with radiation fluid. *Class. Quantum Grav.*, **30**:175006, 2013. [arXiv:1306.3208].

[99] R. M. Zalaletdinov. Averaging out the Einstein equations and macroscopic space-time geometry. *Gen. Relativ. Grav.*, **24**:1015, 1992.

[100] R. M. Zalaletdinov. Towards a theory of macroscopic gravity. *Gen. Relativ. Grav.*, **25**:673, 1993.

[101] R. M. Zalaletdinov. Averaging problem in general relativity, macroscopic gravity and using Einstein's equations in cosmology. *Bull. Astron. Soc. India*, **25**:401, 1997. [gr-qc/9703016].

[102] T. Buchert. Dark Energy from Structure: A Status Report. *Gen. Rel. Grav.*, **40**:467, 2008. [arXiv:0707.2153].

[103] I. Ben-Dayan, M. Gasperini, G. Marozzi, F. Nugier, and G. Veneziano. Backreaction on the luminosity-redshift relation from gauge invariant light cone averaging. *J. Cosmol. Astropart. Phys.*, (04):36, 2012. [arXiv:1202.1247].

[104] S. Räsänen. Light propagation in statistically homogeneous and isotropic dust universes. *J. Cosmol. Astropart. Phys. JCAP*, (02):011, 2009. [arXiv:0812.2872].

[105] S. Räsänen. Light propagation in statistically homogeneous and isotropic universes with general matter content. *J. Cosmol. Astropart. Phys. JCAP*, (03):018, 2010. [arXiv:0912.3370].

[106] N. Uzun. Reduced phase space optics for general relativity: Symplectic ray bundle transfer. 2018. [arXiv:1811.10917].

[107] C. A. Clarkson, G. F. R. Ellis, J. Larena, and O. C. Umeh. On cosmological backreaction and its dependence on space-time foliation. *Rep. Prog. Phys.*, **74**:112901, 2011. [arXiv:1109.2314].

[108] A. Heinesen and Mourier. *In preparation*. 2019.

[109] T. Buchert, P. Mourier, and X. Roy. On average properties of inhomogeneous fluids in general relativity. III: General fluid cosmologies. *In preparation*. 2019.

[110] T. Buchert, P. Mourier, and X. Roy. On cosmological backreaction and its dependence on space-time foliation. *Class. Quantum Grav. Lett.*, **35**:24LT02, 2018. [arXiv:1805.10455].

[111] H. Skarke. Inhomogeneity implies accelerated expansion. *Phys. Rev. D*, **89**:043506, 2014. [arXiv:1310.1028].

[112] R. A. Sussman. Quasi–local variables and inhomogeneous cosmological sources with spherical symmetry. *AIP Conf. Proc.*, **1**:228, 2008. [arXiv:0810.1120].

[113] R. A. Sussman. Back-reaction and effective acceleration in generic LTB dust models. *Class. Quantum Grav.*, **28**:235002, 2011. [arXiv:1102.2663].

[114] T. Buchert and J. Ehlers. Averaging inhomogeneous Newtonian cosmologies. *Astron. Astrophys.*, **320**:1, 1997. [astro-ph/9510056].

[115] T. Buchert and M. Carfora. Regional averaging and scaling in relativistic cosmology. *Gen. Relativ. Grav.*, **19**:6109, 2002. [gr-qc/0210037].

[116] G. F. R. Ellis and T. Buchert. Density-gradient–vorticity relation in perfect-fluid Robertson-Walker perturbations. *Phys. Lett. A*, **347**:38, 2005. [gr-qc/0506106].

[117] E. Gourgoulhon. $3+1$ *Formalism in general relativity. Bases of numerical relativity* . Springer, 2012.

[118] G. F. R. Ellis, M. Bruni, and J. Hwang. Density-gradient–vorticity relation in perfect-fluid Robertson-Walker perturbations. *Phys. Rev. D*, **42**:1035, 1990.

[119] S. Räsänen. Light propagation in statistically homogeneous and isotropic universes with general matter content. *J. Cosmol. Astropart. Phys.*, (03):018, 2010. [arXiv:0912.3370].

[120] I. Delgado Gaspar, J. C. Hidalgo, and R. A. Sussman. Non-comoving baryons and cold dark matter in cosmic voids. *Eur. Phys. J. C*, **79**:106, 2019. [arXiv:1811.03634].

[121] J. Larena, J. M. Alimi, T. Buchert, and P.-S. Corasaniti. Testing backreaction effects with observations. *Phys. Rev. D*, **79**:083011, 2009. [arXiv:0808.1161].

[122] M. Grasso, M. Korzyński, and J. Serbenta. Geometric optics in general relativity using bilocal operators. *Phys. Rev. D*, **99**:064038, 2018. [arXiv:1811.10284].

[123] M. Betoule *et al.* Improved cosmological constraints from a joint analysis of the SDSS-II and SNLS supernova samples. *Astron. Astrophys.*, **568**:A22, 2014. [arXiv:1401.4064].

[124] B. M. Leith, S. C. C. Ng, and D. L. Wiltshire. Gravitational energy as dark energy: Concordance of cosmological tests. *Astrophys. J.*, **672**:L91, 2008. [arXiv:0709.2535].

[125] P. R. Smale and D. L. Wiltshire. Supernova tests of the timescape cosmology. *Mon. Not. R. Astr. Soc.*, **413**:367, 2011. [arXiv:1009.5855].

[126] P. R. Smale. Gamma-ray burst distances and the timescape cosmology. *Mon. Not. R. Astr. Soc.*, **418**:2779, 2011. [arXiv:1107.5596].

[127] M. A. Nazer and D. L. Wiltshire. Cosmic microwave background anisotropies in the timescape cosmology. *Phys. Rev. D.*, **91**:063519, 2015. [arXiv:1410.3470].

[128] D. L. Wiltshire. Cosmic structure, averaging and dark energy. In Perez Bergliaffa, S. E. and Novello, M., editor, *Proceedings of XVth Brazilian School of Cosmology and Gravitation*, p. 203. Cambridge: Cambridge Scientific Publishers, 2014. [arXiv:1311.3787].

[129] C. Clarkson, B. Bassett, and T. H. Lu. A general test of the Copernican Principle. *Phys. Rev. Lett.*, **101**:011301, 2008. [arXiv:0712.3457].

[130] S. Räsänen, K. Bolejko, and A. Finoguenov. New test of the Friedmann-Lemaître-Robertson-Walker metric using the distance sum rule. *Phys. Rev. Lett.*, **115**:101301, 2015. [arXiv:1412.4976].

[131] J. Larena, J.-M. Alimi, T. Buchert, M. Kunz, and Corasaniti P.-S. Testing backreaction effects with observations. *Phys. Rev. D.*, **79**:083011, 2009. [arXiv:0808.1161].

[132] M. Lavinto, S. Räsänen, and S. J. Szybka. Average expansion rate and light propagation in a cosmological Tardis spacetime. *J. Cosmol. Astropart. Phys. JCAP*, (12):051, 2013. [arXiv:1308.6731].

[133] D. Sapone, E. Majerotto, and S. Nesseris. Curvature versus distances: Testing the FLRW cosmology. *Phys. Rev. D.*, **90**:023012, 2014. [arXiv:1402.2236].

[134] S. Jha, A. G. Riess, and R. P. Kirshner. Improved distances to type Ia supernovae with Multicolor Light Curve Shapes: MLCS2k2. *Astrophys. J.*, **659**:122, 2007. [astro-ph/0612666].

[135] J. Guy *et al.* SALT: a spectral adaptive light curve template for type Ia supernovae. *Astron. Astrophys*, **443**:781, 2005. [astro-ph/0506583].

[136] J. Guy *et al.* SALT2: using distant supernovae to improve the use of Type Ia supernovae as distance indicators. *Astron. Astrophys*, **466**:11, 2007. [astro-ph/0701828].

[137] J. T. Nielsen, A. Guffanti, and S. Sarkar. Marginal evidence for cosmic acceleration from Type Ia supernovae. *Sci. Rep.*, **6**:35596, 2016. [arXiv:1506.01354].

[138] M. C. March, R. Trotta, P. Berkes, G. D. Starkman, and P. M. Vaudrevange. Improved constraints on cosmological parameters from SNIa data. *Mon. Not. Roy. Astron. Soc.*, **418**:2308, 2011. [arXiv:1102.3237].

[139] D. Rubin and B. Hayden. Is the expansion of the universe accelerating? All signs point to yes. *Astrophys. J.*, **833**:L30, 2016. [arXiv:1610.08972].

[140] F. Feroz and M. P. Hobson. MultiNest: an efficient and robust Bayesian inference tool for cosmology and particle physics. *Mon. Not. R. Astr. Soc.*, **398**:1601, 2009. [arXiv:0809.3437].

[141] J. Skilling. Nested sampling. *AIP Conf. Proc.*, **735**:395, 2004.

[142] J. Buchner *et al.* X-ray spectral modelling of the AGN obscuring region in the CDFS: Bayesian model selection and catalogue. *Astron. Astrophys*, **564**:A125, 2014. [arXiv:1402.0004].

[143] H. Shariff *et al.* BAHAMAS: New analysis of type Ia supernovae reveals inconsistencies with standard cosmology. *Astrophys. J.*, **827**:1, 2016. [arXiv:1510.05954].

[144] P. A. R. Ade *et al.* Planck 2015 results. XIII. Cosmological parameters. *Astron. Astrophys*, **594**:A13, 2016. [arXiv:1502.01589].

[145] É. Aubourg *et al.* Cosmological implications of baryon acoustic oscillation measurements. *Phys. Rev.D*, **92**:123516, 2015. [arXiv:1411.1074].

[146] A. Aghamousa, A. Shafieloo, M. Arjunwadkar, and T. Souradeep. Unveiling acoustic physics of the CMB using nonparametric estimation of the temperature angular power spectrum for Planck. *J. Cosmol. Astropart. Phys. JCAP*, (02):007, 2015. [arXiv:1412.3552].

[147] D. W. Hogg *et al.* Cosmic homogeneity demonstrated with luminous red galaxies. *Astrophys. J.*, **624**:54, 2005. [astro-ph/0411197].

[148] M. Scrimgeour *et al.* The WiggleZ Dark Energy Survey: the transition to large-scale cosmic homogeneity. *Mon. Not. Roy. Astron. Soc.*, **425**:116, 2012. [arXiv:1205.6812].

[149] A. G. Riess *et al.* New Hubble Space Telescope Discoveries of Type Ia Supernovae at $z > 1$: Narrowing Constraints on the Early Behavior of Dark Energy. *Astrophys. J.*, **659**:98, 2007. [astro-ph/0611572].

[150] B. S. Haridasu, V. V. Lukovi$\acute{c}$, R. D'Agostino, and N. Vittorio. Strong evidence for an accelerating universe. *Astron. Astrophys*, **600**:L1, 2017. [arXiv:1702.08244].

[151] I. Tutusaus *et al.* Is cosmic acceleration proven by local cosmological probes? *Astron. Astrophys*, **602**:A73, 2017. [arXiv:1706.05036].

[152] G. F. Lewis, L. A. Barnes, and R. Kaushik. Primordial nucleosynthesis in the $R_h = ct$ cosmology: Pouring cold water on the simmering Universe. *Mon. Not. R. Astr. Soc.*, **460**:291, 2016. [arXiv:1604.07460].

[153] J. Mosher *et al.* Cosmological parameter uncertainties from SALT-II Type Ia supernova light curve models. *Astrophys. J.*, **793**:16, 2014. [arXiv:1401.4065].

[154] R. Gaur. Understanding The Universe's Accelerated Expansion by Probing Type Ia Supernovae Light-curves. *Internship report Phys391, University of Canterbury*, 2019.

[155] D. M. Scolnic *et al.* The Complete Light-curve Sample of Spectroscopically Confirmed SNe Ia from Pan-STARRS1 and Cosmological Constraints from the Combined Pantheon Sample. *Astrophys. J.*, **859**:101, 2018. [arXiv:1710.00845].

[156] M. Visser. Jerk and the cosmological equation of state. *Class. Quantum Grav.*, **21**:2603, 2004. [gr-qc/0309109].

[157] J. Calcino and T. Davis. The need for accurate redshifts in supernova cosmology. *J. Cosmol. Astropart. Phys. JCAP*, (01):038, 2017. [arXiv:1610.07695].

[158] K. Bolejko, M. A. Nazer, and D. L. Wiltshire. Differential cosmic expansion and the Hubble flow anisotropy. *J. Cosmol. Astropart. Phys. JCAP*, (06):035, 2016. [arXiv:1512.07364].

[159] D. L. Wiltshire. Hubble flow variance and the cosmic rest frame. *Phys. Rev.D*, **88**:083529, 2013. [arXiv:1201.5371].

[160] J. H. McKay and D. L. Wiltshire. Defining the frame of minimum nonlinear Hubble expansion variation. *Mon. Not. R. Astr. Soc.*, **457**:3285, 2016. Err. **463**:3113, 2016.

[161] A. Conley *et al.* Is there evidence for a Hubble bubble? The nature of type Ia supernova colors and dust in external galaxies. *Astrophys. J.*, **664**:L13, 2007. [arXiv:0705.0367].

[162] M. Hicken *et al.* Improved dark energy constraints from $\simeq$100 new CfA supernova type Ia light curves. *Astrophys. J.*, **700**:1097, 2009. [arXiv:0901.4804].

[163] D. J. Fixen *et al.* The cosmic microwave background spectrum from the full COBE/FIRAS data set. *Astrophys. J.*, **473**:576, 1996. [astro-ph/9605054].

[164] M. J. Hudson *et al.* Streaming motions of galaxy clusters within 12000 km s^{-1}. 5. The peculiar velocity field. *Mon. Not. R. Astr. Soc.*, **352**:61, 2004. [astro-ph/0404386].

[165] A. Conley *et al.* Supernova constraints and systematic uncertainties from the first 3 years of the Supernova Legacy Survey. *Astrophys. J. Suppl.*, **192**:1, 2011. [arXiv:1104.1443].

[166] H. Akaike. A new look at the statistical model identification. *IEEE Trans. Automat. Contr.*, **19**:716, 1974.

[167] G. Schwarz. Estimating the dimension of a model. *Ann. Statist.*, **6**:461, 1978.

[168] R. E. Kass and A. E. Raftery. Bayes factors. *J. Am. Statist. Assoc.*, **90**:773, 1995.

[169] R. Trotta. Applications of Bayesian model selection to cosmological parameters. *Mon. Not. R. Astr. Soc.*, **378**:72, 2007. [astro-ph/0504022].

[170] D. J. Spiegelhalter *et al.* Bayesian measures of model complexity and fit. *J. Royal. Stat. Soc. B*, **64**:583, 2002.

[171] D. Tytler *et al.* Review of big bang nucleosynthesis and primordial abundances. *Phys. Scripta*, **T85**:12, 2000. [astro-ph/0001318].

[172] K. A. Olive, G. Steigman, and T. P. Walker. Primordial nucleosynthesis: Theory and observations. *Phys. Rept.*, **333**:389, 2000. [astro-ph/9905320].

[173] T. Buchert, J. Larena, and J.-M. Alimi. Correspondence between kinematical backreaction and scalar field cosmologies - the 'morphon field'. *Class. Quantum Grav.*, **23**:6379, 2006. [gr-qc/0606020].

[174] X. Roy, T. Buchert, S. Carloni, and N. Obadia. Global gravitational instability of FLRW backgrounds - interpreting the dark sectors. *Class. Quantum Grav.*, **28**:165004, 2011. [arXiv:1103.1146].

[175] S.-L. Cao, H.-Y. Teng, H.-Y. Wan, H.-R. Yu, and Zhang T.-J. Testing backreaction effects with observational Hubble parameter data. *Eur. Phys. J. C*, **78**:170, 2018. [arXiv:1704.01774].

[176] M. Kasai. Apparent Acceleration through the Large-scale Inhomogeneities: Post-Friedmannian effects of inhomogeneities on the luminosity distance. *Prog. Theor. Phys.*, **117**:1067, 2007. [astro-ph/0703298].

[177] T. Buchert. Dark Energy from structure: a status report. *Gen. Relativ. Gravit.*, **40**:467, 2008. [arXiv:0707.2153].

[178] P. C. Stichel. Analytical solutions for two inhomogeneous cosmological models with energy flow and dynamical curvature. *Phys. Rev. D*, **98**:104022, 2018. [arXiv:1805.08459].

[179] A. Wiegand, T. Buchert, and M. Ostermann. Direct Minkowski Functional analysis of large redshift surveys: a new high–speed code tested on the luminous red galaxy Sloan Digital Sky Survey-DR7 catalogue. *Mon. Not. Roy. Astron. Soc.*, **443**:241, 2014. [arXiv:1311.3661].

[180] L. H. Dam, A. Heinesen, and D. L. Wiltshire. Apparent cosmic acceleration from type Ia supernovae. *Mon. Not. Roy. Astron. Soc.*, **472**:835, 2017. [arXiv:1706.07236].

[181] T. Buchert, C. Nayet, and A. Wiegand. Lagrangian theory of structure formation in relativistic cosmology II: average properties of a generic evolution model. *Phys. Rev. D.*, **87**:123503, 2013. [arXiv:1303.6193].

[182] M. Kerscher and J. Weller. On Model Selection in Cosmology. *SciPost Phys. Lect. Notes*, **9**, 2019. [arXiv:1901.07726].

[183] A. Kashlinsky, F. Atrio-Barandela, D. Kocevski, and H. Ebeling. A measurement of large-scale peculiar velocities of clusters of galaxies: results and cosmological implications. *Astrophys. J.*, **686**:L49, 2009. [arXiv:0809.3734].

[184] B. L'Huillier, A. Shafieloo, E. V. Linder, and A. G. Kim. Model Independent Expansion History from Supernovae: Cosmology versus Systematics. *Mon. Not. Roy. Astron. Soc.*, **485**:2783, 2019. [arXiv:1812.03623].

[185] M. Korzyński. Nonlinear effects of general relativity from multiscale structure. *Class. Quantum Grav.*, **32**:215013, 2015. [arXiv:1412.3865].

[186] M. Korzyński. Backreaction and continuum limit in a closed universe filled with black holes. *Class. Quantum Grav.*, **31**:085002, 2014. [arXiv:1312.0494].

[187] K. Bolejko and J. J. Ostrowski. The environment-dependence of the growth of the most massive objects in the universe. *Phys. Rev. D*, **99**:124036, 2019. [arXiv:1805.11047].

[188] M. Kasai and T. Futamase. A possible solution to the Hubble constant discrepancy – Cosmology where the local volume expansion is driven by the domain average density. arXiv:1904.09689. 2019. [arXiv:1904.09689].

[189] F. Montanari and S. Räsänen. Backreaction and FRW consistency conditions. *J. Cosmol. Astropart. Phys. JCAP*, (11):032, 2017. [arXiv:1709.06022].

[190] A. Wiegand and T. Buchert. Multiscale cosmology and structure-emerging Dark Energy: A plausibility analysis. *Phys. Rev. D*, **82**:023523, 2010. [arXiv:1002.3912].

[191] S. Krastanov. Constraints from Observations on Backreaction Models. *Master thesis M1, École Normale Supérieure de Lyon*, 2012.

[192] L. Amendola *et al.* Cosmology and Fundamental Physics with the Euclid Satellite. *Living Rev. Rel.*, **21**:1, 2018. [arXiv:1606.00180].

[193] L. Anderson *et al.* The clustering of galaxies in the SDSS-III Baryon Oscillation Spectroscopic Survey: baryon acoustic oscillations in the Data Releases 10 and 11 Galaxy samples. *Mon. Not. R. Astr. Soc.*, **441**:24, 2014. [arXiv:1312.4877].

[194] A. J. Cuesta *et al.* The clustering of galaxies in the SDSS-III Baryon Oscillation Spectroscopic Survey: Baryon Acoustic Oscillations in the correlation function of LOWZ and CMASS galaxies in Data Release 12. *Mon. Not. R. Astr. Soc.*, **457**:1770, 2016. [arXiv:1509.06371].

[195] D. J. Eisenstein, H. Seo, E. Sirko, and D. Spergel. Improving Cosmological Distance Measurements by Reconstruction of the Baryon Acoustic Peak. *Astrophys. J.*, **664**:675, 2007. [astro-ph/0604362].

[196] C. Blake, I. Achitouv, A. Burden, and Y. Rasera. The environmental dependence of the baryon acoustic peak in the Baryon Oscillation Spectroscopic Survey CMASS sample. *Mon. Not. R. Astr. Soc.*, **482**:578, 2018. [arXiv:1810.01655].

[197] B. F. Roukema, T. Buchert, J. J. Ostrowski, and M. J. France. Evidence for an environment-dependent shift in the baryon acoustic oscillation peak. *Mon. Not. R. Astr. Soc.*, **448**:1660, 2015. [arXiv:1410.1687].

[198] M. C. Neyrinck *et al.* Density-dependent clustering - I. Pulling back the curtains on motions of the BAO peak. *Mon. Not. R. Astr. Soc.*, **478**:2495, 2018. [arXiv:1610.06215].

[199] X. Xu, A. J. Cuesta, N. Padmanabhan, D. J. Eisenstein, and C. K. McBride. Measuring D_A and H at $z = 0.35$ from the SDSS DR7 LRGs using baryon acoustic oscillations. *Mon. Not. R. Astr. Soc.*, **431**:2834, 2013. [arXiv:1206.6732].

[200] S. Räsänen. Light propagation in statistically homogeneous and isotropic dust universes. *J. Cosmol. Astropart. Phys. JCAP*, (03):018, 2010. [arXiv:0812.2872].

[201] M. Kerscher, I. Szapudi, and A. S. Szalay. A comparison of estimators for the two-point correlation function. *Astrophys. J.*, **535**:L13, 2000. [astro-ph/9912088].

[202] S. D. Landy and A. S. Szalay. Bias and variance of angular correlation functions. *Astrophys. J.*, **412**:64, 1993.

[203] D. J. Eisenstein *et al.* SDSS-III: Massive Spectroscopic Surveys of the Distant Universe, the Milky Way, and Extra-Solar Planetary Systems. *Astron. J.*, **142**:72, 2011. [arXiv:1101.1529].

[204] K. S. Dawson *et al.* The Baryon Oscillation Spectroscopic Survey of SDSS-III. *Astron. J.*, **145**:10, 2013. [arXiv:1208.0022].

[205] S. Alam *et al.* The Eleventh and Twelfth Data Releases of the Sloan Digital Sky Survey: Final Data from SDSS-III. *Astrophys. J. Suppl.*, **219**:12, 2015. [arXiv:1501.00963].

[206] B. Reid *et al.* SDSS-III Baryon Oscillation Spectroscopic Survey Data Release 12: galaxy target selection and large scale structure catalogues. *Mon. Not. R. Astr. Soc.*, **455**:1553, 2016. [arXiv:1509.06529].

[207] H. A. Feldman, N. Kaiser, and J. A. Peacock. Power spectrum analysis of three-dimensional redshift surveys. *Astrophys. J.*, **426**:23, 1994. [astro-ph/9304022].

[208] M. Vargas-Magaña and S. Ho. The clustering of galaxies in the completed SDSS-III Baryon Oscillation Spectroscopic Survey: theoretical systematics and Baryon Acoustic Oscillations in the galaxy correlation function. *Mon. Not. R. Astr. Soc.*, **477**:1153, 2018. [arXiv:1610.03506].

[209] R. E. Smith, R. Scoccimarro, and R. K. Sheth. Motion of the acoustic peak in the correlation function. *Phys. Rev. D.*, **77**:043525, 2008. [astro-ph/0703620].

[210] E. Sanchez *et al.* Tracing The Sound Horizon Scale With Photometric Redshift Surveys. *Mon. Not. R. Astr. Soc.*, **411**:227, 2011. [arXiv:1006.3226].

[211] E. Sanchez, D. Alonso, F. J. Sanchez, J. G. Bellido, and I. Sevilla. Precise Measurement of the Radial Baryon Acoustic Oscillation Scales in Galaxy Redshift Surveys. *Mon. Not. R. Astr. Soc.*, **434**:2008, 2013. [arXiv:1210.6446].

[212] H.-J. Seo, E. R. Siegel, D. J. Eisenstein, and M. White. Non-linear structure formation and the acoustic scale. *Astrophys. J.*, **686**:13, 2008. [arXiv:0805.0117].

[213] L. H. Dam. Inhomogeneous cosmological models and the cosmic microwave background. *M.Sc. thesis, University of Canterbury, Christchurch*, 2016.

[214] N. Kaiser. Clustering in real space and in redshift space. *Mon. Not. R. Astr. Soc.*, **227**:1, 1987.

[215] M. White *et al.* The clustering of massive galaxies at z$\sim$0.5 from the first semester of BOSS data. *Astrophys. J.*, **728**:126, 2011. [arXiv:1010.4915].

[216] C. Blake *et al.* The WiggleZ Dark Energy Survey: testing the cosmological model with baryon acoustic oscillations at z = 0.6. *Mon. Not. R. Astr. Soc.*, **415**:2892, 2011. [arXiv:1105.2862].

[217] C. Alcock and B. Paczyński. An evolution free test for non-zero cosmological constant. *Nature*, **281**:358, 1979.

[218] W. E. Ballinger, J. A. Peacock, and A. F. Heavens. Measuring the cosmological constant with redshift surveys. *Mon. Not. R. Astr. Soc.*, **282**:877, 1996. [astro-ph/9605017].

[219] T. Matsubara and Y. Suto. Cosmological redshift distortion of correlation functions as a probe of the density parameter and the cosmological constant. *Astrophys. J.*, **470**:L1, 1996. [astro-ph/9604142].

[220] N. Padmanabhan and M. White. Constraining Anisotropic Baryon Oscillations. *Phys. Rev. D.*, **77**:123540, 2008. [arXiv:0804.0799].

[221] P. Carter *et al.* The Impact of the Fiducial Cosmology Assumption on BAO Cosmological Parameter Inference. arXiv:1906.03035. 2019. [astro-ph/1906.03035].